University of Bath

UNIVERSITY OF BATH

PHD

Front Propagation for Nematic Liquid Crystals

Spicer, Amy

Award date:
2017

Awarding institution:
University of Bath

Link to publication

Front Propagation for Nematic Liquid Crystals

submitted by

Amy Spicer

for the degree of Doctor of Philosophy

of the

University of Bath

Department of Mathematical Sciences

September 2016

COPYRIGHT

Signature of Author. . . . .

Amy Spicer

Contents

Acknowledgements

First of all, I would like to thank my supervisor Apala Majumdar. This thesis would not have been possible without her continuous input and support. I am especially grateful for Apala's guidance and excellent feedback as I have been writing up. I have thoroughly enjoyed being her student over the last four years. I would like to thank Paul Milewski for his advice on the numerical work in this thesis. Paul has been a fantastic help and so much fun to work with. My thanks goes to Giacomo Canevari, Patrick Dondl and Nicolas Dirr with whom it has been a pleasure to collaborate and to my examiners Chris Budd and Peter Howell for their helpful comments on this thesis. I gratefully acknowledge support from an EPSRC studentship.

A big thank you goes to all my family and friends. My Mum and my Nan, for all their support and encouragement. My cousin Adam, for always being so funny. My Dad, for sparking my interest in mathematics when I was little. My time in Bath was made so much more enjoyable by my fantastic office mates, Katy, Jen, Steve and Jack. Lastly, thank you for everything Graham, you always have so much confidence in me and I'm so incredibly grateful.

Abstract

We study the gradient flow model of the Landau-de Gennes energy functional for nematic liquid crystals at the isotropic-nematic transition temperature on prototype geometries. We focus on the three-dimensional droplet, the disc and the square with Dirichlet boundary conditions and different types of initial conditions, with the aim of observing interesting transient dynamics which may be of practical relevance. We use a fourth-order Landau-de Gennes bulk potential which admits isotropic and uniaxial minima at the transition temperature. For a droplet with radial boundary conditions, a large class of physically relevant initial conditions generate dynamic solutions with a well-defined isotropic-nematic front which propagates according to mean curvature for significant times. We introduce radially symmetric obstacles into the droplet and prove the existence of pulsating wave solutions of the gradient flow model in certain parameter regimes. The average velocity of the pulsating wave is determined by some critical forcing which can be verified numerically. On the unit disc, we make a distinction between planar and non-planar initial conditions and minimal and non-minimal Dirichlet boundary conditions. Planar initial conditions generate solutions with an isotropic core for all times whereas non-planar initial conditions generate solutions that escape into the third dimension. Non-minimal boundary conditions result in solutions with boundary layers. These solutions can have either a largely nematic interior profile or a largely isotropic interior profile, depending on the initial conditions. On the square, we provide an analytic description of the Well Order Reconstruction solution first reported numerically by Kralj and Majumdar in 2014. We interpret the Well Order Reconstruction solution as a critical point of a related scalar variational problem and prove that the solution is globally stable on small domains. We use the gradient flow model of the Landau-de Gennes energy to numerically study the emergence of new solution branches from the Well Order Reconstruction solution. We conclude this thesis by studying a triple phase Landau-de Gennes model with a sixth-order bulk potential which admits isotropic, uniaxial and biaxial minima at a special temperature known as the triple point temperature. For some model problems, we can use asymptotic methods to prove that isotropic-uniaxial, uniaxial-biaxial and isotropic-biaxial fronts propagate according to mean curvature and to prove an angle condition that holds when the fronts intersect at a triple junction. We corroborate our formal calculations with a numerical investigation of the full Landau-de Gennes gradient flow system.

Introduction to liquid crystals

We begin with an introduction to liquid crystals, reviewing the molecular structure and history of this intriguing phase of matter. We discuss the nematic liquid crystal phase in detail and outline the particular aspects to be studied in this thesis. This chapter finishes with an overview of further liquid crystal phases and applications.

1.1 The liquid crystal phase

Liquid crystals are an intermediate phase of matter between the conventional solid and liquid phases. The liquid phase is isotropic with randomly diffusing molecules and the solid phase is anisotropic with highly ordered molecules. Liquid crystals are anisotropic materials in which the molecules have a combination of orientational and positional order with positional ordering imposed in at most two dimensions [31]. Orientational ordering is the result of attractive forces between rod- or disc-shaped molecules which are stronger when the molecules are aligned. The molecular order in liquid crystals leads to the formation of fascinating textures, see Figure 1-1 [26].

Liquid crystals were first discovered in 1888 by Friedrich Reinitzer whilst extracting cholesterol compounds from carrots. It seemed to Reinitzer that cholesteryl benzoate had two melting points; melting from a solid to a cloudy liquid and then from a cloudy to clear liquid. Reinitzer consulted physicist Otto Lehmann who began his own study of these materials, first investigating the cloudy

phase of cholesteryl benzoate and then similar compounds. Lehmann described these phases as flowing crystals but in 1900 they became known as liquid crystals. In 1907 Daniel Vorländer attributed the characteristics of this phase to rod-shaped molecules. This enabled the synthesis of hundreds of liquid crystal compounds and the discovery that a material may transition through many liquid crystal phases. In 1922 Georges Friedel classified these liquid crystal phases based on their molecular order into three phases; nematic, smectic and cholesteric [106, 37]. We will discuss each of these phases later in this chapter.

Since 1888, thousands of materials have been found to exhibit a liquid crystalline phase and liquid crystals have been the subject of much research, both analytical and experimental. Liquid crystals in confinement are an exciting source of challenges for mathematicians and practical scientists alike and the mathematical analysis of liquid crystal phenomena plays a key role in the next generation of experiments and future applications.
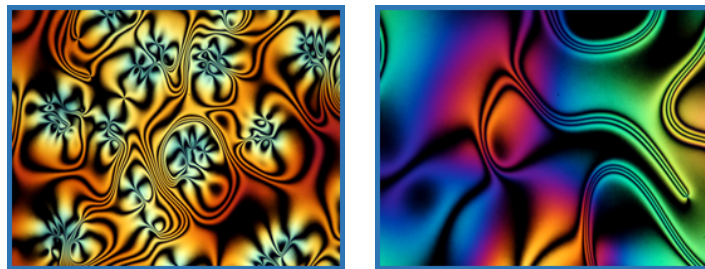
Figure 1-1: Microphotographs of liquid crystal samples [83].

1.2   The nematic liquid crystal phase

A material may go through several liquid crystal phases as it transitions between the solid and liquid states. The molecules in each phase have different positional and orientational order. The simplest of these liquid crystal phases is the nematic phase. In the nematic phase the molecules have orientational order only and align along preferred directions as they diffuse. These special directions are known as directors. Uniaxial nematic liquid crystals have a single distinguished direction as illustrated in Figure 1-2. This anisotropy leads to birefringence where light propagation through a material depends on the direction and polarisation of the light. The molecules in the uniaxial phase are generally rod-shaped and of roughly 2nm in length and 0.5nm in width. Alternatively in the biaxial nematic phase there are two special directions of molecular alignment. In this case the molecules are often cuboid-shaped, this allows for the second axis of reflective symmetry necessary for two directors [31].
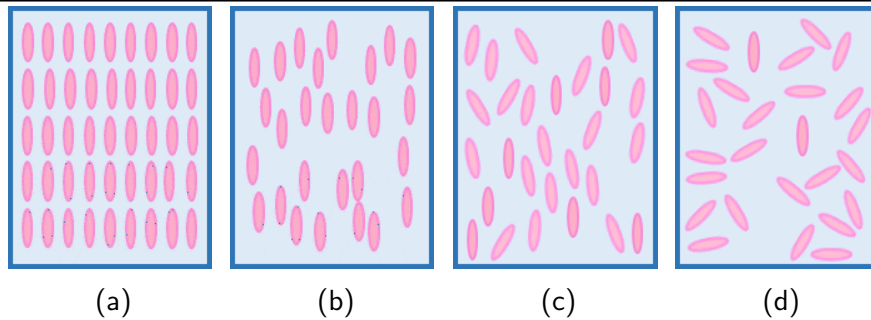
Figure 1-2: The molecules of a material in a) the solid phase, b) the uniaxial nematic phase with high orientational order, c) the uniaxial nematic phase with low orientational order and d) the isotropic phase.

1.2.1 Phase transitions

Phase transitions between isotropic and nematic phases occur due to changes in environment. In thermotropic liquid crystals phase transitions are induced by temperature change and in a lyotropic liquid crystal, by concentration change [22]. In thermotropic materials, the molecules become more ordered as temperature decreases, inducing the transition between isotropic and nematic phases. This is illustrated in Figure 1-3 where bright droplets of nematic liquid crystal invade the dark isotropic phase as temperature is decreased. The random isotropic phase is energetically preferable in higher temperatures but as the temperature falls, the ordered nematic phase becomes favourable. The boundary of the droplets, distinguished by a fast change in nematic order, expands accordingly as the temperature decreases.
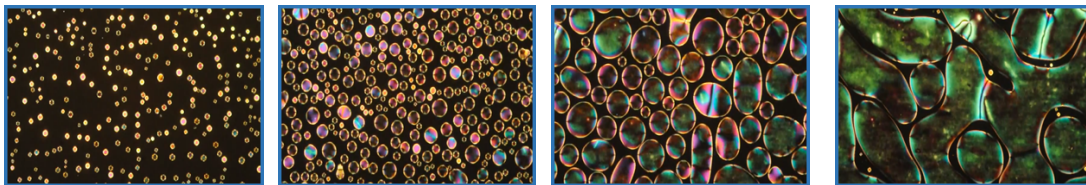
Figure 1-3: An isotropic to nematic phase transition occurs as temperature decreases [111].

1.2.2 Defects

The anisotropy of nematic liquid crystals leads to the formation of fascinating patterns and textures as seen in Figure 1-4. These patterns are somewhat caused by defects which occur where there is a rapid change in the director profile [38]. In a nematic liquid crystal sample these defects can occur at a point or along a line. Two point defects are seen in the first photo of Figure 1-4 and line defects are illustrated in the second.
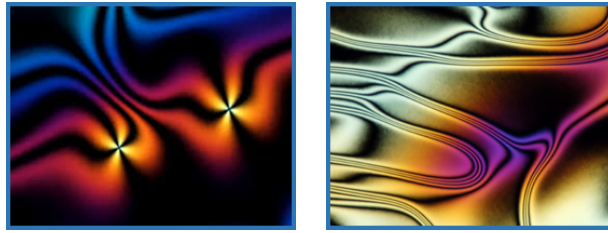
Figure 1-4: Microphotographs of liquid crystal samples [83].

Some examples of the molecular arrangements in points defects are shown in Figure 1-5. The strength of a point defect is labelled by the winding number m and given by the number of anticlockwise rotations of the director in traversing an anticlockwise path [98]. In particular, the first defect in Figure 1-5 is known as the Radial Hedgehog defect and has winding number $+1$. This is a three-dimensional point defect which occurs in spherical droplets filled with nematic liquid crystal. The Radial Hedgehog has perfect radial symmetry with radial nematic alignment and an isolated isotropic point at the centre which corresponds to the point defect [80].
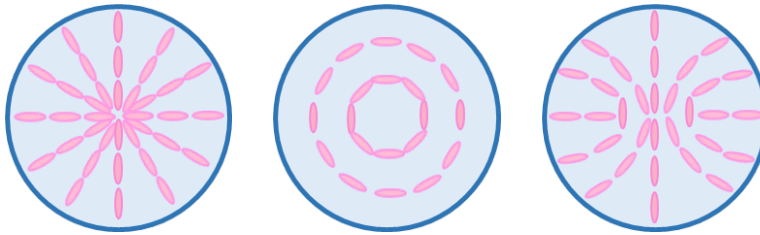
Figure 1-5: Example director profiles which result in point defects [48, 27].

1.2.3 Nematodynamics

The dynamics of nematic liquid crystals in confinement are known as nematodynamics. Often a macroscopic approach is employed to model nematodynamics with a system of three coupled equations. This system comprises a continuity equation and an equation for the time evolution of the fluid velocity, as would be seen in a model for an isotropic liquid. However, a third equation is required for the time evolution of the director field. Nematic flows are typically more complex than those of ordinary fluids due to this coupling of the velocity and director fields [31, 101].

1.3 Other liquid crystal phases

Many different liquid crystal phases may be observed as a material transitions between different states. Here we briefly discuss some of the common liquid crystal phases. In a smectic liquid

crystal the molecules are arranged in layers. In the smectic A phase the preferred direction of molecular alignment is perpendicular to the layers but in the smectic C phase the molecules align at some angle to the layers [88].
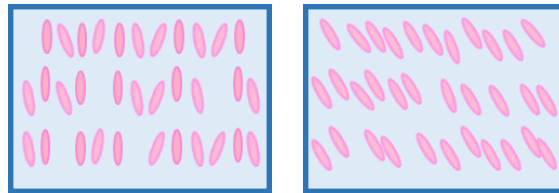
Figure 1-6: Molecular arrangement in smectic A (left) and smectic C (right) phases.

In the cholesteric liquid crystal phase the molecules form a helical structure. As depicted in Figure 1-7, the molecules are positioned in layers of nematic liquid crystal with the preferred direction of molecular alignment rotating through the levels. This twisting is described by the pitch, the distance over which the director rotates by 2π [59]. The molecular order displayed in the cholesteric phase is achieved by dissolving a chiral compound in a nematic liquid crystal [31].
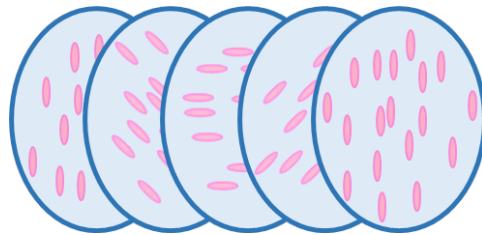
Figure 1-7: Molecular arrangement in a cholesteric liquid crystal.

The blue liquid crystal phase has been detected during the cholesteric to isotropic phase transition as temperature is increased. A cubic molecular structure forms as this phase transition occurs. This phase typically has limited stability and is only observed for very small temperature regimes [77, 25]. A microphotograph of the blue phase is shown in Figure 1-8.
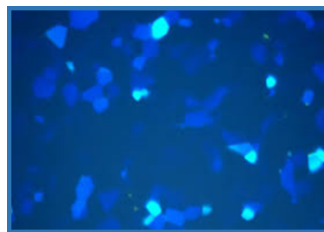
Figure 1-8: Microphotograph of a blue phase liquid crystal [83].

1.4 Applications of nematic liquid crystals

Nematic liquid crystals have unique optical properties and hence have numerous and diverse applications. These include technological applications, most famously in Liquid Crystal Displays. These displays have a key property; the display supports two contrasting states which one can switch between. Typically, the surfaces of pixels are treated so that the molecules can be manipulated into two different arrangements with contrasting optical properties [107]. One specific example of a Liquid Crystal Display is the Twisted Nematic Display. This display became very popular in the 1970s in small devices such as watches and calculators due to its low power consumption [32]. The display consists of a layer of nematic liquid crystal sandwiched between two plates which are treated in order to induce a fixed molecular orientation in the plane of the plates. The preferred directions on the top and bottom plates are orthogonal. In the absence of an electric field, the molecules twist uniformly between the plates. This twisted state is transparent to incident light. When a voltage is applied, the molecules align with the field and block incident light, resulting in an opaque state [52, 37].

One disadvantage of the Twisted Nematic Display is that a voltage is required to maintain the dark state. A bistable display is such that both optically contrasting states can be maintained with no applied voltage and power is only required for switching between the states. This means that a bistable display requires less power than a Twisted Nematic Display and also has much shorter switching times between states [37]. Several bistable devices have been developed using nematic liquid crystals but many use cholesteric and smectic phases as well. The most popular nematic bistable device is the Zenithal Bistable Display which consists of nematic liquid crystal between a flat top plate and a bottom plate with a wedge-shaped grating. This display supports two stable states; a defect-free state and a state which contains defects near the bottom plate. The curvature of the wedges on the bottom plate is chosen to ensure the stability of both states [69, 57].

There are numerous other applications. For example, many of the optical properties of a liquid crystal are temperature dependent. This means that liquid crystalline materials can change colour as temperature varies. Naturally such materials have been used in rough thermometers where the temperature is read using a colour key. Further, this has allowed liquid crystals to be used in medical applications to detect small changes in temperature such as during a caesarean or a skin graft [78].

Preliminary material and review

In Chapter 2 we discuss the mathematical modelling of nematic liquid crystals and introduce the particular variational theory and gradient flow model studied throughout this thesis. We review relevant front propagation and phase field theory and give an example of a model problem. We then discuss the numerical methods employed to complement the analysis in each chapter. This chapter is concluded with a thesis overview and literature review.

2.1 Mathematical modelling of nematic liquid crystals

Nematic liquid crystals can be mathematically modelled using macroscopic approaches such as mean field or variational theories. In mean field theories, the nematic sample is described using a probability distribution for molecular orientations on the unit ball. The mean of this distribution gives the preferred direction of molecular alignment and a standard deviation-type measurement gives the degree of orientational order [82]. In this thesis we focus on variational theories where equilibrium configurations of a liquid crystal sample in a domain Ω correspond to critical points of a given energy functional subject to appropriate boundary conditions. There are three main variational approaches in the theory of nematic liquid crystals.

The simplest, the Oseen-Frank theory, is used in the context of uniaxial nematic liquid crystals. In the uniaxial liquid crystal phase there is a unique preferred direction at each point in space,

known as the director $\mathbf{n}$. The Oseen-Frank theory assumes constant degree of orientational order [109] and is given by

$$\mathbf{I}_{OF}[\mathbf{n}] = \int_{\Omega} L_1(\nabla \cdot \mathbf{n}) + L_2(\mathbf{n} \cdot (\nabla \times \mathbf{n}))^2 + L_3(\mathbf{n} \times (\nabla \times \mathbf{n}))^2 \, dV.$$

As shown above, the integrand of the Oseen-Frank energy has three components corresponding to penalizing the splaying, twisting and bending of molecules respectively. For the one-constant approximation it is assumed that $L_1 = L_2 = L_3 = L$. We take $L = 1$ and so the one-constant approximation of the Oseen-Frank energy is given by

$$\mathbf{I}_{OF}[\mathbf{n}] = \int_{\Omega} |\nabla \mathbf{n}|^2 \, dV.$$

Subject to suitable boundary conditions, minimizers of the one-constant approximation $\mathbf{I}_{OF}(\mathbf{n})$ are examples of harmonic maps [12, 76]. The Oseen-Frank theory is restricted as the assumption of a constant degree of orientational order allows only for point defects but not line or surface defects [68, 76].

The more general Ericksen theory is also used to describe uniaxial nematic liquid crystals but allows for varying orientational order which is described by an order parameter s [39]. The Ericksen energy functional is given by

$$\mathbf{I}_E[\mathbf{n}, s] = \int_{\Omega} s^2|\nabla \mathbf{n}|^2 + k|\nabla s|^2 + W_0(s) \, dV,$$

where k is an elastic constant and W_0 is a bulk potential. The order parameter s is zero where $\mathbf{n}$ has a singularity which allows this variational theory to account for all defects [4, 67, 76].

This thesis focuses on the Landau-de Gennes theory, the most general continuum theory for nematic liquid crystals. As well as uniaxial nematic liquid crystals, the Landau-de Gennes theory also accounts for the biaxial nematic liquid crystal phase [76]. At each point in this phase the molecules can have two preferred directions of alignment and hence two directors [54]. As a result there are two axes of symmetry in the molecular alignment, as opposed to the unique axis of symmetry seen in the uniaxial phase. Within the Landau-de Gennes framework, a $\mathbf{Q}$-tensor parameter is used to describe the state of the liquid crystal. The parameter $\mathbf{Q}$ is a symmetric,

traceless, 3×3 matrix [82], so that $\mathbf{Q} \in S_0$ where

$$S_0 := \left\{ \mathbf{Q} \in \mathbb{R}^{3\times 3} : Q_{ij} = Q_{ji}, \sum Q_{ii} = 0 \right\}.$$

A $\mathbf{Q}$-tensor is said to be

- isotropic if $\mathbf{Q} = 0$.

- uniaxial if $\mathbf{Q}$ has a pair of degenerate non-zero eigenvalues.

- biaxial if $\mathbf{Q}$ has three distinct eigenvalues [31, 82].

Any matrix $\mathbf{Q} \in S_0$ can be written in the form

$$\mathbf{Q} = s \left(\mathbf{n} \otimes \mathbf{n} - \frac{\mathbf{I}}{3} \right) + r \left(\mathbf{m} \otimes \mathbf{m} - \frac{\mathbf{I}}{3} \right),$$

where $\mathbf{n}$ and $\mathbf{m}$ are unit eigenvectors of $\mathbf{Q}$. In particular, a uniaxial $\mathbf{Q}$-tensor can be written as

$$\mathbf{Q} = s \left(\mathbf{n} \otimes \mathbf{n} - \frac{\mathbf{I}}{3} \right), \tag{2.1}$$

where $\mathbf{n}$ is the unit eigenvector of $\mathbf{Q}$ with non-degenerate eigenvalue [76]. The eigenvectors of $\mathbf{Q}$ correspond to the directors of the nematic sample. The scalar order parameters s and r give the degree of alignment with respect to the relevant director. In general, boundary behaviour is dictated by enforcing Dirichlet boundary conditions. This is known as strong anchoring. Alternatively, we can work with the more physically realistic weak anchoring and impose a given surface energy [106].

With no surface energies or external fields, the most general Landau-De Gennes energy functional is of the form

$$\mathbf{I}_{LG}[\mathbf{Q}] = \int_\Omega \omega(\mathbf{Q}, \nabla\mathbf{Q}) + f_B(\mathbf{Q}) \, dV, \tag{2.2}$$

where $\omega(\mathbf{Q}, \nabla\mathbf{Q})$ represents an elastic energy penalty which penalises spatial inhomogeneities [76]. The simplest case is a one-constant elastic energy density, as described above for the Oseen-Frank energy. This is given by

$$\omega = \frac{L}{2} |\nabla\mathbf{Q}|^2 \quad \text{where} \quad |\nabla\mathbf{Q}|^2 = \sum_{i,j,k=1}^{3} \left(\frac{\partial Q_{ij}}{\partial x_k} \right)^2.$$

The bulk energy density $f_B(\mathbf{Q})$ is a potential function which accounts for the preferred state of the material. We choose $f_B(\mathbf{Q})$ to allow for multiple local minima and a first-order transition between isotropic and nematic states [61, 76]. The simplest appropriate function is a quartic polynomial in $\mathbf{Q}$, hence we let

$$f_B(\mathbf{Q}) = \frac{A}{2}\mathrm{tr}\mathbf{Q}^2 - \frac{B}{3}\mathrm{tr}\mathbf{Q}^3 + \frac{C}{4}\left(\mathrm{tr}\mathbf{Q}^2\right)^2, \tag{2.3}$$

where

$$\mathrm{tr}\mathbf{Q}^2 = \sum_{i,j=1}^{3} Q_{ij}Q_{ji} \quad \text{and} \quad \mathrm{tr}\mathbf{Q}^3 = \sum_{i,j,k=1}^{3} Q_{ij}Q_{jk}Q_{ki}.$$

The constants A, B, C and L are material and temperature dependent constants. In practice it is assumed only the dependence of A on temperature is important, with the linear relationship $A = A_0(T - T^*)$ where A_0 is a positive constant and T^* is the supercooling temperature below which the isotropic state is unstable [22].

2.1.1 The gradient flow model

We study the dynamics predicted by the gradient flow model associated with the Landau-de Gennes energy. Gradient flows are evolution equations driven by a decreasing energy [87] and the gradient flow model used here describes the Landau-de Gennes energy with the L^2-norm as the dissipation mechanism. These relaxation principles dictate that, for a given initial condition, the system should evolve to a nearby equilibrium or local minimizer of the Landau-de Gennes energy. The gradient flow model is often used in the context of nematic liquid crystals dynamics [90, 91] and is believed to be a good approximation to these dynamics at a constant temperature without any fluid flow. The dynamic equations of the gradient flow system associated with the Landau-de Gennes energy are given by

$$\gamma \mathbf{Q}_t = L\nabla^2\mathbf{Q} - A\mathbf{Q} + B\left(\mathbf{Q}\mathbf{Q} - \frac{\mathbf{I}}{3}|\mathbf{Q}|^2\right) - C|\mathbf{Q}|^2\mathbf{Q}, \tag{2.4}$$

where γ is a positive rotational viscosity and $\mathbf{Q}\mathbf{Q} = \mathbf{Q}_{ip}\mathbf{Q}_{pj}$ for $i, j, p = 1, 2, 3$ [70]. The right-hand side of this equation is given by the right-hand side of the relevant Euler-Lagrange equations:

$$0 = LQ_{ij,kk} - \frac{\partial f_B(\mathbf{Q})}{\partial Q_{ij}} + \frac{1}{3}\frac{\partial f_B(\mathbf{Q})}{\partial Q_{kk}}\delta_{ij} \quad \text{for} \quad i, j, k = 1, 2, 3. \tag{2.5}$$

These equations include a Lagrange multiplier which accounts for the traceless condition [71].

Let R be the characteristic size of the domain. We work in the limit of vanishing elastic constant which describes domains with length scales much larger than the nematic correlation length $\xi \propto \sqrt{LC/B^2}$. We non-dimensionalize the system (2.4) by setting $\bar{t} = \frac{tL}{\gamma R^2}$, $\bar{\mathbf{x}} = \frac{\mathbf{x}}{R}$ to yield

$$\mathbf{Q}_{\bar{t}} = \overline{\nabla}^2 \mathbf{Q} - \frac{1}{\tilde{L}}\left[A\mathbf{Q} - B\left(\mathbf{Q}\mathbf{Q} - \frac{\mathbf{I}}{3}|\mathbf{Q}|^2\right) + C|\mathbf{Q}|^2\mathbf{Q}\right], \tag{2.6}$$

where $\overline{\nabla}^2$ denotes the Laplacian with respect to the rescaled coordinate $\bar{\mathbf{x}}$ and $\tilde{L} = \frac{L}{R^2}Nm^{-2}$. We now drop the tilde from L and the bars from the dimensionless variables.

The gradient flow model of the Landau-de Gennes energy is a system of five coupled nonlinear parabolic partial differential equations for the $\mathbf{Q}$-tensor. We impose a Dirichlet boundary condition and set $\mathbf{Q}$ equal to some $\mathbf{Q}$-tensor $\mathbf{Q}_b$ on $\partial\Omega$. We can use standard results in the theory of parabolic partial differential equations to prove that the gradient flow system (2.6) has a unique solution for physically relevant initial and boundary conditions:

Proposition 2.1. *Let $\Omega \subset \mathbb{R}^3$ be a bounded domain with smooth boundary $\partial\Omega$. Given a smooth fixed boundary condition $\mathbf{Q}(\mathbf{x}, t) = \mathbf{Q}_b(\mathbf{x})$ on $\partial\Omega$ and smooth initial condition $\mathbf{Q}(\mathbf{x}, 0) = \mathbf{Q}_0(\mathbf{x})$, the parabolic system (2.6) has a unique solution $\mathbf{Q}(\mathbf{x}, t) \in C^\infty(\Omega)$ for all $t \geq 0$.*

Proof. The existence of a solution for the system (2.6) is standard, see [81] for a proof. From [76], we have that, for suitable initial and boundary conditions, the dynamic solution is bounded with $|\mathbf{Q}(\mathbf{r}, t)| \leq \sqrt{\frac{2}{3}\frac{B}{3C}}$ for all $t \geq 0$. The uniqueness result follows from an immediate application of Gronwall's inequality to the difference $\mathbf{Q}_d = \mathbf{Q}_1 - \mathbf{Q}_2$ of two supposed solutions, $\mathbf{Q}_1$ and $\mathbf{Q}_2$, subject to the fixed boundary condition and the same initial condition [94]. In particular, $\mathbf{Q}_d(\mathbf{x}, t) = 0$ on $\partial\Omega$ and $\mathbf{Q}_d(\mathbf{x}, 0) = 0$ for $\mathbf{x} \in \Omega$. One can then show that $\mathbf{Q}_d(\mathbf{x}, t) = 0$ for $\mathbf{x} \in \Omega$ and for all $t \geq 0$. $\qquad\square$

2.1.2 The isotropic-nematic transition temperature

It is well known that the critical points of the quartic bulk potential $f_B(\mathbf{Q})$ are given by either uniaxial or isotropic $\mathbf{Q}$-tensors:

Proposition 2.2. *The stationary points of the bulk energy density $f_B(\mathbf{Q})$ are given by $\mathbf{Q}$-tensors of the form*

$$\mathbf{Q} = s\left(\mathbf{n} \otimes \mathbf{n} - \frac{\mathbf{I}}{3}\right). \tag{2.7}$$

That is, by either isotropic or uniaxial $\mathbf{Q}$-tensors.

Proof. Follows as in Majumdar 2010 [71] and Ball 2012 [7]. We can write $\mathrm{tr}(\mathbf{Q}^n) = \sum_{i=1}^{3} \lambda_i^n$ where λ_i are the eigenvalues of $\mathbf{Q}$, and hence

$$f_B(\mathbf{Q}) = f(\lambda_1, \lambda_2, \lambda_3) = \frac{A}{2}\sum_{i=1}^{2}\lambda_i^2 - \frac{B}{3}\sum_{i=1}^{3}\lambda_i^3 + \frac{C}{4}\left(\sum_{i=1}^{3}\lambda_i^2\right)^2 - 2\delta\sum_{i=1}^{3}\lambda_i.$$

The Lagrange multiplier δ is introduced due to the traceless condition. The stationary points of $f(\lambda_1, \lambda_2, \lambda_3)$ will solve $\frac{\partial f}{\partial \lambda_i} = 0$ for $i = 1, 2, 3$ or

$$A\lambda_i - B\lambda_i^2 + C\left(\sum_{k=1}^{3}\lambda_k^2\right)\lambda_i = 2\delta \quad \text{for} \quad i = 1, 2, 3,$$

and the traceless condition $\sum_{i=1}^{3}\lambda_i = 0$. This system can be written as

$$(\lambda_i - \lambda_j)\left(A - B(\lambda_i + \lambda_j) + C\sum_{k=1}^{3}\lambda_k^2\right) = 0 \quad \text{for} \quad 1 \le i < j \le 3. \tag{2.8}$$

Suppose, for a contradiction, that we have three distinct eigenvalues. Then the system (2.8) yields

$$A - B(\lambda_1 + \lambda_2) + C\sum_{k=1}^{3}\lambda_k^2 = 0 \quad \text{and} \quad A - B(\lambda_1 + \lambda_3) + C\sum_{k=1}^{3}\lambda_k^2 = 0,$$

which simplifies to $B(\lambda_2 - \lambda_3) = 0$. This contradicts our assumption that all eigenvalues are distinct. Therefore we have two or three equal eigenvalues and hence a uniaxial or isotropic $\mathbf{Q}$-tensor. $\qquad\square$

For $\mathbf{Q}$-tensors of the form (2.7), $f_B(\mathbf{Q})$ is a function of the scalar order parameter s with

$$f_B(\mathbf{Q}) = f_B(s) = \frac{A}{3}s^2 - \frac{2B}{27}s^3 + \frac{C}{9}s^4.$$

For this bulk energy expression there are three steady states given by solutions of $\frac{df_B}{ds} = 0$:

$$s_0 = 0,$$
$$s_+ = \frac{B + \sqrt{B^2 - 24AC}}{4C},$$
$$s_- = \frac{B - \sqrt{B^2 - 24AC}}{4C}.$$

These steady states define three temperature regimes in terms of A:

- $A \leq 0$, where the stable states are s_+ and s_- with s_+ the global minimizer.

- $0 < A \leq \frac{B^2}{27C}$, where the stable states are s_+ and 0 with s_+ the global minimizer.

- $\frac{B^2}{27C} < A \leq \frac{B^2}{24C}$, where the stable states are s_+ and 0 with 0 the global minimizer.

Hence, we have three characteristic values of A:

- $A = 0$, below which the isotropic phase is unstable.

- $A = \frac{B^2}{27C}$, where the isotropic phase and the stable nematic phase have equal energies.

- $A = \frac{B^2}{24C}$, above which the nematic equilibria do not exist.

We focus on the special temperature $A = \frac{B^2}{27C}$, this is known as the *isotropic-nematic transition temperature*. At this temperature $f_B(s)$ becomes a double welled potential with two equal energy minima. This is illustrated in Figure 2-1 with a plot of $f_B(s)$ for $A = \frac{B^2}{27C}$.
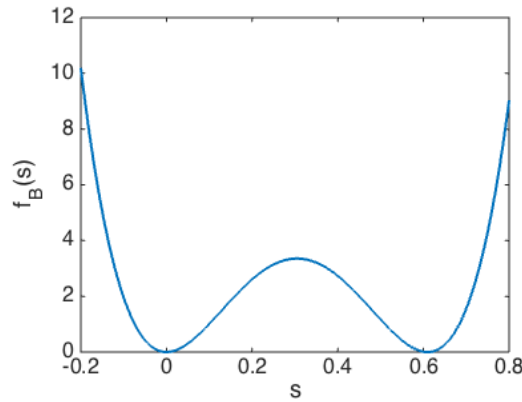
Figure 2-1: Bulk potential $f_B(s)$ for $A = \frac{B^2}{27C}$, $B = 0.64 \times 10^4 \ Nm^{-2}$ and $C = 0.35 \times 10^4 \ Nm^{-2}$ [71].

2.1.3 The Radial Hedgehog defect

As discussed in Chapter 1, the director of a nematic sample need not be smooth everywhere and the director profile may include point and line defects [31]. A point defect of particular interest is the Radial Hedgehog defect which occurs in spherical droplets of nematic liquid crystal. The Radial Hedgehog defect is described by the **Q**-tensor

$$\mathbf{H} = s(r) \left(\hat{\mathbf{r}} \otimes \hat{\mathbf{r}} - \frac{\mathbf{I}}{3} \right),$$

where $\hat{\mathbf{r}} = (\cos\phi\sin\theta, \sin\phi\sin\theta, \cos\theta)$ is the three-dimensional unit radial vector (given in spherical polar coordinates defined by $r^2 = x^2 + y^2 + z^2$, $\phi = \arctan(\frac{y}{x})$ and $\theta = \arccos(\frac{z}{r})$ where $\phi \in [0, 2\pi)$ and $\theta \in [0, \pi)$). The tensor $\mathbf{H}$ satisfies the Landau-de Gennes Euler-Lagrange equations (2.5) provided $s(r)$ is a solution of

$$L\left(\frac{d^2s}{dr^2} + \frac{2}{r}\frac{ds}{dr} - \frac{6s}{r^2}\right) - \frac{s}{3}(2Cs^2 - Bs + 3A) = 0. \tag{2.9}$$

The resulting $\mathbf{Q}$-tensor is an example of an explicit critical point of the Landau-de Gennes energy functional [73]. The director of this radially symmetric solution is given by the three-dimensional unit radial vector $\hat{\mathbf{r}}$ with an isolated point defect at the droplet centre [80], as illustrated in Figure 2-2. The point defect corresponds to an isotropic core where the order parameter s is zero.

The scalar order parameter equation (2.9) is shown to have a unique solution which is monotonic in Majumdar 2012 [73] for large radii, in the limit $T \to -\infty$ and in Lamy 2013 [61] for $T < T^*$ (the supercooling temperature below which the isotropic state is unstable). In Henao and Majumdar 2012 [54] the authors show that uniaxial global minimizers of the Landau-de Gennes energy must be of Radial Hedgehog-type for low temperatures. In Lamy 2015 [63] the author studies the Radial Hedgehog solution in the Landau-de Gennes framework and imposes radial Dirichlet boundary conditions on the surface of the sphere. These boundary conditions dictate that $\mathbf{Q} = s_0(\hat{\mathbf{r}} \otimes \hat{\mathbf{r}} - \frac{I}{3})$ on $r = 1$ where s_0 is chosen so that this $\mathbf{Q}$-tensor minimizes the bulk potential. In this case, it is shown that the Radial Hedgehog solution is the unique uniaxial critical point of the Landau-de Gennes energy on the sphere for all temperatures. The Radial Hedgehog is unstable to symmetry breaking biaxial perturbations for low temperatures as discussed in Mkaddem and Gartland 2000 [80] and Majumdar 2012 [73]. In Ignat et al 2015 [56] the Radial Hedgehog is shown to be stable to arbitrary perturbations for temperatures close to the supercooling temperature T^*.
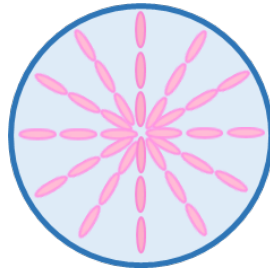
Figure 2-2: Molecular arrangement in the Radial Hedgehog defect.

2.2 Front propagation and phase field models

A phase field consists of two or more phases co-existing inside a single domain. These different states are separated by a sharp interface or front where the material transitions between the two phases [18]. Both bulk phases are local minimizers of an appropriate energy so the front is maintained and front motion is driven by the relative stability of the opposing phases. A phase field model employs an order parameter to describe the appearance and evolution of the front described above [6]. This order parameter varies quickly and smoothly in the transition region of the domain and is constant within each region of uniform phase [47]. Reaction diffusion equations can be used to model phase fields. A standard example of such an equation is

$$\frac{\partial s}{\partial t} = L\nabla^2 s + f(s), \tag{2.10}$$

for small parameter L. The bulk phases are given by the stable steady states. These are the solutions of $f(s) = 0$ which are local minimizers of the potential $V(s) = -\int_0^s f(s)\,ds$. If the system has two or more stable steady states, a sharp front can separate two regions with s taking a steady state value in each region and changing rapidly in between. The system will advance to minimize the potential $V(s)$ and the front will propagate to this end [89].

In the case of nematic liquid crystals, a phase field model is used to describe the interplay between stable isotropic and nematic states within the Landau-de Gennes framework. We are interested in the propagation of the dividing interface, particularly the longevity of the front and front propagation velocity. In what follows we present a simple model problem to motivate the rest of the thesis.

2.2.1 Travelling wave solutions in one-dimension

In one-dimension the reaction diffusion equation (2.10) simplifies to

$$\frac{\partial s}{\partial t} = L\frac{\partial^2 s}{\partial x^2} + f(s),$$

and we assume that $f(s)$ admits at least two stable steady states. In one-dimension, a steady state s^* is stable if $f'(s^*) < 0$ and unstable if $f'(s^*) > 0$. Assuming a planar front connects stable steady states $s_1 > s_2$, we can rewrite the reaction diffusion equation in a co-moving frame and in terms of a single variable $\xi = x - ct$. The constant c is the speed at which the front propagates

[89]. Together with the appropriate boundary conditions at $\xi = \pm\infty$, we have

$$Ls''(\xi) + cs'(\xi) + f(s) = 0, \tag{2.11}$$

$$s \to s_1 \text{ as } \xi \to \infty, \quad s \to s_2 \text{ as } \xi \to -\infty. \tag{2.12}$$

A solution of (2.11)-(2.12) exists for a unique value of c. This is because both steady states correspond to saddle points in the phase plane with exactly one trajectory leaving and entering each point. The relevant trajectories only coincide for one value of the parameter c. As a front solution of (2.11) corresponds to a heteroclinic trajectory in the phase plane, we find a solution for this particular value of c [89]. This is illustrated in Figure 2-3.
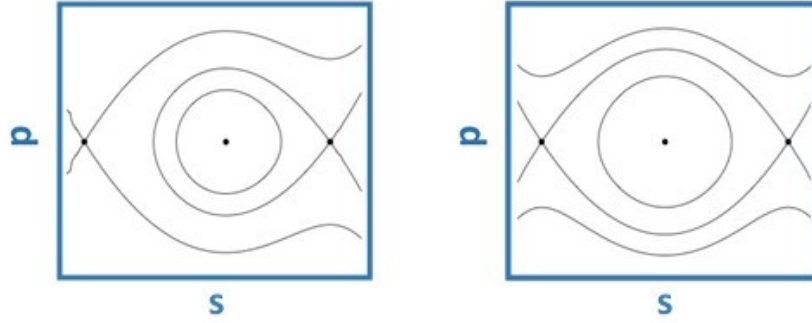
Figure 2-3: A phase plane where $p = \frac{ds}{d\xi}$ with no connecting trajectory, left, and a connecting trajectory, right [89].

2.2.2   A model problem

In the simple case of a uniaxial nematic liquid crystal with constant director and order parameter $s = s(x, t)$ for $\Omega := \{0 \leq x \leq 1\}$, the Landau-de Gennes energy functional becomes

$$I_{LG}[s] = \int_0^1 \frac{L}{2}\left(\frac{\partial s}{\partial x}\right)^2 + \frac{A}{3}s^2 - \frac{2B}{27}s^3 + \frac{C}{9}s^4 \, dx.$$

In this case, the gradient flow dynamic equations simplify to

$$\frac{\partial s}{\partial t} = L\frac{\partial^2 s}{\partial x^2} - \frac{2}{9}s(2Cs^2 - Bs + 3A). \tag{2.13}$$

On the change of variables $\xi = x - ct$, (2.13) becomes

$$L\frac{d^2s}{d\xi^2} + c\frac{ds}{d\xi} - \frac{2}{9}s(2Cs^2 - Bs + 3A) = 0. \tag{2.14}$$

The appropriate boundary conditions are dependent on the stable steady states of the bulk potential $f_B(s)$ and hence the temperature regime. To find travelling wave solutions for $A \leq 0$, we change to phase plane variables by defining $p = \frac{ds}{d\xi}$ and so (2.14) becomes

$$Lp\frac{dp}{ds} + cp - \frac{2}{9}s(2Cs^2 - Bs + 3A) = 0, \tag{2.15}$$

and impose the boundary conditions $p(s_+) = p(s_-) = 0$. Following a standard paradigm, for example from [89], we suppose $p(s) = N(s_+ - s)(s - s_-)$ for some constant N. Substitution into equation (2.15) yields

$$N = \frac{2}{3}\sqrt{\frac{C}{2L}} \quad \text{and} \quad c = -\frac{B}{3}\sqrt{\frac{L}{2C}}.$$

We can now find travelling wave solutions of (2.13) by integrating

$$\frac{ds}{d\xi} = \frac{2}{3}\sqrt{\frac{C}{2L}}(s_+ - s)(s - s_-).$$

Choosing $s(0) = 0$ gives

$$s(x, t) = s_- s_+ \frac{1 - \exp\left((s_+ - s_-)\frac{2}{3}\sqrt{\frac{C}{2L}}(x - ct)\right)}{s_+ - s_- \exp\left((s_+ - s_-)\frac{2}{3}\sqrt{\frac{C}{2L}}(x - ct)\right)}.$$

Following the same method for $0 < A \leq \frac{B^2}{24C}$ we find

$$s(x, t) = \frac{s_+ s_- \exp\left(s_+(x - ct)\frac{2}{3}\sqrt{\frac{C}{2L}}\right)}{s_+ - s_- + s_- \exp\left(s_+(x - ct)\frac{2}{3}\sqrt{\frac{C}{2L}}\right)} \quad \text{where} \quad c = \sqrt{\frac{L}{2C}}\left(\frac{B}{6} - \frac{\sqrt{B^2 - 24AC}}{2}\right).$$

Note that at the isotropic-nematic transition temperature $A = \frac{B^2}{27C}$, the above expression gives $c = 0$. Hence propagation speed is zero and the front is stationary. This would be expected because the isotropic state and the stable nematic state are equal energy minimizers of the bulk potential at this temperature and we are working in one-dimension.

We make note of a well-known result regarding the stability of such travelling waves:

Theorem 2.1. *Suppose $s(x,t)$ is a solution of the reaction diffusion equation* (2.13) *in the* $0 < A \leq \frac{B^2}{24C}$ *regime with an initial condition such that*

$$\limsup_{x \to -\infty} s(x,0) < s_-, \quad \liminf_{x \to \infty} s(x,0) > s_-, \quad 0 \leq s(x,0) \leq s_+.$$

Then there exists z_0, K and ω, with K, $\omega > 0$, such that

$$|s(x,t) - S(x - ct - z_0)| < K\exp(-\omega t),$$

where $S(x,t)$ is a travelling wave solution of (2.13).

Proof. The proof is standard and can be adapted from [44]. The first step is to prove the uniform convergence of $s(x,t) \to S(x - ct - z_0)$ as $t \to \infty$. To finish the proof, convergence is shown to occur at an exponential rate. $\square$

2.3 Numerical methods

Throughout this thesis, our formal analysis is complemented by numerical investigations. We solve the full gradient flow system associated with the Landau-de Gennes energy functional in (2.6), imposing Dirichlet boundary conditions, on various domains.

We use finite difference schemes to estimate the spatial derivatives in the Laplacian. Our domain is embedded into either the square $[-1, 1]^2$ for two-dimensional domains or the cube $[-1, 1]^3$ for three-dimensional domains which are discretised with the following grids. Most often, we use a finite difference scheme on a square grid with step size h, as illustrated in the left diagram of Figure 2-4, and a four-point Laplacian with

$$\nabla^2 u_{j,k} \approx \frac{u_E + u_N + u_W + u_S - 4u_{j,k}}{h^2}.$$

Here $u_{j,k}$ estimates the value of $u(-1 + jh, -1 + kh)$. This scheme is extended to the three-dimensional case in the intuitive way. In Chapter 6 it is necessary to adopt a hexagonal grid and a six-point Laplacian, as shown in the right diagram of Figure 2-4. Here

$$\nabla^2 u_{j,k} \approx \frac{2}{3} \frac{u_N + u_{NE} + u_{SE} + u_S + u_{SW} + u_{NW} - 6u_{j,k}}{h^2},$$

for h and $u_{j,k}$ as before [42].
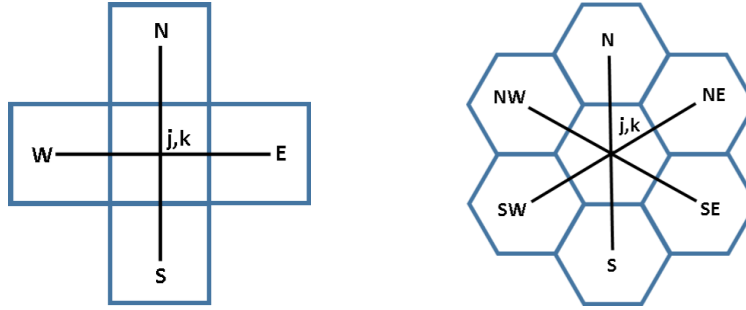
Figure 2-4: A square finite difference grid (left) and a hexagonal finite difference grid (right) [42].

These cartesian grids are utilised even when working on spherical domains as they allow us to avoid both the singularity at the origin associated with polar coordinates and the additional stability constraints imposed by the necessity of grid refinement at the origin. Once the spatial domain is discretised, we solve the equations in (2.6) by the method of lines [66]. That is, the system of partial differential equations is recast as a system of ordinary differential equations of the form

$$\frac{d\mathbf{y}}{dt} = f(t, \mathbf{y}), \quad \mathbf{y}(t_0) = \mathbf{y}_0, \tag{2.16}$$

where $\mathbf{y}$ represents all the grid values of the solution.

To accomplish time stepping in our numerical simulations we use the standard RK4 Runge-Kutta method [23]. Runge-Kutta methods are used to numerically solve ordinary differential equations of the form (2.16). Each step is of the form

$$\mathbf{y}_{i+1} = \mathbf{y}_i + (a_1\mathbf{k}_1 + a_2\mathbf{k}_2 + \ldots + a_n\mathbf{k}_n)\Delta t, \tag{2.17}$$

for step size Δt, constant a's, p's and q's and

$$\mathbf{k}_1 = f(t_i, \mathbf{y}_i),$$
$$\mathbf{k}_j = f(t_i + p_{j-1}\Delta t, \mathbf{y}_i + q_{j-1,1}\mathbf{k}_1\Delta t + \ldots + q_{n-1,n-1}\mathbf{k}_{n-1}\Delta t) \quad \text{for} \quad j > 1.$$

We use a fourth-order Runge-Kutta scheme taking $n = 4$. The relevant constants ($a_1 - a_4$, $p_1 - p_3$ and q_{11}, q_{21}, q_{22}, q_{31}, q_{32}, q_{33}) are found by equating the right-hand side of equation (2.17) with a Taylor expansion of the left-hand side about t_i [23]. The most common fourth-order Runge-Kutta scheme (RK4) takes $q_{31} = q_{32} = q_{21} = 0$, $q_{11} = q_{22} = \frac{1}{2}$, $q_{33} = 1$; $p_1 = p_2 = 1/2$

$p_3 = 1$ and $a_1 = a_4 = \frac{1}{6}$, $a_2 = a_3 = \frac{1}{3}$ [17]. Therefore our scheme is given by

$$\mathbf{y}_{i+1} = \mathbf{y}_i + \frac{1}{6}(\mathbf{k}_1 + 2\mathbf{k}_2 + 2\mathbf{k}_3 + \mathbf{k}_4),$$

where

$$\mathbf{k}_1 = f(t_i, \mathbf{y}_i), \qquad \mathbf{k}_2 = f\left(t_i + \frac{\Delta t}{2}, \mathbf{y}_i + \mathbf{k}_1\frac{\Delta t}{2}\right),$$

$$\mathbf{k}_3 = f\left(t_i + \frac{\Delta t}{2}, \mathbf{y}_i + \mathbf{k}_2\frac{\Delta t}{2}\right) \quad \text{and} \quad \mathbf{k}_4 = f(t_i + \Delta t, \mathbf{y}_i + \mathbf{k}_3\Delta t).$$

As RK4 is explicit we must satisfy stability constraints on the time step. In particular we need that $\frac{\Delta t}{h^2} < C$ (where, for RK4 and a diffusive problem with a normal discretisation matrix, C is approximately 4 [66, 93]). This implies that the errors for the computed solution, $O(\Delta t^4) + O(h^2)$, are dominated by the spatial discretisation and that the overall accuracy is $O(h^2)$. The problem is stiff: the time step needs to be chosen on stability considerations rather than based on accuracy. Further, given that we focus on the propagation of sharp fronts which typically have characteristic width $O(\sqrt{L})$, we must choose $h \ll \sqrt{L}$.

The Dirichlet boundary conditions are implemented at the points of the grid outside a radius of $1 - \frac{h}{2}$. This is a simple form of an embedded boundary method, see [65, 19, 24], and is carried out as follows. We divide the points of the grid into three categories; outer points, inner points and boundary points. Outer points are in cells of the grid completely outside the unit sphere and the value of the solution at these points is dictated by the Dirichlet boundary condition. Inner cells are completely inside the unit sphere and these points evolve according to the numerical scheme described above. Boundary cells, through which the boundary of the domain passes, are treated as outer cells and the value of the solution at these points is also dictated by the boundary conditions. Figure 2-5 provides an illustration of the method described above for the disc.
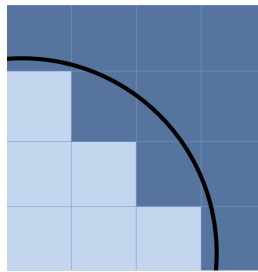
Figure 2-5: Dirichlet boundary conditions are imposed at the grid points at the centres of the dark blue cells. The solution evolves in the light blue cells according to our numerical scheme.

As in [24], we recall that our finite difference numerical scheme induces $O(h^2)$ truncation errors in the interior and note that this boundary method causes $O(h)$ truncation errors on the boundary. Hence, we find the truncation error $\tau_{j,k}$ at $(-1+jh, -1+kh)$ is given by

$$
\tau_{j,k} = \begin{cases} O(h) & \text{if } (-1+jh, -1+kh) \text{ is a boundary point or is adjacent to a boundary point,} \\ O(h^2) & \text{otherwise.} \end{cases}
$$

As the $O(h)$ error is limited to the boundary region, the solution error is still $O(h^2)$ in the interior and overall error is $O(h^2)$ in L^1 [24].

The methods described above are sufficient for the computations attempted here. For more accurate or complex problems implicit schemes may be necessary as they do not have such strict stability restrictions.

2.4 Thesis overview and literature review

Chapter 3 focuses on a nematic filled three-dimensional droplet with Dirichlet radial boundary conditions in the Landau-de Gennes framework. We work at the isotropic-nematic transition temperature and with the one-constant elastic energy density in the limit of vanishing elastic constant. This limit is studied in detail in the context of energy minimizers of the Landau-de Gennes energy functional. In Majumdar and Zarnescu 2010 [76], the authors show that global Landau-de Gennes minimizers on suitable three-dimensional domains are well approximated by a limiting harmonic map away from singularities. This limiting harmonic map is a minimizer of the bulk potential and hence corresponds to a uniaxial **Q**-tensor with the director given by a minimizer of a relevant harmonic map problem.

We adopt the gradient flow model to describe the nematodynamics in the absence of fluid flow at a constant temperature. Standard theory for parabolic systems shows that there exists a unique dynamic time-dependent solution for physically relevant initial and boundary conditions. Gradient flows have often been used in the context of liquid crystal dynamics. For example, in Popa-Nita and Sluckin 1996 [90] and Popa-Nita, Sluckin and Wheeler 1997 [91] the authors study a one-dimensional gradient flow model and the effects of biaxiality and elastic anisotropy in the Landau-de Gennes framework. In Fei et al 2015 [43], the authors study isotropic-nematic front propagation using the method of matched asymptotic expansions within the more general Beris-Edwards theory for nematodynamics [102]. In particular, the authors account for fluid flow and the coupling between fluid flow and nematic order. They derive evolution laws for the velocity

field, the director field of nematic alignment and the isotropic-nematic front but without any special attention to the effects of boundary and initial conditions. We work in a simpler dynamical framework with no fluid flow but with focus on how the dynamics are affected by the choice of boundary and initial data.

At the isotropic-nematic transition temperature, the Landau-de Gennes bulk potential bears strong resemblance to the Ginzburg-Landau potential in superconductivity [50]. In our first model problem we use the concept of normalized energy introduced in Bronsard and Kohn 1991 [13] and Bronsard and Stoth 1996 [15], to prove that isotropic-nematic interfaces propagate according to mean curvature in certain model situations. That is, the front moves with normal velocity equal to the average of its principal curvatures. At each point, the principal curvatures κ_1 and κ_2 are the maximum and minimum curvatures of the front surface, corresponding to the directions along which the front surface bends the most and least respectively. The long-time dynamics are described by an explicit critical point of the Landau-de Gennes energy - the Radial Hedgehog solution. As introduced in Chapters 1 and 2, the Radial Hedgehog solution is radially symmetric, with radial nematic alignment and a point defect at the centre corresponding to an isotropic core. We finish Chapter 3 with some numerical simulations of the full Landau-de Gennes gradient flow system. We focus on the interplay between initial conditions and transient dynamics followed by convergence to the static Radial Hedgehog solution using four different representative initial conditions. The transient dynamics have universal features which could have experimental repercussions.

Chapter 4 builds on the results of Chapter 3 with a study of the propagation of isotropic-nematic fronts in the presence of obstacles in three-dimensional spherical droplets. These obstacles, imposed by periodic forcing terms, affect the speed of the front resulting in an outward propagating space-time periodic pulsating wave solution. Such periodic forcing terms can be used to model front motion across porous media or through material impurities [35]. These types of forcing terms are also used to study front propagation over dislocation lines, such as in Kardar 1998 [58] where the author discusses interface pinning in solids with line defects.

Our problem is inspired by the work in Dirr and Yip 2006 [35] for the Allen-Cahn equation with unit elastic constant in one-dimension. We adapt the arguments to the case with small elastic constant on the three-dimensional sphere where forcing terms are dominant over mean curvature contributions to front propagation. This yields a critical minimal forcing strength required for pulsating wave solutions and an average front velocity for near critical forcing.

A key concept in [35] is a front motion phenomenon called an avalanche. Avalanches are periods of very quick front motion. Successive avalanches are separated by times of very slow front motion.

Avalanche motion is studied in many cases of obstacle driven motion and reaction diffusion equations. In Fisher 1998 [45] the author discusses avalanche interface motion and pinning and de-pinning in the presence of random obstacles using mean field theory for various model processes. In Carpio and Bonilla 2003 [21] alternating fast and slow front motion is observed for discrete bistable reaction diffusion equations for obstacle strength close to a critical de-pinning forcing. Chapter 4 is complemented with numerical simulations on a three-dimensional annulus and a two-dimensional square. We work on the annulus in order to minimize front motion by mean curvature and to better estimate the critical forcing required for pulsating wave solutions. We work with a range of initial conditions and compare our numerical results to our analytical predictions. Next we solve the Landau-de Gennes gradient flow system with forcing terms on the square. We introduce forcing terms which are periodic in the y-direction and induce front propagation down the square. We impose Dirichlet boundary conditions on the top and bottom edges. Inspired by two papers by Xia, Ponson, Ravichandran and Bhattacharya, we investigate the effect of a moon-shaped obstacle which opposes front motion. In particular, we are interested in how the orientation of the obstacle with respect to the front affects interface motion. In 2013 [112] the authors study the adhesion between surfaces and thin films, studying the force required to peel various thin films away from a given surface. In 2015 [113] a film with a circular arc-shaped heterogeneity is considered using numerical simulations and experiments. The arc-shaped area of the film has a higher adhesion to the surface. This is achieved experimentally by creating the shape on the film using an ink. The authors found that if the film is peeled from the surface starting from the rounded side of the arc, more peeling force is required to separate the film and surface than if the film is peeled from the surface starting from the pointed side of the arc. We make similar observations for certain forcings. First, we orientate the moon-shaped obstacle in the square so that the long rounded edge will meet the isotropic-nematic front as it travels down the square. We find the isotropic-nematic front becomes pinned by the obstacle in this case. However, if the moon-shaped obstacle is rotated by π, so the front meets the two points of the moon first, the interface is able to pass through.

In Chapter 5 we first consider a two-dimensional disc with Dirichlet boundary conditions subject to two distinct types of initial condition; planar and non-planar. Planar **Q**-tensors have zero Q_{13} and Q_{23} components and non-planar **Q**-tensors do not. We prove that planar initial conditions evolve to planar dynamic solutions which have an isotropic point at the centre of the disc for all times. These solutions develop an isotropic-nematic front which propagates inwards and is arrested near the origin. Non-planar initial conditions, including small non-planar perturbations of

planar initial conditions, converge to a universal non-planar profile. The small-time dynamics are almost indistinguishable from the planar case, however the front collapses at the origin and the dynamic solution escapes into an entirely nematic state. We track the transient dynamics and numerically compute quantitative estimates for the persistence time of the interface.

Our results are largely numerical, complemented by an analysis of a class of radially symmetric planar critical points of the Landau-de Gennes energy on a disc introduced in Ignat et al 2015 [55] and Fratta et al 2016 [33] for low temperatures. These solutions are labelled by two order parameters u and v that only depend on the radial distance from the origin. The theoretical results in this section are a generalization to the isotropic-nematic transition temperature of the results in [55] and [33]. In these papers the authors use (u, v)-solutions to study the existence and stability of defects of half-integer degree in the Landau-de Gennes framework.

We use the (u, v)-critical points to construct radially symmetric and non-symmetric initial conditions for the numerical simulations. The different types of initial conditions suggest that the transient dynamics have universal features independent of the symmetry or uniaxiality/biaxiality of the initial condition. For example, in all cases we have a well-defined isotropic-nematic front as a clear feature of the evolution trajectory.

So far, the model problems in Chapter 5 have minimal boundary conditions which are minimizers of the Landau-de Gennes bulk potential. In the last section, we study two-dimensional and three-dimensional dynamic solutions on a disc with non-minimal boundary conditions. The two-dimensional case can be easily understood and all dynamic solutions exhibit a rapidly growing isotropic core with a thin boundary layer. The three-dimensional case is more exciting and the transient dynamics are sensitive to the initial condition. In particular, the transient dynamics are dependent on the initial front location, a feature not seen in the model problems with minimal Dirichlet boundary conditions. For a planar initial condition with an isotropic-nematic front relatively close to the centre of the disc, the interface propagates inwards and replicates the planar dynamics observed for minimal boundary conditions. If the planar initial condition has an isotropic-nematic front close to the boundary of the disc, the interface propagates outwards and yields an almost entirely isotropic interior. In all cases, we have a boundary layer to match the fixed non-minimal Dirichlet condition.

In Chapter 6 we construct an Order Reconstruction-type Landau-de Gennes critical point on a square domain of edge length λ. This critical point is distinguished by a uniaxial cross with negative scalar order parameter along the square diagonals. This chapter is motivated by the Well Order Reconstruction solution (WORS) numerically reported in Kralj and Majumdar 2014

[60] for nematic-filled square wells. Nematic-filled square wells have been widely studied in the literature. For example, in Tsakonas et al 2007 [107], the authors study a planar bistable device consisting of a periodic array of micron-scale shallow square wells. The surfaces are treated to induce tangent boundary conditions so that the molecules in contact with the well edges lie in the plane of the surface. The authors complement their experiments with numerical modelling in the two-dimensional Landau-de Gennes framework. The authors observe two different static equilibria: a diagonal state for which the molecules roughly align along one of the square diagonals and a rotated state for which the molecules roughly rotate by π radians between a pair of opposite edges. In [60], the authors numerically model this device within the Landau-de Gennes theory. The authors recover the diagonal and rotated solutions for square dimensions much larger than a material dependent length scale known as the biaxial correlation length. However, for squares of edge length comparable to the biaxial correlation length, the authors find a new solution for which the $\mathbf{Q}$-tensor has a constant set of eigenvectors, one of which is $\hat{\mathbf{z}}$, the unit vector in the z-direction. The Well Order Reconstruction solution has a uniaxial diagonal cross along which the $\mathbf{Q}$-tensor has two equal positive eigenvalues and hence negative scalar order parameter. This uniaxial cross is surrounded by a ring of maximal biaxiality (where the $\mathbf{Q}$-tensor has a zero eigenvalue) which matches the uniaxial tangent Dirichlet conditions on the square edges. The WORS is interesting because it a two-dimensional example of an Order Reconstruction solution on the square. That is, the $\mathbf{Q}$-tensor mediates between the uniaxial diagonal cross and the uniaxial boundary via an eigenvalue exchange where the eigenframe is constant and only the eigenvalues change.

Order Reconstruction solutions have a long history in the context of nematic liquid crystals. They were reported in [100, 80] for uniaxial nematic defect cores where the defect core is surrounded by a torus of maximal biaxiality. The torus mediates between the uniaxial nematic state at the defect core and a uniaxial nematic state away from the core. Order Reconstruction solutions have been studied for hybrid nematic cells, typically consisting of a layer of nematic material sandwiched between a pair of parallel plates with a preferred boundary orientation on each plate [86, 10]. In Palffy-Muhoray, Gartland and Kelly 1994 [86], the authors work with orthogonal preferred boundary orientations. For small cell gaps, the authors find an Order Reconstruction solution with a constant eigenframe which connects the two opposing boundary alignments through one-dimensional eigenvalue variations along the normal of the plates. This Order Reconstruction solution is the only observable solution for cell gaps smaller than a certain critical value. For larger cell gaps, the authors observe the familiar twisted profiles where the eigenvectors rotate continuously throughout the cell to match the boundary alignments. The authors numerically compute a bifurcation diagram and show that the Order Reconstruction solution undergoes a

supercritical pitchfork bifurcation at a critical cell gap. In Lamy 2014 [62], the author studies the hybrid cell in a one-dimensional setting in the Landau-de Gennes framework. For a range of temperatures, the author proves the existence and uniqueness of the Order Reconstruction solution for small cell gaps as well as a supercritical pitchfork bifurcation as the cell gap increases. In Bisi et al 2003 [10], the authors consider the hybrid cell problem for non-orthogonal preferred boundary alignments. Their findings are contrasting to those of [86] and an unstable Order Reconstruction solution is observed for cell gaps larger than a critical value with the familiar twisted solutions always being preferred irrespective of cell gap.

We analytically study the two-dimensional Well Order Reconstruction solution on a square of edge length λ. We impose Dirichlet tangent conditions consistent with the experiments in [107] and look for Landau-de Gennes critical points which have a constant eigenframe with $\hat{\mathbf{z}}$ as an eigenvector and a uniaxial cross along the square diagonals. We parametrize these critical points by three order parameters, q_1, q_2 and q_3. At a fixed temperature, we can prove the existence of a class of Landau-de Gennes critical points with $q_2 = 0$ and constant q_3, with one degree of freedom labelled by q_1, for all values of λ. These critical points have a constant eigenframe by construction. The uniaxial cross is equivalent to $q_1 = 0$ along the square diagonals and in this case these critical points mimic the WORS. We interpret q_1 as a minimizer of a scalar variational problem with Dirichlet conditions and prove that the WORS is the unique critical point for small λ and that the critical point undergoes a supercritical pitchfork bifurcation as λ increases.

This chapter finishes with a numerical study of the gradient flow model of the Landau-de Gennes energy on a square of edge length λ with Dirichlet boundary conditions and WORS-type initial conditions. The long-time dynamic solutions converge to the WORS for small λ and we numerically compute estimates for the critical λ at which the WORS loses stability. The critical λ is proportional to the biaxial correlation length as predicted from the numerical simulations in [60] where the authors solve the Landau-de Gennes Euler-Lagrange equations with effectively constant initial conditions. Next we prove the existence of an Order Reconstruction-type solution on a regular hexagon of edge length λ. The method of proof is different to that on a square and we require Palais's principle of symmetric criticality [85, 62]. Again, we numerically observe the Order Reconstruction-type solution for small λ and find the critical stability criterion is proportional to the biaxial correlation length. This suggests that Order Reconstruction-type solutions may be generic for some regular convex polygons, raising interesting questions about the geometry, symmetry and multiplicity of Landau-de Gennes equilibria.

In Chapter 7 we consider a sixth-order Landau-de Gennes bulk potential which can admit biaxial minimizers in contrast to the fourth-order bulk potential which can only admit isotropic and uniaxial critical points. The biaxial phase, in which the molecules align with respect to two directors, has been predicted theoretically and observed experimentally. The existence of the biaxial nematic state was first predicted in Freiser 1970 [46]. Using the mean field Maier-Saupe theory, Freiser suggested that a phase transition from the uniaxial to the biaxial phase would occur as temperatures are lowered, due to the asymmetry of the molecules.

First- and second-order phase transitions between isotropic, uniaxial and biaxial states have been observed with decreasing temperature in thermotropic liquid crystals. A potassium-based compound was the subject of Yu and Saupe 1980 [114]. The authors focused on a small concentration range and detected a phase sequence containing isotropic, biaxial and multiple uniaxial states. This phase sequence was observed to be reversible on heating and cooling. Another thermotropic liquid crystalline material was considered in Merkel et al 2004 [79]. A low temperature biaxial phase was found after cooling the sample caused a second-order phase transition.

Although the biaxial state was initially theoretically studied using mean fields theories, variational approaches have also been employed. In Gramsbergen, Longa and de Jeu 1986 [51], the Landau-de Gennes energy functional is generalised by an additional sixth-order term in the bulk energy which allows for a biaxial phase. In Prostakov, Larin and Stryukov 2002 [92] a further extended bulk potential is explored with three additional terms of orders 4 to 6. In both papers phase diagrams are presented for various parameter ranges showing first- and second-order phase transitions between isotropic, uniaxial and biaxial states.

We follow the methods in Allender and Longa 2008 [3] where the Landau-de Gennes energy functional is generalised to allow for stable biaxial states using the sixth-order bulk potential discussed in [92]. In [3] the authors plot phase planes for different parameter values and, in particular, show the existence of a triple point temperature at which there exists equal energy isotropic, uniaxial and biaxial minimizers of the sixth-order bulk potential.

We return to the (u, v)-solutions introduced in [33] and discussed in Chapter 5. We study the gradient flow system for the (u, v)-parameters resulting from the Landau-de Gennes energy functional with sixth-order bulk potential. We focus on the evolution of fronts which separate the isotropic, uniaxial and biaxial phases at the triple point temperature. These fronts are imposed by suitable boundary and initial conditions. We use asymptotic methods to show that each interface evolves according to mean curvature in the limit of vanishing elastic constant and that, if the fronts meet at a triple junction, the interfaces meet at angles of $\frac{2\pi}{3}$. Asymptotic methods have been used to study three phase motion in Bronsard and Reitich 1993 [14] and Garcke, Nestler

and Stoth 1998 [47]. In [14] the authors discuss three phase front motion for the vector-valued Allen-Cahn, proving interface motion by mean curvature and an angle condition at the triple junction. Results from Rubinstein, Sternberg and Keller 1989 [96], which focuses on front motion in the scalar Allen-Cahn framework, are quoted in [14]. The methods from these two papers can be adapted to the (u, v)-system.

We complete Chapter 7 with numerical simulations, solving the full Landau-de Gennes gradient flow system associated with the sixth-order bulk potential. We impose different initial and boundary conditions to demonstrate the existence and behaviour of sharp fronts between the three co-existing states. There are situations where the numerical results depart from the asymptotic predictions and we discuss plausible reasons for this effect.

2.5   Publication and collaboration details

Chapters 3 and 5 of this thesis are joint work with Apala Majumdar and Paul Milewski. This work has been published in the SIAM Journal on Applied Mathematics as reference [74]. Chapter 4 of this thesis is joint work with Apala Majumdar and Nicolas Dirr. A paper on this work is currently in preparation. Chapter 6 is joint work with Apala Majumdar and Giacomo Canevari. This work has been also been accepted for publication in the SIAM Journal on Applied Mathematics and is reference [20].

Front propagation in spherical droplets

In Chapter 3 we focus on the Landau-de Gennes gradient flow system in the three-dimensional nematic droplet with Dirichlet radial boundary conditions. First we use the concept of normalized energy, introduced in Bronsard and Kohn 1991 [13], to prove motion by mean curvature of isotropic-nematic fronts at the isotropic-nematic transition temperature in a certain asymptotic limit. In the second half of Chapter 3 we numerically study the interplay between initial conditions and transient dynamics for four representative initial conditions.

3.1 Problem formulation

We take our domain to be the unit sphere given by $\Omega := \{\mathbf{x} \in \mathbb{R}^3; |\mathbf{x}| \leq 1\}$. Throughout this chapter we work at the isotropic-nematic transition temperature where $A = \frac{B^2}{27C}$ and investigate the propagation of fronts which separate the isotropic phase from the stable nematic phase in the limit $L \to 0$. To this end, we look for dynamic Radial Hedgehog-type solutions of the gradient flow system in (2.6). That is, we work with an ansatz of the form

$$\mathbf{Q} = h(r, t) \left(\hat{\mathbf{r}} \otimes \hat{\mathbf{r}} - \frac{\mathbf{I}}{3} \right), \tag{3.1}$$

where $\hat{\mathbf{r}} = (\cos \phi \sin \theta, \sin \phi \sin \theta, \cos \theta)$ is the three-dimensional unit radial vector and $h(r, t)$ is a scalar order parameter. We refer to these as Radial Hedgehog-type solutions by analogy with

the static Radial Hedgehog solution described in Chapter 2. We impose the Dirichlet Radial Hedgehog-type boundary condition

$$\mathbf{Q}_b = \frac{B}{3C}\left(\hat{\mathbf{r}} \otimes \hat{\mathbf{r}} - \frac{\mathbf{I}}{3}\right) \quad \text{on} \quad \partial\Omega. \tag{3.2}$$

Note that $\mathbf{Q}_b$ is a minimizer of the normalised bulk potential at the isotropic-nematic transition temperature. We work with uniaxial Radial Hedgehog-type initial conditions with front structures, such as

$$\mathbf{Q}(\mathbf{x}, 0) = \begin{cases} 0 & \text{for} \quad 0 \leq |\mathbf{x}| < r_0, \\ \frac{B}{3C}\left(\hat{\mathbf{r}} \otimes \hat{\mathbf{r}} - \frac{\mathbf{I}}{3}\right) & \text{for} \quad r_0 < |\mathbf{x}| \leq 1, \end{cases}$$

where $\frac{1}{2} < r_0 < 1$. This initial condition describes a sharp front at r_0 which separates the two minimizers of the bulk potential. We substitute the ansatz (3.1) into the non-dimensionalized gradient flow model associated with the Landau-de Gennes energy which we normalize by letting $\bar{\mathbf{Q}} = \mathbf{Q}/s_+ = \frac{3C}{B}\mathbf{Q}$. This yields

$$\bar{\mathbf{Q}}_t = \nabla^2\bar{\mathbf{Q}} - \frac{9}{\bar{L}}\left[\frac{1}{3}\bar{\mathbf{Q}} - 3\left(\bar{\mathbf{Q}}\bar{\mathbf{Q}} - \frac{\mathbf{I}}{3}|\bar{\mathbf{Q}}|^2\right) + |\bar{\mathbf{Q}}|^2\bar{\mathbf{Q}}\right], \tag{3.3}$$

where $\bar{L} = \frac{81C}{B^2}L$. We impose $\bar{\mathbf{Q}} = \bar{\mathbf{Q}}_b$ and $\bar{\mathbf{Q}}(\mathbf{x}, 0) = \bar{\mathbf{Q}}(\mathbf{x}, 0)$, where $\bar{\mathbf{Q}}_b$ and $\bar{\mathbf{Q}}(\mathbf{x}, 0)$ are related to $\mathbf{Q}_b$ and $\mathbf{Q}(\mathbf{x}, 0)$ by the change of variables described above. We drop the bars on the normalized $\mathbf{Q}$-tensor in what follows. On substitution we find that we have a solution of the gradient flow dynamic equations (3.3) of the form (3.1) provided $h(r, t)$ satisfies

$$h_t = h_{rr} + \frac{2}{r}h_r - \frac{6h}{r^2} + \frac{3}{L}h(1-h)(2h-1). \tag{3.4}$$

The boundary conditions on $h(r, t)$ are $h(0, t) = 0$ and $h(1, t) = 1$ for all $t \geq 0$ and the initial conditions require that

$$h(r, 0) = \begin{cases} 0 & \text{for} \quad 0 \leq r < r_0, \\ 1 & \text{for} \quad r_0 < r \leq 1. \end{cases} \tag{3.5}$$

The partial differential equation for the evolution of $h(r, t)$ in (3.4) can be interpreted as the gradient flow model associated with the one-dimensional energy functional

$$\frac{1}{4\pi\sqrt{\bar{L}}}\mathbf{I}_{LG}[h] = \int_0^1 \left[\sqrt{\bar{L}}\left(\frac{h_r^2}{3} + \frac{2h^2}{r^2}\right) + \frac{h^2(h-1)^2}{\sqrt{\bar{L}}}\right]r^2\,\mathrm{d}r. \tag{3.6}$$

We briefly discuss the behaviour of the solution $h(r, t)$ of (3.4) close to the origin. Taking an expansion $h(r, t) = \sqrt{\bar{L}} h_1(s, t) + \bar{L} h_2(s, t) + ...$, where $s = \frac{r}{\sqrt{\bar{L}}}$, we find to leading order

$$0 = \frac{d^2 h_1}{ds^2} + \frac{2}{s} \frac{dh_1}{ds} - \frac{6h}{s^2} - 3h_1.$$

Following the steps in [110], we make the change of variables $H(z) z^{-\frac{1}{2}} = h_1(s)$ where $z = ks$ and $k = 3i$. This yields

$$z^2 \frac{d^2 H}{dz^2} + z \frac{dH}{dz} + \left[z^2 - \left(\frac{5}{2} \right)^2 \right] H = 0.$$

The solutions to this equation are Bessel Functions and we have

$$H(z) = A J_{\frac{5}{2}}(z) + B Y_{\frac{5}{2}}(z),$$

for constants A and B, where J_n is the Bessel Function of the First Kind of order n and Y_n is the Bessel Function of the Second Kind of order n [110]. We set $B = 0$ as Bessel Functions of the Second Kind tend to infinity at the origin. Therefore, returning to the original variables, we have

$$h(r) = A \frac{J_{\frac{5}{2}}\left(\frac{k}{\sqrt{\bar{L}}} r \right)}{\sqrt{\frac{k}{\sqrt{\bar{L}}} r}},$$

close to the origin. The expansion of the Bessel Function $J_{\frac{5}{2}}$ in powers of r allows us to check that this behaviour is in agreement with that described in [73]. That is,

$$h(r) = \sum_{m=0}^{\infty} A_m r^m = A_2 r^2 \left(1 - \frac{r^2}{14} + o(r^4) \right)$$

where $A_m = 0$ for all m odd, as $r \to 0$.

Given a solution $h(r, t)$ of (3.4), we can construct a Radial Hedgehog-type dynamic solution of the gradient flow equations (3.3). By virtue of the uniqueness result in Proposition 2.1, this is the physically relevant solution for this model problem and hence we reduce the five-dimensional evolution problem to a one-dimensional evolution problem.

In [13] the authors study a closely related problem for front propagation in the Ginzburg-Landau framework. They rigorously prove front propagation by mean curvature for suitably defined initial

conditions with appropriately bounded energy. Our governing equation (3.4) is similar to that studied in [13], however we have an extra $-\frac{6h}{r^2}$ term. In particular, we cannot quote results from [13] (and [15]) without verifying that key inequalities are unchanged for $\bar{L}$ sufficiently small.

In this chapter we show that for suitable initial conditions $h(r, 0)$, the solution $h(r, t)$ will retain the front structure for all times $0 \le t \le T$ (where T will be defined later) and that the front will evolve according to mean curvature. In the case of a spherical interface evolving according to mean curvature, the front position $\rho(t)$ satisfies

$$\frac{d\rho}{dt} = -\frac{2}{\rho}, \quad \rho(0) = r_0.$$

Define the step function

$$f(r, t) = \begin{cases} 0 & \text{for} \quad 0 \le r < \rho(t), \\ 1 & \text{for} \quad \rho(t) < r \le 1. \end{cases}$$

We will show that the solution $h(r, t)$ of (3.4) tends to the function $f(r, t)$ in L^1. That is,

$$\int_0^1 |h(r, t) - f(r, t)| r^2 \, dr \to 0 \quad \text{as} \quad \bar{L} \to 0.$$

3.2 The weighted energy functional

We move into a co-moving frame by making the change of variables $R = r - \rho(t)$, $\tau = t$ and defining

$$w(R, \tau) = h(R + \rho(\tau), \tau) \quad \text{for} \quad -\rho(\tau) \le R \le 1 - \rho(\tau), \quad \tau \ge 0.$$

Then $h_r = w_R$ and $h_t = w_\tau - w_R \frac{d\rho}{d\tau} = w_\tau + \frac{2}{\rho} w_R$ so we can rewrite (3.4) to yield

$$\sqrt{\bar{L}} w_\tau = \sqrt{\bar{L}} \left(w_{RR} - \frac{2R}{\rho(R + \rho)} w_R - \frac{6w}{(R + \rho)^2} \right) + \frac{3}{\sqrt{\bar{L}}} w(1 - w)(2w - 1), \qquad (3.7)$$

with $w(-\rho(\tau), \tau) = 0$ and $w(1 - \rho(\tau), \tau) = 1$. Next, inspired by [13] and [15], we introduce a weight function $\phi(R, \tau)$ defined to be a solution of

$$\phi_R = -\frac{2R}{\rho(R + \rho)} \phi,$$

and note that

$$\phi(R, \tau) = \exp\left(-\frac{2R}{\rho} \right) \left(1 + \frac{R}{\rho} \right)^2,$$

is a solution of this equation. We will use that this solution satisfies

$$0 \leq \phi \leq 1, \quad \phi(-\rho(\tau), \tau) = 0, \quad \phi(0, \tau) = 1 \quad \text{and} \quad \phi_\tau \leq 0,$$

$$\phi(R, \tau) \geq 1 - \frac{4}{\rho(T_1)^2} R^2 \quad \text{for} \quad -a \leq R \leq a, \quad \tau \leq T_1. \tag{3.8}$$

In particular, $\phi(R, \tau) \geq \frac{1}{2}$ for $-a \leq R \leq a$, $\tau \leq T_1$ where $a = \min(\frac{1}{4\sqrt{2}}, 1-r_0)$ and $T_1 = \frac{1}{4}(r_0^2 - \frac{1}{4})$ is the first time for which $\rho(t) = \frac{1}{2}$. We now write (3.7) as

$$\sqrt{\bar{L}} w_\tau - \frac{\sqrt{\bar{L}}}{\phi} (\phi w_R)_R + \frac{6w\sqrt{\bar{L}}}{(R+\rho)^2} - \frac{3}{\sqrt{\bar{L}}} w(1-w)(2w-1) = 0, \tag{3.9}$$

for $-\rho(\tau) \leq R \leq 1 - \rho(\tau)$. The next step is to define the weighted energy

$$E_\phi[w](\tau) = \int_{-\rho(\tau)}^{1-\rho(\tau)} \phi(R, \tau) \left[\sqrt{\bar{L}} \left(\frac{w_R^2}{3} + \frac{2w^2}{(R+\rho)^2} \right) + \frac{w^2(1-w)^2}{\sqrt{\bar{L}}} \right] dR. \tag{3.10}$$

The rate of change of the weighted energy with respect to τ is given by

$$\frac{d}{d\tau} E_\phi[w](\tau) = \int_{-\rho(\tau)}^{1-\rho(\tau)} \phi_\tau \left[\sqrt{\bar{L}} \left(\frac{w_R^2}{3} + \frac{2w^2}{(R+\rho)^2} \right) + \frac{w^2(1-w)^2}{\sqrt{\bar{L}}} \right] dR$$

$$+ \int_{-\rho(\tau)}^{1-\rho(\tau)} \phi \left[\sqrt{\bar{L}} \left(\frac{2}{3} w_R w_{R\tau} + 4 \frac{w w_\tau}{(R+\rho)^2} \right) - 2 \frac{w_\tau}{\sqrt{\bar{L}}} w(1-w)(2w-1) \right] dR$$

$$- \phi \frac{d\rho}{dt} \left[\sqrt{\bar{L}} \left(\frac{w_R^2}{3} + \frac{2w^2}{(R+\rho)^2} \right) + \frac{w^2(1-w)^2}{\sqrt{\bar{L}}} \right] \Bigg|_{R=-\rho(\tau)}^{R=1-\rho(\tau)},$$

using Leibniz's rule of integration.

Following the steps in [13], the first integral in the expression is non-positive since $\phi_\tau \leq 0$. Further, noting that $(\phi w_R w_\tau)_R - w_\tau (\phi w_R)_R = \phi w_R w_{R\tau}$ and recalling (3.9) we can show

$$\int_{-\rho(\tau)}^{1-\rho(\tau)} \phi \left[\sqrt{\bar{L}} \left(\frac{2}{3} w_R w_{R\tau} + 4 \frac{w w_\tau}{(R+\rho)^2} \right) - 2 \frac{w_\tau}{\sqrt{\bar{L}}} w(1-w)(2w-1) \right] dR$$

$$= -\frac{2}{3} \sqrt{\bar{L}} \int_{-\rho(\tau)}^{1-\rho(\tau)} \phi w_\tau^2 \, dR + \frac{2}{3} \sqrt{\bar{L}} \phi w_R w_\tau \Bigg|_{R=1-\rho(\tau)}.$$

Using that $\phi = 0$ at $R = -\rho(\tau)$ and $w = 1$ at $R = 1 - \rho(\tau)$ we have

$$\frac{d}{d\tau}E_\phi[w](\tau) \le -\frac{2}{3}\sqrt{\bar{L}}\int_{-\rho(\tau)}^{1-\rho(\tau)}\phi w_\tau^2\, dR + \frac{2}{3}\sqrt{\bar{L}}\phi w_R w_\tau\Big|_{R=1-\rho(\tau)}$$
$$-\frac{1}{3}\sqrt{\bar{L}}\phi\frac{d\rho}{dt}w_R^2\Big|_{R=1-\rho(\tau)} + \frac{4}{\rho}\sqrt{\bar{L}}\phi.$$

Further $h_t = w_\tau - \frac{d\rho}{d\tau}w_R = 0$ at $R = 1 - \rho(\tau)$ so we can write

$$\frac{2}{3}\sqrt{\bar{L}}\phi w_R w_\tau - \frac{1}{3}\sqrt{\bar{L}}\phi\frac{d\rho}{d\tau}w_R^2\Big|_{R=1-\rho(\tau)} = \frac{1}{3}\sqrt{\bar{L}}\phi\frac{d\rho}{d\tau}w_R^2\Big|_{R=1-\rho(\tau)} = -\frac{2}{3\rho}\sqrt{\bar{L}}\phi w_R^2\Big|_{R=1-\rho(\tau)} < 0.$$

As $\phi \le 1$ and $\rho \ge \frac{1}{2}$ for $\tau \le T_1$, we finally have

$$\frac{d}{d\tau}E_\phi[w](\tau) \le -\frac{2}{3}\sqrt{\bar{L}}\int_{-\rho(\tau)}^{1-\rho(\tau)}\phi(R,\tau)w_\tau^2\, dR + 8\sqrt{\bar{L}},$$

for $\tau \le T_1$. Hence we have proved:

Proposition 3.1. *For $E_\phi[w](\tau)$, the weighted energy defined in (3.10), we have the following inequality*

$$\frac{d}{d\tau}E_\phi[w](\tau) \le -\frac{2}{3}\sqrt{\bar{L}}\int_{-\rho(\tau)}^{1-\rho(\tau)}\phi(R,\tau)w_\tau^2\, dR + 8\sqrt{\bar{L}},$$

for all $\tau \le T_1$.

For the similar problem in the Ginzburg-Landau framework discussed in [13], the weighted energy is strictly decreasing. We have an additional positive contribution from the $-\frac{6h}{r^2}$ term in (3.4) and hence have less control on the weighted energy. However, we will see that this bound suffices for $\bar{L}$ sufficiently small. The next step is to find a lower bound on the weighted energy.

Define the function

$$g(s) = \frac{2}{\sqrt{3}}\int_0^s w(1-w)\, dw.$$

The interface energy associated with the front is thought of as $g(1) = \frac{1}{3\sqrt{3}}$. Further, define the step function

$$v(R) = \begin{cases} 0 & \text{for} \quad -\rho(\tau) \le R < 0, \\ 1 & \text{for} \quad 0 < R \le 1 - \rho(\tau), \end{cases}$$

and proceed with the following proposition adapted from [15].

Proposition 3.2. *Let $0 < \alpha \leq \frac{1}{4}$. If for some smooth function w*

$$E_\phi[w](\tau) \leq C_1 \quad \text{and} \quad \int_{-a}^{a} |g(w) - g(v)|\, \mathrm{d}R \leq \frac{g(1)}{4}\bar{L}^\alpha, \tag{3.11}$$

then

$$E_\phi[w](\tau) \geq g(1) - C_2\bar{L}^{\frac{1}{2}-\alpha} - C_3\bar{L}^{2\alpha},$$

for all $\tau \leq T_1$. C_1, C_2, C_3 are positive constants and independent of $\bar{L}$.

Proof. We begin the proof by defining two regions:

$$S_+ = \left\{R : w(R) \geq \frac{1}{2}\right\} \quad \text{and} \quad S_- = \left\{R : w(R) < \frac{1}{2}\right\}.$$

Since $v = 0$ for $R < 0$, (3.11) implies

$$\int_{-2\bar{L}^\alpha}^{0} |g(w) - g(0)|\, \mathrm{d}R \leq \frac{g(1)}{4}\bar{L}^\alpha.$$

As $g(w(R))$ is bounded below by $g\left(\frac{1}{2}\right)$ over S_+, we must have that

$$\int_{S_+\cap(-2\bar{L}^\alpha,0)} |g(w) - g(0)|\, \mathrm{d}R \geq |S_+ \cap (-2\bar{L}^\alpha, 0)|\left[g\left(\frac{1}{2}\right) - g(0)\right].$$

Using these two inequalities we deduce

$$|S_+ \cap (-2\bar{L}^\alpha, 0)| \leq \frac{1}{2}\bar{L}^\alpha,$$

and so

$$|S_- \cap (-2\bar{L}^\alpha, 0)| \geq \frac{3}{2}\bar{L}^\alpha.$$

From the assumption of the proposition

$$E_\phi[w](\tau) = \int_{-\rho(\tau)}^{1-\rho(\tau)} \phi(R, \tau)\left[\sqrt{\bar{L}}\left(\frac{w_R^2}{3} + \frac{2w^2}{(R+\rho)^2}\right) + \frac{w^2(1-w)^2}{\sqrt{\bar{L}}}\right]\mathrm{d}R \leq C_1,$$

and so, in particular,

$$\int_{S_-\cap(-2\bar{L}^\alpha,0)} \phi\frac{w^2(1-w)^2}{\sqrt{\bar{L}}}\, \mathrm{d}R \leq C_1.$$

As $\phi \geq \frac{1}{2}$ for $-a \leq R \leq a$ and $\tau \leq T_1$ this yields

$$\int_{S_- \cap (-2\bar{L}^\alpha, 0)} w^2 (1-w)^2 \, \mathrm{d}R \leq 2C_1 \sqrt{\bar{L}}.$$

Therefore there exists $R_1 \in S_- \cap (-2\bar{L}^\alpha, 0)$ for which

$$w^2(R_1)(1 - w(R_1))^2 \leq \frac{4}{3} C_1 \bar{L}^{\frac{1-2\alpha}{2}}.$$

However $w(R_1) < \frac{1}{2}$ as $R \in S_-$ so we can conclude that

$$w(R_1) \leq L_1 \bar{L}^{\frac{1-2\alpha}{4}},$$

for some positive constant L_1 independent of $\bar{L}$. Following the same methods, it is possible to show the existence of a point $R_2 \in (0, 2\bar{L}^\alpha)$ for which

$$w(R_2) \geq 1 - L_2 \bar{L}^{\frac{1-2\alpha}{4}},$$

for some positive constant L_2 independent of $\bar{L}$. The last step is to compute bounds for the weighted energy following [15]. Note that

$$\begin{aligned}
E_\phi[w](\tau) &\geq \int_{R_1}^{R_2} \phi \left(\sqrt{\bar{L}} \frac{w_R^2}{3} + \frac{w^2(1-w)^2}{\sqrt{\bar{L}}} \right) \mathrm{d}R, \\
&\geq \int_{R_1}^{R_2} \frac{2}{\sqrt{3}} \phi |w_R| w(1-w) \, \mathrm{d}R,
\end{aligned} \tag{3.12}$$

and recall the lower bound in (3.8) which gives $\phi(R, \tau) \geq 1 - 64\bar{L}^{2\alpha}$ for $R \in (R_1, R_2)$. Further

$$|g_R| = \frac{2}{\sqrt{3}} |w_R| w(1-w),$$

and hence for $0 < \alpha \leq \frac{1}{4}$, (3.12) becomes

$$\begin{aligned}
E_\phi[w](\tau) &\geq (1 - 64\bar{L}^{2\alpha}) |g(w(R_2)) - g(w(R_1))|, \\
&\geq (1 - 64\bar{L}^{2\alpha}) \left(g(1) - L_4 \bar{L}^{\frac{1-2\alpha}{2}} \right), \\
&\geq g(1) - L_5 \bar{L}^{\frac{1}{2}-\alpha} - L_6 \bar{L}^{2\alpha},
\end{aligned}$$

for positive constants L_3, L_4, L_5, L_6 independent of $\bar{L}$. $\qquad \square$

The next propositions concern the existence of a function w which satisfies the hypotheses of Proposition 3.2. Proposition 3.3 constructs a function which satisfies the energy bound in (3.11) initially and will be used in conjunction with Proposition 3.1 to give the energy bound for all times. The construction is very similar to that described in [104] and we give a statement for completeness. In Proposition 3.4 we prove that for the initial condition constructed in Proposition 3.3, the second assumption in (3.11) holds all $\tau \leq T_2$ for some time T_2 of order one.

Proposition 3.3. *Define the function*

$$\sigma(R) = \frac{1}{1 + \exp(-\sqrt{3}R)}.$$

Further, for $\bar{L}$ sufficiently small define

$$w(R) = \begin{cases} 1 & \text{for} \quad 2\bar{L}^{1/4} < R \leq 1, \\[2mm] 1 + \left(\frac{1 - \sigma\left(\frac{1}{\bar{L}^{1/4}}\right)}{\bar{L}^{1/4}} \right) (R - 2\bar{L}^{1/4}) & \text{for} \quad \bar{L}^{1/4} \leq R \leq 2\bar{L}^{1/4}, \\[2mm] \sigma\left(\frac{R}{\sqrt{\bar{L}}} \right) & \text{for} \quad -\bar{L}^{1/4} \leq R \leq \bar{L}^{1/4}, \\[2mm] \frac{\sigma\left(-\frac{1}{\bar{L}^{1/4}}\right)}{\bar{L}^{1/4}} (R + 2\bar{L}^{1/4}) & \text{for} \quad -2\bar{L}^{1/4} \leq R \leq -\bar{L}^{1/4}, \\[2mm] 0 & \text{for} \quad 0 \leq R < -2\bar{L}^{1/4}. \end{cases} \tag{3.13}$$

Then

$$E_\phi[w](0) \leq g(1) + C_1 \bar{L}^{1/4}, \tag{3.14}$$

and

$$\int_{-\rho(\tau)}^{\rho(\tau)} g(w(R)) - g(v(R)) \, dR \leq C_2 \bar{L}^{1/8}, \tag{3.15}$$

for some positive constants C_1 and C_2 independent of $\bar{L}$.

Proof. Follows the same steps as [104]. The proof of the inequality (3.14) follows by a direct computation of the weighted energy $E_\phi[w]$ for w as in (3.13), using that $\frac{d\sigma}{dR} = \sqrt{3}\sigma(1 - \sigma)$. Inequality (3.15) follows from the convergence of w to v as $\bar{L} \to 0$. $\quad\square$

Proposition 3.4. *Let $0 < \alpha \leq \frac{1}{6}$. Assume that $E_\phi[w](0) \leq g(1) + C_1 \bar{L}^{2\alpha}$ for some positive constant C_1 independent of $\bar{L}$ and that for a as introduced previously*

$$\int_{-a}^{a} |g(w(R,0)) - g(v)| \, dR \leq \frac{g(1)}{8} \bar{L}^{\alpha}.$$

Let T_2 be the first time for which

$$\int_{-a}^{a} |g(w(R, T_2)) - g(w(R, 0))| \, dR = \frac{g(1)}{8} \bar{L}^{\alpha}.$$

Then $T_2 \geq \min(T_1, C)$ (so T_2 is order one) for some positive constant C independent of $\bar{L}$ and

$$\int_{-a}^{a} |g(w(R, \tau)) - g(v)| \, dR \leq \frac{g(1)}{4} \bar{L}^{\alpha},$$

for all $\tau \leq T_2$.

Proof. The proof closely follows that in [15]. From the assumptions of the proposition and the triangle inequality we have, for all $\tau \leq T_2$,

$$\int_{-a}^{a} |g(w(R, \tau)) - g(v)| \, dR \leq \frac{g(1)}{4} \bar{L}^{\alpha}.$$

If $T_2 \geq T_1$ the result follows so suppose that $T_2 \leq T_1$. We recall that for all $\tau \leq T_2 \leq T_1$ we have

$$\phi(R, \tau) \geq \frac{1}{2} \quad \text{for} \quad -a \leq R \leq a.$$

Proposition 3.1 and the initial bound on the weighted energy yield

$$E_\phi[w](T_2) \leq g(1) + C_1 \bar{L}^{2\alpha} + 8\sqrt{\bar{L}} \, T_2. \tag{3.16}$$

Therefore the assumptions of Proposition 3.2 apply and we can obtain a lower bound for the weighted energy of the form

$$E_\phi[w](T_2) \geq g(1) - C_2 \bar{L}^{\frac{1}{2}-\alpha} - C_3 \bar{L}^{2\alpha}.$$

Hence

$$E_\phi[w](0) - E_\phi[w](T_2) \leq L_1 \bar{L}^{2\alpha} + L_2 \bar{L}^{\frac{1}{2}-\alpha}, \tag{3.17}$$

for positive constants L_1 and L_2 independent of $\bar{L}$. Next, we note that

$$
\begin{aligned}
\frac{g(1)}{8}\bar{L}^\alpha &= \int_{-a}^{a} |g(w(R, T_2)) - g(w(R, 0))| \, \mathrm{d}R, \\
&\leq \int_{-a}^{a} \int_{0}^{T_2} |\partial_\tau g(w(R, \tau))| \, \mathrm{d}\tau \, \mathrm{d}R, \\
&\leq \frac{4}{\sqrt{3}} \int_{-a}^{a} \int_{0}^{T_2} \phi |w_\tau| w(1 - w) \, \mathrm{d}\tau \, \mathrm{d}R, \\
&\leq \frac{2}{\sqrt{3}} \left(\delta \bar{L}^{\frac{1-2\alpha}{2}} \int_{0}^{T_2} \int_{-a}^{a} \phi |w_\tau|^2 \, \mathrm{d}R \, \mathrm{d}\tau + \frac{1}{\delta \bar{L}^{\frac{1-2\alpha}{2}}} \int_{0}^{T_2} \int_{-a}^{a} \phi w^2 (1 - w)^2 \, \mathrm{d}R \, \mathrm{d}\tau \right),
\end{aligned}
$$

for any $\delta > 0$. Proposition 3.1 implies

$$
\frac{2}{3} \sqrt{\bar{L}} \int_{-\rho(\tau)}^{1-\rho(\tau)} \phi(R, \tau) w_\tau^2 \, \mathrm{d}R \leq -\frac{d}{d\tau} E_\phi[h](\tau) + 8\sqrt{\bar{L}},
$$

and so

$$
\int_{0}^{T_2} \int_{-a}^{a} \phi |w_\tau|^2 \, \mathrm{d}R \, \mathrm{d}\tau \leq \frac{3}{2\sqrt{\bar{L}}} (E_\phi[w](0) - E_\phi[w](T_2)) + 12 T_2.
$$

Hence we can conclude using inequality (3.17) that

$$
\frac{g(1)}{8}\bar{L}^\alpha \leq \frac{2}{\sqrt{3}} \left[\delta \left(L_3 \bar{L}^\alpha + L_4 \bar{L}^{\frac{1-4\alpha}{2}} + L_5 \bar{L}^{\frac{1-2\alpha}{2}} \right) + \frac{\bar{L}^\alpha}{\delta} T_2 E_\phi[w](T_2) \right],
$$

for postive constants L_3, L_4 and L_5 independent of $\bar{L}$. Dividing through by $\bar{L}^\alpha$ yields

$$
\frac{g(1)}{8} \leq \frac{2}{\sqrt{3}} \left[\delta \left(L_3 + L_4 \bar{L}^{\frac{1-6\alpha}{2}} + L_5 \bar{L}^{\frac{1-4\alpha}{2}} \right) + \frac{1}{\delta} T_2 E_\phi[w](T_2) \right].
$$

We choose δ sufficiently small and recall (3.16) to deduce that for $0 < \alpha \leq \frac{1}{6}$ and for $\bar{L}$ sufficiently small, T_2 is order one. $\qquad \square$

Equipped with a weighted energy and estimates of the rate of change and bounds for this weighted energy, we are now in a position to adapt arguments from [13] to prove our main result.

3.3 Front propagation by mean curvature

Theorem 3.1. *Suppose $h(0,0) = 0$, $h(1,0) = 1$ and that $h(r,0)$ satisfies*

$$\int_0^1 \psi_0(r) \left[\sqrt{\bar{L}} \left(\frac{h_r(r,0)^2}{3} + \frac{2h(r,0)^2}{r^2} \right) + \frac{h(r,0)^2(1 - h(r,0))^2}{\sqrt{\bar{L}}} \right] r^2 \, dr \leq g(1) + C_1 \bar{L}^{2\alpha},$$

where

$$\psi_0(r) = \frac{1}{r_0^2} \exp\left[-2 \left(\frac{r}{r_0} - 1 \right) \right],$$

and

$$\int_0^1 |g(h(r,0)) - g(f(r,0))| \, dR \leq C_2 \bar{L}^{\alpha},$$

for positive constants C_1 and C_2 independent of $\bar{L}$. (The existence of an initial condition satisfying these conditions follows from Proposition 3.3 for $\alpha = \frac{1}{8}$.) Then for $t \leq T = \min(T_2, T_1)$

$$\int_0^1 |h_{\bar{L}}(r,t) - f(r,t)| r^2 \, dr \to 0, \tag{3.18}$$

as $\bar{L} \to 0$, where $h_{\bar{L}}(r,t)$ is the solution of (3.4) subject to initial condition (3.5) and

$$f(r,t) = \begin{cases} 0 & \text{for} \quad 0 \leq r < \rho(t), \\ 1 & \text{for} \quad \rho(t) < r \leq 1. \end{cases}$$

Proof. For a contradiction, suppose (3.18) does not hold. In this case there exists a sequence $\bar{L}_j > 0$ with $\bar{L}_j \to 0$ as $j \to \infty$ and some constant δ such that

$$\int_0^T \int_0^1 |h_{\bar{L}_j}(r,t) - f(r,t)| r^2 \, dr \, dt \geq \delta.$$

By [13, Theorem 2.3] there exists a subsequence $\bar{L}_j$ and a function $h^*(r,t)$ such that $h_{\bar{L}_j}(r,t) \to h^*(r,t)$ as $j \to \infty$ and

$$\int_0^T \int_0^1 |h^*(r,t) - f(r,t)| r^2 \, dr \, dt \geq \delta.$$

Let $v^*(R,\tau) = h^*(R + \rho(\tau), \tau)$, then the initial bound on the weighted energy implies that $E_\phi[v^*](0) \leq g(1) + C_1 \bar{L}^{2\alpha}$. From Proposition 3.1, we have that for any $\tau \leq T$

$$E_\phi[v^*](\tau) \leq g(1) + C_1 \bar{L}^{2\alpha} + K\sqrt{\bar{L}} T, \tag{3.19}$$

for positive constant K independent of $\bar{L}$. Proposition 3.4 gives us that

$$\int_{-a}^{a} |g(v^*(R,\tau)) - g(v(R))| \mathrm{d}R \leq \frac{g(1)}{4} \bar{L}^\alpha,$$

for all $\tau \leq T$. Hence the lower bound on the weighted energy in (3.12) applies to yield

$$\int_{-2\bar{L}^\alpha}^{2\bar{L}^\alpha} \phi \left[\sqrt{\bar{L}} \left(\frac{v_R^{*2}}{3} + \frac{2v^{*2}}{(R+\rho)^2} \right) + \frac{v^{*2}(1-v^*)^2}{\sqrt{\bar{L}}} \right] \mathrm{d}R \geq g(1) - C_2 \bar{L}^{\frac{1}{2}-\alpha} - C_3 \bar{L}^{2\alpha}, \quad (3.20)$$

for positive constants C_2 and C_3 independent of $\bar{L}$. Therefore combining the upper bound (3.19), the lower bound (3.20) and that $\phi(R,\tau) \geq \frac{1}{2}$ for $-a \leq R \leq a$ and $\tau \leq T$, we find

$$\int_{-\rho(\tau)}^{-2\bar{L}^\alpha} \frac{1}{2} \left[\sqrt{\bar{L}} \left(\frac{v_R^{*2}}{3} + \frac{2v^{*2}}{(R+\rho)^2} \right) + \frac{v^{*2}(1-v^*)^2}{\sqrt{\bar{L}}} \right] \mathrm{d}R \leq C_4 \bar{L}^{\frac{1}{2}-\alpha} + C_5 \bar{L}^{2\alpha} + C_6 \bar{L}^{\frac{1}{2}},$$

for positive constants C_4, C_5 and C_6 independent of $\bar{L}$. However

$$|g_R(v^*)| \leq \sqrt{\bar{L}} \left(\frac{v_R^{*2}}{3} + \frac{2v^{*2}}{(R+\rho)^2} \right) + \frac{v^{*2}(1-v^*)^2}{\sqrt{\bar{L}}},$$

because

$$|g_R(v^*)| = \frac{2}{\sqrt{3}} |v_R^*| v^*(1-v^*) \leq \sqrt{\bar{L}} \frac{v_R^{*2}}{3} + \frac{v^{*2}(1-v^*)^2}{\sqrt{\bar{L}}}.$$

Therefore

$$\int_{-\rho(\tau)}^{-2\bar{L}^\alpha} \frac{1}{2} |g_R| \, \mathrm{d}R \leq C_4 \bar{L}^{\frac{1}{2}-\alpha} + C_5 \bar{L}^{2\alpha} + C_6 \bar{L}^{\frac{1}{2}}.$$

This implies that g is essentially constant on $(-\rho(\tau), -2\bar{L}^\alpha)$ and since there exists $R_1 \in (-2\bar{L}^\alpha, 0)$ for which $v^* = 0$ as $\bar{L} \to 0$, we deduce that $g(v^*) = g(0)$ for $R \in (-\rho(\tau), -2\bar{L}^\alpha)$. Hence $v^* = 0$ for $R \leq -2\bar{L}^\alpha$. Similarly we can show that $v^* = 1$ for $R \geq 2\bar{L}^\alpha$. Therefore in the limit $\bar{L} \to 0$, we have $v^* = f(r,t)$ and a contradiction which finishes the proof. $\qquad\square$

Intuitively, this theorem gives that for suitable initial conditions with efficient fronts, the system does not have the energy to create additional interfaces away from $\rho(\tau)$. Hence v^* is effectively constant away from the front, which evolves according to mean curvature at least for an order one length of time.

3.4 Numerical simulations in spherical droplets

In this section we numerically study the full non-dimensionalized Landau-de Gennes gradient flow system on the sphere at the isotropic-nematic transition temperature. Recall we normalized the five coupled nonlinear parabolic partial differential equations to yield (3.3), which can be written explicitly as

$$\frac{\partial Q_{11}}{\partial t} = \nabla^2 Q_{11} - \frac{9}{\bar{L}} \Bigg(2(Q_{11}^2 + Q_{22}^2 + Q_{12}^2 + Q_{11}Q_{22} + Q_{13}^2 + Q_{23}^2)Q_{11}$$
$$- (Q_{11}^2 + Q_{12}^2 + Q_{13}^2 - 2Q_{22}^2 - 2Q_{11}Q_{22} - 2Q_{23}^2) + \frac{1}{3}Q_{11} \Bigg), \qquad (3.21)$$

$$\frac{\partial Q_{22}}{\partial t} = \nabla^2 Q_{22} - \frac{9}{\bar{L}} \Bigg(2(Q_{11}^2 + Q_{22}^2 + Q_{12}^2 + Q_{11}Q_{22} + Q_{13}^2 + Q_{23}^2)Q_{22}$$
$$- (Q_{12}^2 + Q_{22}^2 + Q_{23}^2 - 2Q_{11}^2 - 2Q_{11}Q_{22} - 2Q_{13}^2) + \frac{1}{3}Q_{22} \Bigg), \qquad (3.22)$$

$$\frac{\partial \bar{Q}_{12}}{\partial t} = \nabla^2 Q_{12} - \frac{9}{\bar{L}} \Bigg(2(Q_{11}^2 + Q_{22}^2 + Q_{12}^2 + Q_{11}Q_{22} + Q_{13}^2 + Q_{23}^2)Q_{12}$$
$$- 3(Q_{11}Q_{12} + Q_{12}Q_{22} + \bar{Q}_{13}Q_{23}) + \frac{1}{3}Q_{12} \Bigg), \qquad (3.23)$$

$$\frac{\partial Q_{13}}{\partial t} = \nabla^2 Q_{13} - \frac{9}{\bar{L}} \Bigg(2Q_{11}^2 + Q_{22}^2 + Q_{12}^2 + Q_{11}Q_{22} + Q_{13}^2 + Q_{23}^2)Q_{13}$$
$$- 3(Q_{12}Q_{23} - Q_{22}Q_{13}) + \frac{1}{3}Q_{13} \Bigg), \qquad (3.24)$$

$$\frac{\partial Q_{23}}{\partial t} = \nabla^2 Q_{23} - \frac{9}{\bar{L}} \Bigg(2(Q_{11}^2 + Q_{22}^2 + Q_{12}^2 + Q_{11}Q_{22} + Q_{13}^2 + Q_{23}^2)Q_{23}$$
$$- 3(Q_{12}Q_{13}Q_{23}Q_{11}) + \frac{1}{3}Q_{23} \Bigg). \qquad (3.25)$$

In the above $\bar{L} = \frac{81C}{B^2}L$ as before. We work with $\bar{L} = 6.9 \times 10^{-4}$ unless specified otherwise.

3.4.1 Numerical methods

In this section, and for other geometries in later chapters unless specified otherwise, the system of partial differential equations (3.21) - (3.25) is solved using the methods described in Chapter 2. The unit sphere is embedded into the cube $[-1, 1]^3$ which is discretised with a uniform cartesian grid with spatial resolution h. The Dirichlet boundary conditions are implemented at the points of the grid within distance $\frac{h}{2}$ of the boundary of the unit sphere. For interior points, the solution satisfies the system (3.21)-(3.25) and in the exterior of the physical domain, we solve $\mathbf{Q}_t = 0$.

We use finite difference schemes for spatial derivatives and time stepping is accomplished with a standard fourth-order Runge-Kutta scheme.

3.4.2 Numerical simulations

We solve the system (3.21)-(3.25) with four different sets of initial conditions subject to the fixed boundary condition

$$\mathbf{Q}_b = \hat{\mathbf{r}} \otimes \hat{\mathbf{r}} - \frac{\mathbf{I}}{3} \quad \text{on} \quad r = 1, \tag{3.26}$$

where $\hat{\mathbf{r}}$ is the three-dimensional unit radial vector. The first two initial conditions concern uniaxial Radial Hedgehog-type initial conditions of the form

$$\mathbf{Q}(\mathbf{r}, 0) = h(r, 0) \left(\hat{\mathbf{r}} \otimes \hat{\mathbf{r}} - \frac{\mathbf{I}}{3} \right). \tag{3.27}$$

Case I prescribes an initial condition $h(r, 0)$ with a front structure given by

$$h(r, 0) = \frac{1}{2} \left[1 + \tanh \left(\frac{r - r_0}{\sqrt{\bar{L}}} \right) \right],$$

and **Case II** focuses on initial conditions without a front structure with

$$h(r, 0) = r. \tag{3.28}$$

For Cases I and II, by virtue of the well-posedness of the gradient flow system, we can check that the corresponding dynamic solution $\mathbf{Q}(\mathbf{r}, t)$ is given by

$$\mathbf{Q}(\mathbf{r}, t) = h(r, t) \left(\hat{\mathbf{r}} \otimes \hat{\mathbf{r}} - \frac{\mathbf{I}}{3} \right),$$

where $h(r, t)$ is a solution of (3.4) subject to the relevant initial condition.

For each initial condition we study several aspects of the solution generated. First we study $|\mathbf{Q}(\mathbf{r}, t)|^2$ to illustrate the evolution of the order parameter $h(r, t)$ and the interface introduced by the initial condition. We plot the position of the front with time and make comparisons with the motion by mean curvature predicted in Section 3.3. Next we consider the eigenvalues of $\mathbf{Q}(\mathbf{r}, t)$. Recall that the eigenvalues of a $\mathbf{Q}$-tensor determine whether the nematic sample is in an isotropic, uniaxial or biaxial phase. The evolution of the initial interface can also be tracked by studying the eigenvalues of $\mathbf{Q}(\mathbf{r}, t)$.

In [76], the authors present a general analysis of Landau-de Gennes energy minimizers in the $\bar{L} \to 0$ limit. Based on their analysis, it is expected the minimizers will be of the form

$$\mathbf{Q}^* = s \left(\mathbf{n}^* \otimes \mathbf{n}^* - \frac{\mathbf{I}}{3} \right),$$

where $s = 0$ or $s = 1$ (so that $\mathbf{Q}$ is a minimizer of $f_B(\mathbf{Q})$) and $\mathbf{n}^*$ is a solution of the harmonic map equations

$$\nabla^2 \mathbf{n}^* + |\nabla \mathbf{n}^*|^2 \mathbf{n}^* = 0.$$

These are the minimizers predicted by the Oseen-Frank theory. One solution of the harmonic map equations on a sphere subject to the boundary condition (3.26) is

$$\mathbf{n}^* = \hat{\mathbf{r}} = (\cos \phi \sin \theta, \sin \phi \sin \theta, \cos \theta).$$

Hence, we also numerically compute the differences $\left| \mathbf{Q}(\mathbf{r}, t)_{ij} - \mathbf{Q}^*_{ij} \right|$ for $s = 1$ and observe that

$$\mathbf{Q}(\mathbf{r}, t) \to |\mathbf{Q}(\mathbf{r}, t)| \left(\hat{\mathbf{r}} \otimes \hat{\mathbf{r}} - \frac{\mathbf{I}}{3} \right) \quad \text{as} \quad t \to \infty,$$

where $|\mathbf{Q}(\mathbf{r}, t)|$ has a front structure close to the origin which connects $s = 0$ and $s = 1$. This behaviour is illustrated with plots for the Q_{11} component of the $\mathbf{Q}$-tensor matrix.

Case I is within the remit of Theorem 3.1. The numerics demonstrate that the solution retains the front structure for all times as in Figure 3-1. The interface propagates towards the origin according to mean curvature for small times, as illustrated in Figure 3-2, which also shows the improved comparison as $\bar{L}$ decreases. For long times the front equilibrates near the origin. The radius of the isotropic core scales with $\sqrt{\bar{L}}$, as expected, and arises out of the saddle structure of $\mathbf{Q}(\mathbf{r}, t)$ at the origin. This structure is visible in the final time panel of Figure 3-3. Further, this figure demonstrates the convergence of $\mathbf{Q}(\mathbf{r}, t) \to \mathbf{Q}^*$ for the Q_{11} entry of the $\mathbf{Q}$-tensor matrix. Figure 3-4 shows that $\mathbf{Q}(\mathbf{r}, t)$ has exactly two eigenvalues for $r > \rho(t)$, where $\rho(t)$ is the front position (and one eigenvalue for $r < \rho(t)$). Therefore the nematic region of the solution is uniaxial for all times.
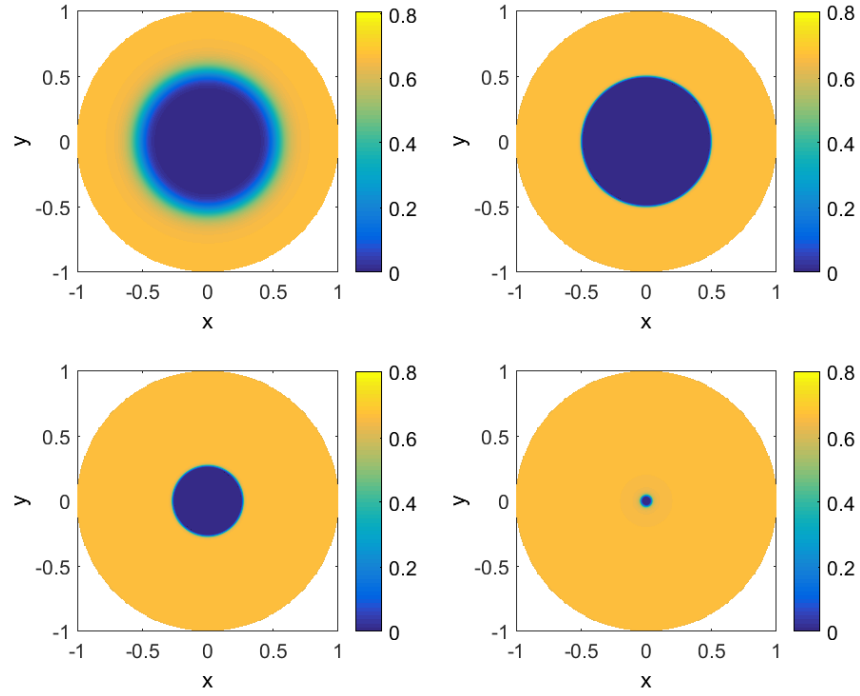
Figure 3-1: $|\mathbf{Q}(\mathbf{r}, t)|^2$ for a cross-section of the sphere for Case I at $t = 0$, $t = 0.001$, $t = 0.05$ and $t = 0.125$ (top left to bottom right). The spatial resolution is $h = \frac{1}{256}$.
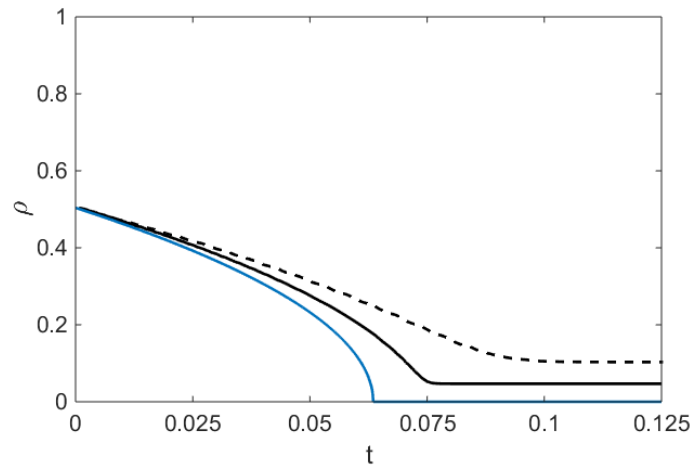

Figure 3-2: Front position ρ for Case I with $r_0 = 0.5$ for $\bar{L} = 3.5 \times 10^{-3}$ (dashed) and $\bar{L} = 6.9 \times 10^{-4}$ (solid) and predicted position according to motion by mean curvature (blue). The radius of the isotropic core of the steady solution scales with $\sqrt{\bar{L}}$ and hence the front is arrested at an $O(\sqrt{\bar{L}})$ distance away from the origin. Here $\sqrt{\bar{L}} = 5.92 \times 10^{-2}$ (dashed) and 2.62×10^{-2} (solid). This contributes to the deviations from the predicted evolution by mean curvature seen in this figure. As $\bar{L}$ decreases, the isotropic core gets smaller and interface evolution approaches that according to mean curvature.

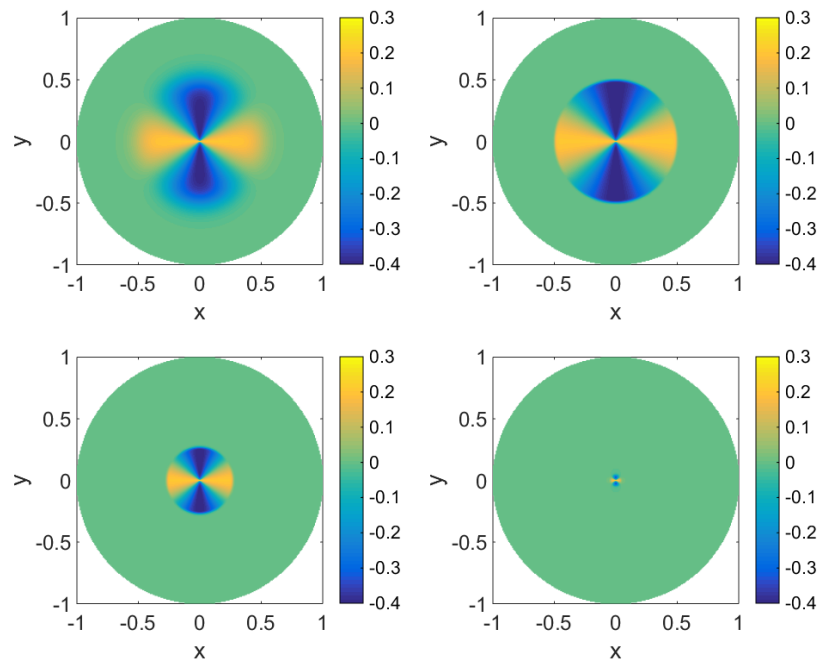Figure 3-3: $\mathbf{Q}(\mathbf{r}, t)_{11} - \mathbf{Q}^*_{11}$ for a cross-section of the sphere for Case I at $t = 0$, $t = 0.001$, $t = 0.05$ and $t = 0.125$.
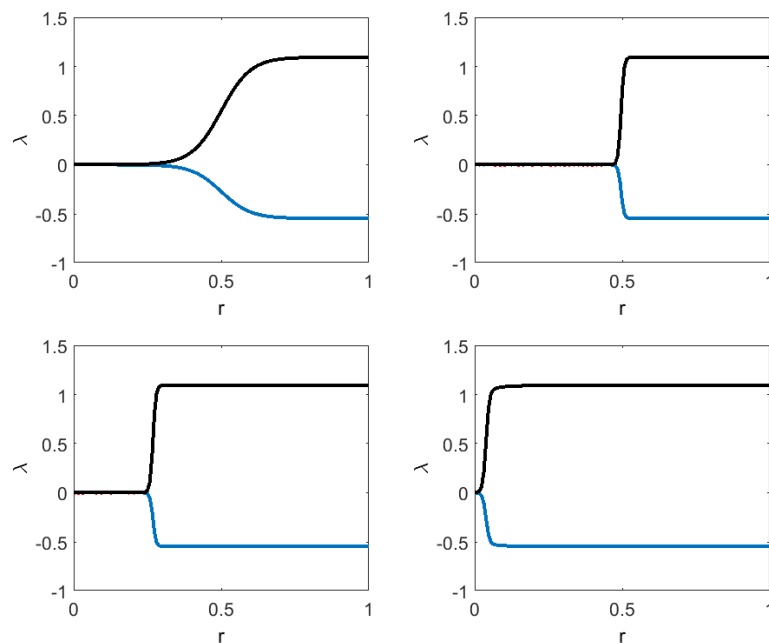

Figure 3-4: Radial profiles of the eigenvalues of $\mathbf{Q}(\mathbf{r}, t)$ for Case I at $t = 0$, $t = 0.001$, $t = 0.05$ and $t = 0.125$.

Case II is not within the remit of Theorem 3.1 as the initial condition (3.28) does not have an initial front. However, illustrated by the eigenvalue plots in Figure 3-5, the dynamic solution quickly develops an inwards-propagating interface separating the isotropic core from the nematic state. The long-time behaviour of the dynamic solutions for Cases I and II are indistinguishable and we have the same comparison to mean curvature motion, see Figure 3-6.
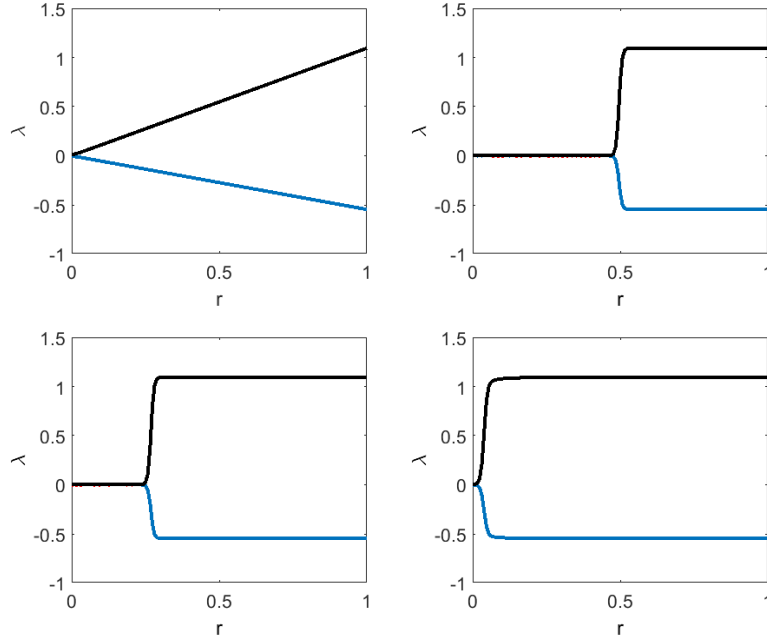

Figure 3-5: Radial profiles of the eigenvalues of $\mathbf{Q}(\mathbf{r}, t)$ for Case II at $t = 0$, $t = 0.001$, $t = 0.05$ and $t = 0.125$. The spatial resolution is $h = \frac{1}{256}$.
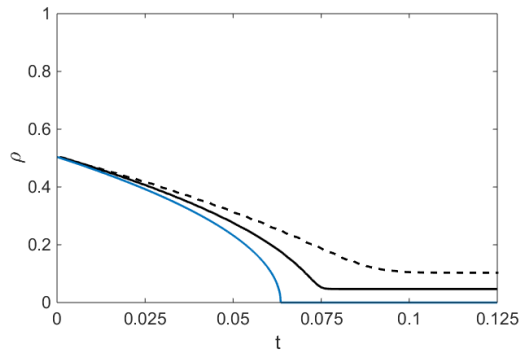
Figure 3-6: Front position ρ for Case II with $r_0 = 0.5$ for $\bar{L} = 3.5 \times 10^{-3}$ (dashed) and $\bar{L} = 6.9 \times 10^4$ (solid) and predicted position according to motion by mean curvature (blue). As for Case I, the front is arrested at an $O(\sqrt{\bar{L}})$ distance away from the origin. For this figure, $\sqrt{\bar{L}} = 5.92 \times 10^{-2}$ (dashed) and 2.62×10^{-2} (solid). This results in deviations from the predicted evolution by mean curvature which improve as $\bar{L}$ gets smaller and the isotropic core of the steady solution decreases.

For **Case III**, the initial condition is biaxial with

$$\mathbf{Q}(\mathbf{r}, 0) = h(r, 0) \left(\hat{\mathbf{r}} \otimes \hat{\mathbf{r}} - \frac{\mathbf{I}}{3} \right) + s(r) \left(\mathbf{m} \otimes \mathbf{m} - \mathbf{p} \otimes \mathbf{p} \right),$$

where **m** and **p** are given by

$$\mathbf{m} = (\cos \theta \cos \phi, \cos \theta \sin \phi, - \sin \theta) \quad \text{and} \quad \mathbf{p} = (\cos \phi, \sin \phi, 0).$$

The function $h(r, 0)$ has a front structure, as given in Case I, and $s(r) = r(1 - r)$. This initial condition and the subsequent dynamics are outside the scope of Theorem 3.1. In particular, we are not guaranteed the radial symmetry of the dynamic solution, as with Cases I and II above. The numerics show that the solution quickly becomes uniaxial as demonstrated by the evolution of the eigenvalues of $\mathbf{Q}(\mathbf{r}, t)$ in Figure 3-7. The dynamic solution exhibits an inwards propagating interface which equilibrates near the origin, also see Figure 3-7. Figure 3-8 shows the convergence of $\mathbf{Q}(\mathbf{r}, t)$ to $\mathbf{Q}^*$. Unlike in Case I, the $\mathbf{Q}$-tensor in the nematic region is not initially equal to $\mathbf{Q}^*$.

Figure 3-7: Radial profiles of the eigenvalues of $\mathbf{Q}(\mathbf{r}, t)$ for Case III at $t = 0$, $t = 10^{-5}$, $t = 1.5 \times 10^{-4}$ and $t = 0.085$. The spatial resolution is $h = \frac{1}{256}$.
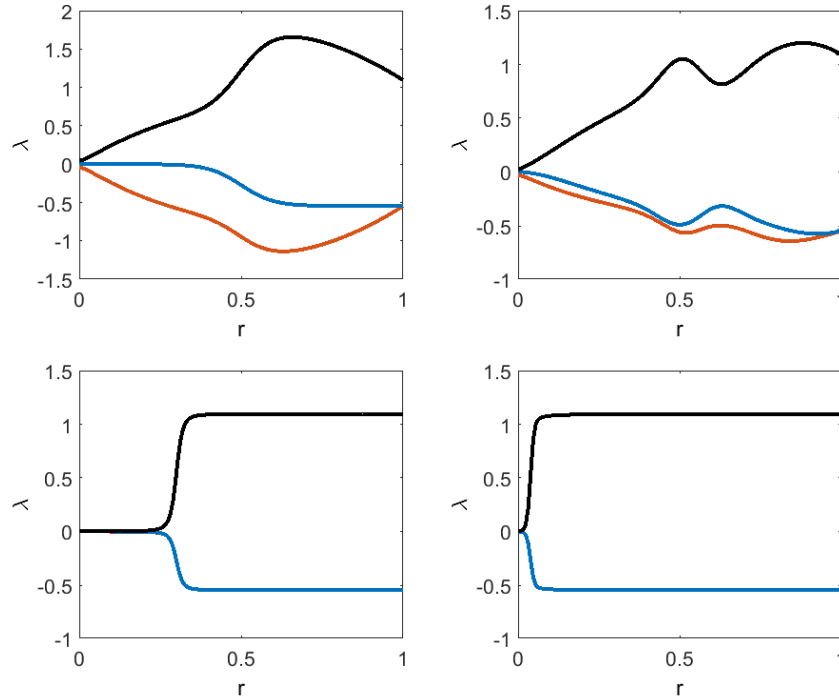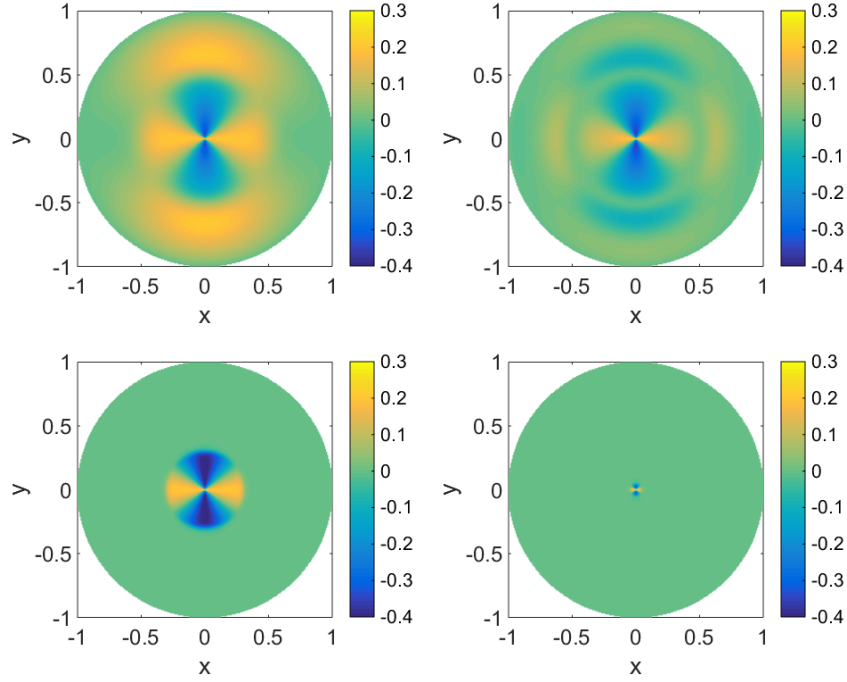
Figure 3-8: $\mathbf{Q}(\mathbf{r}, t)_{11} - \mathbf{Q}_{11}^*$ for a cross-section of the sphere for Case III at $t = 0$, $t = 10^{-5}$, $t = 1.5 \times 10^{-4}$ and $t = 0.085$.

Case IV breaks the radial symmetry of the initial order parameter by employing a uniaxial initial condition of the form (3.27) with

$$h(r, 0) = \frac{1}{2} \left[1 + \tanh \left(\frac{r^2 \sin^2 \theta \cos^2 \phi + 4r^2 \sin^2 \theta \sin^2 \phi + 2r^2 \cos^2 \theta - 0.5}{\sqrt{\bar{L}}} \right) \right].$$

For this initial condition the initial interface is ellipsoidal in shape. The dynamic front becomes radially symmetric as it collapses which suggests front evolution by mean curvature. The subsequent dynamics are indistinguishable from Case I as seen in Figure 3-9.

Based on these four representative cases, we would expect that all dynamic solutions, irrespective of initial condition, to numerically converge to a Radial Hedgehog-type solution, $|\mathbf{Q}(\mathbf{r}, t)| \left(\hat{\mathbf{r}} \otimes \hat{\mathbf{r}} - \frac{1}{3} \right)$, where $|\mathbf{Q}(\mathbf{r}, t)|$ has an isotropic core near $r = 0$ and $|\mathbf{Q}(\mathbf{r}, t)|^2 \to \frac{2}{3} h_+^2$ rapidly away from $r = 0$. This is consistent with the analysis of Landau-de Gennes energy minimizers in the $\bar{L} \to 0$ limit.
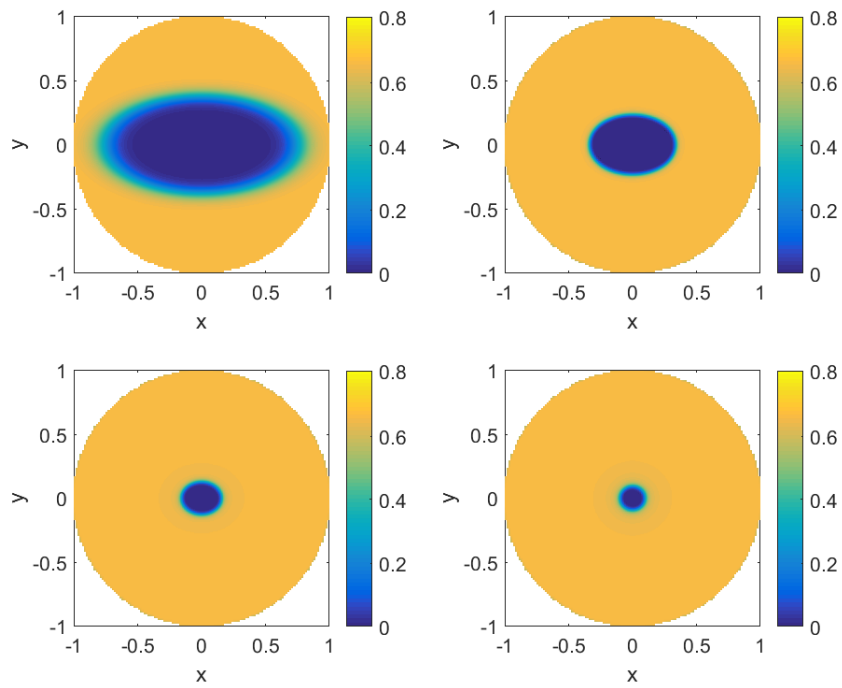
Figure 3-9: $|\mathbf{Q}(\mathbf{r}, t)|^2$ for a cross-section of the sphere for Case IV with $\bar{L} = 3.5 \times 10^{-3}$ at $t = 0$, $t = 0.025$, $t = 0.05$ and $t = 0.1$. The spatial resolution is $h = \frac{1}{128}$.

Front propagation in heterogeneous materials

Chapter 4 continues the study of the Landau-de Gennes gradient flow system on the three-dimensional nematic droplet. In this chapter we consider isotropic-nematic front propagation at the isotropic-nematic transition temperature in the presence of radially symmetric, periodic obstacles. First we prove the existence of pulsating wave solutions and calculate an average front velocity for a range of obstacle strengths by adapting the methods in Dirr and Yip 2006 [35].

At the end of Chapter 4 we carry out several numerical experiments, simulating the full Landau-de Gennes gradient flow system in the presence of obstacles. Firstly, we work on a three-dimensional annulus with periodic radial obstacles as studied previously. Secondly, we work on a square domain with two types of obstacle; periodic obstacles and a stronger moon-shaped obstacle motivated by the work in Xia et al 2015 [113]. We study how the moon's orientation affects front motion.

4.1   Problem formulation

We adapt the non-dimensionalized and normalized gradient flow model associated with the Landau-de Gennes energy at the isotropic-nematic transition temperature in (3.21)-(3.25) (setting $R = 1$ in the non-dimensionalization) and consider the dynamic equations

$$\mathbf{Q}_t = \nabla^2 \mathbf{Q} - \frac{9}{L}\left[\frac{1}{3}\mathbf{Q} - 3\left(\mathbf{Q}\mathbf{Q} - \frac{\mathbf{I}}{3}|\mathbf{Q}|^2\right) + |\mathbf{Q}|^2\mathbf{Q}\right] + \frac{2}{3}\frac{\delta}{L}\left(\hat{\mathbf{r}} \times \hat{\mathbf{r}} - \frac{\mathbf{I}}{3}\right)(g(r) + F), \quad (4.1)$$

where $\hat{\mathbf{r}} = (\cos\phi\sin\theta, \sin\phi\sin\theta, \cos\theta)$ denotes the three-dimensional unit radial vector and $\bar{L} = \frac{81C}{B^2}L$ as in Chapter 3. This set-up is inspired by [35], where the Allen-Cahn equation in one-dimension is considered:

$$v_t = v_{xx} - W'(v) + \delta(g(x) + F) \quad \text{for } x \in \mathbb{R}, \tag{4.2}$$

and $W(v) = (1 - v^2)^2$. In both cases, the forcing terms are given by a periodic forcing function g with small period p and mean zero which represents a heterogeneous material and a constant F which corresponds to an external force. The parameter δ is small but lower bounds on δ in terms of L will be specified later. We look for dynamic Radial Hedgehog-type solutions of (4.1) of the form

$$\mathbf{Q} = h(r, t)\left(\hat{\mathbf{r}} \otimes \hat{\mathbf{r}} - \frac{\mathbf{I}}{3}\right).$$

We substitute this ansatz into the dynamic equations (4.1) to show that $h(r, t)$ evolves according to

$$h_t = h_{rr} + \frac{2}{r}h_r - \frac{6}{r^2}h - \frac{W'(h)}{\bar{L}} + \frac{\delta(g(r) + F)}{\bar{L}}. \tag{4.3}$$

The function $W(h) = \frac{3}{2}h^2(h-1)^2$ is a double welled potential, $g(\cdot)$ is a periodic function with small period p and mean zero, as described above, F is a constant and $\bar{L} = \frac{81C}{B^2}$ as in Chapter 3. We are interested in pulsating wave solutions of equation (4.3). These are solutions which are space-time periodic. For certain ranges of δ and $\bar{L}$ we show that there exists a constant $\hat{F}$ such that for $F < \hat{F} < 0$ there are pulsating wave solutions of (4.3). These pulsating waves propagate with an average velocity proportional to $\sqrt{\hat{F} - F}$ provided that $\hat{F} - F$ is small. Throughout this chapter, we use the norms defined by

$$||f||_{0,b} = \sup\{|f(z)\exp(b\sqrt{\bar{L}}|z|)|\} \quad \text{and} \quad ||f||_{1,b} = ||f||_{0,b} + ||f'||_{0,b},$$

where $0 < b < \min\left(\frac{W''(1)}{\bar{L}}, \frac{W''(0)}{\bar{L}}\right)$.

4.2 Existence of pulsating waves solutions

We look for solutions of (4.3) with moving fronts which connect the zeroes of $-\frac{6}{r^2}h - W'(h) + \delta(g(r) + F)$. The zeros are perturbed from 0 and 1 by terms of $O(\delta + \bar{L})$ due to the presence of the forcing terms and the term $\frac{6}{r^2}h$ in the evolution equation (4.3). Expanding on the approach in

[35], we account for these perturbations by defining functions $m^{\pm}(r)$ and $w^{+}(r)$ such that

$$h \approx \delta m^{-}(r) \quad \text{and} \quad h \approx 1 + \delta m^{+}(r) + \bar{L}w^{+}(r),$$

close to $r = 0$ and $r = 1$ respectively. Hence at either end point we have

$$\delta\left(m_{rr}^{-}(r) + \frac{2}{r}m_r^{-}(r) - \frac{6}{r^2}m^{-}(r)\right) - \frac{W'(\delta m^{-}(r))}{\bar{L}} + \frac{\delta(g(r) + F)}{\bar{L}} = 0, \tag{4.4}$$

$$\delta\left(m_{rr}^{+}(r) + \frac{2}{r}m_r^{+}(r) - \frac{6}{r^2}m^{+}(r)\right) - \frac{6}{r^2} + \bar{L}\left(w_r^{+}(r, t) + \frac{2}{r}w_r^{+}(r, t) - \frac{6}{r^2}w^{+}(r, t)\right) \tag{4.5}$$

$$- \frac{W'(1 + \delta m^{+}(r) + \bar{L}w^{+}(r, t))}{\bar{L}} + \frac{\delta(g(r) + F)}{\bar{L}} = 0,$$

with $m^{-}(0) = 0$. We transfer (4.3) to a co-moving frame by making the change of variables

$$z = r - k(t) = r - \rho(t) - c(t), \tag{4.6}$$

where $k(t) = \rho(t) + c(t)$ is the position of the front. The function $\rho(t)$ satisfies

$$\frac{d\rho}{dt} = -\frac{2}{k(t)} = -\frac{2}{\rho(t) + c(t)},$$

and accounts for front motion due to mean curvature motivated by the work in Chapter 3. The function $c(t)$ accounts for front motion due to the forcing terms. We choose the parameters δ and $\bar{L}$ so that $\dot{c}(t)$ is much larger than $\dot{\rho}(t)$ and is the main contribution to interface motion. Our main task in this chapter is to prove the following theorem.

Theorem 4.1. *Suppose $\sqrt{\bar{L}} \ll \delta$, then for any $\sigma > 0$ there exists C_1, C_2, $\bar{L}^* > 0$ such that for $0 < \bar{L} < \bar{L}^*$, suitable initial conditions and a forcing term F which satisfies*

$$0 < C_1\frac{\sqrt{\bar{L}}}{\delta} \leq \hat{F} - F \leq C_2,$$

there exists a constant T_F and a solution H_F of (4.3) such that

$$H_F(r, t) = H_F(r + p, t + T_F).$$

Further, the average front velocity $V_F = p/T_F$ satisfies

$$(1-\sigma)p\frac{\hat{\alpha}\delta\sqrt{\hat{\beta}(\hat{F}-F)}}{\sqrt{\bar{L}}\pi} \leq V_F \leq (1+\sigma)p\frac{\hat{\alpha}\delta\sqrt{\hat{\beta}(\hat{F}-F)}}{\sqrt{\bar{L}}\pi}.$$

This theorem is analogous to [35, Theorem 3] where (4.2) is shown to have inward propagating pulsating wave solutions with fronts which advance with average velocity $V_F \approx \frac{\hat{\alpha}\delta}{\pi}(\hat{\beta}(F-\hat{F}))^{\frac{1}{2}}$ for $0 < C_1\delta \leq F - \hat{F} \leq C_2$ when g has period 1. In Theorem 4.1 we have used the following quantities:

$$s(a) = -\int_{-\infty}^{\infty} g(z+a)m_z(z)\,\mathrm{d}z, \tag{4.7}$$

$$\hat{F} = s^*, \quad \hat{\alpha} = \frac{1}{\sqrt{\bar{L}}\int_{-\infty}^{\infty}m_z^2\,\mathrm{d}z} \quad \text{and} \quad \hat{\beta} = \frac{s''(0)}{2}, \tag{4.8}$$

where s^* is the minimum of s, which without loss of generality, is attained at $a = 0, \pm p, \pm 2p....$

The function $m(z)$ is a solution of

$$0 = m_{zz} - \frac{W'(m)}{\bar{L}}, \tag{4.9}$$

with $m(z) \to 0$ as $z \to -\infty$ and $m(z) \to 1$ as $z \to \infty$. A solution of (4.9) is given by

$$m(z) = \frac{1}{\exp\left(-\sqrt{\frac{3}{\bar{L}}}z\right)+1}. \tag{4.10}$$

There exists a positive constant C such that this solution satisfies

$$|m(z) - 1| \leq C\exp\left(-a\sqrt{\bar{L}}z\right) \quad \text{for} \quad z \geq 0, \tag{4.11}$$

$$|m(z)| \leq C\exp\left(a\sqrt{\bar{L}}z\right) \quad \text{for} \quad z \leq 0, \tag{4.12}$$

$$|m_z(z)| \leq \frac{C}{\sqrt{\bar{L}}}\exp\left(-a\sqrt{\bar{L}}|z|\right), \tag{4.13}$$

for any a such that $0 < a < \frac{\sqrt{3}}{\bar{L}}$. The bound $\sqrt{\bar{L}} \ll \delta$ in the theorem statement ensures that the forcing terms have the dominant contribution to front motion.

Inspired by [35], we assume the following ansatz for $h(r, t)$:

$$h(r, t) = m(z) + \tilde{m}(z) + E(z, t) + \phi(z, t), \tag{4.14}$$

where $m(z)$ is as described previously and $z = r - k(t)$ as introduced in (4.6). The functions $\tilde{m}(z)$ and $E(z, t)$ are given by

$$E(z, t) = \alpha(z)\delta m^-(r) + \beta(z)(\delta m^+(r) + \bar{L}w^+(r)),$$
$$\tilde{m}(z) = \gamma_1(z)(1 - m(z)) + \gamma_2(z)(-m(z)).$$

The functions $\alpha(z)$, $\beta(z)$, $\gamma_1(z)$ and $\gamma_2(z)$ are smooth positive functions such that for some suitable positive constants K_1 large and $K_2 < 1$ we have,

$$\alpha(z) = \begin{cases} 1 & \text{for} \quad z \leq -\sqrt{\bar{L}}K_1 p, \\ 0 & \text{for} \quad z \geq -\sqrt{\bar{L}}(K_1 - 1)p, \end{cases} \qquad \gamma_1(z) = \begin{cases} 1 & \text{for} \quad z \geq K_2 p, \\ 0 & \text{for} \quad z \leq \frac{K_2}{2}p, \end{cases}$$

$$\beta(z) = \begin{cases} 0 & \text{for} \quad z \leq \sqrt{\bar{L}}(K_1 - 1)p, \\ 1 & \text{for} \quad z \geq \sqrt{\bar{L}}K_1 p. \end{cases} \qquad \gamma_2(z) = \begin{cases} 1 & \text{for} \quad z \leq -K_2 p, \\ 0 & \text{for} \quad z \geq -\frac{K_2}{2}p. \end{cases}$$

The ansatz in (4.14) compares $h(r, t)$ to $m(z)$. The difference between $h(r, t)$ and $m(z)$ is accounted for by $E(z, t)$ at the end points and by $\phi(z, t)$ near $z = 0$ (the front position). We have assumed $h \approx \delta m^-(r)$ near $r = 0$ and $h \approx 1 + \delta m^+(r) + \bar{L}w^+(r)$ near $r = 1$ and hence $\phi(z, t) = 0$ and $\phi_z(z, t) = 0$ at the end points. The functions $\gamma_1(z)$ and $\gamma_2(z)$ are chosen so that $m(z) + \tilde{m}(z) = 0$ and $m(z) + \tilde{m}(z) = 1$ near $r = 0$ and $r = 1$ respectively. The ansatz for $h(r, t)$ given in (4.14) now connects the values $\{0, 1 + \delta m^+(1) + \bar{L}w(1)\}$, as needed (as equation (4.4) requires $m^-(0) = 0$).

Substituting the ansatz (4.14) into the evolution equation (4.3) with change of variables (4.6) yields

$$\phi_t = \phi_{zz} + \dot{c}((m + \tilde{m})_z + E_z + \phi_z) - E_t + (m + \tilde{m})_{zz} + E_{zz}$$
$$+ \left(\frac{2}{z + \rho + c} - \frac{2}{\rho + c} \right)((m + \tilde{m})_z + E_z + \phi_z) - \frac{6}{(z + \rho + c)^2}(m + \tilde{m} + E + \phi)$$
$$- \frac{W'(m + \tilde{m} + E + \phi)}{\bar{L}} + \frac{\delta(g(z + \rho + c) + F)}{\bar{L}}. \tag{4.15}$$

This chapter proceeds following the steps in [35]. Firstly, we find an expression for $\dot{c}(t)$ (the front motion induced by the forcing terms as introduced in (4.6)) and show that this expression is always well-defined. This requires proving bounds on $||\phi(\cdot, t)||_{1,b}$ and $||\phi(\cdot, t)||_{0,b}$ given suitable initial conditions. In [35], the authors bound $||\phi(\cdot, t)||_{0,b} \leq ||\phi(\cdot, t)||_{1,b}$ and find bounds on $||\phi(\cdot, t)||_{1,b}$ only. However, due to the small parameter $\bar{L}$ in our problem, this bound on $||\phi(\cdot, t)||_{0,b}$ is too weak for our purposes. Instead we need to prove two bounds; $||\phi(\cdot, t)||_{0,b} \leq A(\delta + \bar{L})$ and $||\phi(\cdot, t)||_{1,b} \leq \frac{A}{\sqrt{\bar{L}}}(\bar{L} + \delta)$ for some positive constant A. The first step is then to prove that if

$$\sup_{t \in [0,T]} ||\phi(\cdot, t)||_{1,b} \leq B_1(\sqrt{\bar{L}} + \delta/\sqrt{\bar{L}}) \quad \text{and} \quad \sup_{t \in [0,T]} ||\phi(\cdot, t)||_{0,b} \leq B_2(\bar{L} + \delta), \qquad (4.16)$$

for some $T > 0$ and constants B_1 and B_2 then

$$\sup_{t \in [0,T]} ||\phi(\cdot, t)||_{1,b} \leq \bar{B}_1(\sqrt{\bar{L}} + \delta/\sqrt{\bar{L}}) \quad \text{and} \quad \sup_{t \in [0,T]} ||\phi(\cdot, t)||_{0,b} \leq \bar{B}_2(\bar{L} + \delta),$$

for all time (for some constants $\bar{B}_1$ and $\bar{B}_2$). This allows us to show that for suitable initial conditions we can bound $||\phi(\cdot, t)||_{1,b}$ and $||\phi(\cdot, t)||_{1,b}$ as required for all time. In fact, if (4.16) holds, then we can expand:

$$W'(m + \tilde{m} + E + \phi) \approx W'(m + \tilde{m} + E) + \phi W''(m + \tilde{m} + E) + O(\phi^2),$$
$$\phi W''(m + \tilde{m} + E) \approx \phi W''(m) + O((E + \tilde{m})\phi).$$

Using the bounds on $m(z)$ in (4.11)-(4.12) and the range where $\gamma_1(z)$ and $\gamma_2(z)$ are non-zero together with $E = O(\delta + \bar{L})$, we find

$$W'(m + \tilde{m} + E + \phi) \approx W'(m + \tilde{m} + E) + \phi W''(m) + O((\delta + \bar{L})\phi) + O(\phi^2).$$

Then (4.15) reduces to
$$\phi_t = \phi_{zz} - \frac{W''(m)}{\bar{L}}\phi + H(z, \phi, t), \qquad (4.17)$$

where

$$H(z, \phi, t) = T_1 + T_2 + T_3 + O_1\left(\frac{(\delta + \bar{L})\phi}{\bar{L}}\right) + O_2\left(\frac{\phi^2}{\bar{L}}\right),$$

and

$$T_1 = \dot{c}((m + \tilde{m})_z + E_z + \phi_z) - E_t - \frac{2}{\rho + c}E_z,$$

$$T_2 = (m + \tilde{m})_{zz} + \left(\frac{2}{z + \rho + c} - \frac{2}{\rho + c}\right)(m + \tilde{m})_z - \frac{6}{(z + \rho + c)^2}(m + \tilde{m})$$

$$- \frac{W'(m + \tilde{m} + E)}{\bar{L}} + E_{zz} + \frac{2}{z + \rho + c}E_z - \frac{6}{(z + \rho + c)^2}E + \frac{\delta(g(z + \rho + c) + F)}{\bar{L}},$$

$$T_3 = \left(\frac{2}{z + \rho + c} - \frac{2}{\rho + c}\right)\phi_z - \frac{6}{(z + \rho + c)^2}\phi.$$

Next we simplify the expression for $\dot{c}(t)$ and find a differential equation for the front position, yielding an expression for the average front velocity in certain parameter regimes. Our computations are in three-dimensions, as opposed to the one-dimensional work in [35]. As a result, we have an extra contribution to front motion driven by the curvature of the front. We take this contribution into account when defining the co-moving frame in (4.6) and work in a regime where obstacle driven motion is dominant over motion by mean curvature.

Lastly, we use stronger bounds on $||\phi(\cdot, t)||_{1,b}$ to prove the existence of pulsating wave solutions for forcing strengths above some critical value. An extension to an unequal welled potential is discussed in Subsection 4.2.4. Our analytical results are corroborated by numerical simulations on a three-dimensional annulus in Section 4.3, where we numerically estimate the value of the critical forcing and consider initial conditions outside the remit of the analysis.

4.2.1 Bounds on $H(z, \phi, t)$

The next step is to find a bound on $||H(\cdot, t)||_{0,b}$. To this end we have split $H(z, \phi, t)$ into three terms. The first term T_1 can be written as

$$T_1 = \dot{c}((m + \tilde{m})_z + \phi_z) - E_t + (\dot{c}(t) + \dot{\rho}(t))E_z.$$

Note that, as $r = z + c(t) + \rho(t)$,

$$(\dot{c}(t) + \dot{\rho}(t))E_z - E_t = (\dot{c}(t) + \dot{\rho}(t))(\alpha'(z)\delta m^-(r) + \beta'(z)(\delta m^+(r) + \bar{L}w^+(r, t))).$$

Hence we find

$$T_1 = \dot{c}(t)((m + \tilde{m})_z + \phi_z) + (\dot{c}(t) + \dot{\rho}(t))(\alpha'(z)\delta m^-(r) + \beta'(z)(\delta m^+(r) + \bar{L}w^+(r, t))),$$

and finally

$$||T_1||_{0,b} \leq A \left[|\dot{c}(t)| \left(\frac{1}{\sqrt{\bar{L}}} + ||\phi(\cdot, t)||_{1,b} \right) + \frac{\delta + \bar{L}}{\sqrt{\bar{L}}} \right]. \tag{4.18}$$

To find this bound we have used that $\frac{d\rho}{dt} = -\frac{2}{k(t)} = -\frac{2}{\rho(t)+c(t)}$ is bounded above by a constant. Initially we consider interface movement across one period of spatial variation, well away from the origin. The analysis will show that the forcing terms induce outwards front motion and hence $\dot{\rho}(t)$ is bounded for all time.

Next, we deal with the second groups of terms which can be written as:

$$T_2 = (m + \tilde{m})_{zz} + \left(\frac{2}{z + \rho + c} - \frac{2}{\rho + c} \right)(m + \tilde{m})_z - \frac{6}{(z + \rho + c)^2}(m + \tilde{m}) + \frac{6\beta(z)}{(z + \rho + c)^2}$$
$$+ \frac{W'(\beta(z) + E)}{\bar{L}} - \frac{W'(m + \tilde{m} + E)}{\bar{L}}$$
$$+ E_{zz} + \frac{2}{z + \rho + c}E_z - \frac{6}{(z + \rho + c)^2}E - \frac{6\beta(z)}{(z + \rho + c)^2} - \frac{W'(\beta(z) + E)}{\bar{L}} + \frac{\delta(g(z + \rho + c) + F)}{\bar{L}}.$$

We note that for $|z| > \sqrt{\bar{L}}K_1 p$, equations (4.4)-(4.5) hold and hence the terms on the last line of T_2 vanish after this point. Further on recalling the definition of $\tilde{m}$, m and the bounds on m in (4.11)-(4.13), we find

$$||T_2||_{0,b} \leq A \left(1 + \frac{\delta}{\bar{L}} \right). \tag{4.19}$$

The last set of terms is given by

$$T_3 = \left(\frac{2}{z + \rho + c} - \frac{2}{\rho + c} \right)\phi_z - \frac{6}{(z + \rho + c)^2}\phi.$$

Therefore, we can see that $||T_3||_{0,b} \leq A||\phi(\cdot, t)||_{1,b}$ and combining the above, we have

$$||H(\cdot, t)||_{0,b} \leq A \left[1 + \frac{\delta}{\bar{L}} + |\dot{c}| \left(\frac{1}{\sqrt{\bar{L}}} + ||\phi(\cdot, t)||_{1,b} \right) \right.$$
$$\left. + ||\phi(\cdot, t)||_{1,b} + \frac{\delta + \bar{L}}{\bar{L}}||\phi(\cdot, t)||_{0,b} + \frac{1}{\bar{L}}||\phi(\cdot, t)||_{0,b}^2 \right]. \tag{4.20}$$

As in [35], we choose $c(t)$ such that

$$\int_{-k(t)}^{1-k(t)} \phi(z, t) m_z(z)\, dz = 0,$$

for all $t \geq 0$. Note that this is the integral across the full range of z as $0 \leq r \leq 1$. We can make this choice of $c(t)$ provided $\int_{-k(0)}^{1-k(0)} \phi(z, 0) m_z(z) dz = 0$ and

$$\int_{-k(t)}^{1-k(t)} \phi_t(z, t) m_z(z)\, dz = 0. \tag{4.21}$$

Here we have made use of the assumption that $\phi(z, t) = 0$ and $\phi_z(z, t) = 0$ at the end points. That is, we assume $E(z, t)$ completely accounts for the difference between $h(r, t)$ and $m(z)$ near $r = 0$ and $r = 1$. For the rest of the chapter we use the following notation for the L^2 inner product:

$$\langle f(z, t), g(z, t) \rangle = \int_{-k(t)}^{1-k(t)} f(z, t) g(z, t)\, dz,$$

$$\|f\|^2 = \langle f, f \rangle.$$

We note that integration by parts yields

$$\left\langle \phi_{zz} - \frac{W''(m)}{\bar{L}} \phi, m_z \right\rangle = -\int_{-k(t)}^{1-k(t)} \phi_z \left(m_{zz} - \frac{W'(m)}{\bar{L}} \right) dz,$$

$$= 0.$$

Therefore (4.21), together with evolution equation (4.17), implies $0 = \langle H(t, z, \phi), m_z \rangle$ and hence

$$0 = \dot{c}(t) \langle (m + \tilde{m})_z + \phi_z + \alpha'(z)\delta m^-(r) + \beta'(z)(\delta m^+(r) + \bar{L}w^+(r)), m_z \rangle$$

$$+ \left\langle T_2 + T_3 + O\left(\frac{(\delta + \bar{L} + \phi)\phi}{\bar{L}} + \frac{\delta + \bar{L}}{\sqrt{\bar{L}}} \right), m_z \right\rangle.$$

Therefore $\dot{c}(t)$ is given by

$$\dot{c}(t) = -\frac{\left\langle (m+\tilde{m})_{zz} + \left(\frac{2}{z+\rho+c} - \frac{2}{\rho+c}\right)(m+\tilde{m})_z - \frac{6}{(z+\rho+c)^2}(m+\tilde{m}) - \frac{W'(m+\tilde{m}+E)}{\bar{L}}, m_z \right\rangle}{\left\langle m_z + \tilde{m}_z + \phi_z + \alpha'(z)\delta m^-(r) + \beta'(z)(\delta m^+(r) + \bar{L}w^+(r)), m_z \right\rangle}$$
$$-\frac{\left\langle E_{zz} + \frac{2}{z+\rho+c}E_z - \frac{6}{(z+\rho+c)^2}E + \frac{\delta(g(z+\rho+c)+F)}{\bar{L}}, m_z \right\rangle}{\left\langle m_z + \tilde{m}_z + \phi_z + \alpha'(z)\delta m^-(r) + \beta'(z)(\delta m^+(r) + \bar{L}w^+(r)), m_z \right\rangle}$$
$$-\frac{\left\langle \left(\frac{2}{z+\rho+c} - \frac{2}{\rho+c}\right)\phi_z - \frac{6}{(z+\rho+c)^2}\phi + O\left(\frac{(\delta+\bar{L}+\phi)\phi}{\bar{L}} + \frac{\delta+\bar{L}}{\sqrt{\bar{L}}}\right), m_z \right\rangle}{\left\langle m_z + \tilde{m}_z + \phi_z + \alpha'(z)\delta m^-(r) + \beta'(z)(\delta m^+(r) + \bar{L}w^+(r)), m_z \right\rangle}.$$

This can be simplified by using the equation for $m(z)$ in (4.9). Further we can note

$$\left\langle E_{zz} - \frac{EW''(m)}{\bar{L}}, m_z \right\rangle = E_z m_z - \left.\frac{EW'(m)}{\bar{L}}\right|_{-k(t)}^{1-k(t)} - \left\langle m_{zz} - \frac{W'(m)}{\bar{L}}, E_z \right\rangle < O\left(\frac{\delta+\bar{L}}{\sqrt{\bar{L}}}\right)$$

$$\text{and} \quad \left\langle \frac{E_z}{z+\rho+c}, m_z \right\rangle = \left.\frac{Em_z}{(z+\rho+c)}\right|_{-k(t)}^{1-k(t)} - \left\langle E, \frac{d}{dz}\frac{m_z}{z+\rho+c} \right\rangle < O\left(\frac{\delta+\bar{L}}{\sqrt{\bar{L}}}\right).$$

The upper bounds on the above expressions are weak but suffice as we already have an $O\left(\frac{\delta+\bar{L}}{\sqrt{\bar{L}}}\right)$ term in the expression for $\dot{c}(t)$. The $\tilde{m}(z)$ and $E(z,t)$ terms in $\dot{c}(t)$ are also much smaller than $O\left(\frac{\delta+\bar{L}}{\sqrt{\bar{L}}}\right)$ and hence can be neglected. Therefore $\dot{c}(t)$ simplifies to

$$\dot{c}(t) = -\frac{\left\langle \left(\frac{2}{z+\rho+c} - \frac{2}{\rho+c}\right)m_z - \frac{6}{(z+\rho+c)^2}m, m_z \right\rangle}{\left\langle m_z + \tilde{m}_z + \phi_z + \alpha'(z)\delta m^-(r) + \beta'(z)(\delta m^+(r) + \bar{L}w^+(r,t)), m_z \right\rangle}$$
$$-\frac{\left\langle \frac{\delta(g(z+\rho+c)+F)}{\bar{L}}, m_z \right\rangle}{\left\langle m_z + \tilde{m}_z + \phi_z + \alpha'(z)\delta m^-(r) + \beta'(z)(\delta m^+(r) + \bar{L}w^+(r,t)), m_z \right\rangle}$$
$$-\frac{\left\langle \left(\frac{2}{z+\rho+c} - \frac{2}{\rho+c}\right)\phi_z - \frac{6}{(z+\rho+c)^2}\phi + O\left(\frac{(\delta+\bar{L}+\phi)\phi}{\bar{L}} + \frac{\delta+\bar{L}}{\sqrt{\bar{L}}}\right), m_z \right\rangle}{\left\langle m_z + \tilde{m}_z + \phi_z + \alpha'(z)\delta m^-(r) + \beta'(z)(\delta m^+(r) + \bar{L}w^+(r,t)), m_z \right\rangle}.$$

We note that this expression for $\dot{c}(t)$ is well-defined provided the denominator never vanishes. In particular, we can see that the bounds we assumed in (4.16) hold, that is

$$\sup_{t\in[0,T]} ||\phi(\cdot,t)||_{1,b} \leq B_1(\sqrt{\bar{L}} + \delta/\sqrt{\bar{L}}) \quad \text{and} \quad \sup_{t\in[0,T]} ||\phi(\cdot,t)||_{0,b} \leq B_2(\bar{L}+\delta), \qquad (4.22)$$

for some $T > 0$, the bounds on $m(z)$ in (4.11)-(4.13) and the definition of $E(z, t)$ give

$$|\dot{c}(t)| \leq B_3 \left(\sqrt{\bar{L}} + \frac{\delta}{\sqrt{\bar{L}}} \right), \tag{4.23}$$

for all $t \in [0, T]$. We have used that $||m_z||^2 = O\left(\frac{1}{\sqrt{\bar{L}}}\right)$ to find (4.23). Further, in this case, the bound on $||H(\cdot, t)||_{0,b}$ in (4.20) can be written as

$$\begin{aligned}
||H(\cdot, t)||_{0,b} \leq A \Bigg[1 + \frac{\delta}{\bar{L}} &+ B \left(\sqrt{\bar{L}} + \frac{\delta}{\sqrt{\bar{L}}} \right) ||\phi(\cdot, t)||_{1,b} \\
&+ ||\phi(\cdot, t)||_{1,b} + \frac{\delta + \bar{L}}{\bar{L}} ||\phi(\cdot, t)||_{0,b} + \frac{1}{\bar{L}} ||\phi(\cdot, t)||_{0,b}^2 \Bigg],
\end{aligned} \tag{4.24}$$

for some positive constants A and B and for all $t \in [0, T]$. The key step in proving Theorem 4.1 is showing that the bounds on $\sup ||\phi(\cdot, t)||_{1,b}$ and $\sup ||\phi(\cdot, t)||_{0,b}$ in (4.22) hold for all time.

4.2.2 Bounds on $\phi(z, t)$

In this subsection we prove the necessary bounds on $||\phi(t)||_{1,b}$ and $||\phi(t)||_{0,b}$ using the following results.

Proposition 4.1. *Let $v(x, t)$ be the solution of*

$$v_t = v_{xx} - \frac{W''(m(x))}{\bar{L}} v, \quad v(x, 0) = v_0,$$

where $v_0 \in \{f : ||f||_{1,b} < \infty\}$ and $\int_{-k_0}^{1-k_0} v_0(x) m'(x) \, dx = 0$. Then there exists $N \geq 1$ and $\omega > 0$ such that

$$||v(t)||_{0,b} \leq N \exp\left(-\frac{\omega}{\bar{L}} t \right) ||v_0||_{0,b}, \tag{4.25}$$

$$||v(t)||_{1,b} \leq N \frac{\exp\left(-\frac{\omega}{\bar{L}} t\right)}{\sqrt{t}} ||v_0||_{0,b}, \tag{4.26}$$

$$||v(t)||_{1,b} \leq N \exp\left(-\frac{\omega}{\bar{L}} t \right) ||v_0||_{1,b}, \tag{4.27}$$

for all $t \geq 0$.

Proof. The proof follows the same method as in [97, 35]. The strategy involves defining the linear operator $\bar{\mathcal{L}}\psi := \psi_{zz} - \frac{W''(m(z))}{\bar{L}} \psi$. The proof proceeds by considering the equation $\left(\bar{\mathcal{L}} - \frac{\lambda}{\bar{L}} \right) \phi = 0$ for some complex number λ and proving bounds on $|| \left(\bar{\mathcal{L}} - \frac{\lambda}{\bar{L}} \right)^{-1} g ||_{0,b}$ and $|| \left(\bar{\mathcal{L}} - \frac{\lambda}{\bar{L}} \right)^{-1} g ||_{1,b}$.

These bounds are used to find bounds on $||v(t)||_{0,b}$ and $||v(t)||_{1,b}$ by writing $v(t)$ as a contour integral. □

Proposition 4.2. *Let $f(t)$ be a continuous positive function such that for some constants $P \geq 1$, Q, R, ω:*

$$f(t) \leq P \exp(-\omega t) f(0) + \int_0^t \exp(-\omega(t-s))(Q + Rf(s)) \, ds. \tag{4.28}$$

If $R \leq \omega/2$, then $f(t) \leq Pf(0) + 2Q/\omega$ for all $t \geq 0$.

Proof. The proof is standard and can be found in [35]. □

To apply Proposition 4.2, we need to prove inequalities of the form (4.28) for $||\phi(t)||_{1,b}$ and $||\phi(t)||_{0,b}$.

Proposition 4.3. *If $\sup_{t \in [0,T]} ||\phi(t)||_{1,b} \leq B_1(\sqrt{\bar{L}} + \delta/\sqrt{\bar{L}})$ and $\sup_{t \in [0,T]} ||\phi(t)||_{0,b} \leq B_2(\bar{L} + \delta)$ then there exists $N > 1$ and $\omega > 0$ such that*

$$
\begin{aligned}
||\phi(t)||_{1,b} \leq & N \exp\left(-\frac{\omega}{\bar{L}} t\right) ||\phi(0)||_{1,b} \\
& + \int_0^t \frac{N}{\sqrt{\bar{L}}} \exp\left(-\frac{\omega}{\bar{L}}(t-s)\right) A\left[1 + \frac{\delta}{\bar{L}} + B\left(\sqrt{\bar{L}} + \frac{\delta}{\sqrt{\bar{L}}}\right) ||\phi(s)||_{1,b} \right. \\
& \left. + ||\phi(s)||_{1,b} + \frac{(\delta + \bar{L})}{\bar{L}} ||\phi(s))||_{0,b} + \frac{1}{\bar{L}} ||\phi(s)||_{0,b}^2 \right] ds, \tag{4.29}
\end{aligned}
$$

for some positive constants A and B and for all $0 \leq t \leq T$.

Proposition 4.4. *If $\sup_{t \in [0,T]} ||\phi(t)||_{1,b} \leq B_1(\sqrt{\bar{L}} + \delta/\sqrt{\bar{L}})$ and $\sup_{t \in [0,T]} ||\phi(t)||_{0,b} \leq B_2(\bar{L} + \delta)$ then there exists $N > 1$ and $\omega > 0$ such that*

$$
\begin{aligned}
||\phi(t)||_{0,b} \leq & N \exp(-\frac{\omega}{\bar{L}} t) ||\phi(0)||_{0,b} \\
& + \int_0^t N \exp\left(-\frac{\omega}{\bar{L}}(t-s)\right) A\left[1 + \frac{\delta}{\bar{L}} + B\left(\sqrt{\bar{L}} + \frac{\delta}{\sqrt{\bar{L}}}\right) ||\phi(s)||_{1,b} \right. \\
& \left. + ||\phi(s)||_{1,b} + \frac{(\delta + \bar{L})}{\bar{L}} ||\phi(s))||_{0,b} + \frac{1}{\bar{L}} ||\phi(s)||_{0,b}^2 \right] ds, \tag{4.30}
\end{aligned}
$$

for some positive constants A and B and for all $0 \leq t \leq T$.

Proof of Propositions 4.3 and 4.4. The proofs follow the strategy in [35, Proposition 15]. The key step is to note that the solution $\phi(z, t)$ of (4.17) satisfies, for example,

$$||\phi(t)||_{1,b} = ||S(t)\phi(0)||_{1,b} + \int_0^t ||S(t-s)H(s)||_{1,b}\,ds,$$

where $S(t)$ is the solution operator of the equation $\phi_t = \bar{\mathcal{L}}\phi = \phi_{zz} - \frac{W''(m(z))}{\bar{L}}\phi$. We recall the bound for H in (4.24) and apply the bounds (4.25)-(4.27) in Proposition 4.1 using that $\langle H, m_z \rangle = 0$. □

To summarize Propositions 4.3 and 4.4: if for some $T > 0$, $\phi(z, t)$ satisfies

$$\sup_{t \in [0,T]} ||\phi(t)||_{1,b} \le M\left(\sqrt{\bar{L}} + \frac{\delta}{\sqrt{\bar{L}}}\right),$$

$$\sup_{t \in [0,T]} ||\phi(t)||_{0,b} \le M(\bar{L} + \delta),$$

then there are positive constants E_1, E_2, F_{M1} and F_{M2} such that

$$||\phi(t)||_{1,b} \le N\exp\left(-\frac{\omega}{\bar{L}}t\right)||\phi(0)||_{1,b}$$
$$+ \int_0^t \exp\left(-\frac{\omega}{\bar{L}}(t-s)\right)\left[\frac{E_1}{\sqrt{\bar{L}}}\left(1+\frac{\delta}{\bar{L}}\right) + \frac{F_{M1}}{\sqrt{\bar{L}}}\left(1+\frac{\delta}{\sqrt{\bar{L}}}\right)||\phi(s)||_{1,b}\right]\,ds,$$

$$||\phi(t)||_{0,b} \le N\exp\left(-\frac{\omega}{\bar{L}}t\right)||\phi(0)||_{0,b}$$
$$+ \int_0^t \exp\left(-\frac{\omega}{\bar{L}}(t-s)\right)\left[E_2\left(1+\frac{\delta}{\bar{L}}\right) + F_{M2}\left(1+\frac{\delta}{\bar{L}}\right)||\phi(s)||_{0,b}\right]\,ds,$$

for all $0 \le t \le T$. Proposition 4.2 then gives that, provided $\bar{L}$ and δ are sufficiently small so that,

$$\frac{F_{M1}}{\sqrt{\bar{L}}}\left(1+\frac{\delta}{\sqrt{\bar{L}}}\right) < \frac{\omega}{2\bar{L}} \quad \text{and} \quad F_{M2}\left(1+\frac{\delta}{\bar{L}}\right) < \frac{\omega}{2\bar{L}}, \tag{4.31}$$

we have

$$\sup_{t \in [0,T]} ||\phi(t)||_{1,b} \le N||\phi(0)||_{1,b} + \frac{2E_1}{\omega}\sqrt{\bar{L}}\left(1+\frac{\delta}{\bar{L}}\right), \tag{4.32}$$

$$\sup_{t \in [0,T]} ||\phi(t)||_{0,b} \le N||\phi(0)||_{0,b} + \frac{2E_2}{\omega}\bar{L}\left(1+\frac{\delta}{\bar{L}}\right), \tag{4.33}$$

for all $0 \le t \le T$. We can now prove bounds on $||\phi(t)||_{1,b}$ and $||\phi(t)||_{0,b}$ which hold for all time, applying the methods in [35] for each bound.

Proposition 4.5. *Choose M so that $M/4 \geq 2E_1/\omega$ and $M/4 \geq 2\bar{E}_2/\omega$. Choose $\bar{L}$ and δ to satisfy* (4.31). *If the initial condition is bounded such that*

$$||\phi(0)||_{1,b} \leq \frac{M}{4N}\sqrt{\bar{L}}\left(1+\frac{\delta}{\bar{L}}\right) \quad \text{and} \quad ||\phi(0)||_{0,b} \leq \frac{M}{4N}\bar{L}\left(1+\frac{\delta}{\bar{L}}\right), \qquad (4.34)$$

where N is the constant introduced in Propositions 4.3 and 4.4, then

$$||\phi(t)||_{1,b} \leq M\sqrt{\bar{L}}\left(1+\frac{\delta}{\bar{L}}\right) \quad \text{and} \quad ||\phi(t)||_{0,b} \leq M\bar{L}\left(1+\frac{\delta}{\bar{L}}\right), \qquad (4.35)$$

for all $t \geq 0$.

Proof. Suppose for a contradiction

$$T_M = \inf\left\{t : ||\phi(t)||_{1,b} = M\sqrt{\bar{L}}\left(1+\frac{\delta}{\bar{L}}\right) \quad \text{or} \quad ||\phi(t)||_{0,b} = M\bar{L}\left(1+\frac{\delta}{\bar{L}}\right)\right\} < \infty.$$

Suppose at $t = T_M$ we have that $||\phi(t)||_{1,b} = M\sqrt{\bar{L}}(1+\delta/\bar{L})$. Then for $t \leq T_M$, we have

$$\sup_{t\in[0,T_M]} ||\phi(t)||_{1,b} \leq M\sqrt{\bar{L}}\left(1+\frac{\delta}{\bar{L}}\right) \quad \text{and} \quad \sup_{t\in[0,T_M]} ||\phi(t)||_{0,b} \leq M\bar{L}\left(1+\frac{\delta}{\bar{L}}\right), \qquad (4.36)$$

and hence we can use (4.32) to yield

$$\sup_{t\in[0,T_M]} ||\phi(t)||_{1,b} \leq N||\phi(0)||_{1,b} + \frac{2E_1}{\omega}\sqrt{\bar{L}}\left(1+\frac{\delta}{\bar{L}}\right) \leq \frac{M}{2}\sqrt{\bar{L}}\left(1+\frac{\delta}{\bar{L}}\right).$$

Hence $||\phi(t)||_{1,b} < M\sqrt{\bar{L}}(1+\delta/\bar{L})$ for all $t \in [T_M, T_M + \epsilon]$ for some small ϵ and we have the required contradiction. A similar contradiction follows if $||\phi(t)||_{0,b} = M\bar{L}(1+\delta/\bar{L})$ at $T = T_M$. $\square$

The previous proposition gives bounds on $||\phi(t)||_{1,b}$ and $||\phi(t)||_{0,b}$ for all time and we conclude that our expression for $\dot{c}(t)$ is well-defined. To prove the existence of pulsating wave solutions, we need a tighter bound on $||\phi(t)||_{1,b}$. This bound is applicable for sufficient times (of $O(\bar{L})$) only:

Proposition 4.6. *Choose δ as before, M such that $M/16N \geq E_1/\omega$ and an $\bar{L}$ that satisfies* (4.31) *and is such that $\sqrt{\bar{L}} \leq w/16NF_{M1}$. If $||\phi(0)||_{1,b} \leq \frac{M}{4N}\sqrt{\bar{L}}(1+\frac{\delta}{L})$ then $||\phi(t)||_{1,b} \leq \frac{M}{4N}\sqrt{\bar{L}}(1+\frac{\delta}{L})$ for all $t \geq \frac{\bar{L}}{\omega}\ln(2N)$.*

Proof. Our assumptions mean we have satisfied the conditions for Proposition 4.5. We also make

use of Proposition 4.3, which gives

$$\|\phi(t)\|_{1,b} \leq N \exp\left(-\frac{\omega}{\bar{L}}t\right)\|\phi(0)\|_{1,b} + \int_0^t \exp\left(-\frac{\omega}{\bar{L}}(t-s)\right)\left[\frac{E_1}{\sqrt{\bar{L}}}\left(1+\frac{\delta}{\bar{L}}\right) + \frac{F_{M1}}{\sqrt{\bar{L}}}\|\phi(s)\|_{1,b}\right]ds,$$

$$\leq \frac{M}{4}\sqrt{\bar{L}}\left(1+\frac{\delta}{\bar{L}}\right)\exp\left(-\frac{\omega}{\bar{L}}t\right) + \frac{\bar{L}}{\omega}\left[\frac{E_1}{\sqrt{\bar{L}}}\left(1+\frac{\delta}{\bar{L}}\right) + F_{M1}M\left(1+\frac{\delta}{\bar{L}}\right)\right],$$

$$\leq \frac{M}{8N}\sqrt{\bar{L}}\left(1+\frac{\delta}{\bar{L}}\right) + \frac{E_1}{\omega}\sqrt{\bar{L}}\left(1+\frac{\delta}{\bar{L}}\right) + \frac{F_{M1}M}{\omega}\bar{L}\left(1+\frac{\delta}{\bar{L}}\right),$$

$$\leq \frac{M}{4N}\sqrt{\bar{L}}\left(1+\frac{\delta}{\bar{L}}\right),$$

for all $t \geq \frac{\bar{L}}{\omega}\ln(2N)$. $\qquad\square$

4.2.3 Front speed and existence of a fixed point

We are now in a position to prove Theorem 4.1. Recall that

$$\dot{c}(t) = -\frac{\left\langle\left(\frac{2}{z+\rho+c} - \frac{2}{\rho+c}\right)m_z - \frac{6}{(z+\rho+c)^2}m, m_z\right\rangle}{\left\langle m_z + \tilde{m}_z + \phi_z + \alpha'(z)\delta m^-(r) + \beta'(z)(\delta m^+(r) + \bar{L}w^+(r,t)), m_z\right\rangle}$$

$$-\frac{\left\langle\frac{\delta(g(z+\rho+c)+F)}{\bar{L}}, m_z\right\rangle}{\left\langle m_z + \tilde{m}_z + \phi_z + \alpha'(z)\delta m^-(r) + \beta'(z)(\delta m^+(r) + \bar{L}w^+(r,t)), m_z\right\rangle}$$

$$-\frac{\left\langle\left(\frac{2}{z+\rho+c} - \frac{2}{\rho+c}\right)\phi_z - \frac{6}{(z+\rho+c)^2}\phi + O\left(\frac{(\delta+\bar{L}+\phi)\phi}{\bar{L}} + \frac{\delta+\bar{L}}{\sqrt{\bar{L}}}\right), m_z\right\rangle}{\left\langle m_z + \tilde{m}_z + \phi_z + \alpha'(z)\delta m^-(r) + \beta'(z)(\delta m^+(r) + \bar{L}w^+(r,t)), m_z\right\rangle}.$$

which, on applying the definitions and properties of $m(z)$, $\tilde{m}(z)$, $E(z)$ and $\phi(z,t)$, has leading order behaviour

$$\dot{c}(t) = \frac{\delta}{\bar{L}}\frac{\langle g(z+\rho+c)+F, -m_z\rangle}{\|m_z\|^2 + O(\delta/\sqrt{\bar{L}}+\sqrt{\bar{L}})}.$$

Now recalling the quantities

$$s(a) = -\int_{-\infty}^{\infty} g(z+a)m_z(z)\,dz, \quad \hat{F} = s^*, \quad \hat{\alpha} = \frac{1}{\sqrt{\bar{L}}\int_{-\infty}^{\infty} m_z^2\,dz} \quad \text{and} \quad \hat{\beta} = \frac{s''(0)}{2},$$

where s^* is the minimum value of s attained at $0, \pm p, \pm 2p...$, we have

$$\dot{c}(t) = \frac{\delta}{\bar{L}}\left(\frac{-F + s(c(t)+\rho(t))}{\|m_z\|^2 + O\left(\delta/\sqrt{\bar{L}}+\sqrt{\bar{L}}\right)}\right). \tag{4.37}$$

We note that any disparities in running the integral over $(-\infty, \infty)$ as opposed to $(-k(t), 1-k(t))$ in the definitions of $\hat{\alpha}$ and $s(a)$ are exponentially small and can be neglected. We can now write down a general differential equation for the front position $k(t) = c(t) + \rho(t)$,

$$
\begin{aligned}
\dot{k}(t) = \dot{c}(t) + \dot{\rho}(t) &= \frac{\delta}{\bar{L}}\left(\frac{-F + s(c(t) + \rho(t))}{||m_z||^2 + O(\delta/\sqrt{\bar{L}} + \sqrt{\bar{L}})}\right) - \frac{2}{c(t) + \rho(t)}, \\
&= \frac{\delta}{\bar{L}}\left(\frac{-F + s(k(t))}{||m_z||^2 + O(\delta/\sqrt{\bar{L}} + \sqrt{\bar{L}})}\right) - \frac{2}{k(t)}.
\end{aligned}
\tag{4.38}
$$

Due to the bounds on F in theorem statement, namely $F < \hat{F} < 0$, the $\dot{c}(t)$ component of the above expression is smallest in magnitude when the interface position is such that $s(k(t))$ is minimized. Therefore, we begin by considering front motion near $k(t) = p,\ 2p,\ 3p....$ Following the ideas in [35], we fix a small constant $0 < P \ll p$. During the time t_P it takes for the front to travel distance P into a spatial heterogeneity, say from $2p$ to $2p + P$, we have

$$
\dot{k}(t) = \frac{\delta}{\sqrt{\bar{L}}}\hat{\alpha}(\eta + \hat{\beta}(k(t) - 2p)^2) - \frac{2}{k(t)},
\tag{4.39}
$$

where $\eta = \hat{F} - F$, having used that $s'(2p) = 0$ as $2p$ is a minimizer of s.

Proof of Theorem 4.1.
In the case that $\delta/\sqrt{\bar{L}} \gg 1$, the expression for $\dot{k}(t)$ in (4.39) and the change of variables $\hat{k} = k - 2p$ give that the time taken by the front to travel from $2p$ to $2p + P$ can be expressed as

$$
t_P = \frac{\sqrt{\bar{L}}}{\hat{\alpha}\delta}\int_0^P \frac{d\hat{k}}{\eta + \hat{\beta}(\hat{k}(t))^2 + O(\sqrt{\bar{L}}/\delta)}.
$$

Upon integration, provided $\bar{L}^*$ is sufficiently small and C_1 is sufficiently large so that $\eta > O(\sqrt{\bar{L}}/\delta)$ (where $\bar{L}^*$ and C_1 are as in the statement of Theorem 4.1), we find that

$$
t_P = \frac{\sqrt{\bar{L}}}{\hat{\alpha}\delta}\frac{1}{\sqrt{\eta\hat{\beta}}}\left(\tan^{-1}\left(\frac{\sqrt{\hat{\beta}}P}{\sqrt{\eta}}\right)\right).
\tag{4.40}
$$

Recall $\eta \leq C_2$ in statement of Theorem 4.1. Suppose C_2 is sufficiently small so that

$$\tan^{-1}\left(\frac{\sqrt{\hat{\beta}}P^*}{\sqrt{\eta}}\right) \approx \frac{\pi}{2},$$

for some $0 < P^* < P$. Then t_{P^*} follows from (4.40) and $t_P - t_{P^*}$ is very small. This means the front takes a very small amount of time to travel from $2p + P^*$ to $2p + P$ in comparison to the time taken to travel from $2p$ to $2p + P^*$. Hence the front displays avalanche motion; slower phases of motion for interface positions $k(t)$ close to minimizers of $s(\cdot)$ and faster phases of motion away from these critical points. For the sufficiently small C_2 we have

$$t_P \approx \frac{\sqrt{\bar{L}}}{\hat{\alpha}\delta}\frac{1}{\sqrt{\eta\hat{\beta}}}\frac{\pi}{2}.$$

Therefore, for any $\sigma > 0$, we can find C_1, C_2 and $\bar{L}^*$ such that

$$\frac{\sqrt{\bar{L}}(1-\sigma)\pi}{2\hat{\alpha}\delta\sqrt{\hat{\beta}\eta}} \leq t_P \leq \frac{\sqrt{\bar{L}}(1+\sigma)\pi}{2\hat{\alpha}\delta\sqrt{\hat{\beta}\eta}}. \tag{4.41}$$

As discussed above, we observe very quick front motion for $k(t)$ away from minimizers of $s(\cdot)$. Therefore, we conclude that the total time for the front to travel one period of the spatial heterogeneity (for example, from $k = 2p$ to $k = 3p$) is well approximated by $2t_P$. This is because the time taken to travel from $2p + P$ to $3p - P$ is much smaller than from $2p$ to $2p + P$ and $3p - P$ to $3p$ (where front motion is slow as the front position is close to a minimizer of $s(\cdot)$). Hence we have the average front velocity $V_F = p/T_F$ satisfies

$$(1-\sigma)p\frac{\hat{\alpha}\delta\sqrt{\hat{\beta}(\hat{F}-F)}}{\sqrt{\bar{L}}\pi} \leq V_F \leq (1+\sigma)p\frac{\hat{\alpha}\delta\sqrt{\hat{\beta}(\hat{F}-F)}}{\sqrt{\bar{L}}\pi}. \tag{4.42}$$

The bounds on V_F in (4.42) give that it takes sufficient time for the front to travel the distance p (recall $\hat{F} - F \leq C_2$ in the theorem statement of Theorem 4.1). This means the condition of sufficient time (of order $\bar{L}$) in Proposition 4.6 is satisfied and we can use the proposition in the next result. We are now able to prove the existence of pulsating wave solutions which follows from the existence of a fixed point.

Theorem 4.2 (Existence of fixed point). *For M, δ, $\bar{L}$ and F as in Theorem 4.1 and Proposition 4.6, there exists ϕ_0 such that $\|\phi_0\|_{1,b} \leq \frac{M}{4N}\sqrt{\bar{L}}(1 + \delta/\bar{L})$ and $0 < T(\phi) < \infty$ such that*

$\phi(T(\phi_0)) = \phi_0$, where $\phi(t)$ is the solution of (4.17) with initial condition ϕ_0.

Proof. The proof of this theorem follows verbatim from [35, Theorem 19], the key step follows from Proposition 4.6 which gives $||\phi(t)||_{1,b} \leq ||\phi_0||_{1,b}$ for all $t \geq \frac{\bar{L}}{\omega} \ln(2N)$. □

This completes the proof of Theorem 4.1. □

4.2.4 Extension to an unequal welled potential

In this section we consider the more general case where $W(h)$ is an unequal welled potential. For an arbitrary value of the rescaled temperature A we have

$$W'(h) = 6h^2 (h - 1) \left(h - \frac{h_-}{h_+} \right),$$

where

$$h_+ = \frac{B + \sqrt{B^2 - 24AC}}{4C} \quad \text{and} \quad h_- = \frac{B - \sqrt{B^2 - 24AC}}{4C}.$$

Again, we study the equation

$$h_t = h_{rr} + \frac{2}{r}h_r - \frac{6}{r^2}h - \frac{W'(h)}{\bar{L}} + \frac{\delta(g(r) + F)}{\bar{L}}, \tag{4.43}$$

and consider the following proposition.

Proposition 4.7. *The front position $k(t)$ of a solution of (4.43) with suitable initial conditions evolves according to*

$$\dot{k}(t) = \frac{\delta}{\bar{L}} \frac{-F + s(k(t))}{||m_z||^2} - \frac{2}{k(t)} + \dot{d}(t),$$

where $\dot{d}(t) = \sqrt{\frac{3}{\bar{L}}} \left(2\frac{h_-}{h_+} - 1 \right)$.

In this case, we make the change of variable $z = r - \rho(t) - c(t) - d(t)$, where $c(t)$ is as before and $\rho(t)$ now satisfies

$$\frac{d\rho}{dt} = -\frac{2}{\rho + c + d}.$$

The function $d(t)$ is a linear term accounting for front motion driven by the unequal well structure of the bulk potential. Again we suppose that $h(r, t) = m(z) + \tilde{m}(z) + E(z, t) + \phi(z, t)$ with

$E(z, t)$ and $\tilde{m}(z)$ as before. In the case of an unequal welled potential, let $m(z)$ be a solution of

$$m_{zz} + \dot{d}m_z - \frac{W'(m)}{\bar{L}} = 0. \tag{4.44}$$

We see in Chapter 2 that (4.44) has a solution for a unique value of $\dot{d}$ which is given by

$$\dot{d}(t) = \sqrt{\frac{3}{\bar{L}}}\left(2\frac{h_-}{h_+} - 1\right). \tag{4.45}$$

The solution $m(z)$ of (4.44) satisfies the bounds in (4.11)-(4.13), in particular

$$|m_z(z)| \leq \frac{C}{\sqrt{\bar{L}}} \exp\left(-a\sqrt{\bar{L}}|z|\right), \tag{4.46}$$

for any a satisfying $0 < a < \frac{\sqrt{3}}{\bar{L}}$ [44]. It is now possible to proceed exactly as before.

4.3 Numerical simulations in heterogeneous materials

We numerically study the full non-dimensionalized and normalized Landau-de Gennes gradient flow system with forcing terms at the isotropic-nematic transition temperature as in (4.1) given by

$$\mathbf{Q}_t = \nabla^2\mathbf{Q} - \frac{9}{\bar{L}}\left[\frac{1}{3}\mathbf{Q} - 3\left(\mathbf{QQ} - \frac{\mathbf{I}}{3}|\mathbf{Q}|^2\right) + |\mathbf{Q}|^2\mathbf{Q}\right] + \frac{2}{3}\frac{\delta}{\bar{L}}\left(\hat{\mathbf{r}} \times \hat{\mathbf{r}} - \frac{\mathbf{I}}{3}\right)(g(r) + F),$$

We take Ω to be the three-dimensional annulus given by

$$\Omega := \{\mathbf{x} \in \mathbb{R}^3; \, 9 \leq |\mathbf{x}| \leq 10\}.$$

In this section we work with initial conditions with front structures positioned well away from the origin in order to minimize the curvature driven contribution to front velocity. This is necessary as even the most refined mesh achievable with our numerical methods only allows for $\bar{L} = O(10^{-4})$. This means that $\delta/\sqrt{\bar{L}}$ is too small for obstacle driven motion to dominate in the unit sphere. It is more practical to work on a unit annulus than a large sphere, especially as we expect outwards front motion. For these simulations, the annulus is discretised with a spherical polar grid (as our domain no longer contains the origin) and the remaining numerical details are as introduced in Chapter 2.

We work with either $\bar{L} = 3.5 \times 10^{-3}$ or 6.9×10^{-4}. We consider the periodic forcing term

$g(r) = \cos(12\pi r)$ which has period $p = \frac{1}{6}$. We impose the boundary conditions

$$\mathbf{Q}(9, t) = 0 \quad \text{and} \quad \mathbf{Q}(10, t) = \hat{\mathbf{r}} \otimes \hat{\mathbf{r}} - \frac{\mathbf{I}}{3},$$

where $\hat{\mathbf{r}}$ is the three-dimensional unit radial vector. We study the resultant dynamic solutions for a range of initial conditions, discussing the existence of pulsating wave solutions and making comparisons with our analytical results when appropriate. We first consider a radially symmetric initial condition, within the remit of the analysis, given by

$$\mathbf{Q}(\mathbf{r}, 0) = h(r) \left(\hat{\mathbf{r}} \otimes \hat{\mathbf{r}} - \frac{\mathbf{I}}{3} \right), \tag{4.47}$$

where

$$h(r) = \frac{1}{2} \left[1 + \tanh \left(\frac{r - r_0}{\sqrt{\bar{L}}} \right) \right], \tag{4.48}$$

and $r_0 = 9.3$. We work with $\delta = 2$ throughout. Comparison to the average velocity V_F is not appropriate as these values of L are far too big for our estimate to be valid. However we can study the existence of pulsating wave solutions, in particular as F decreases past some critical F^*. We also compare this F^* to the critical $\hat{F}$ predicted in Section 4.2, however we expect $|F^*|$ to be larger than $|\hat{F}|$ due to the curvature contribution. Recall that $\hat{F} = s^*$ and in this case

$$s^* = \min_a \left(- \int_{-\infty}^{\infty} \cos(12\pi(z + a)) m_z(z) \, dz \right),$$
$$= \min_a \left(-\frac{1}{4} \int_{-\infty}^{\infty} \cos(12\pi(z + a)) \text{sech}^2 \left(\sqrt{\frac{3}{4\bar{L}}} z \right) dz \right).$$

This follows from the solution $m(z)$ in (4.10). We compute $\hat{F}$ by numerically integrating the above expression to yield s^*. Firstly, let $\bar{L} = 3.5 \times 10^{-3}$, then $\hat{F}$ is found to be $\hat{F} = -0.14$. Figure 4-1 shows the front position for various values of F and suggests that we get a qualitative change in solution as F increases past F^* for $-0.84 < F^* < -0.83$. As expected $|\hat{F}| < |F^*|$. Figure 4-2 shows how the eigenvalues of $\mathbf{Q}(\mathbf{r}, t)$ evolve, with time shots taken at $t = 0.025$ intervals for $F = -0.89$. The figure confirms that the system remains uniaxial and illustrates the front velocity increasing and decreasing as the front travels over the obstacles. Next we take $\bar{L} = 6.9 \times 10^{-4}$. For this value of $\bar{L}$, we find $\hat{F} = -0.61$. Figure 4-3 yields that for $\bar{L} = 6.9 \times 10^{-4}$, $-0.99 < F^* < -0.98$. Figures 4-3 and 4-1 together suggest that the comparison between F^* and $\hat{F}$ improves as $\bar{L}$ decreases.
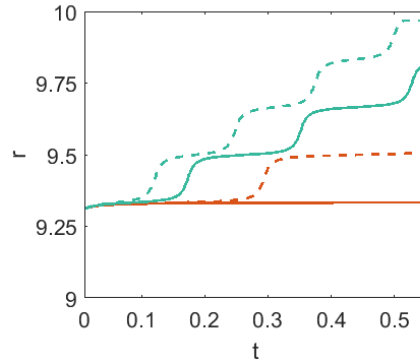
Figure 4-1: Front position k for initial condition (4.47) and (4.48) for $F = -0.83$ (orange), $F = -0.84$ (orange dash), $F = -0.86$ (blue) and $F = -0.89$ (blue dash) for $L = 3.5 \times 10^{-3}$ and $\delta = 2$.
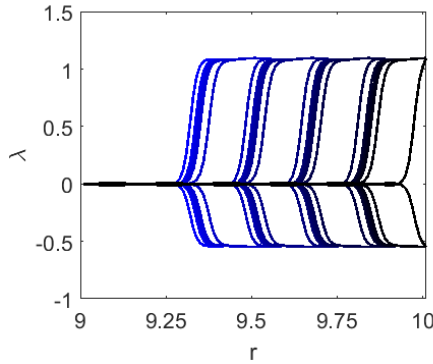

Figure 4-2: Radial profiles of the eigenvalues of $\mathbf{Q}(\mathbf{r}, t)$ for initial condition (4.47) and (4.48) for $F = -0.89$, $\bar{L} = 3.5 \times 10^{-3}$ and $\delta = 2$ with time shots taken at $t = 0.025$ intervals starting at $t = 0$ (light blue) to $t = 0.5$ (black).
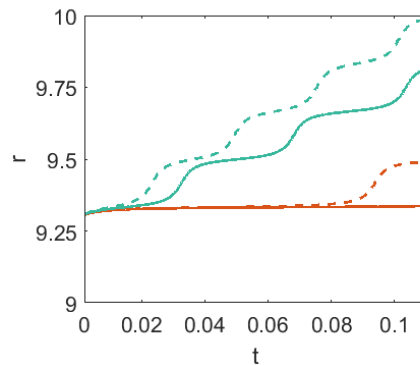

Figure 4-3: Front position k for initial condition (4.47) and (4.48) for $F = -0.98$ (orange), $F = -0.99$ (orange dash), $F = -1.1$ (blue) and $F = -1.2$ (blue dash) for $\bar{L} = 6.9 \times 10^{-4}$ and $\delta = 2$.

75

We now consider initial conditions outside the remit of the analysis, working with $F = -0.89$, $\bar{L} = 3.5 \times 10^{-3}$ and $\delta = 2$. An example of such an initial condition is

$$\mathbf{Q}(\mathbf{r}, 0) = (r - 9)\left(\hat{\mathbf{r}} \otimes \hat{\mathbf{r}} - \frac{\mathbf{I}}{3}\right). \qquad (4.49)$$

This initial condition has no front structure however, as shown in Figure 4-4, a propagating front quickly evolves and the long-time behaviour is as for the previous initial condition.
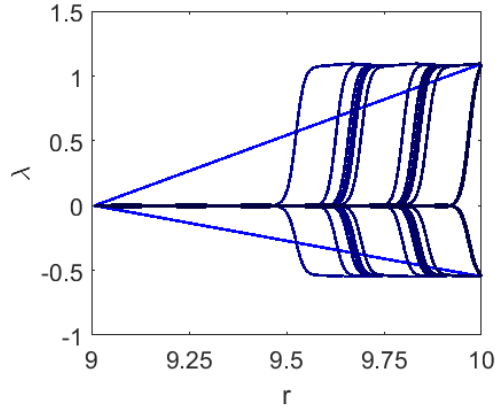

Figure 4-4: Radial profiles of the eigenvalues of $\mathbf{Q}(\mathbf{r}, t)$ for initial condition (4.47) and (4.49) with time shots taken at $t = 0.025$ intervals starting at $t = 0$ (light blue) to $t = 0.3$ (black).

Our third initial condition is biaxial for $9 \leq r \leq 9.5$ and is given by

$$\mathbf{Q}(\mathbf{r}, 0) = h(r)\left(\hat{\mathbf{r}} \otimes \hat{\mathbf{r}} - \frac{\mathbf{I}}{3}\right) + s(r)\left(\mathbf{m} \otimes \mathbf{m} - \mathbf{p} \otimes \mathbf{p}\right), \qquad (4.50)$$

where $h(r)$ is given in (4.48), $s(r) = \frac{1}{10}\left(1 + \tanh\left(50(r - 9.5)\right)\right)(r - 9)(10 - r)$ and $\mathbf{m}$ and $\mathbf{p}$ are as in Chapter 3. Plots of the eigenvalues of $\mathbf{Q}(\mathbf{r}, t)$ show that the solution quickly becomes uniaxial, see Figure 4-5. Radial symmetry is recovered and a pulsating wave solution is generated. For initial conditions which are biaxial for all $9 \leq r \leq 10$, we find the radial symmetry in the exterior is lost. We no longer observe the formation of radially symmetric rings of alternating high and low obstacle strength and hence do not find pulsating wave solutions for these initial conditions.

Next we consider an initial condition with a radially asymmetric front, choosing $h(r)$ to impose an ellipsoidal initial interface in (4.47), see the first time panel of Figure 4-6 (where the annulus has been rescaled for illustrative purposes). Plots of $|\mathbf{Q}(\mathbf{r}, t)|^2$ in Figure 4-6 show the ellipsoidal front
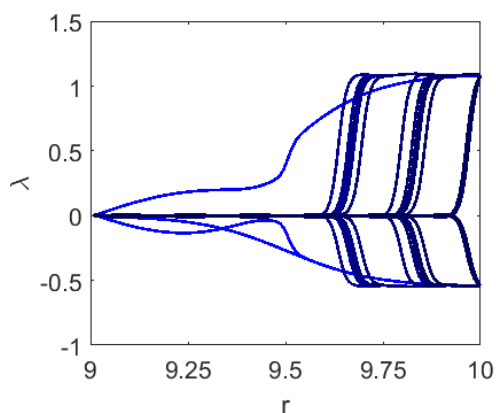
Figure 4-5: Radial profiles of the eigenvalues of $\mathbf{Q}(\mathbf{r}, t)$ for initial condition (4.50) with time shots taken at $t = 0.025$ intervals starting at $t = 0$ (light blue) to $t = 0.3$ (black).

becoming more symmetric through the bands of low obstacle strength and slow front motion, and more eccentric again when the edges of the ellipse reach the bands of high obstacle strength first. Figure 4-7 demonstrates the existence of pulsating waves solutions for this initial condition.
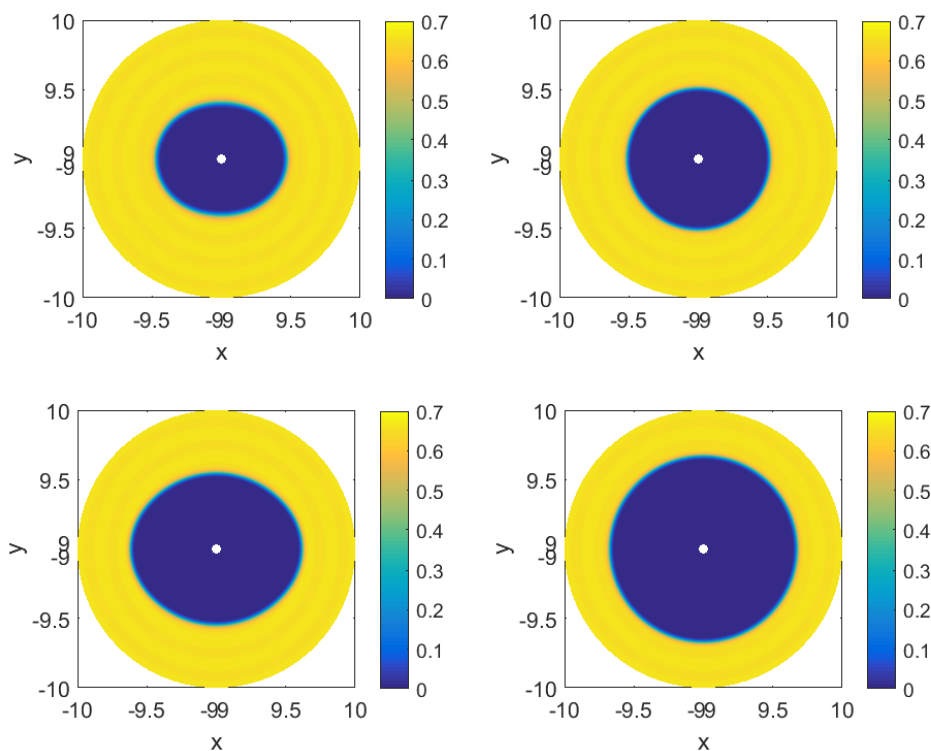

Figure 4-6: $|\mathbf{Q}(\mathbf{r}, t)|^2$ for a cross-section of the annulus for a radially asymmetric initial condition at $t = 0$, $t = 0.08$, $t = 0.12$ and $t = 0.18$ (top left to bottom right).
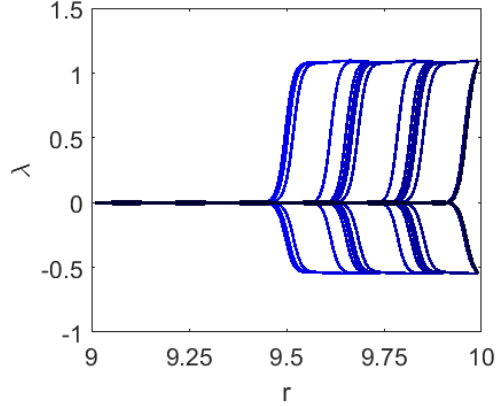
Figure 4-7: Radial profiles of the eigenvalues of $\mathbf{Q}(\mathbf{r}, t)$ for a radially asymmetric initial condition with time shots taken at $t = 0.025$ intervals starting at $t = 0$ (light blue) to $t = 0.3$ (black).

Finally, we consider the contribution of motion driven by the curvature of the front. Imposing initial condition (4.47) and (4.48) on annuli of various radii, we compare front speed for different initial front positions. We take our domain to be

$$\Omega := \{\mathbf{x} \in \mathbb{R}^3; \, R_1 \leq |\mathbf{x}| \leq R_1 + 1\},$$

for various R_1 with $r_0 = \frac{2R_1+1}{2}$ in (4.48). We expect there to be a large range of R_1 for which the front becomes pinned. Suppose the front travels inwards from $\frac{2R_1+1}{2}$, that is, mean curvature motion dominates on this annulus. As we increase R_1, the mean curvature contribution to front motion decreases and the front becomes pinned when the outwards-motion inducing forcing terms in a band of high forcing strength (where $g(r) < 0$) arrests the front. As we increase R_1 further, it is not until the outwards-motion inducing forcing terms in a band of low forcing strength (where $g(r) > 0$) can overcome the mean curvature contribution that the front advances.

First we take $\delta = 2$ and plot the front position with time for various R_1. From the first graph in Figure 4-8 we can see how outward front propagation becomes slower as R_1 decreases. The front motion is only slightly inhibited as we decrease from $R_1 = 9$ (the radius considered in all previous simulations) to $R_1 = 7$, however for $R_1 = 4$ the front becomes pinned and yields a stationary solution. We decrease δ in order to observe inwards front motion and take $\delta = 0.3$. For $R_1 = 1$, the front travels inwards and the second graph in Figure 4-8 illustrates the change in speed as the front advances over alternating regions of high and low opposition. As we increase to $R_1 = 2$, the front is arrested and we have a stationary solution. It is not until $R_1 = 35$ that low bands of outwards forcing strength are able to overcome mean curvature and the front moves outwards.
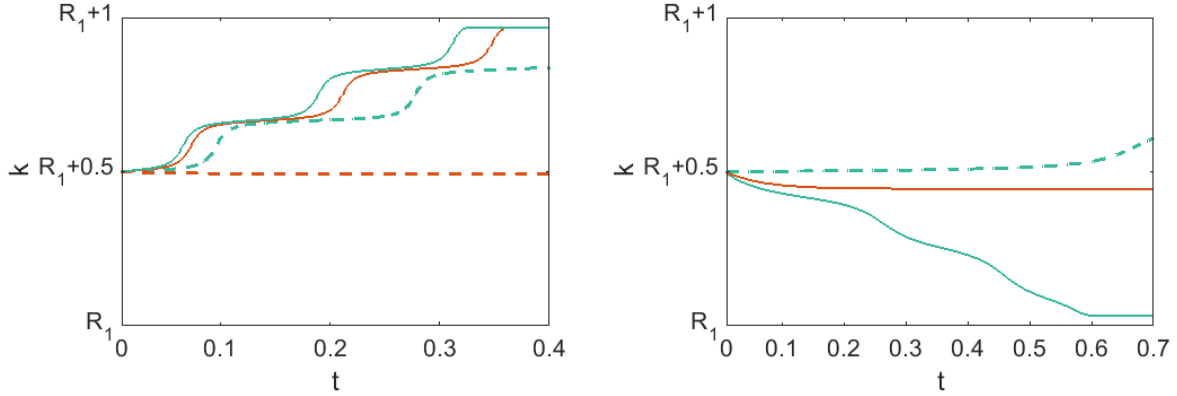
Figure 4-8: Front position k with $R_1 = 4$ (orange dash), $R_1 = 5$ (blue dash), $R_1 = 7$ (orange), $R_1 = 9$ (blue) and $\delta = 2$ (left), and $R_1 = 1$ (blue), $R_1 = 2$ (orange), $R_1 = 35$ (blue dash) and $\delta = 0.3$ (right).

4.4 Numerical simulations with a moon-shaped obstacle

Here we solve the full Landau-de Gennes gradient flow system in the unit square given by $\Omega := \{(x, y) \in \mathbb{R}^2; 1 \leq x \leq 2, 1 \leq y \leq 2\}$. We consider the presence of two types of obstacle; periodic forcing of the form $\delta(\cos(12\pi y) + F)$ and a moon-shaped obstacle given by $\phi f(x, y)$ where $f(x, y)$ is shown in Figure 4-9 and ϕ is a constant. The periodic forcing terms induce front movement down the square. Inspired by the work in [112] and [113] we study the pinning of an isotropic-nematic front as it encounters the moon, demonstrating that pinning is dependent on moon orientation for certain forcings. We work with an initial condition with a front structure separating the isotropic and nematic states given by

$$\mathbf{Q}(x, y, 0) = \frac{1}{2}\left[1 + \tanh\left(\frac{y - y_0}{\sqrt{\bar{L}}}\right)\right]\left(\hat{\mathbf{n}} \otimes \hat{\mathbf{n}} - \frac{\mathbf{I}}{3}\right),$$

where $\hat{\mathbf{n}} = (1, 0, 0)$ and impose the Dirichlet boundary conditions $\mathbf{Q}(x, 1, t) = 0$ and $\mathbf{Q}(x, 2, t) = \hat{\mathbf{n}} \otimes \hat{\mathbf{n}} - \frac{\mathbf{I}}{3}$. The remaining sides are free boundaries. In this case the non-dimensionalized and normalized Landau-de Gennes gradient flow system at the isotropic-nematic transition temperature is given by

$$\mathbf{Q}_t = \nabla^2\mathbf{Q} - \frac{9}{\bar{L}}\left[\frac{1}{3}\mathbf{Q} - 3\left(\mathbf{Q}\mathbf{Q} - \frac{\mathbf{I}}{3}|\mathbf{Q}|^2\right) + |\mathbf{Q}|^2\mathbf{Q}\right] + \left(\hat{\mathbf{n}} \times \hat{\mathbf{n}} - \frac{\mathbf{I}}{3}\right)\left(\frac{\delta}{\bar{L}}(g(r) + F) + \frac{\phi}{\bar{L}}f(x, y)\right).$$

We take $\delta = 2$, $F = 1.2$, $\phi = -4$ and $\bar{L} = 3.5 \times 10^{-3}$. We find if the front meets the rounded edge of the moon first the interface becomes pinned. However, the front is able to pass through

the obstacle if the moon is orientated so the front meets the two points. This is illustrated with plots of $|\mathbf{Q}(\mathbf{r}, t)|^2$ in Figures 4-10 and 4-11.
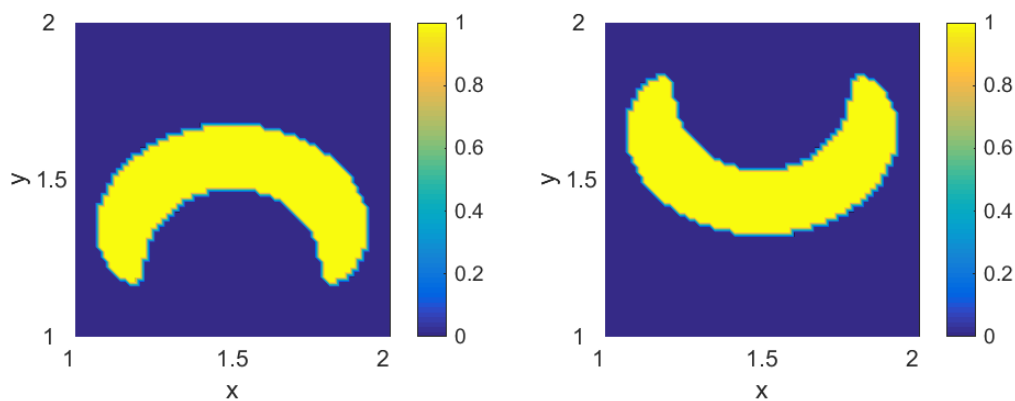

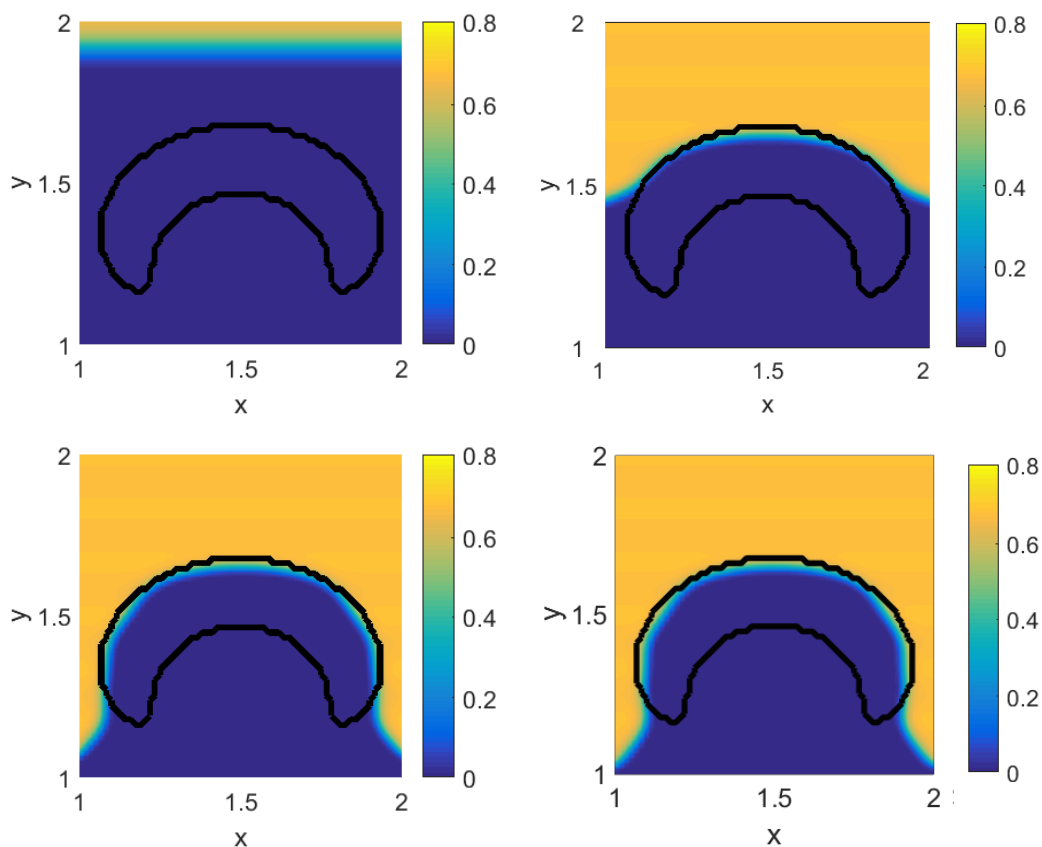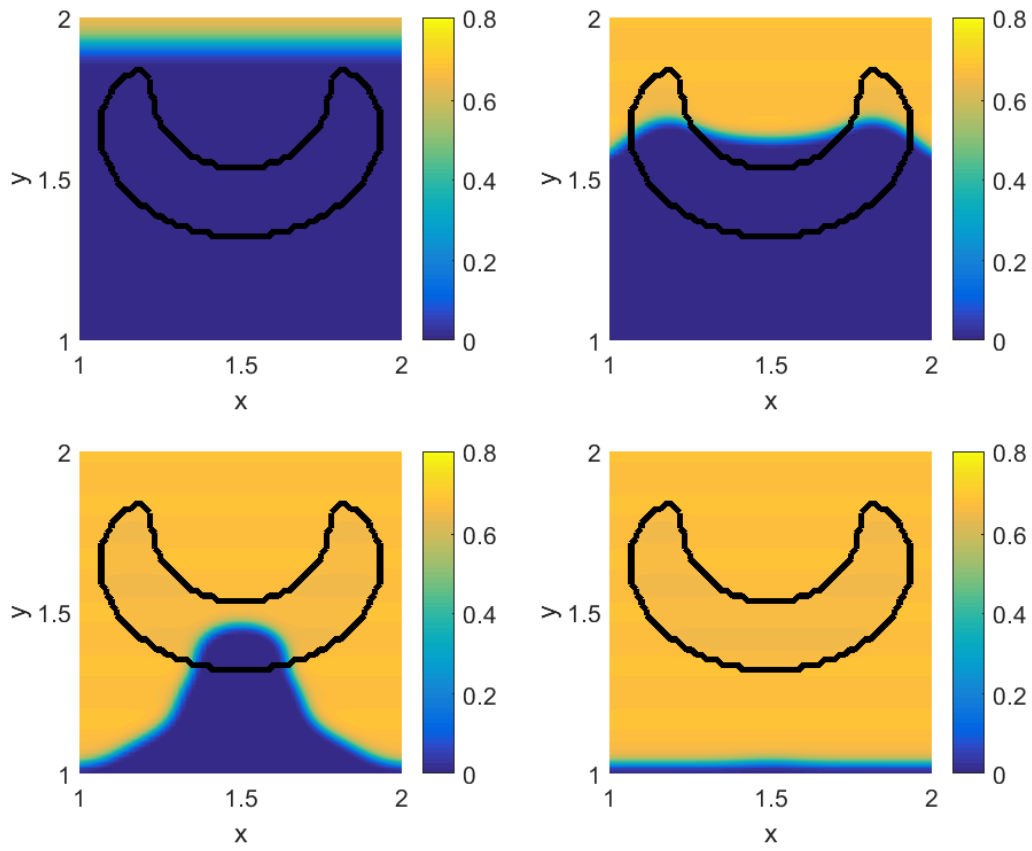Figure 4-9: $f(x, y)$ for the two orientations of the moon studied.

Figure 4-10: $|\mathbf{Q}(\mathbf{r}, t)|^2$ for orientation 1 at $t = 0$, $t = 2$, $t = 4$ and $t = 7$ (top left to bottom right). The spatial resolution is $h = \frac{1}{128}$.

Figure 4-11: $|\mathbf{Q}(\mathbf{r}, t)|^2$ for orientation 2 at $t = 0$, $t = 1.5$, $t = 4.5$ and $t = 7$.

Equilibrium configurations on the disc

In Chapter 5 we consider dynamic solutions of the Landau-de Gennes gradient flow system on the two-dimensional unit disc with Dirichlet boundary conditions subject to two distinct types of initial condition; planar and non-planar. Working at the isotropic-nematic transition temperature we compare the resulting transient dynamics and long-term behaviour, including how the initial condition affects the persistence of isotropic-nematic fronts. Our numerical results are complemented by the analysis of a class of planar critical points of the Landau-de Gennes energy introduced in Fratta et al 2016 [33]. These solutions are labelled by two radially symmetric order parameters u and v. The first parameter u is a measure of the biaxiality of the solution and the uniaxial part of the solution is accounted for by v.

5.1   Problem formulation

We take our domain to be the unit disc given by

$$\Omega := \{\mathbf{x} \in \mathbb{R}^2; |\mathbf{x}| \le 1\},$$

and impose the fixed boundary condition

$$\mathbf{Q}_b = \hat{\mathbf{r}} \otimes \hat{\mathbf{r}} - \frac{\mathbf{I}}{3} \quad \text{on} \quad r = 1, \tag{5.1}$$

where $\hat{\mathbf{r}} = (\cos\theta, \sin\theta, 0)$ is the two-dimensional unit radial vector. We study dynamic solutions of the Landau-de Gennes gradient flow system (2.4) at the isotropic-nematic transition temperature, which can be normalised to yield

$$\mathbf{Q}_t = \nabla^2\mathbf{Q} - \frac{9}{\bar{L}}\left(\frac{1}{3}\mathbf{Q} - 3\left(\mathbf{QQ} - \frac{\mathbf{I}}{3}|\mathbf{Q}|^2\right) + |\mathbf{Q}|^2\mathbf{Q}\right), \tag{5.2}$$

subject to the boundary condition (5.1). We work with small values of the elastic constant $\bar{L} = \frac{81C}{B^2}L$. The fixed boundary condition is purely uniaxial and is a minimum of the relevant bulk potential.

We begin with some heuristics for the dynamic solutions of (5.2) driven by an understanding of Landau-de Gennes energy minimizers on the disc. The gradient flow model is based on the principle that dynamic solutions evolve along a path of decreasing energy and converge to a critical point of the Landau-de Gennes energy for long times [87]. Hence the long-time behaviour can be predicted by a study of the critical points or local minimizers of the Landau-de Gennes energy. As discussed in Chapter 3, in [76] the authors present an analysis of Landau-de Gennes energy minimizers in the $\bar{L} \to 0$ limit. Based on their analysis the minimizers converge strongly in $W^{1,2}(\Omega, S_0)$ to a limiting harmonic map of the form

$$\mathbf{Q} = s\left(\mathbf{n}^* \otimes \mathbf{n}^* - \frac{\mathbf{I}}{3}\right),$$

where $\mathbf{n}^*$ is a solution of the harmonic map equations and $s = 0$ or $s = 1$ so that $\mathbf{Q}$ is a minimum of the normalised bulk potential. Boundary condition (5.1) dictates that $s = 1$ and $\mathbf{n}^* = (\cos\theta, \sin\theta, 0)$ on $r = 1$. The convergence is shown to be uniform away from the singularities of the limiting harmonic map, which may not be unique. (Also see Golovaty and Montero 2014 [49], where the authors focus on Landau-de Gennes minimizers on planar domains.) Two solutions of the harmonic map equations $\nabla^2\mathbf{n}^* + |\nabla\mathbf{n}^*|^2\mathbf{n}^* = 0$ on the disc subject to the boundary condition $\mathbf{n}^* = (\cos\theta, \sin\theta, 0)$ on $r = 1$, are given by

$$\mathbf{n}_1 = (\cos\theta, \sin\theta, 0) \quad \text{and} \quad \mathbf{n}_2 = \left(\frac{2x}{1+r^2}, \frac{2y}{1+r^2}, \frac{1-r^2}{1+r^2}\right).$$

We conjecture there are two competing limiting harmonic maps defined in terms of $\mathbf{n}_1$ and $\mathbf{n}_2$:

$$\mathbf{Q}_1 = s\left(\mathbf{n}_1 \otimes \mathbf{n}_1 - \frac{\mathbf{I}}{3}\right) \quad \text{and} \quad \mathbf{Q}_2 = \left(\mathbf{n}_2 \otimes \mathbf{n}_2 - \frac{\mathbf{I}}{3}\right).$$

Since $\mathbf{n}_1$ is not defined at $r = 0$ we must have $s = 0$ at $r = 0$ for $\mathbf{Q}_1$. Therefore $\mathbf{Q}_1$ must have an isotropic core at the origin with $s \to 1$ rapidly (over a distance of $\sqrt{\bar{L}}$) away from $r = 0$. However, $\mathbf{n}_2$ has no singularity on Ω since the vector escapes into the third dimension and hence $\mathbf{Q}_2$ is not required to have an isotropic core. We predict that the dynamic solutions of (5.2) subject to (5.1) converge to either $\mathbf{Q}_1$ or $\mathbf{Q}_2$ for long times. They converge to $\mathbf{Q}_2$ if escape into the third dimension is possible. If escape into the third dimension is not allowed, dynamic solutions converge to $\mathbf{Q}_1$ instead. We prove that escape into third dimension is impossible for certain initial conditions with the following lemma. We refer to a $\mathbf{Q}$-tensor as being *planar* if $Q_{13} = Q_{23} = 0$ and *non-planar* if Q_{13} and Q_{23} are not identically zero. In particular, the boundary condition in (5.1) is a planar $\mathbf{Q}$-tensor.

Lemma 5.1. *Let $\mathbf{Q}(\mathbf{r}, t)$ be a solution of the gradient flow system associated with the Landau -de Gennes energy functional (5.2) on Ω subject to (5.1) with a planar initial condition $\mathbf{Q}(\mathbf{r}, 0)$ such that $|\mathbf{Q}(\mathbf{r}, 0)| \leq \sqrt{\frac{2}{3}}$. Then $Q_{13} = Q_{23} = 0$ for all $t \geq 0$.*

Proof. The proof is an immediate application of Gronwall's inequality [94]. From [72] we have the following bound for the dynamic solution:

$$|\mathbf{Q}(\mathbf{r}, t)| \leq \sqrt{\frac{2}{3}} \quad \text{for all} \quad t \geq 0. \tag{5.3}$$

The two governing partial differential equations for Q_{13} and Q_{23} can be written in the form

$$\frac{\partial Q_{13}}{\partial t} - \nabla^2 Q_{13} = \frac{1}{\bar{L}} F(\mathbf{Q}) Q_{13} + B Q_{12} Q_{23},$$
$$\frac{\partial Q_{23}}{\partial t} - \nabla^2 Q_{23} = \frac{1}{\bar{L}} G(\mathbf{Q}) Q_{23} + B Q_{12} Q_{13},$$

where F and G are bounded functions due to (5.3). We multiply the first equation by Q_{13} and the second equation by Q_{23}, add the two equations together, integrate by parts and use the fact that $Q_{13} = Q_{23} = 0$ on $r = 1$ to get

$$\frac{1}{2} \frac{d}{dt} \left(\int_\Omega Q_{13}^2 + Q_{23}^2 \, dV \right) + \int_\Omega |\nabla Q_{13}|^2 + |\nabla Q_{23}|^2 \, dV$$
$$= \frac{1}{\bar{L}} \int_\Omega F(\mathbf{Q}) Q_{13}^2 + G(\mathbf{Q}) Q_{23}^2 + 2 B Q_{12} Q_{13} Q_{23} \, dV.$$

Hence we have

$$\frac{d}{dt} \int_{\Omega} Q_{13}^2 + Q_{23}^2 \, dV \le \frac{\delta}{\bar{L}} \int_{\Omega} Q_{13}^2 + Q_{23}^2 \, dV,$$

where δ is a positive constant. An immediate application of Gronwall's inequality shows that

$$\int_{\Omega} Q_{13}^2 + Q_{23}^2 \, dV \le \exp\left(\frac{\delta}{\bar{L}} t\right) \left(\int_{\Omega} Q_{13}^2 + Q_{23}^2 \, dV\right)\bigg|_{t=0} = 0,$$

so that $Q_{13} = Q_{23} = 0$ for all $t \ge 0$. $\qquad\square$

5.2 The (u, v)-static solutions

We illustrate the difference between planar and non-planar initial conditions by focussing on (u, v)-type initial conditions inspired by the (u, v)-critical points of the Landau-de Gennes energy reported in [33] for low temperatures where $A < 0$. We work at $A = \frac{B^2}{27C}$ and, by analogy with the work in [33], look for special solutions of the normalized Landau-de Gennes Euler-Lagrange equations at the isotropic-nematic transition temperature given by

$$0 = \bar{L}\nabla^2 \mathbf{Q} - 9\left(\frac{1}{3}\mathbf{Q} - 3\left(\mathbf{Q}\mathbf{Q} - \frac{\mathbf{I}}{3}|\mathbf{Q}|^2\right) + |\mathbf{Q}|^2\mathbf{Q}\right),$$

of the form

$$\mathbf{Q} = \frac{u(r)}{2}\left(\mathbf{n}_1 \otimes \mathbf{n}_1 - \mathbf{m} \otimes \mathbf{m}\right) + v(r)\left(\mathbf{p} \otimes \mathbf{p} - \frac{\mathbf{I}}{3}\right), \tag{5.4}$$

where $\mathbf{m} = (-\sin\theta, \cos\theta, 0)$ and $\mathbf{p} = (0, 0, 1)$. Such solutions, if they exist, are given by solutions of the following system of coupled second-order ordinary differential equations

$$u_{rr} + \frac{u_r}{r} - \frac{4u(r)}{r^2} = \frac{u}{\bar{L}}\left(3 + 18v + \frac{9}{2}u^2 + 6v^2\right), \tag{5.5}$$

$$v_{rr} + \frac{v_r}{r} = \frac{v}{\bar{L}}\left(3 - 9v + \frac{9}{2}u^2 + 6v^2\right) + \frac{27}{4\bar{L}}u^2, \tag{5.6}$$

with $u(0) = v_r(0) = 0$ and $u(1) = 1$, $v(1) = -\frac{1}{2}$ to be consistent with the boundary condition in (5.1). As in [33], we can prove the existence of a solution pair (u, v) of (5.5)-(5.6) by appealing

to a variational problem. Define the energy

$$\mathcal{E}(u, v) = \int_0^1 \left[\frac{1}{4}u_r^2 + \frac{1}{3}v_r^2 + \frac{1}{r^2}u^2 + \frac{1}{\bar{L}}\left(\frac{3u^2}{4} + v^2\right) \right.$$
$$\left. + \frac{1}{\bar{L}}\left(\frac{9u^4}{16} + \frac{3u^2v^2}{2} + v^4\right) - \frac{1}{\bar{L}}v\left(2v^2 - \frac{9u^2}{2}\right) \right] r\, dr.$$

(5.7)

This is simply the rescaled Landau-de Gennes energy of the (u, v)-ansatz. The energy is defined on the admissible set

$$S := \left\{(u, v) : [0, 1] \to \mathbb{R}^2 \,\middle|\, \sqrt{r}u_r,\ \sqrt{r}v_r,\ \frac{u}{\sqrt{r}},\ \sqrt{r}v \in L^2(0, 1),\ u(1) = 1,\ v(1) = -\frac{1}{2}\right\}.$$

Lemma 5.2. *For each $\bar{L} > 0$, there exists a global minimizer $(u, v) \in [C^\infty(0, 1) \cap C([0, 1])] \times [C^\infty(0, 1) \cap C^1([0, 1])]$ of the energy (5.7) on S which satisfies (5.5)-(5.6).*

Proof. The proof follows verbatim from [33, Theorem 3.2] for low temperatures. Note that $\mathcal{E}(u, v) > -K$ for all $(u, v) \in S$ for some constant K. This gives the existence of a sequence (u_n, v_n) such that $\lim_{n \to \infty} \mathcal{E}(u_n, v_n) = \inf_S \mathcal{E}(u, v)$ and that, for some subsequence, $(u_n, v_n) \rightharpoonup (u, v)$ as $n \to \infty$ in $[W^{1,2}((0, 1); r\, dr) \cap L^2((0, 1); \frac{dr}{r})] \times W^{1,2}((0, 1); r\, dr)$. The Rellich-Kondrachov theorem [1] and the weak lower semi-continuity of the Dirichlet energy give that $\liminf_{n \to \infty} \mathcal{E}(u_n, v_n) \geq \mathcal{E}(u, v)$. Hence there exists a minimizer $(u, v) \in S$. This implies that (u, v) is a solution of the Euler-Lagrange equations of $\mathcal{E}(u, v)$ in (5.5)-(5.6). Further, the **Q**-tensor in (5.4) must be a classical solution of the Landau-de Gennes Euler-Lagrange equations (see Appendix A). From this it follows that $(u, v) \in [C^\infty(0, 1) \cap C([0, 1])] \times [C^\infty(0, 1) \cap C^1([0, 1])]$. $\square$

Next we discuss some qualitative properties of the (u, v)-solutions. Similar questions have been considered in the recent paper [55] for the low temperature regime $A < 0$ with exception of the monotonicity result in Lemma 5.4. Our method of proof is somewhat different and is presented here for completeness.

Lemma 5.3. *Let (u, v) be a global minimizer of the energy $\mathcal{E}$ in (5.7) subject to $u(1) = 1$ and $v(1) = -\frac{1}{2}$. Then we have the following bounds*

$$0 \leq u(r) \leq 1 \quad \text{and} \quad -\frac{1}{2} \leq v(r) \leq 0 \quad \text{for} \quad 0 \leq r \leq 1.$$

Proof. We prove the non-negativity of u and non-positivity of v by following the arguments in [33, 55]. The analyticity of the pair (u, v) and the symmetry $\mathcal{E}[u, v] = \mathcal{E}[-u, v]$ give that $u \geq 0$

since $u(1) > 0$. We assume for a contradiction that $v(r_1) = v(r_2) = 0$ with $v(r) > 0$ for some $r_1 < r < r_2$. Define the perturbation

$$\bar{v}(r) = \begin{cases} v(r) & \text{for} \quad 0 \leq r \leq r_1, \\ 0 & \text{for} \quad r_1 < r < r_2, \\ v(r) & \text{for} \quad r_2 \leq r \leq 1. \end{cases}$$

A direct computation shows that

$$\mathcal{E}[u, v] - \mathcal{E}[u, \bar{v}] = \int_{r_1}^{r_2} \left[\frac{v_r^2}{3} + \frac{v^2}{L}(v-1)^2 + \frac{u^2}{L}\left(\frac{9v}{2} + 9v^2\right) \right] r\, dr > 0,$$

contradicting the global minimality of the pair (u, v).

Next let us assume that $v_{min} < -\frac{1}{2}$ at some $r = r_0$. At $r = r_0$, the left-hand side of (5.6) is non-negative by definition of a minimum. From the maximum principle we have

$$|\mathbf{Q}|^2 = \frac{u^2}{2} + \frac{2v^2}{3} \leq \frac{2}{3}.$$

Hence if $v_{min} < -\frac{1}{2}$, then $u^2(r_0) < 1$. Then for $v_{min} < -\frac{1}{2}$ we have

$$3v_{min} - 9v_{min}^2 + 6v_{min}^3 < -\frac{9}{2},$$

$$u^2 \left(\frac{27}{4} + \frac{9}{2}v_{min}\right) < \frac{9}{2},$$

so that the right-hand side of (5.6) is negative, yielding a contradiction.

Similarly, let us assume for a contradiction that $u_{max} > 1$ at some $r = r_0$. Then the left-hand side of (5.5) is strictly negative at $r = r_0$ by definition of a maximum. Recalling that $-\frac{1}{2} \leq v \leq 0$ then

$$u_{max}\left(18v + 6v^2\right) > -\frac{15}{2},$$

$$3u_{max} + \frac{9}{2}u_{max}^3 > \frac{15}{2},$$

so that the right-hand side of (5.5) is strictly positive, yielding the desired contradiction. $\quad\square$

Next we show that u and v are monotonic functions by borrowing an idea from [61]. We make the observation that $u_r(r) > 0$ for $0 < r < \sigma$ where $\sigma > 0$ is sufficiently small. This is an immediate consequence of $u(0) = u_r(0) = 0$ and $u \geq 0$. We compute the second variation of the energy $\mathcal{E}$ in (5.7) by considering perturbations of the form

$$u_\epsilon(r) = u(r) + \epsilon\alpha(r) \quad \text{and} \quad v_\epsilon(r) = v(r) + \epsilon\beta(r), \tag{5.8}$$

with $\alpha(1) = \beta(1) = 0$. A standard computation shows that the second variation in this case is

$$\delta^2\mathcal{E}[\alpha, \beta] = \int_0^1 \left[\frac{\alpha_r^2}{4} + \frac{\beta_r^2}{3} + \frac{\alpha^2}{r^2} + \frac{1}{L}\left(\frac{3}{4}\alpha^2 + \frac{27}{8}u^2\alpha^2 + \frac{3}{2}v^2\alpha^2 + 9v\alpha^2 \right.\right.$$
$$\left.\left. + \beta^2 - 6v\beta^2 + 6v^2\beta^2 + \frac{3}{2}u^2\beta^2 + 9u\alpha\beta + 18uv\alpha\beta \right) \right] r\,dr.$$

In particular, $\delta^2\mathcal{E}[\alpha, \beta] \geq 0$ for all admissible α and β by the global minimality of (u, v).

Lemma 5.4. Let (u, v) be a global minimizer of the energy in (5.7). Then $u_r(r) > 0$ and $v_r(r) < 0$ for $r > 0$.

Proof. We assume for a contradiction that u and v are not monotone. Then there exist points $r_1, r_2, r_3, r_4 \in [0, 1)$ such that

$$u_r(r_1) = u_r(r_2) = 0, \quad u_r < 0 \quad \text{for} \quad r_1 < r < r_2,$$
$$v_r(r_3) = v_r(r_4) = 0, \quad v_r > 0 \quad \text{for} \quad r_3 < r < r_4.$$

We differentiate the equations for u and v in (5.5)-(5.6), multiply by ru_r and rv_r respectively and integrate over $r \in [r_1, r_2]$ and $r \in [r_3, r_4]$ to get the following equalities:

$$\int_{r_1}^{r_2} \frac{r}{4}u_{rr}^2 + \frac{5}{4r}u_r^2 - \frac{2}{r^2}uu_r \tag{5.9}$$
$$+ \frac{r}{L}\left[u_r^2\left(\frac{3}{4} + \frac{27}{8}u^2 + \frac{3}{2}v^2 + 9v \right) + uu_rv_r\left(\frac{2}{9} + 54v \right) \right] dr = 0,$$

$$\int_{r_3}^{r_4} \frac{r}{3}v_{rr}^2 + \frac{v_r^2}{3r} \tag{5.10}$$
$$+ \frac{r}{L}\left[v_r^2\left(1 - 6v + 6v^2 + \frac{3}{2}u^2 \right) + uu_rv_r\left(\frac{9}{2} + 54v \right) \right] dr = 0.$$

We define the perturbations α and β as follows:

$$\alpha(r) = \begin{cases} 0 & \text{for} \quad u_r \geq 0, \\ u_r & \text{for} \quad u_r < 0, \end{cases} \quad \text{and} \quad \beta(r) = \begin{cases} 0 & \text{for} \quad v_r \leq 0, \\ v_r & \text{for} \quad v_r > 0. \end{cases}$$

These perturbations satisfy $\alpha(1) = \beta(1) = 0$ since u attains its maximum and v attains its minimum on $r = 1$. Substituting this choice of (α, β) and recalling (5.9)-(5.10), we obtain $\delta^2 \mathcal{E}[\alpha, \beta] < 0$ and the required contradiction. $\square$

5.3 Stability of (u, v)-solutions

Next we study the stability of the (u, v)-solution as a critical point of the full Landau-de Gennes energy. We compute the second variation of the Landau-de Gennes energy about the (u, v)-critical point and construct an admissible perturbation for which the second variation is negative. This gives the instability of the (u, v)-critical point where (u, v) is a global minimizer of (5.7).

Consider a perturbation about the (u, v)-critical point $\mathbf{Q}$ given in (5.4) of the form $\mathbf{W} = \mathbf{Q} + \epsilon \mathbf{V}$ where $\mathbf{V} = 0$ on $r = 1$ so that $\mathbf{W}$ satisfies the Dirichlet condition in (5.1). Computing the second variation gives

$$\delta^2 \mathbf{I} = \int \int \int \frac{\bar{L}}{2} |\nabla \mathbf{V}|^2 + 3|\mathbf{V}|^2 - 54 Q_{ij} V_{jp} V_{pi} + 18 (\mathbf{Q} \cdot \mathbf{V})^2 + 9|\mathbf{Q}|^2 |\mathbf{V}|^2 \, dV.$$

We define a basis for the space of symmetric traceless 3×3 matrices, choosing

$$\left\{ (\mathbf{n}_1 \otimes \mathbf{n}_1 - \mathbf{m} \otimes \mathbf{m}), \ (\mathbf{n}_1 \otimes \mathbf{m} + \mathbf{m} \otimes \mathbf{n}_1), \ (\mathbf{n}_1 \otimes \mathbf{p} + \mathbf{p} \otimes \mathbf{n}_1), \ (\mathbf{m} \otimes \mathbf{p} + \mathbf{p} \otimes \mathbf{m}), \ \left(\mathbf{p} \otimes \mathbf{p} - \frac{\mathbf{I}}{3} \right) \right\},$$

and write $\mathbf{V}$ as a linear combination of these matrices given by

$$\mathbf{V} = a \left(\mathbf{n}_1 \otimes \mathbf{n}_1 - \mathbf{m} \otimes \mathbf{m} \right) + b \left(\mathbf{n}_1 \otimes \mathbf{m} + \mathbf{m} \otimes \mathbf{n}_1 \right)$$
$$+ c \left(\mathbf{n}_1 \otimes \mathbf{p} + \mathbf{p} \otimes \mathbf{n}_1 \right) + d \left(\mathbf{m} \otimes \mathbf{p} + \mathbf{p} \otimes \mathbf{m} \right) + e \left(\mathbf{p} \otimes \mathbf{p} - \frac{\mathbf{I}}{3} \right),$$

for functions a, b, c, d and e which vanish on $r = 1$. This allows us to write the second variation

of the Landau-de Gennes energy in terms of the functions $a - e$ to obtain

$$\delta^2 \mathbf{I} = \int \int \int \bar{L} \left((\partial_k b + 2a\partial_k \theta)^2 + (\partial_k a - 2b\partial_k \theta)^2 + (\partial_k c - d\partial_k \theta)^2 + (\partial_k d + c\partial_k \theta)^2 + \frac{|\nabla e|^2}{3} \right) dV$$

$$+ \int \int \int 6 \left(a^2 + b^2 + c^2 + d^2 + \frac{e^2}{3} \right) dV$$

$$+ \int \int \int 27u(d^2 - c^2 + \frac{4}{3}ae) + 18v(2a^2 + 2b^2 - c^2 - d^2) - 12v^2 \, dV$$

$$+ \int \int \int 18u^2 a^2 + 8v^2 e^2 + 24uvae + 18 \left(\frac{u^2}{2} + \frac{2v^2}{3} \right) \left(a^2 + b^2 + c^2 + d^2 + \frac{e^2}{3} \right) dV,$$

where $\partial_k \theta = \left(-\frac{y}{r^2}, \frac{x}{r^2}, 0 \right) = \left(-\frac{\sin\theta}{r}, \frac{\cos\theta}{r}, 0 \right)$.

Set $a = b = d = e = 0$ and let

$$c(r) = \frac{100r^2(1 - r^2)^2}{(1 + 100r^2)}.$$

Then

$$\delta^2 I = \int \int \int \left[\bar{L} \left(c'(r)^2 + \frac{c(r)^2}{r^2} \right) + \left(6 - 27u - 18v + 18 \left(\frac{u^2}{2} + \frac{2v^2}{3} \right) \right) c(r)^2 \right] r \, dr d\theta.$$

Computing numerical solutions of (5.5) - (5.6) to find u and v, we can evaluate this integral numerically. We find that $\delta^2 I < 0$ for $\log_{10} \bar{L} < -1.7 \times 10^{-3}$, as illustrated in Figure 5-1. We recall that $\bar{L} = \frac{81C}{B^2} L$ and in this figure we use $B = 0.64 \times 10^4 \, Nm^{-2}$ and $C = 0.35 \times 10^4 \, Nm^{-2}$. As the second variation of the Landau-de Gennes energy about the (u, v)-critical point is negative for this perturbation, minimizers of the reduced (u, v)-energy functional are unstable critical points of the full Landau-de Gennes energy.
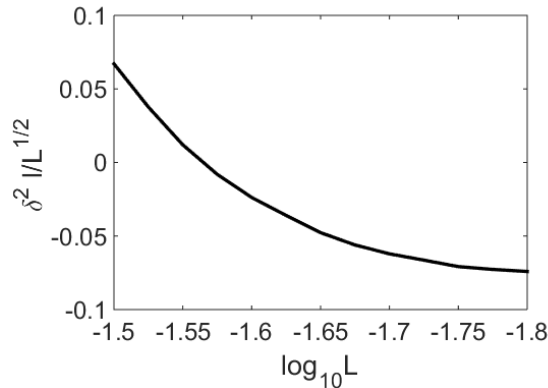

Figure 5-1: $\delta^2 I / L^{1/2}$.

5.4   Numerical simulations on the disc

We work at the isotropic nematic transition temperature and numerically solve the non-dimensionalized and normalized full Landau-de Gennes gradient flow system given in (3.3) on the disc subject to the boundary condition

$$\mathbf{Q}_b = \hat{\mathbf{r}} \otimes \hat{\mathbf{r}} - \frac{\mathbf{I}}{3} \quad \text{on} \quad r = 1,$$

where $\hat{\mathbf{r}}$ is the two-dimensional unit radial vector. We work with $\bar{L} = 6.9 \times 10^{-4}$ unless stated otherwise. We focus on the distinction between planar and non-planar initial conditions. Based on the heuristics presented in Section 5.1, we expect that all dynamic solutions develop a front separating an isotropic core around $r = 0$ from the uniaxial nematic phase away from $r = 0$. For planar initial conditions, the isotropic-nematic front and isotropic core around the origin persist for all times whereas for non-planar initial conditions, the interface collapses at the origin and the dynamic solution escapes to the completely uniaxial state $\mathbf{Q}_2$.

Firstly, we consider planar (u, v)-type initial conditions of the form

$$\mathbf{Q}(\mathbf{r}, 0) = \frac{u(r, 0)}{2} (\mathbf{n}_1 \otimes \mathbf{n}_1 - \mathbf{m} \otimes \mathbf{m}) + v(r, 0) \left(\mathbf{p} \otimes \mathbf{p} - \frac{\mathbf{I}}{3} \right), \tag{5.11}$$

where $\mathbf{n}_1$, $\mathbf{m}$ and $\mathbf{p}$ are as in the previous sections. Recall that our boundary condition fixes $u(1) = 1$ and $v(1) = -\frac{1}{2}$. We define $u(r, 0)$ and $v(r, 0)$ with front structures, setting

$$u(r, 0) = \frac{1}{2} \left(1 + \tanh \left(\frac{r - u_0}{\sqrt{\bar{L}}} \right) \right) \quad \text{and} \quad v(r, 0) = -\frac{1}{4} \left(1 + \tanh \left(\frac{r - v_0}{\sqrt{\bar{L}}} \right) \right),$$

for various values of u_0 and v_0. The corresponding dynamic solution of the full system (2.6) is of the form

$$\mathbf{Q}(\mathbf{r}, t) = \frac{u(r, t)}{2} (\mathbf{n}_1 \otimes \mathbf{n}_1 - \mathbf{m} \otimes \mathbf{m}) + v(r, t) \left(\mathbf{p} \otimes \mathbf{p} - \frac{\mathbf{I}}{3} \right), \tag{5.12}$$

where

$$u_{rr} + \frac{u_r}{r} - \frac{4u(r)}{r^2} = \frac{u}{\bar{L}} \left[3 + 18v + \frac{9}{2}u^2 + 3v^2 \right],$$

$$v_{rr} + \frac{v_r}{r} = \frac{v}{\bar{L}} \left[3 - 9v + \frac{9}{2}u^2 + 3v^2 \right] + \frac{27}{4\bar{L}}u^2,$$

subject to $u(1, t) = 1$ and $v(1, t) = -\frac{1}{2}$ for all $t \geq 0$. From Proposition 2.1, this is the unique

solution for this model problem. In fact, we can go further and apply the methods in Bronsard and Stoth 1998 [16] to the (u, v)-system in order to compare isotropic-nematic front motion with mean curvature motion. As in Chapter 3, we cannot quote the results because the dynamic equations differ from the vector-valued Ginzburg-Landau model in [16] by the additional term $-\frac{4u}{r^2}$. However, for $\bar{L}$ sufficiently small, this term may be controllable.

Solving the full system (2.6) on the disc with the initial conditions and boundary condition described above, we observe the typical solution as in Figure 5-2. We find good agreement with mean curvature propagation for small times, especially as $\bar{L}$ decreases, as shown in Figure 5-3. Both of these figures demonstrate the front being arrested near the origin. In order to observe the quick relaxation to uniaxiality we plot the eigenvalues of the dynamic solution $\mathbf{Q}(\mathbf{r}, t)$, see Figure 5-4. Varying the values of u_0 and v_0 does not change the qualitative dynamics: if $u_0 \neq v_0$, then $\mathbf{Q}(\mathbf{r}, 0)$ is biaxial but $\mathbf{Q}(\mathbf{r}, t)$ quickly becomes uniaxial. Numerically computing the tensor-difference $\mathbf{Q}(\mathbf{r}, t) - \mathbf{Q}_1$ as a function of time, we find that $\mathbf{Q}(\mathbf{r}, t) \to \mathbf{Q}_1$ away from $r = 0$ as expected. This is shown in Figure 5-5.
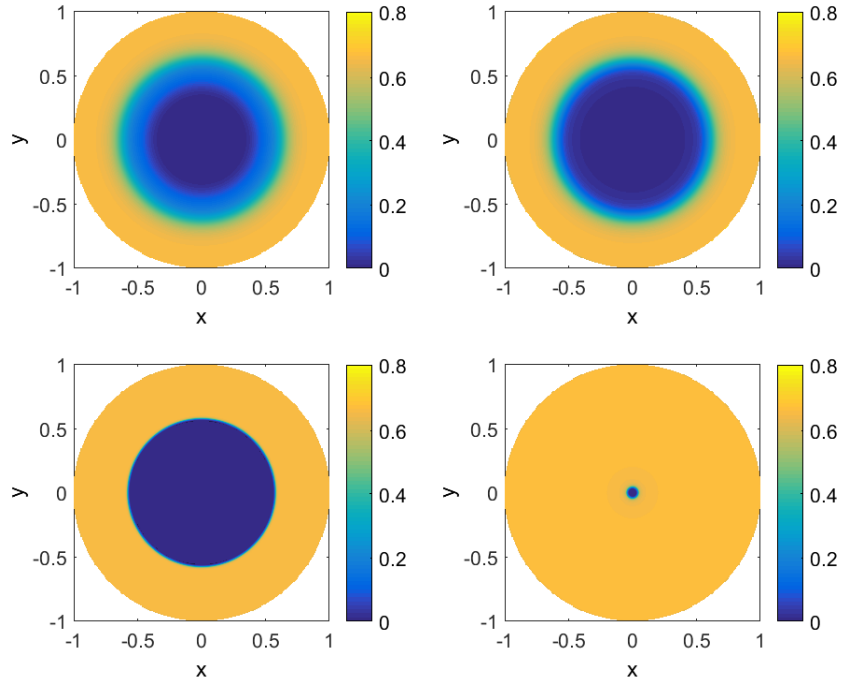

Figure 5-2: $|\mathbf{Q}(\mathbf{r}, t)|^2$ for initial condition (5.11) with $u_0 = 0.6$ and $v_0 = 0.4$ at $t = 0$, $t = 10^{-5}$, $t = 0.001$ and $t = 0.25$ (top left to bottom right). The spatial resolution is $h = \frac{1}{256}$.
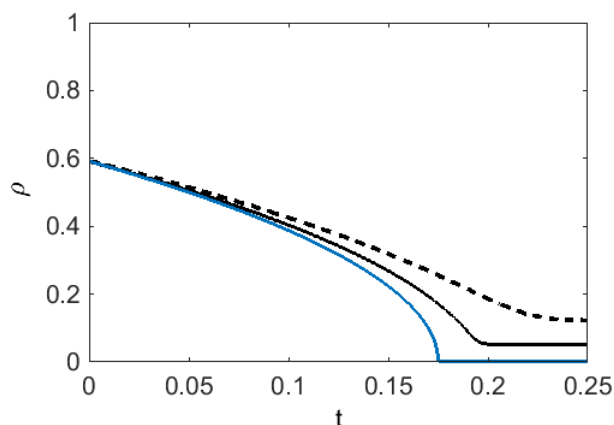
Figure 5-3: Front position ρ for initial condition (5.11) with $u_0 = 0.6$ and $v_0 = 0.4$ for $\bar{L} = 3.5 \times 10^{-3}$ (dashed) and $\bar{L} = 6.9 \times 10^{-4}$ (solid) and predicted position according to mean curvature (blue). As in Chapter 3, the radius of the isotropic core of the steady solution scales with $\sqrt{L}$ and hence the front is arrested at an $O(\sqrt{\bar{L}})$ distance from the origin. Here $\sqrt{\bar{L}} = 5.92 \times 10^{-2}$ (dashed) and 2.62×10^{-2} (solid). This contributes to the deviations from the predicted evolution by mean curvature seen in this figure. As $\bar{L}$ decreases, the isotropic core gets smaller and interface evolution approaches that according to mean curvature.

Figure 5-4: Radial profiles of the eigenvalues of $\mathbf{Q}(\mathbf{r}, t)$ for initial condition (5.11) with $u_0 = 0.6$ and $v_0 = 0.4$ at $t = 0$, $t = 10^{-5}$, $t = 0.001$ and $t = 0.25$.

Figure 5-5: $\mathbf{Q}(\mathbf{r},t)_{11} - (\mathbf{Q}_1)_{11}$ for initial condition (5.11) with $u_0 = 0.6$ and $v_0 = 0.4$ at $t = 0$, $t = 10^{-5}$, $t = 0.001$ and $t = 0.25$.

Next we consider a small perturbation to the (u, v)-initial condition in (5.11) that results in a non-planar initial condition. Let

$$\mathbf{Q}(r, 0) = u(r, 0)\left(\mathbf{n} \otimes \mathbf{n} - \frac{\mathbf{I}_2}{2}\right) + v(r, 0)\left(\mathbf{p} \otimes \mathbf{p} - \frac{\mathbf{I}}{3}\right), \qquad (5.13)$$

where $\mathbf{n} = \left(\sqrt{(1 - \epsilon^2(1 - r)^2)}\cos\theta, \sqrt{(1 - \epsilon^2(1 - r)^2)}\sin\theta, \epsilon(1 - r)\right)$ and $\mathbf{I}_2 = \mathbf{n}_1 \otimes \mathbf{n}_1 + \mathbf{m} \otimes \mathbf{m}$. The functions $u(r, 0)$ and $v(r, 0)$ are the same as in the previous initial condition. Again, the dynamic solution quickly becomes uniaxial irrespective of u_0 and v_0 and develops a well-defined front separating an interior isotropic region from the ordered uniaxial nematic state. This is shown in Figure 5-6. The third time panel of this figure illustrates how the front propagates inwards and collapses at the origin, instead of being arrested a small distance away. After the interface is lost, the dynamic solution relaxes to $\mathbf{Q}_2$ as illustrated in Figure 5-7 for the Q_{11} component of the $\mathbf{Q}$-tensor matrix. Figure 5-8 shows the time evolution of the eigenvalues of $\mathbf{Q}(\mathbf{r}, t)$ at the origin, demonstrating the convergence to a completely uniaxial solution. Figure 5-9 plots front position with time and illustrates that the agreement with mean curvature propagation becomes stronger as $\bar{L}$ decreases.

Figure 5-6: Radial profiles of the eigenvalues of $\mathbf{Q}(\mathbf{r}, t)$ for initial condition (5.13) with $\epsilon = 0.1$, $u_0 = 0.6$ and $v_0 = 0.4$ at $t = 0$, $t = 10^{-5}$, $t = 0.001$ and $t = 0.25$. The spatial resolution is $h = \frac{1}{256}$.
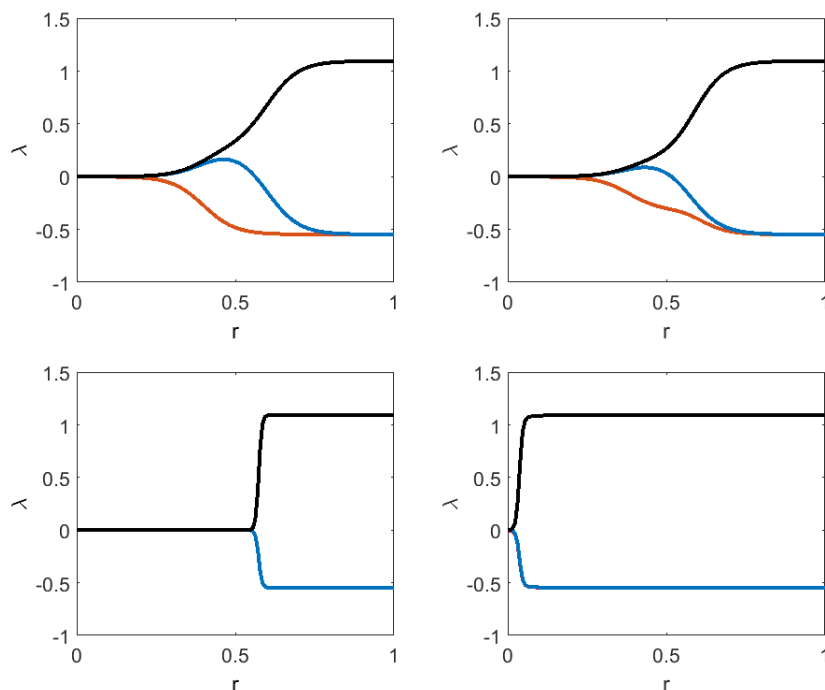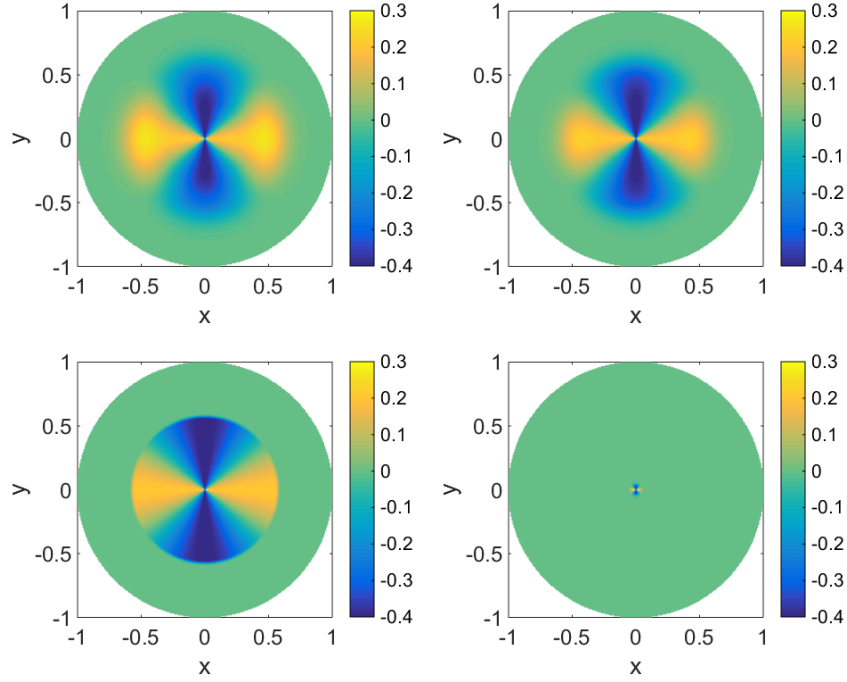

Figure 5-7: $\mathbf{Q}(\mathbf{r}, t)_{11} - (\mathbf{Q}_2)_{11}$ for initial condition (5.13) with $\epsilon = 0.1$, $u_0 = 0.6$ and $v_0 = 0.4$ at $t = 0$, $t = 0.001$, $t = 0.25$ and $t = 0.6$.
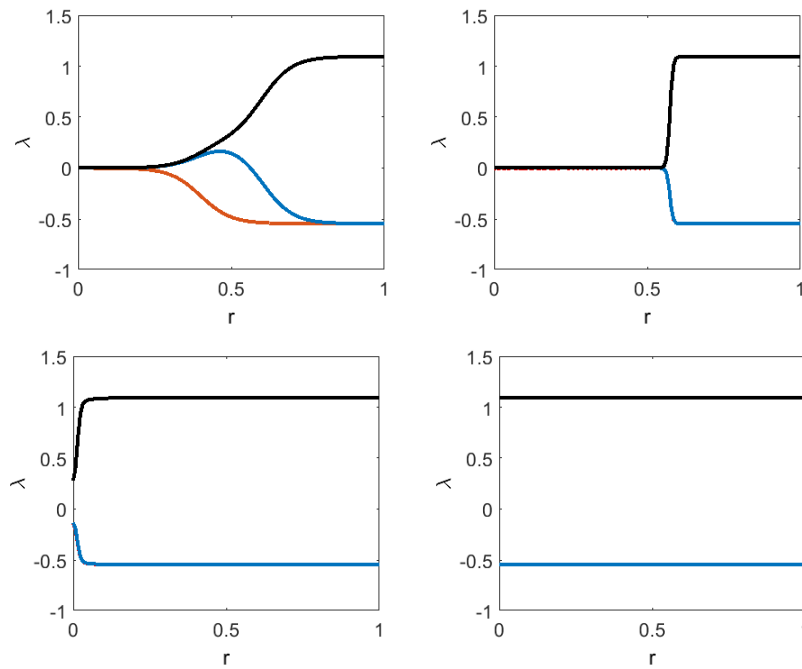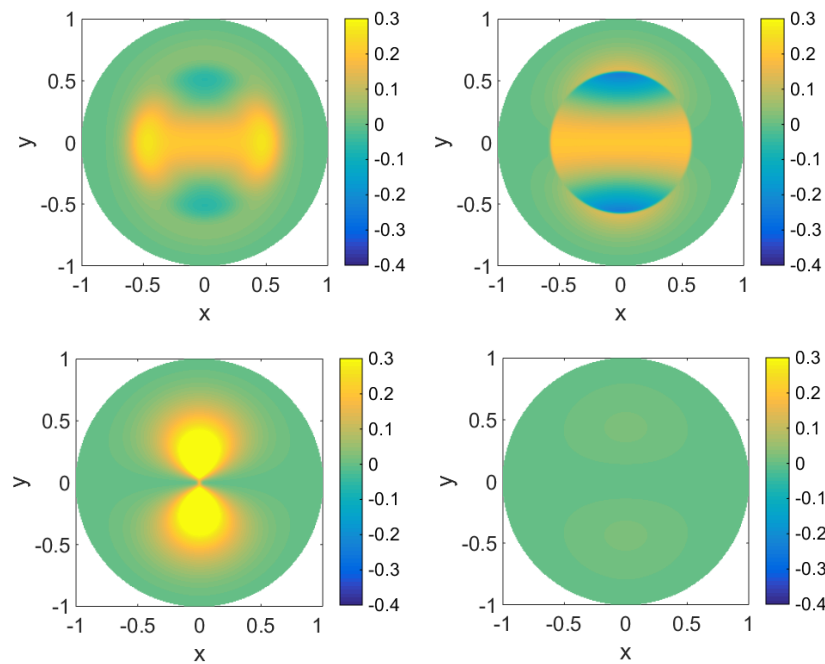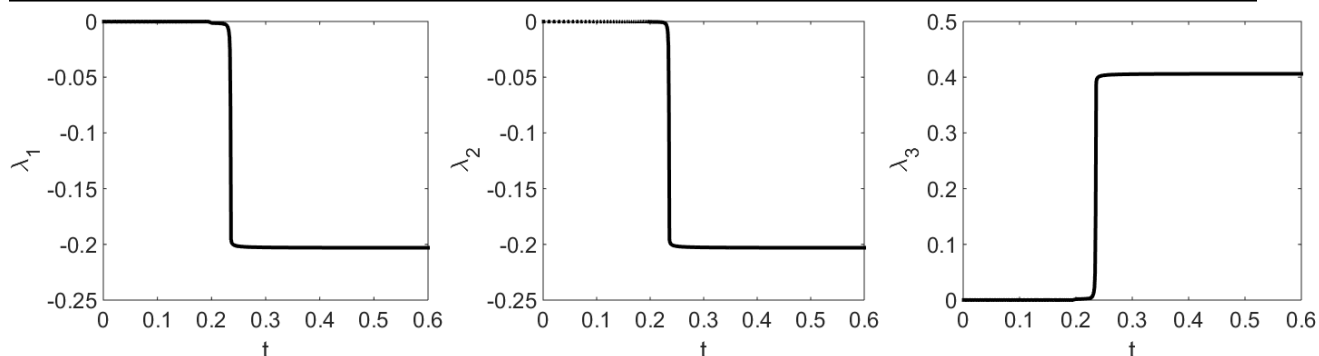
Figure 5-8: Time evolution of the eigenvalues of $\mathbf{Q}(0, t)$ for initial condition (5.13) with $\epsilon = 0.1$, $u_0 = 0.6$ and $v_0 = 0.4$.
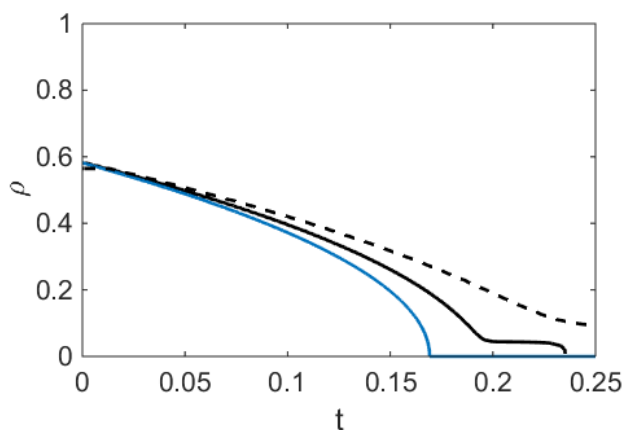
Figure 5-9: Front position ρ for initial condition (5.13) with $\epsilon = 0.1$, $u_0 = 0.6$ and $v_0 = 0.4$ for $\bar{L} = 3.5 \times 10^{-3}$ (dashed) and $L = 6.9 \times 10^{-4}$ (solid) and predicted position according to motion by mean curvature (blue). Initially, the front is arrested at an $O(\sqrt{L})$ distance away from the origin (before eventually collapsing). Here $\sqrt{L} = 5.92 \times 10^{-2}$ (dashed) and 2.62×10^{-2} (solid). Therefore as L decreases, interface evolution more closely resembles that according to mean curvature.

We also study how the initial non-planarity, as measured by ϵ, affects the relaxation time to $\mathbf{Q}_2$. We observe that the modulus $|\mathbf{Q}(0, t)|^2$ jumps abruptly from zero to $\frac{2}{3}$ at some critical time. Let t^* be the first time for which $|\mathbf{Q}(0, t^*)|^2 > \frac{1}{3}$. We define t^* as the time at which there is loss of front structure. Figure 5-10 shows t^* as a function of $-\log_{10} \epsilon$ for various u_0 and v_0. We find that $t^* \propto -\log_{10} \epsilon$. This may give some quantitative estimates for the real-time persistence of isotropic-nematic fronts and their experimental relevance for model problems with non-planar initial conditions.
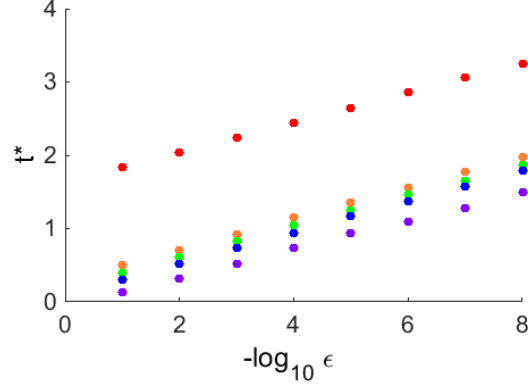
Figure 5-10: Time t^* at which there is a loss of front structure, for various ϵ with $v_0 = 1 - u_0$ and u_0: $u_0 = 0.1$ (purple), $u_0 = 0.4$ (blue), $u_0 = 0.5$ (green), $u_0 = 0.6$ (orange) and $u_0 = 0.9$ (red), for initial condition (5.13) and $\bar{L} = 3.5 \times 10^{-3}$. The spatial resolution is $\frac{1}{128}$.

5.4.1 Numerical simulations with biaxial boundary conditions

The Dirichlet conditions imposed so far in Chapter 5 are uniaxial minima of the bulk potential $f_B(\mathbf{Q})$ and are referred to as minimal boundary conditions. We now focus on dynamic solutions subject to a biaxial planar boundary condition at $r = 1$ given by

$$\mathbf{Q}_b = \mathbf{n}_1 \otimes \mathbf{n}_1 - \mathbf{m} \otimes \mathbf{m}, \tag{5.14}$$

and a planar biaxial initial condition of the form

$$\mathbf{Q}(\mathbf{r}, 0) = s\,(r, 0)\,(\mathbf{n}_1 \otimes \mathbf{n}_1 - \mathbf{m} \otimes \mathbf{m})\,, \tag{5.15}$$

where $s(r, 0)$ has a sharp front at $r_0 \in (0, 1)$ connecting $s = 0$ and $s = 1$. The boundary condition (5.14) is maximally biaxial (with one zero eigenvalue) and is not a minimum of the bulk potential $f_B(\mathbf{Q})$. Subject to such a boundary condition, we expect Landau-de Gennes energy minimizers to develop a boundary layer as $\bar{L} \to 0$ based on [103].

We study two-dimensional and three-dimensional dynamic solutions separately. A two-dimensional solution is a symmetric and traceless 2×2 matrix [70]. Such two-dimensional $\mathbf{Q}$-tensor matrices have $\text{tr}(\mathbf{Q}^3) = 0$ and the corresponding evolution law simplifies to

$$\mathbf{Q}_t = \nabla^2 \mathbf{Q} - \frac{1}{\bar{L}}(3\mathbf{Q} + 9|\mathbf{Q}|^2 \mathbf{Q}). \tag{5.16}$$

The simplest two-dimensional dynamic solution consistent with (5.14) is

$$\mathbf{Q}(\mathbf{r}, t) = s(r, t)\left(\mathbf{n}_1 \otimes \mathbf{n}_1 - \mathbf{m} \otimes \mathbf{m}\right). \tag{5.17}$$

The gradient flow model (5.16) admits a solution of this form provided the function $s(r, t)$ is a solution of

$$s_t = s_{rr} + \frac{s_r}{r} - \frac{4s}{r^2} - \frac{s}{L}\left(3 + 18s^2\right), \tag{5.18}$$

with fixed boundary conditions $s(0, t) = 0$ and $s(1, t) = 1$ for all $t \geq 0$. The equation (5.18) is the gradient flow model associated with the functional

$$I[s] = \int_0^1 \left[s_r^2 + \frac{4s^2}{r^2} + \frac{1}{L}\left(3s^2 + \frac{9}{4}s^4\right)\right] r \, dr.$$

The two-dimensional potential has a single minimum at $s = 0$ and hence the initial front in (5.15) will not be maintained for dynamic solutions of (5.16). Instead, a large interior isotropic core is expected to form with a sharp boundary layer to match the Dirichlet condition at $r = 1$. Next we study dynamic solutions of the full gradient flow system (2.6) subject to the Dirichlet boundary condition (5.14) and the planar initial condition (5.15) for three-dimensional $\mathbf{Q}$-tensors. Based on the analysis in the previous section, we expect all dynamic solutions to remain planar and for $\mathbf{Q}(\mathbf{r}, t)$ to have an isotropic core around $r = 0$, to converge to $\mathbf{Q}_1$ away from $r = 0$ and to have a boundary layer near $r = 1$ to match the Dirichlet condition. However, if r_0 is sufficiently close to 1, it is possible that three-dimensional solutions exhibit an outward growing isotropic core since the isotropic phase is also a minimizer of the bulk potential and this scenario may be energetically favourable compared to relaxation to $\mathbf{Q}_1$ in the interior.

There is a big difference in the behaviour of two-dimensional and three-dimensional solutions. The two-dimensional dynamic solutions are largely isotropic except near $r = 1$ and three-dimensional dynamic solutions are largely uniaxial (at least for a range of r_0) except near $r = 0$ and $r = 1$. We present numerical results to corroborate the heuristics above, beginning with a numerical study of the three-dimensional solutions.

We numerically solve the system (2.6) on the disc subject to the fixed boundary condition (5.14) on $r = 1$. All other parameter values are the same as in previous sections in this chapter with

$\bar{L} = 6.9 \times 10^{-4}$. The initial condition is given in (5.15) with

$$s(r, 0) = \frac{1}{2}\left[1 + \tanh\left(\frac{r - r_0}{\sqrt{\bar{L}}}\right)\right].$$

For $r_0 = 0.5$, the solution quickly becomes uniaxial in the interior and develops an inward propagating front separating the isotropic and nematic phases, see Figure 5-11. The solution converges to $\mathbf{Q}_1$, except for an isotropic core and a thin boundary layer near $r = 1$, as shown in Figure 5-12. Next we consider $r_0 = 0.92$ and observe a different behaviour. The interface evolves so there is a thin boundary layer near $r = 1$ with a large isotropic core in the interior as illustrated in Figure 5-13. We compare this three-dimensional behaviour with two-dimensional solutions for the system (5.16). Here the solution develops an almost entirely isotropic interior with a thin boundary layer near $r = 1$ as shown by the eigenvalue evolution in Figure 5-14. Hence our numerical simulations corroborate our previous analytic reasoning.
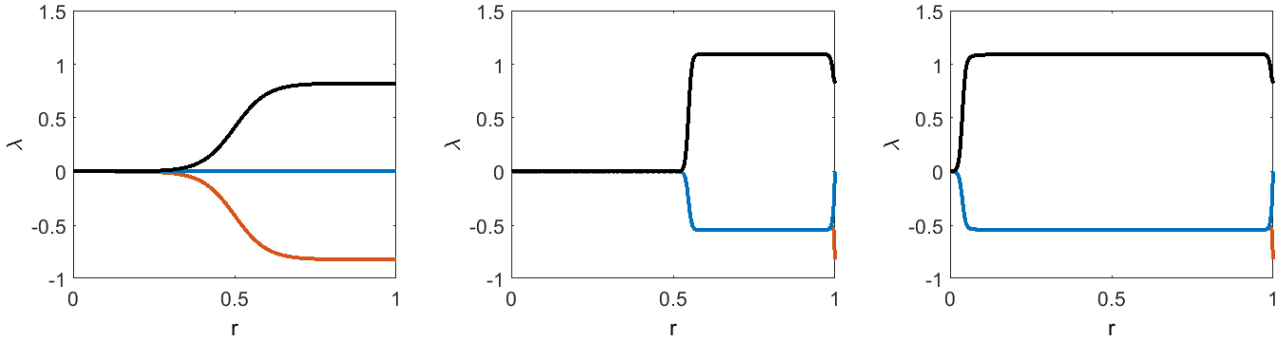
Figure 5-11: Radial profiles of the eigenvalues of the three-dimensional $\mathbf{Q}(\mathbf{r}, t)$ for initial condition (5.15) with $r_0 = 0.5$ at $t = 0$, $t = 0.001$ and $t = 0.25$. The spatial resolution is $h = \frac{1}{256}$.
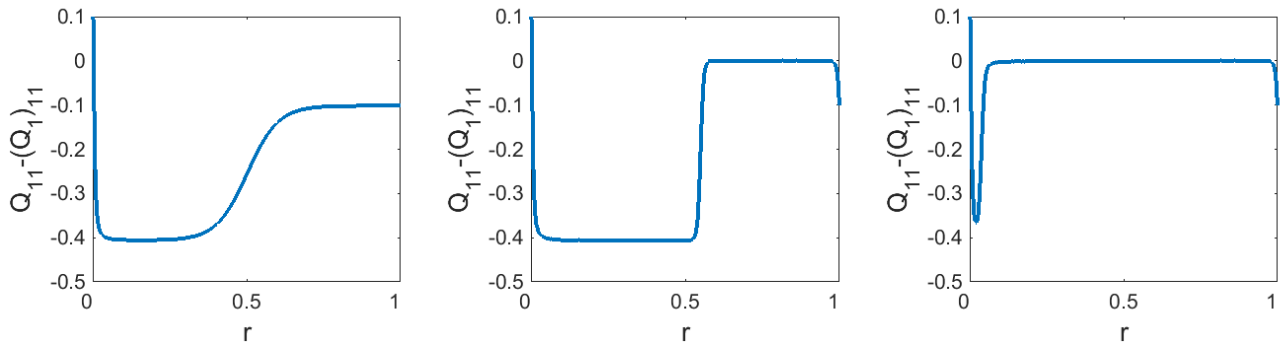
Figure 5-12: Radial profiles of $Q(\mathbf{r}, t)_{11} - (\mathbf{Q}_1)_{11}$ for initial condition (5.15) with $r_0 = 0.5$ at $t = 0$, $t = 0.001$ and $t = 0.25$.
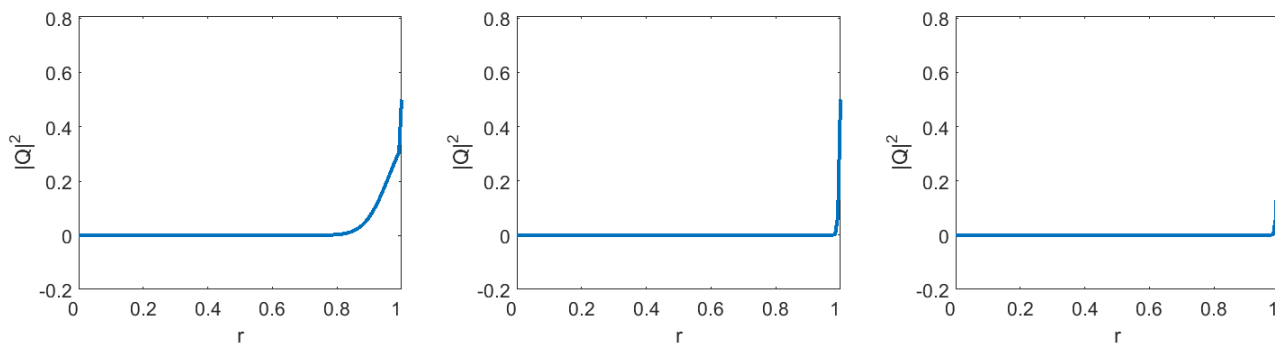
Figure 5-13: Radial profiles of $|\mathbf{Q}(\mathbf{r}, t)|^2$ for initial condition (5.15) with $r_0 = 0.92$ at $t = 0$, $t = 0.1$ and $t = 0.5$.
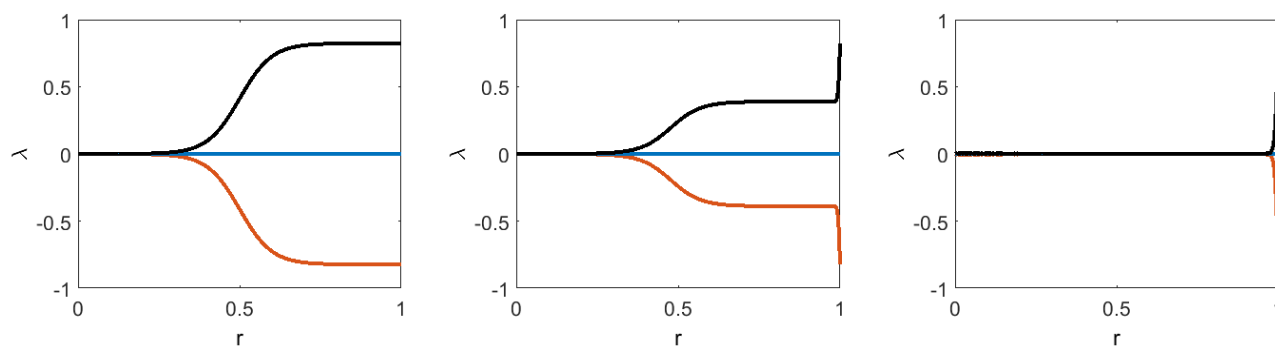
Figure 5-14: Radial profiles of the eigenvalues of the two-dimensional $\mathbf{Q}(\mathbf{r}, t)$ for initial condition (5.15) at $t = 0$, $t = 2 \times 10^{-5}$ and $t = 2 \times 10^{-4}$.

Overall, in this numerical section of Chapter 5, we have compared the affect of planar and non-planar initial conditions and minimal and non-minimal boundary conditions. In the three-dimensional setting with minimal boundary conditions, both planar and non-planar initial conditions result in an inwards propagating front. If the initial condition is non-planar the solution escapes to the third dimension and the front is lost. The front persists for a time proportional to $\log(\epsilon)$, where ϵ is a measure of the non-planarity of the initial condition, before collapsing. If the initial condition is planar the front is arrested at the origin and persists for all time. Non-minimal boundary conditions with planar initial conditions, in general, result in an inwards travelling front. However if the initial front position is close enough to $r = 1$ we observe a different behaviour: the front travels outwards, leaving a large isotropic core.

Equilibrium configurations on the square

In Chapter 6 we work on a truncated square of edge length λ and construct a Well Order Reconstruction-type critical point of the Landau-de Gennes energy inspired by the numerical work in Krajl and Majumdar 2014 [60]. This critical point has a uniaxial cross with negative scalar order parameter along the square diagonals and can be defined in terms of a critical point of a relevant scalar variational problem. We show that the Well Order Reconstruction solution is globally stable for small λ and undergoes a pitchfork bifurcation as λ becomes large. We numerically estimate the critical value of λ on a square and study the analogous problem on a hexagon.

6.1 Problem formulation

We begin by non-dimensionalizing the Landau-de Gennes energy functional using the change of variables $\bar{\mathbf{x}}_i = \frac{\mathbf{x}_i}{\lambda}$, where λ is the characteristic length scale of the domain Ω. This yields a rescaled energy given by

$$\bar{\mathbf{I}}_{LG}[\mathbf{Q}] = \int_{\overline{\Omega}} \frac{1}{2}|\overline{\nabla}\mathbf{Q}|^2 + \frac{\lambda^2}{L} f_B(\mathbf{Q}) \, \overline{\mathrm{d}A},$$

where $\overline{\Omega}$ is the rescaled domain, $\overline{\nabla}$ is the rescaled gradient and $\overline{\mathrm{d}A}$ is the rescaled area element. The associated Euler-Lagrange equations are given by

$$\overline{\nabla}^2\mathbf{Q} = \frac{\lambda^2}{L}\left[A\mathbf{Q} - B\left(\mathbf{Q}\mathbf{Q} - \frac{\mathbf{I}}{3}|\mathbf{Q}|^2\right) + C|\mathbf{Q}|^2\mathbf{Q}\right]. \tag{6.1}$$

In what follows we drop the bars and all statements are in terms of the rescaled variables. We take our domain to be a truncated square whose diagonals lie along the axes:

$$\Omega := \left\{(x, y) \in \mathbb{R}^2; |x| < 1 - \varepsilon, \ |y| < 1 - \varepsilon, \ |x + y| < 1, \ |x - y| < 1\right\}.$$

The boundary $\partial\Omega$ consists of four long edges $C_1 - C_4$ which are parallel to the lines $y = x$ and $y = -x$ and four short edges $S_1 - S_4$ of length 2ε which are parallel to the x and y axes, see Figure 6-1. The four long edges are labelled anticlockwise with C_1 in the first quadrant. The short edges are introduced to remove the sharp square vertices and are also labelled anticlockwise.
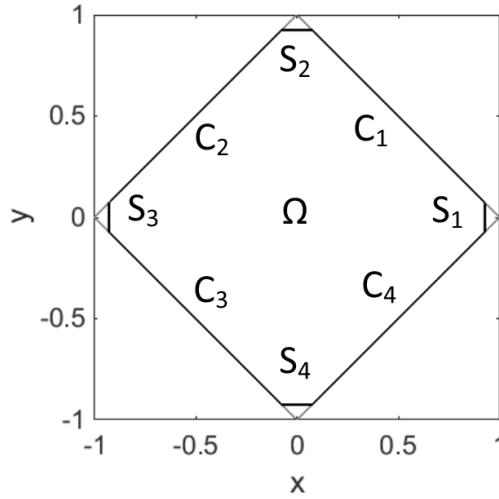
Figure 6-1: The truncated square Ω. The regular square is also plotted.

We work with Dirichlet boundary conditions on $\partial\Omega$. Following the literature on planar multistable nematic systems [107, 60], we impose tangent uniaxial Dirichlet conditions on the long edges. These conditions require the director to be tangent to the edge. To this end we fix $\mathbf{Q} = \mathbf{Q}_b$ on $C_1 - C_4$ where

$$\mathbf{Q}_b = \begin{cases} s_+ \left(\mathbf{n}_1 \otimes \mathbf{n}_1 - \frac{1}{3}\right) & \text{on} \quad C_1 \cup C_3, \\ s_+ \left(\mathbf{n}_2 \otimes \mathbf{n}_2 - \frac{1}{3}\right) & \text{on} \quad C_2 \cup C_4, \end{cases} \tag{6.2}$$

for $\mathbf{n}_1 = \frac{1}{\sqrt{2}}(-1, 1, 0)$ and $\mathbf{n}_2 = \frac{1}{\sqrt{2}}(1, 1, 0)$. Note that the bulk potential is minimized on $C_1 - C_4$ by these boundary conditions. We impose Dirichlet conditions on the short edges too but these conditions are for mathematical convenience. The Dirichlet conditions on the short edges are chosen to mediate between the boundary conditions on the long edges. One way this can be achieved is to define the boundary conditions on the short edges in terms of a function given by

$$g(s) = \frac{s_+}{2} \left(e^{-\mu\varepsilon} \frac{e^{\mu s} - e^{-\mu s}}{e^{\mu\varepsilon} - e^{-\mu\varepsilon}} - e^{-\mu s} + 1 \right) \quad \text{for} \quad 0 < s < \varepsilon \quad \text{where} \quad \mu = \frac{\lambda B}{(CL)^{1/2}}.$$

Further, $g(s) = \frac{s_+}{2}$ for $s > \epsilon$ and $g(s) = -g(-s)$ for $s < 0$. We fix $\mathbf{Q} = \mathbf{Q}_b$ on $S_1 - S_4$ where

$$\mathbf{Q}_b = \begin{cases} g(y)\left(\mathbf{n}_1 \otimes \mathbf{n}_1 - \mathbf{n}_2 \otimes \mathbf{n}_2\right) - \frac{s_+}{6}\left(2\hat{\mathbf{z}} \otimes \hat{\mathbf{z}} - \mathbf{n}_1 \otimes \mathbf{n}_1 - \mathbf{n}_2 \otimes \mathbf{n}_2\right) & \text{on} \quad S_1 \cup S_3, \\ g(x)\left(\mathbf{n}_1 \otimes \mathbf{n}_1 - \mathbf{n}_2 \otimes \mathbf{n}_2\right) - \frac{s_+}{6}\left(2\hat{\mathbf{z}} \otimes \hat{\mathbf{z}} - \mathbf{n}_1 \otimes \mathbf{n}_1 - \mathbf{n}_2 \otimes \mathbf{n}_2\right) & \text{on} \quad S_2 \cup S_4. \end{cases} \tag{6.3}$$

Given the Dirichlet conditions (6.2) and (6.3), we define our admissible space to be

$$\mathcal{A} := \left\{ \mathbf{Q} \in W^{1,2}\left(\Omega, S_0\right) : \mathbf{Q} = \mathbf{Q}_b \quad \text{on} \quad \partial\Omega \right\}.$$

It is possible to prove the existence of a global minimizer of the rescaled functional in the admissible space $\mathcal{A}$, for all $A < 0$ and for all values of $\lambda > 0$. This follows from the direct methods in the calculus of variations which are discussed in Appendix A.

6.2 Analysis of a scalar variational problem

The Well Order Reconstruction solution (WORS) was first reported numerically in [60] where the authors observe the WORS solution for small λ. The corresponding $\mathbf{Q}$-tensor is a critical point of the rescaled Landau-de Gennes energy on the square with two key properties:

(1) it has a constant eigenframe with one eigenvector given by $\hat{\mathbf{z}}$, the unit vector in the z-direction.

(2) it has a uniaxial cross with negative scalar order parameter along the square diagonals.

To this end, we look for critical points of the rescaled functional of the form

$$\mathbf{Q}(x, y) = q_1(x, y)\left(\mathbf{n}_1 \otimes \mathbf{n}_1 - \mathbf{n}_2 \otimes \mathbf{n}_2\right) + q_2(x, y)\left(\mathbf{n}_1 \otimes \mathbf{n}_2 + \mathbf{n}_2 \otimes \mathbf{n}_1\right) \tag{6.4}$$
$$+ q_3(x, y)(2\hat{\mathbf{z}} \otimes \hat{\mathbf{z}} - \mathbf{n}_1 \otimes \mathbf{n}_1 - \mathbf{n}_2 \otimes \mathbf{n}_2),$$

subject to the boundary conditions

$$q_1(x, y) = \begin{cases} s_+/2 & \text{on} \quad C_1 \cup C_3, \\ -s_+/2 & \text{on} \quad C_2 \cup C_4, \end{cases} \quad \text{and} \quad q_1(x, y) = \begin{cases} g(y) & \text{on} \quad S_1 \cup S_3, \\ g(x) & \text{on} \quad S_2 \cup S_4, \end{cases} \tag{6.5}$$
$$q_2 = 0 \quad \text{and} \quad q_3 = -\frac{s_+}{6} \quad \text{on} \quad \partial\Omega.$$

The **Q**-tensor in (6.4) can be written explicitly as

$$
\begin{pmatrix}
-q_2(x,y) - q_3(x,y) & -q_1(x,y) & 0 \\
-q_1(x,y) & q_2(x,y) - q_3(x,y) & 0 \\
0 & 0 & 2q_3(x,y)
\end{pmatrix}.
$$

Critical points of the form (6.4) mimic the WORS if $q_2 = 0$ everywhere, which ensures a constant eigenframe with $\hat{\mathbf{z}}$ as an eigenvector, and $q_1 = 0$ along the square diagonals, so that $\mathbf{Q} = 3q_3(x,y)\left(\hat{\mathbf{z}} \otimes \hat{\mathbf{z}} - \frac{1}{3}\right)$ on $x = 0$ and $y = 0$ to give a uniaxial cross. We begin with a result on the existence of such critical points.

Proposition 6.1. *The Landau-de Gennes Euler-Lagrange equations* (6.1) *admit a solution of the form* (6.4) *on the truncated square* Ω *subject to the Dirichlet conditions* (6.2) *and* (6.3), *provided the functions q_1, q_2, q_3 satisfy*

$$
\nabla^2 q_1 = \frac{\lambda^2}{L}\left[Aq_1 + 2Bq_1 q_3 + C\left(2q_1^2 + 2q_2^2 + 6q_3^2\right)q_1\right],
$$

$$
\nabla^2 q_2 = \frac{\lambda^2}{L}\left[Aq_2 + 2Bq_2 q_3 + C\left(2q_1^2 + 2q_2^2 + 6q_3^2\right)q_2\right], \tag{6.6}
$$

$$
\nabla^2 q_3 = \frac{\lambda^2}{L}\left[Aq_3 + B\left(\frac{1}{3}\left(q_1^2 + q_2^2\right) - q_3^2\right) + C\left(2q_1^2 + 2q_2^2 + 6q_3^2\right)q_3\right],
$$

and the boundary conditions in (6.5).

Proof. Consider the energy functional $J[q_1, q_2, q_3]$ given by

$$
J[q_1, q_2, q_3] = \int_\Omega |\nabla q_1|^2 + |\nabla q_2|^2 + 3|\nabla q_3|^2 \tag{6.7}
$$

$$
+ \frac{\lambda^2}{L}\left[A\left(q_1^2 + q_2^2 + 3q_3^2\right) + C\left(q_1^2 + q_2^2 + 3q_3^2\right)^2 + 2Bq_3\left(q_1^2 + q_2^2\right) - 2Bq_3^3\right]\,dA.
$$

The existence of a global minimizer of the functional J among the triplets $(q_1, q_2, q_3) \in W^{1,2}(\Omega, \mathbb{R}^3)$ satisfying the boundary conditions (6.5) follows from the direct methods in the calculus of variations (see Appendix A). The system of partial differential equations in (6.6) are the Euler-Lagrange equations associated with J and hence the globally minimizing (q_1, q_2, q_3) are classical solutions of this system. From the solutions of the system (6.6), we can check that the corresponding tensor in (6.4) is an exact solution of the Landau-de Gennes Euler-Lagrange equations by direct substitution. $\square$

We can check that there is a branch of solutions $(q_1, 0, q_3)$ of the system (6.6) for all $\lambda > 0$ and all $A < 0$. This solution branch has a constant eigenframe, however other properties are required to mimic the WORS. To this end, we focus on a special temperature $A = -\frac{B^2}{3C}$ for which $s_+ = \frac{B}{C}$. Here the system (6.6) admits a branch of solutions $(q_1, q_2, q_3) = (q(x, y), 0, -\frac{B}{6C})$ consistent with the Dirichlet conditions (6.5) for all $\lambda > 0$. It is easier to analyse solutions with just one variable, so we work at this temperature for the remainder of the chapter.

Proposition 6.2. *For $A = -\frac{B^2}{3C}$ and for all $\lambda > 0$, there exists a branch of solutions of the system (6.6) given by*

$$(q_1, 0, q_3) = \left(q_{\min}(x, y), 0, -\frac{B}{6C} \right), \tag{6.8}$$

consistent with the Dirichlet conditions (6.5). This branch is defined by a minimizer $q_{\min}$ of the energy

$$H[q_1] = \int_\Omega |\nabla q_1|^2 + \frac{\lambda^2}{L} \left(C q_1^4 - \frac{B^2}{2C} q_1^2 \right) \, dA, \tag{6.9}$$

subject to boundary conditions (6.5). The minimizer q_{min} is hence a classical solution of

$$\nabla^2 q = \frac{\lambda^2}{L} \left(2C q^3 - \frac{B^2}{2C} q \right). \tag{6.10}$$

(This is the first equation in (6.6) with $q_2 = 0$ and $q_3 = -\frac{B}{6C}$.) Further, we have the bounds

$$-\frac{B}{2C} \leq q_{\min} \leq \frac{B}{2C}. \tag{6.11}$$

Proof. If q is a solution of the partial differential equation (6.10) subject to the Dirichlet conditions (6.5), it follows that the solution branch defined by (6.8) is a solution of the system (6.6) at $A = -\frac{B^2}{3C}$ for all $\lambda > 0$.

Let $q_{\min}$ be a minimizer of H in the admissible space $\mathcal{A}_q := \{q \in W^{1,2}(\Omega) \colon q \text{ satisfies (6.5) on } \partial\Omega\}$. The existence of such a minimizer follows from the direct methods in the calculus of variations. Then $q_{\min}$ is a classical solution of the associated Euler-Lagrange equation (6.10) subject to the boundary conditions (6.5). This gives that the triplet $(q_1, q_2, q_3) = (q_{\min}, 0, -\frac{B}{6C})$ is a solution of the system (6.6) and yields a critical point of the Landau-de Gennes Euler-Lagrange equations.

The bounds (6.11) follow from the maximum principle and the Dirichlet conditions.   □

Lemma 6.1. *There exists $\lambda_0 > 0$ such that for any $\lambda < \lambda_0$, the solution branch defined by $(q_1, q_2, q_3) = (q_{\min}, 0, -\frac{B}{6C})$ in Proposition 6.2 is the unique minimizer of the Landau-de Gennes energy.*

Proof. The proof follows from a uniqueness result for critical points of the Landau-de Gennes energy in [62]. By the maximum principle, a critical point $\mathbf{Q}_c$ of the Landau-de Gennes Euler-Lagrange equations is bounded with $|\mathbf{Q}_c| \leq M$ for some M independent of λ and L [76]. From [62], the Landau-de Gennes energy is strictly convex on the set $\{\mathbf{Q} \in W^{1,2}(\Omega, S_0): |\mathbf{Q}| \leq M\}$ for sufficiently small λ. As a result, for $\frac{\lambda^2}{L} < \lambda_1$ where the constant λ_1 depends on the domain, temperature and material constants, the rescaled Landau-de Gennes energy has a unique critical point. For $A = -\frac{B^2}{3C}$, the triplet $(q_1, q_2, q_3) = (q_{\min}, 0, -\frac{B}{6C})$ introduced in Proposition 6.2 defines a critical point for all $\lambda > 0$. Therefore, the strict convexity of the Landau-de Gennes energy on the set of bounded $\mathbf{Q}$-tensors for small λ and fixed L, gives that this must be the unique Landau-de Gennes critical point and hence the Landau-de Gennes global minimizer for sufficiently small λ. $\qquad\square$

Lemma 6.2. *The function $q_{\min}$ defined in Proposition 6.2 vanishes along the square diagonals defined by $x = 0$ and $y = 0$ provided that $\lambda < \lambda_0$ where λ_0 is as introduced in Lemma 6.1.*

Proof. Note that if $q(x, y)$ is a solution of (6.10) subject to (6.5) then so are the functions $q(-x, -y)$, $-q(-x, y)$ and $-q(x, -y)$. We combine this symmetry with the uniqueness result for $\lambda < \lambda_0$ in Lemma 6.1 to get the desired result. For example, $q(x, y) = -q(-x, y)$ along $x = 0$ gives that $q(0, y) = 0$ and the analogous argument shows $q(x, 0) = 0$. $\qquad\square$

From Lemmas 6.1 and 6.2, we deduce that there is a unique Landau-de Gennes critical point of the form

$$\mathbf{Q}_{\min}(x, y) = q_{\min}(x, y)\left(\mathbf{n}_1 \otimes \mathbf{n}_1 - \mathbf{n}_2 \otimes \mathbf{n}_2\right) - \frac{B}{6C}\left(2\hat{\mathbf{z}} \otimes \hat{\mathbf{z}} - \mathbf{n}_1 \otimes \mathbf{n}_1 - \mathbf{n}_2 \otimes \mathbf{n}_2\right), \quad (6.12)$$

for sufficiently small λ, where $q_{\min}$ is a global minimizer of the functional H in (6.9). This critical point has a constant eigenframe with a uniaxial cross of negative scalar order parameter along the square diagonals and hence mimics the Well Order Reconstruction solution. However, in the next proposition we show that global minimizers of H do not satisfy the property $q_{\min} = 0$ on the coordinate axes for large λ.

For the following proposition we define the quantity Per_Ω to be the Ω-perimeter. For any set E, the Ω-perimeter $\mathrm{Per}_\Omega(E)$ is given by

$$\mathrm{Per}_\Omega(E) := \sup\left\{ \int_E \nabla \cdot \varphi \, dA : \varphi \in C_0^1(\Omega; \mathbb{R}^2), \ |\varphi| \le 1 \text{ on } \Omega \right\}.$$

If E has a smooth boundary, then $\mathrm{Per}_\Omega(E)$ is given by the length of $\partial E \cap \Omega$ by the Divergence Theorem. Let $\mathcal{B}$ denote the set of functions q on Ω that only take the values $\frac{B}{2C}$ and $-\frac{B}{2C}$ and are such that $\mathrm{Per}_\Omega\{q = -\frac{B}{2C}\} < \infty$.

Proposition 6.3. *For $\lambda > 0$, let $q_{\min,\lambda}$ be a minimizer of H. Then there exists a subsequence $\lambda_j \to +\infty$ and a function $q_\infty \in L^1(\Omega)$ such that $q_{\min,\lambda_j} \to q_\infty$ in $L^1(\Omega)$ almost everywhere. Further, q_∞ is a minimizer of the functional $J \colon L^1(\Omega) \to (-\infty, +\infty]$ given by*

$$J[q] = k \, \mathrm{Per}_\Omega\left\{ q = -\frac{B}{2C} \right\} + \int_{\partial\Omega} \phi(q_b(\mathbf{x}), q(\mathbf{x})) \, ds, \tag{6.13}$$

if $q \in \mathcal{B}$ and by $J[q] = +\infty$ otherwise. In the above,

$$\phi(s, t) = 2\sqrt{\frac{C}{L}} \left| \int_s^t \left(\frac{B^2}{4C^2} - \tau^2 \right) d\tau \right| = 2\sqrt{\frac{C}{L}} \left| \frac{1}{3}(s^3 - t^3) - \frac{B^2}{4C^2}(s - t) \right|, \tag{6.14}$$

$$k = \phi\left(-\frac{B}{2C}, \frac{B}{2C} \right) = \frac{B^3}{3C^3}\sqrt{\frac{C}{L}}. \tag{6.15}$$

In (6.13), q_b is the boundary data defined by (6.5) and $q(\mathbf{x})$ for $\mathbf{x} \in \partial\Omega$ is the trace of q at the point $\mathbf{x}$ (see Appendix A).

Proof. For $\lambda > 0$, consider the functional $J_\lambda \colon L^1(\Omega) \to (-\infty, +\infty]$ given by

$$J_\lambda[q] = \frac{1}{\lambda} H[q] + \frac{\lambda B^4}{16 C^3 L} = \int_\Omega \frac{1}{\lambda}|\nabla q|^2 + \frac{\lambda C}{L}\left(q^2 - \frac{B^2}{4C^2} \right)^2 dA,$$

if $q \in W^{1,2}(\Omega)$ satisfies the boundary condition (6.5) and by $J_\lambda[q] = +\infty$ otherwise. A function q minimizes J_λ if and only if it minimizes H. The result follows from the fact that the functional J_λ Γ-converges to J as $\lambda \to +\infty$ in $L^1(\Omega)$ by [11, Theorem 7.10] and this gives the convergence of minimizers $q_{\min,\lambda_j} \to q_\infty$ for a subsequence $\lambda_j \to \infty$ by [11, Theorem 7.3] and [11, Theorem 7.11]. $\square$

The implications of Proposition 6.3 are as follows. Suppose that for any $\lambda > 0$, the minimizer $q_{\min,\lambda}$ mimics the WORS. That is, $q_{\min,\lambda}(x, y) = 0$ on the coordinate axes, $q_{\min,\lambda} > 0$ on the first

and third quadrant and $q_{\min,\lambda} < 0$ on the second and fourth quadrant. Then the limit function q_∞ would be given by

$$q_\infty(x, y) = \begin{cases} \frac{B}{2C} & \text{if} \quad xy > 0, \\ -\frac{B}{2C} & \text{if} \quad xy < 0, \end{cases}$$

with sharp fronts on the square diagonals. Therefore

$$J[q_\infty] \geq k \mathrm{Per}_\Omega \left\{ q_\infty = -\frac{B}{2C} \right\} = 4k(1 - \varepsilon). \tag{6.16}$$

We now consider the constant function $q = \frac{B}{2C}$, which does not match the Dirichlet boundary condition (6.5). However, we are still able to compute $J\left[\frac{B}{2C}\right]$ and compare this function to q_∞. Using the boundary condition (6.5) and the definitions of ϕ and k, we have

$$\begin{aligned} J\left[\frac{B}{2C}\right] &= \int_{C_2 \cup C_4} \phi\left(q_b(\mathbf{x}), \frac{B}{2C}\right) \mathrm{d}s \\ &= k \, \mathrm{Length}\left(C_2 \cup C_4\right) + 4 \int_{-\varepsilon}^{\varepsilon} \phi\left(g(s), \frac{B}{2C}\right) \mathrm{d}s \\ &\leq 2\sqrt{2}k(1 - \varepsilon) + 8k\varepsilon. \end{aligned} \tag{6.17}$$

For ϵ sufficiently small, equations (6.16) and (6.17) give that $J[q_\infty] > J[\frac{B}{2C}]$ which contradicts the minimality of q_∞. Therefore, we can conclude that the minimizers $q_{\min,\lambda}$ of H do not vanish on the coordinate axes for large λ. As a consequence, Landau-de Gennes critical points of the form (6.12) mimic the Well Order Reconstruction solution for small λ only.

6.3 Analysis of the Well Order Reconstruction solution

In this section we study the following aspects of the WORS. Firstly, we study the existence of the WORS for all λ. In particular, we discuss whether it is possible to give a description of the form in (6.12) with an interpretation of q as a critical point, but not a minimizer, of the functional H in (6.9). Secondly, we consider how the stability of the WORS depends on the square size λ.

Again, inspired by [60], we construct WORS-type critical points of the form (6.12) such that $q = 0$ on the square diagonals. This implies that the corresponding $\mathbf{Q}$-tensor has a constant eigenframe and is uniaxial with negative order parameter on the coordinate axes. We define the corresponding q in terms of the critical point q_s of the functional H in (6.9). This definition of q_s is analogous to the saddle solutions of the bistable Allen-Cahn equation studied in [30, 99]. We

normalize the Euler-Lagrange equations associated with H (as in (6.10)), letting $\bar{q} = \frac{2C}{B}q$ which yields

$$\begin{cases} -\nabla^2 \bar{q} + \frac{\lambda^2}{\bar{L}} f(\bar{q}) = 0 & \text{on} \quad \Omega, \\ \bar{q} = \bar{q}_{bd} & \text{on} \quad \partial\Omega, \end{cases} \tag{AC}$$

for $f(\bar{q}) = \bar{q}(\bar{q} - 1)(\bar{q} + 1)$ and $\bar{L} = \frac{2C}{B^2}L$. The boundary condition $\bar{q}_{bd}$ is related to q_{bd} in (6.5) by the change of variables described above. In what follows we drop the bar from the variable q. For a fixed $\lambda > 0$, we define a *Well Order Reconstruction solution*, or *saddle solution*, to be a classical solution $q_s \in C^2(\Omega) \cap C(\overline{\Omega})$ of Problem (AC) which satisfies

$$xy\, q_s(x, y) \geq 0 \quad \text{for} \quad (x, y) \in \Omega. \tag{6.18}$$

That is, q_s is non-negative on the first and third quadrants, non-positive on the second and fourth quadrants and vanishes on the coordinate axes. In the next two lemmas we prove the existence and uniqueness of q_s.

Lemma 6.3. *There exists a Well Order Reconstruction solution q_s for Problem* (AC) *for any* $\lambda > 0$. *Further, we have the bounds* $-1 \leq q_s \leq 1$.

Proof. Define Q to be the truncated quadrant

$$Q := \{(x, y) \in \Omega : x > 0, y > 0\}.$$

We impose the boundary conditions $q = q_{bd}$ on $\partial Q \cap \partial\Omega$ and $q = 0$ on $\partial Q \setminus \partial\Omega$. This boundary data is continuous because $q_{bd} = 0$ at the points where $\partial\Omega$ intersects the coordinate axes. The boundary data is also piecewise C^1. Therefore there exist functions $q \in W^{1,2}(Q)$ which satisfy the boundary conditions in the trace sense. This allows us to find a global minimizer $q_s \in W^{1,2}(Q)$ of H over Q by the direct methods in the calculus of variations. We note that $H[q_s] = H[|q_s|]$ and $q_s = q_{bd} > 0$ on $\partial Q \cap \partial\Omega$. Hence $q_s \geq 0$ almost everywhere on Q. We define a function on Ω by the odd reflection of q_s about the coordinate axes. This new function, which we still denote by q_s, satisfies (6.18) and is a weak solution of (AC) on $\Omega \setminus \{0\}$. The function q_s has bounded gradient for fixed λ so $|\nabla q_s| \leq C$ for some constant C. This allows us to use the arguments in [30, Theorem 3] to show that q_s is a classical solution of (AC) on Ω, including the origin, for fixed λ. By elliptic regularity on convex polygons, we can conclude that $q_s \in C^2(\Omega) \cap C(\overline{\Omega})$ (see Appendix A) [53]. Therefore q_s is a classical solution of the boundary value problem (AC).

The bounds on q_s follow from the maximum principle and the Dirichlet boundary conditions. $\qquad\square$

Lemma 6.4. *For all $\lambda > 0$, there is at most one non-negative solution $q \in C^2(Q) \cap C(\overline{Q})$ to the problem*

$$\begin{cases} -\nabla^2 q + \frac{\lambda^2}{L} f(q) = 0 & \text{on} \quad Q, \\ q = \bar{q}_{\text{bd}} & \text{on} \quad \partial Q \cap \partial \Omega, \\ q = 0 & \text{on} \quad \partial Q \setminus \partial \Omega. \end{cases} \tag{AC$'$}$$

Then there is a unique Well Order Reconstruction solution q_s defined in terms of q.

Proof. The proof follows the steps in [30]. Consider two non-negative solutions q_1, q_2 to (AC$'$). Then $q := \max\{q_1, q_2\}$ is a weak subsolution of (AC$'$) and so

$$\int_Q \nabla q \cdot \nabla \varphi + \frac{\lambda^2}{L} f(q) \varphi \, dA \leq 0 \quad \text{for} \quad \text{any} \quad \phi \in W_0^{1,2}(Q) \quad \text{such} \quad \text{that} \quad \phi \geq 0,$$

$$q \leq \bar{q}_b \quad \text{on} \quad \partial Q \cap \partial \Omega \quad \text{and} \quad q \leq 0 \quad \text{on} \quad \partial Q \setminus \partial \Omega.$$

From the proof of Lemma 6.3, $0 \leq q \leq 1$ as these bounds hold for both q_1 and q_2. Therefore the constant 1 is a supersolution of (AC$'$). By the classical sub and supersolution method there exists a solution p of (AC$'$) such that $q \leq p \leq 1$ and $0 \leq q_1 \leq p$ on Q [40]. We multiply the equation for p with q_1, multiply the equation for q_1 with p, integrate by parts and take the difference to obtain

$$\frac{\lambda^2}{L} \int_Q f(p) q_1 - f(q_1) p \, dA = \int_{\partial Q} \frac{\partial p}{\partial \mathbf{n}} q_1 - \frac{\partial q_1}{\partial \mathbf{n}} p \, ds,$$

where $\mathbf{n}$ is the outward normal to ∂Q. Recalling the definition of f and the boundary conditions we have

$$\frac{\lambda^2}{L} \int_Q q_1 p \left(p^2 - q_1^2\right) \, dA = \int_{\partial Q} \bar{q}_b \left(\frac{\partial p}{\partial \mathbf{n}} - \frac{\partial q_1}{\partial \mathbf{n}}\right) \, ds. \tag{6.19}$$

The left-hand side is non-negative and the right-hand side is non-positive because $0 \leq q_1 \leq p$ on Q and $p = q_1$ on ∂Q. Therefore both sides of (6.19) must vanish. Further, by applying the strong maximum principle to Problem (AC$'$) we deduce that $q_1 > 0$ in the interior of Q which yields $p > 0$ in the interior of Q as well. This implies that $q_1 = p$ and hence $q \leq q_1$ on Q (as $q \leq p$). Therefore, we can conclude that $q_1 > q_2$ on Q. By the symmetric argument we obtain $q_1 < q_2$ on Q and the result follows.

We can repeat these arguments on the remaining three quadrants to deduce that the Well Order Reconstruction solution is unique on Ω. $\qquad\square$

We now define a Well Order Reconstruction Landau-de Gennes critical point on Ω subject to the Dirichlet boundary conditions (6.2)-(6.3) and at the fixed temperature $A = -\frac{B^2}{3C}$ by

$$\mathbf{Q}_s(x, y) = q_s(x, y)\left(\mathbf{n}_1 \otimes \mathbf{n}_1 - \mathbf{n}_2 \otimes \mathbf{n}_2\right) - \frac{1}{3}\left(2\hat{\mathbf{z}} \otimes \hat{\mathbf{z}} - \mathbf{n}_1 \otimes \mathbf{n}_1 - \mathbf{n}_2 \otimes \mathbf{n}_2\right).$$

From the previous propositions, the critical point $\mathbf{Q}_s$ exists for all λ and is the unique Landau-de Gennes critical point and globally stable for sufficiently small λ. Next we consider the stability of the Well Order Reconstruction Landau-de Gennes critical point. We study the stability of $\mathbf{Q}_s$ in terms of the stability of q_s as a critical point of the functional H defined in Proposition 6.2. We write $q_{s,\lambda}$ and H_λ to emphasize the dependence on λ.

Theorem 6.1. *There exists a unique value $\lambda_c > 0$ such that there is a pitchfork bifurcation at $(\lambda_c, q_{s,\lambda_c})$. That is, there exist positive numbers ε, δ and two smooth maps*

$$t \in (-\delta, \delta) \mapsto \lambda(t) \in (\lambda_c - \varepsilon, \lambda_c + \varepsilon) \quad \text{and} \quad t \in (-\delta, \delta) \mapsto h(t) \in W_0^{1,2}(\Omega),$$

such that all the pairs $(\lambda, q) \in \mathbb{R}^+ \times W^{1,2}(\Omega)$ satisfying

$$q \text{ is a solution of (AC)},$$
$$|\lambda - \lambda_c| \leq \varepsilon \quad \text{and}$$
$$\|q - q_{s,\lambda_c}\|_{W^{1,2}(\Omega)} \leq \varepsilon,$$

are either

$$(\lambda, q) = (\lambda, q_s) \quad \text{or} \quad (\lambda, q) = (\lambda(t), q_{s,\lambda(t)} + t\eta_{\lambda_c} + t^2 h(t)).$$

Here $\eta_{\lambda_c} \in W_0^{1,2}(\Omega)$ is an eigenfunction corresponding to the loss of stability at λ_c. That is, $\eta_{\lambda_c} \neq 0$ is a solution of

$$\nabla^2 \eta_{\lambda_c} = \frac{\lambda_c^2}{\bar{L}}\left(3q_{s,\lambda_c}^2 - 1\right)\eta_{\lambda_c} \quad \text{on} \quad \Omega.$$

Therefore, for fixed B, C, $\bar{L} > 0$, $q_{s,\lambda}$ exists as a critical point of the functional H defined in Proposition (6.2) for all $\lambda > 0$ and loses stability for $\lambda > \lambda_c$.

Proof. The proof follows the same strategy as [62, Theorem 5.2]. First, we define the admissible space to be

$$X := \left\{q \in W^{1,2}(\Omega) \colon q = \bar{q}_b \text{ on } \partial\Omega\right\}.$$

We also define the space Y to be

$$Y := \{q \in X : xy\, q(x, y) \geq 0 \quad \text{for} \quad (x, y) \in \Omega\}.$$

Every function in Y vanishes along the square diagonals of Ω. Lemma 6.4 implies that $q_{s,\lambda}$ is the only solution of (AC) that belongs to Y. The stability of $q_{s,\lambda}$ is measured by the quantity

$$\mu(\lambda) = \inf_{\eta \in W_0^{1,2}(\Omega) \setminus \{0\}} \frac{\delta^2 H_\lambda[\eta]}{\int_\Omega \eta^2}, \tag{6.20}$$

where $\delta^2 H_\lambda$ is the second variation of H_λ at $q_{s,\lambda}$ and given by

$$\delta^2 H_\lambda[\eta] = \int_\Omega |\nabla \eta|^2 + \frac{\lambda^2}{L} \left(3q_{s,\lambda}^2 - 1\right) \eta^2 \, dA. \tag{6.21}$$

The proof of the result requires the following lemmas:

Lemma A The map $(0, +\infty) \to \mathbb{R}$ defined by $\lambda \mapsto \mu(\lambda)$ is smooth and $\mu'(\lambda) < 0$ for any $\lambda > 0$.

Lemma B There exists a positive number λ^* such that $\mu(\lambda) < 0$ for any $\lambda \geq \lambda^*$.

From the stability of the Well Order Reconstruction solution in Lemma 6.1 we know that $\mu(\lambda) > 0$ for $0 < \lambda \ll 1$. Combining this with Lemma A and Lemma B, we find a unique $\lambda_c > 0$ such that $\mu(\lambda_c) = 0$. To show that a pitchfork bifurcation arises at $\lambda = \lambda_c$ we apply the Crandall-Rabinowitz bifurcation theorem to the map

$$\mathcal{F}(\lambda, h) = -\nabla^2(q_{s,\lambda} + h) + \frac{\lambda^2}{L} f(q_{s,\lambda} + h),$$

for $(\lambda, h) \in \mathbb{R}^+ \times W_0^{1,2}(\Omega)$.

Theorem 6.2 (Crandell-Rabinowitz bifurcation theorem, [28]). *Let X, Y be Banach spaces, V be a neighbourhood of 0 in X and $\mathcal{F} : (-1, 1) \times V \to Y$ have the properties:*

- *$\mathcal{F}(t, 0) = 0$ for $|t| < 1$.*

- *the partial derivatives $\mathcal{F}_t$, $\mathcal{F}_x$ and $\mathcal{F}_{xt}$ exist and are continuous.*

- *the* kernal$(\mathcal{F}_x(0, 0))$ *and* $Y/$range$(\mathcal{F}_x(0, 0))$ *are one-dimensional.*

- *$\mathcal{F}_{xt}(0, 0)x_0 \notin$ range$(\mathcal{F}_x(0, 0))$ where the* kernal$(\mathcal{F}_x(0, 0)) =$ span$\{x_0\}$.*

If Z is any complement of the kernal$(\mathcal{F}_x(0,0))$ *in* X, *then there exists a neighbourhood U of $(0,0)$ in $\mathbb{R} \times X$, an interval $(-a, a)$ and continuous functions $\phi : (-a, a) \to \mathbb{R}$, $\psi : (-a, a) \to Z$ such that $\phi(0) = 0$, $\psi(0) = 0$ and*

$$F^{-1}(0) \cap U = \{(\phi(\alpha), \alpha x_0 + \alpha \psi(\alpha)) : |\alpha| < a\} \cup \{(t, 0) : (t, 0) \in U\}. \tag{6.22}$$

The assumptions of the theorem follow from Lemma A. In our application $x_0 = \eta_{\lambda_c}$. Therefore, by [28, 62] we can find positive numbers ϵ and δ such that any pair $(\lambda, q) \in \mathbb{R}^+ \times W^{1,2}(\Omega)$ satisfying

$$q \text{ is a solution to (AC)}, \quad |\lambda - \lambda_c| \leq \epsilon \quad \text{and} \quad \|q - q_{s,\lambda_c}\|_{W^{1,2}(\Omega)} \leq \epsilon$$

is either of the form $(\lambda, q_{s,\lambda})$ or

$$(\lambda, q) = (\lambda(t), q_{s,\lambda(t)} + t\eta_{\lambda_c} + t^2 h(t)), \tag{6.23}$$

where $\lambda(t) \in (\lambda_c - \epsilon, \lambda_c + \epsilon)$ and $h(t) \in W_0^{1,2}(\Omega)$ are smooth functions of $t \in (-\delta, \delta)$. $\qquad\square$

6.4 Numerical simulations on the square and the hexagon

In this section we perform numerical experiments to study Order Reconstruction solutions on two two-dimensional regular polygons - the square and the hexagon, with the hexagon illustrating the generality of such solutions. We work with the full and normalized gradient flow system in the Landau-de Gennes framework at the constant temperature $A = -\frac{B^2}{3C}$. We work at this temperature so that we can make comparisons between the numerical and analytical results. First, we non-dimensionalize the system (6.1) by setting $\bar{t} = \frac{tL}{\lambda^2}$ and $\bar{x} = \frac{x}{\lambda}$, where λ is a characteristic length scale. We then normalize the system by setting $\bar{\mathbf{Q}} = \frac{C}{B}\mathbf{Q}$ to get

$$\bar{\mathbf{Q}}_{\bar{t}} = \overline{\nabla}^2 \bar{\mathbf{Q}} - \frac{\lambda^2}{\bar{L}} \left[\frac{2}{3}\bar{\mathbf{Q}} - 2\left(\bar{\mathbf{Q}}\bar{\mathbf{Q}} - \frac{\mathbf{I}}{3}|\bar{\mathbf{Q}}|^2\right) + 2|\bar{\mathbf{Q}}|^2\bar{\mathbf{Q}} \right]. \tag{6.24}$$

where $\bar{L} = \frac{2C}{B^2}L$. We drop the bars from the dimensionless and normalized variables.

6.4.1 Order Reconstruction simulations on the square

We first work on a square centered at the origin with edge length 2 and impose a boundary condition of the form

$$\mathbf{Q}_b = q\left(\hat{\mathbf{x}} \otimes \hat{\mathbf{x}} - \hat{\mathbf{y}} \otimes \hat{\mathbf{y}}\right) - \frac{1}{3}\left(2\hat{\mathbf{z}} \otimes \hat{\mathbf{z}} - \hat{\mathbf{x}} \otimes \hat{\mathbf{x}} - \hat{\mathbf{y}} \otimes \hat{\mathbf{y}}\right), \qquad (6.25)$$

where $\hat{\mathbf{x}}$, $\hat{\mathbf{y}}$, and $\hat{\mathbf{z}}$ are unit vectors in the x, y and z-directions respectively and

$$
\begin{aligned}
q(x, -1) = q(x, 1) = 1 && \text{for} && -1 + \epsilon \leq x \leq 1 - \epsilon, \\
q(x, -1) = q(x, 1) = f(x) && \text{otherwise}, \\
q(-1, y) = q(1, y) = -1 && \text{for} && -1 + \epsilon \leq y \leq 1 - \epsilon, \\
q(-1, y) = q(1, y) = -f(y) && \text{otherwise},
\end{aligned}
\qquad (6.26)
$$

where $f(s) = \frac{1}{\epsilon}(1 - |s|)$ for $0 \leq 1 - |s| \leq \epsilon$. This fixes q to be zero at the vertices. We work with an initial condition of the form (6.25) given by

$$\mathbf{Q}_0 = q_0\left(\hat{\mathbf{x}} \otimes \hat{\mathbf{x}} - \hat{\mathbf{y}} \otimes \hat{\mathbf{y}}\right) - \frac{1}{3}\left(2\hat{\mathbf{z}} \otimes \hat{\mathbf{z}} - \hat{\mathbf{x}} \otimes \hat{\mathbf{x}} - \hat{\mathbf{y}} \otimes \hat{\mathbf{y}}\right), \qquad (6.27)$$

with

$$
q_0 = \begin{cases}
1 & \text{for} & -y < x < y, \\
-1 & \text{for} & -x < y < x,
\end{cases}
\qquad (6.28)
$$

so that $q_0 = 0$ on the diagonals $x = \pm y$. The initial condition $\mathbf{Q}_0$ has a constant eigenframe and a uniaxial cross with negative order parameter connecting the four square vertices and hence mimics the Well Order Reconstruction solution studied analytically.

For a boundary condition and an initial condition of the form (6.25)-(6.28), there is a dynamic solution $\mathbf{Q}(\mathbf{r}, t)$ of the system (6.24) given by

$$\mathbf{Q}(\mathbf{r}, t) = q(x, y, t)\left(\hat{\mathbf{x}} \otimes \hat{\mathbf{x}} - \hat{\mathbf{y}} \otimes \hat{\mathbf{y}}\right) - \frac{1}{3}\left(2\hat{\mathbf{z}} \otimes \hat{\mathbf{z}} - \hat{\mathbf{x}} \otimes \hat{\mathbf{x}} - \hat{\mathbf{y}} \otimes \hat{\mathbf{y}}\right), \qquad (6.29)$$

where the evolution of q is governed by

$$\frac{\partial q}{\partial t} = \nabla^2 q - \frac{\lambda^2}{L} q\,(q - 1)\,(q + 1). \qquad (6.30)$$

We solve (6.30) on the square for different values of λ. We expect to see that $q = 0$ along $x = \pm y$

for small values of λ since the Well Order Reconstruction solution is the unique Landau-de Gennes critical point in this regime. We expect to see transition layers near a pair of opposite edges for large λ due to the result in Proposition 6.3.

In the following simulations we define $\bar{\lambda}^2 = \frac{\lambda^2}{L}$. In Figures 6-2 and 6-4 we solve (6.30) for $\bar{\lambda}^2 = 0.0418$ and $\bar{\lambda}^2 = 167.2$ respectively. For both figures $\epsilon = 0.05$ and the solution is representative of the behaviour for all ϵ small. For $\bar{\lambda}^2 = 0.0418$, the scalar profile relaxes the sharp transition layers at $x = \pm y$ but retains the vanishing diagonal cross with $q(x, \pm y, t) = 0$ for all times. The corresponding dynamic solution $\mathbf{Q}(\mathbf{r}, t)$ in (6.29) has a uniaxial diagonal cross with negative order parameter consistent with the stability and uniqueness results for the Well Order Reconstruction solution. In Figure 6-3, we plot the biaxiality parameter of the converged solution,

$$\beta^2(\mathbf{Q}) = 1 - 6\frac{(\mathrm{tr}\mathbf{Q}^3)^2}{(\mathrm{tr}\mathbf{Q}^2)^3}.$$

For $\bar{\lambda}^2 = 167.2$, the diagonal cross in the initial condition relaxes into a pair of transition layers near $y = -1$ and $y = +1$.

In Figure 6-5 we plot the value of the converged solution at the origin as a function of $\bar{\lambda}^2$. The solution no longer vanishes on the diagonal cross if $q(0,0) \neq 0$ and we deduce that the Well Order Reconstruction solution loses stability for values of $\bar{\lambda}^2$ for which $q(0,0) \neq 0$. In Figure 6-5 we see that $q(0,0) = 0$ if $\bar{\lambda}^2 \leq 7.69$. This numerical bifurcation diagram is consistent with the pitchfork bifurcation established in Theorem 6.1 and predicts that the Well Order Reconstruction solution loses stability on a square domain with edge length 2λ for which $\lambda^2 > \frac{15LC}{B^2}$.
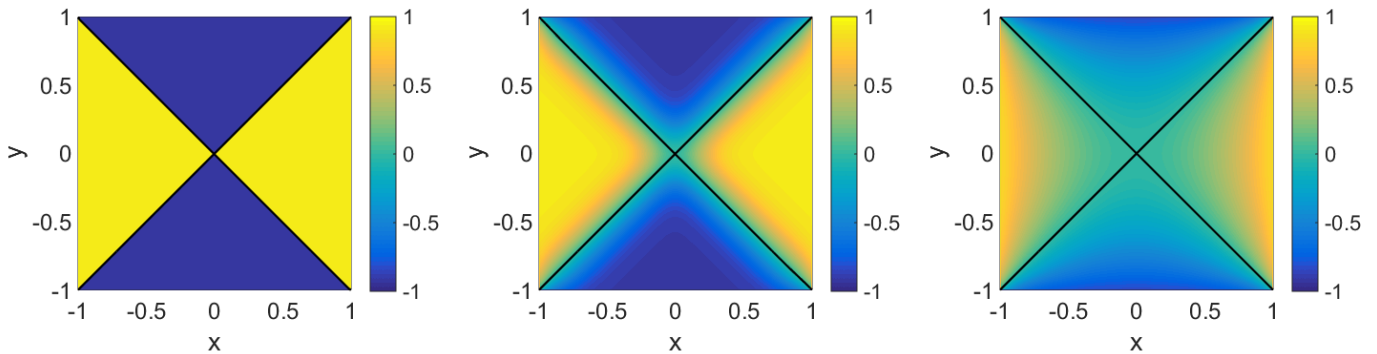

Figure 6-2: $q(x, y, t)$ with contours at level 0 for $\bar{\lambda}^2 = 0.0418$ and $\epsilon = 0.05$ at $t = 0$, $t = 0.01$ and $t = 2$. The spatial resolution is $h = \frac{1}{200}$.
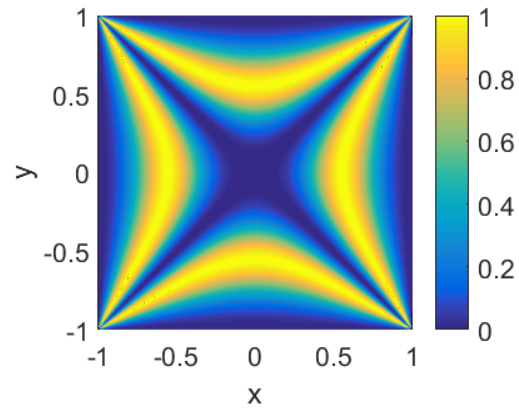
Figure 6-3: Biaxiality parameter $\beta^2(\mathbf{Q}(\mathbf{x}, t))$ for $\bar{\lambda}^2 = 0.0418$ and at $t = 2$.
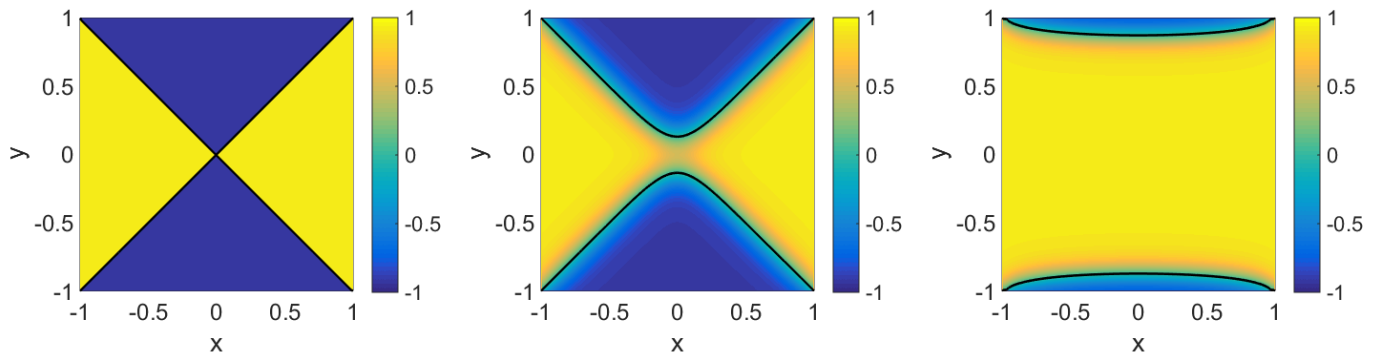

Figure 6-4: $q(x, y, t)$ with contours at level 0 for $\bar{\lambda}^2 = 167.2$ at $t = 0$, $t = 0.5$ and $t = 2$.
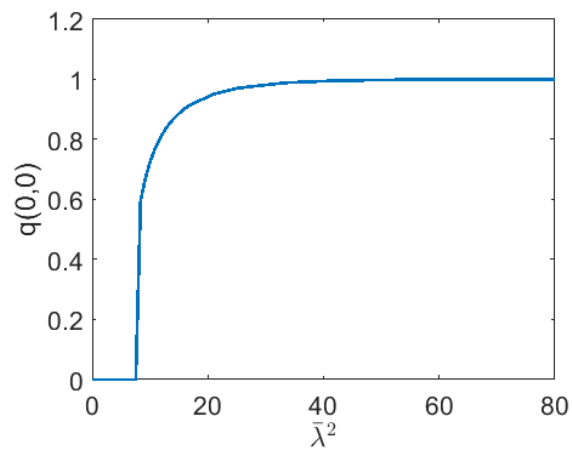

Figure 6-5: $q(0, 0)$ of the converged solution as $\bar{\lambda}^2$ varies. The critical value is $\bar{\lambda}^2 = 7.69$.

6.4.2 Order Reconstruction analysis and simulations on the hexagon

Next we look for Order Reconstruction-type solutions on a regular hexagon of edge length λ, centered at the origin. As before, we work at the fixed temperature $A = -\frac{B^2}{3C}$. We interpret Order Reconstruction solutions loosely and look for critical points of the Landau-de Gennes energy which have an interior ring of maximal biaxiality inside the hexagon. Let H be a regular hexagon which is centred at the origin. We take our rescaled domain Ω to be a truncated hexagon given by the set of points (x, y) in the interior of H which satisfy the inequalities

$$|x| < 1 - \epsilon, \quad \frac{1}{2}|x + \sqrt{3}y| < 1 - \epsilon \quad \text{and} \quad \frac{1}{2}|x - \sqrt{3}y| < 1 - \epsilon.$$

The truncated hexagon Ω is drawn in Figure 6-6 and has the same set of symmetries as the original hexagon H.
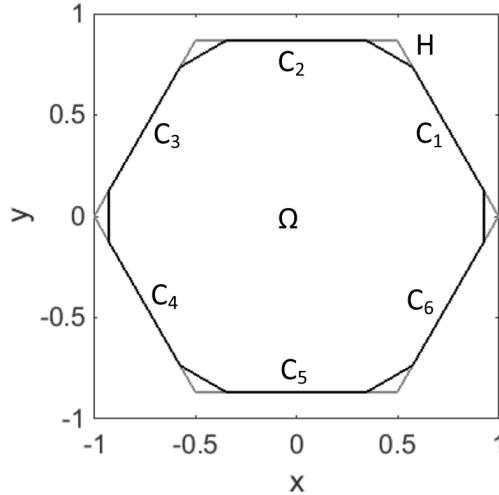
Figure 6-6: The truncated hexagon Ω. The regular hexagon H is also plotted.

The set of symmetries of a hexagon, D_6, consists of six reflection symmetries about the symmetry axes of the hexagon and six rotations of angles $\frac{k\pi}{3}$ for $k \in \{0, \ldots, 5\}$. We label the long edges of $\partial\Omega$ as $C_1 - C_6$ and, as before, the edges are labelled anticlockwise. We impose the following Dirichlet boundary conditions on these long edges:

$$\mathbf{Q}_b = \mathbf{n}_b \otimes \mathbf{n}_b - \frac{\mathbf{I}}{3}, \tag{6.31}$$

where $\mathbf{n}_b$ is the unit tangent vector to ∂H given by

$$\mathbf{n}_b = \begin{cases} (-\frac{1}{2}, \frac{\sqrt{3}}{2}, 0) & \text{on} \quad C_1 \cup C_4, \\ (-1, 0, 0) & \text{on} \quad C_2 \cup C_5, \\ (-\frac{1}{2}, -\frac{\sqrt{3}}{2}, 0) & \text{on} \quad C_3 \cup C_6. \end{cases} \tag{6.32}$$

We also impose Dirichlet boundary conditions on the short edges of $\partial\Omega$. On the short edge connecting the vertices $(1 - \varepsilon, \sqrt{3}\varepsilon)$ and $(1 - \varepsilon, -\sqrt{3}\varepsilon)$, we define

$$\mathbf{Q}_b = \mathbf{n}_b(x, y) \otimes \mathbf{n}_b(x, y) - \frac{\mathbf{I}}{3} \quad \text{where} \quad \mathbf{n}_b(x, y) = \frac{1}{\sqrt{\frac{1}{4} + \frac{y^2}{4\epsilon^2}}} \left(-\frac{1}{2}, \frac{y}{2\epsilon}, 0\right),$$

and extend this boundary data $\mathbf{Q}_b$ to the other short edges by successive rotations of $\frac{\pi}{3}$. Note that the boundary data is consistent with the symmetries of the hexagon.

We look for critical points of the Landau-de Gennes energy on Ω such that:

(1) the corresponding $\mathbf{Q}$-tensor has $\hat{\mathbf{z}}$ as an eigenvector with constant eigenvalue $-\frac{1}{3}$.

(2) the origin is a uniaxial point with negative scalar order parameter.

As the long edges are subject to a uniaxial Dirichlet condition with positive order parameter, we would expect a ring of maximal biaxiality to separate the uniaxial point with negative order parameter at the origin from the uniaxial boundaries with positive order parameter. In view of (1) we look for critical points of the form

$$\mathbf{Q}(\mathbf{x}) = \left(\begin{array}{c|c} \mathbf{P}(\mathbf{x}) + \frac{1}{6}\mathbf{I}_2 & \begin{array}{c} 0 \\ 0 \end{array} \\ \hline \begin{array}{cc} 0 & 0 \end{array} & -\frac{1}{3} \end{array}\right). \tag{6.33}$$

Here $\mathbf{P}(\mathbf{x}) \in S_0^{2\times 2}$ (the set of 2×2, symmetric and traceless matrices) and $\mathbf{I}_2$ is the 2×2 identity matrix. The condition (2) translates to $\mathbf{P}(0, 0) = 0$. By substitution, we see that $\mathbf{Q}$ is a critical point of the Landau-de Gennes energy if $\mathbf{P}$ is a solution of the system

$$\nabla^2 \mathbf{P} = \frac{\lambda^2}{2\bar{L}} \left[-2\mathbf{P} - 4\left(\mathbf{P}\mathbf{P} - \frac{\mathbf{I}_2}{2}|\mathbf{P}|^2\right) - 4|\mathbf{P}|^2\mathbf{P}\right], \tag{6.34}$$

or a critical point of the functional

$$F[\mathbf{P}] = \int_\Omega \frac{1}{2} |\nabla \mathbf{P}|^2 + \frac{\lambda^2}{\bar{L}} \left(-\frac{1}{2} \mathrm{tr} \mathbf{P}^2 - \frac{2}{3} \mathrm{tr} \mathbf{P}^3 + \frac{1}{2} (\mathrm{tr} \mathbf{P}^2)^2 \right) \, \mathrm{d}A. \tag{6.35}$$

Let $\mathbf{P}_b$ denote the boundary data for $\mathbf{P}$. This is related to $\mathbf{Q}_b$ via the change of variables (6.33).

Lemma 6.5. *For any $\lambda > 0$, there exists a critical point $\mathbf{P}_s \in C^2(\Omega) \cap C(\overline{\Omega})$ of (6.35) which satisfies the boundary condition $\mathbf{P}_s = \mathbf{P}_b$ on $\partial\Omega$ and $\mathbf{P}_s(0,0) = 0$.*

The corresponding $\mathbf{Q}$-tensor $\mathbf{Q}_s$ is then related to $\mathbf{P}_s$ via the change of variables (6.33) and is a critical point of the Landau-de Gennes energy with the two required properties, (1) and (2).

Proof. Let $\mathcal{A}$ be the admissible set containing maps $\mathbf{P} \in W^{1,2}(\Omega, S_0^{2\times 2})$ which satisfy the boundary condition $\mathbf{P} = \mathbf{P}_b$ on $\partial\Omega$. Let $\mathcal{A}_{\mathrm{sym}}$ be the admissible set containing the maps $\mathbf{P} \in \mathcal{A}$ which are consistent with the symmetries of the hexagon. That is, all $\mathbf{P} \in \mathcal{A}_{\mathrm{sym}}$ satisfy

$$\mathbf{P}(\mathbf{x}) = S\mathbf{P}(S^\mathsf{T}\mathbf{x})S^\mathsf{T}, \tag{6.36}$$

for almost all $\mathbf{x} \in \Omega$ and any matrix $S \in D_6$. The set $\mathcal{A}_{\mathrm{sym}}$ is non-empty because the boundary data $\mathbf{P}_b$ satisfies (6.36). We can prove the existence of a minimizer $\mathbf{P}_s$ of the energy F in the class $\mathcal{A}_{\mathrm{sym}}$ by the direct methods in the calculus of variations.

Whilst $\mathbf{P}_s$ is a critical point of F over $\mathcal{A}_{\mathrm{sym}}$, we do not know whether it is a critical point of F over $\mathcal{A}$. However, (6.36) defines an isometric action of D_6 on $\mathcal{A}$ and the energy F is invariant with respect to this action. This allows us to apply Palais's principle of symmetric criticality [85, 62] which gives that critical points of F in the restricted space $\mathcal{A}_{\mathrm{sym}}$ are also critical points in the space $\mathcal{A}$. We conclude that $\mathbf{P}_s$ is a critical point of F in $\mathcal{A}$ and a solution of the Euler-Lagrange equations in (6.34). (We obtain that $\mathbf{P}_s \in C^2(\Omega) \cap C(\overline{\Omega})$ by elliptic regularity, Sobolev embeddings and the fact we are working on a Lipchitz domain as discussed in Appendix A.)

Finally, we evaluate (6.36) at the point $\mathbf{x} = (0, 0)$ to obtain that

$$\mathbf{P}(0, 0) = S\mathbf{P}(0, 0)S^\mathsf{T} \quad \text{for} \quad \text{any} \quad S \in D_6, \tag{6.37}$$

which requires that $\mathbf{P}_s(0, 0) = 0$ as needed. □

Next we perform numerical experiments on the regular hexagon of edge length 1. We solve the gradient flow equations (6.24) and investigate the stability of the Order Reconstruction-type

critical point in Lemma 6.5. For these simulations, the hexagon is embedded into the square $[-1,1]^2$ which is discretised by a uniform hexagonal mesh with spatial resolution $h = \frac{1}{200}$ and with the same symmetries as our domain. This discretisation is necessary to observe the predicted uniaxial point at the origin. Spacial derivatives are estimated with a six-point Laplacian, as introduced in Chapter 2. The remaining numerical details remain the same as discussed in Chapter 2.

We impose Dirichlet conditions on all six edges of the form

$$\mathbf{Q}_b(x, y) = \left(\mathbf{n}_b \otimes \mathbf{n}_b - \frac{\mathbf{I}}{3} \right), \tag{6.38}$$

with discontinuities at the vertices. The director $\mathbf{n}_b$ is the unit tangent vector to the relevant edge as given in (6.32) and at each vertex we fix $\mathbf{Q}_b$ to be the average of the two intersecting edges. We impose an initial condition which divides the hexagon into six regions and three alternating uniaxial states, as shown in Figure 6-7. We look for solutions which have $\hat{\mathbf{z}}$ as an eigenvector and a uniaxial point at the origin with negative order parameter. This is equivalent to (i) $Q_{33} = -\frac{1}{3}$ everywhere, (ii) $Q_{13} = Q_{23} = 0$ everywhere, (iii) $Q_{11} = Q_{22} = \frac{1}{6}$ at the origin and (iv) $Q_{12} = 0$ at the origin.
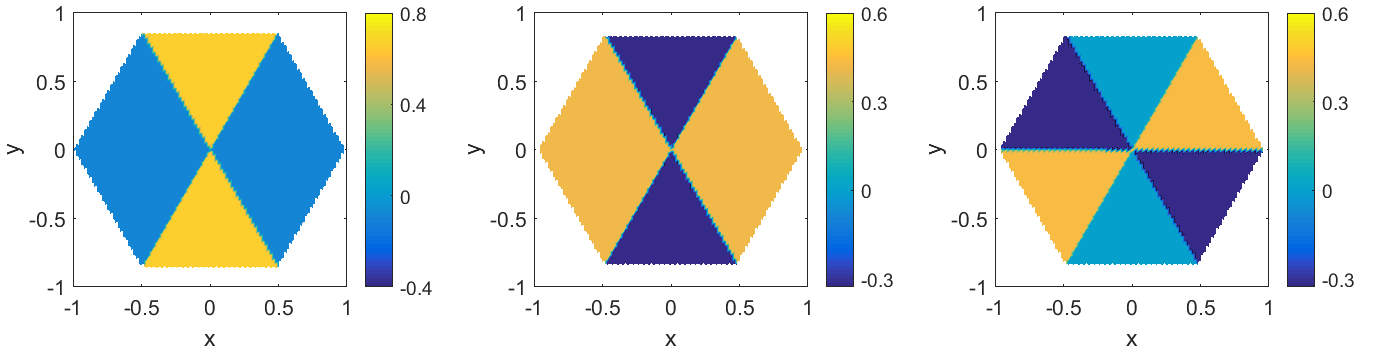
Figure 6-7: The initial conditions on the hexagon for Q_{11}, Q_{22} and Q_{12}.

Firstly, we solve the gradient flow system (6.24) with the Dirichlet boundary condition (6.38) and the initial conditions described above for $\bar{\lambda}^2 = 3 \times 10^{-3}$. In Figure 6-8 we plot Q_{11}, Q_{22} and Q_{12} of the converged solution and see that the origin is indeed a uniaxial point with negative scalar order parameter. Hence the dynamic solution at the origin is given by

$$\mathbf{Q}((0,0), t) = -\frac{1}{2} \left(\hat{\mathbf{z}} \otimes \hat{\mathbf{z}} - \frac{\mathbf{I}}{3} \right),$$

for large times. Further, we numerically verify that $Q_{33}(\mathbf{x}, t) = -\frac{1}{3}$ and $Q_{13}(\mathbf{x}, t) = Q_{23}(\mathbf{x}, t) = 0$ for all times as shown in Figure 6-9. Therefore we can confirm that $\hat{\mathbf{z}}$ is an eigenvector with constant eigenvalue $-\frac{1}{3}$ for all times. In Figure 6-10, we plot the biaxiality parameter of the converged solution,

$$\beta^2(\mathbf{Q}) = 1 - 6\frac{(\mathrm{tr}\mathbf{Q}^3)^2}{(\mathrm{tr}\mathbf{Q}^2)^3}.$$

We see a ring of maximal biaxiality around the origin, yielding an Order Reconstruction-type solution on a regular hexagon. Secondly, in Figures 6-11, 6-12 and 6-13, we plot the components of the converged solution at the origin as functions of $\bar{\lambda}^2$. The converged solution respects $Q_{12} = 0$ and $Q_{11} = Q_{22} = \frac{1}{6}$ at the origin for $\bar{\lambda}^2 \leq 5.85$ and hence we have a uniaxial point with negative order parameter at the origin in this regime. The numerical simulations suggest that the Order Reconstruction-type solution on a regular hexagon loses stability for larger values of $\bar{\lambda}^2$. The qualitative trends are the same as those observed on a regular square.
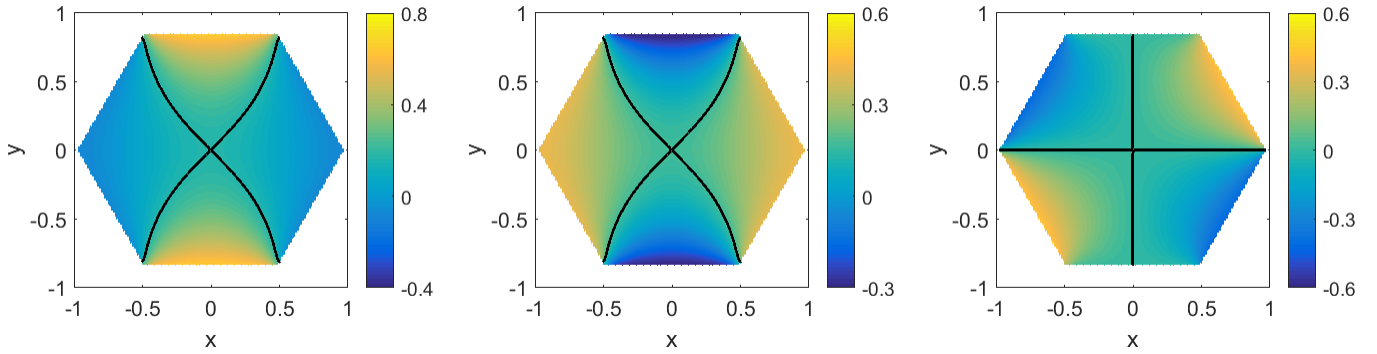
Figure 6-8: $Q_{11}(\mathbf{x}, t)$ and $Q_{22}(\mathbf{x}, t)$ with contours at level $\frac{1}{6}$ and $Q_{12}(\mathbf{x}, t)$ with contours at level 0 for $\bar{\lambda}^2 = 3 \times 10^{-3}$ and at $t = 2$.
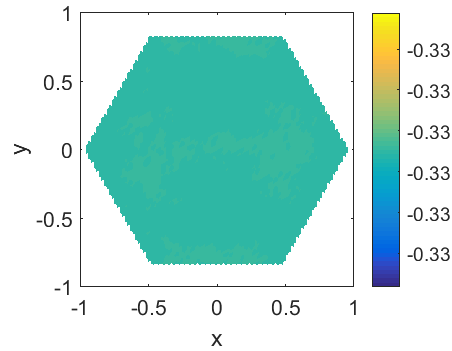
Figure 6-9: $Q_{33}(\mathbf{x}, t) = -Q_{11}(\mathbf{x}, t) - Q_{22}(\mathbf{x}, t)$ for $\bar{\lambda}^2 = 3 \times 10^{-3}$ and at $t = 2$.
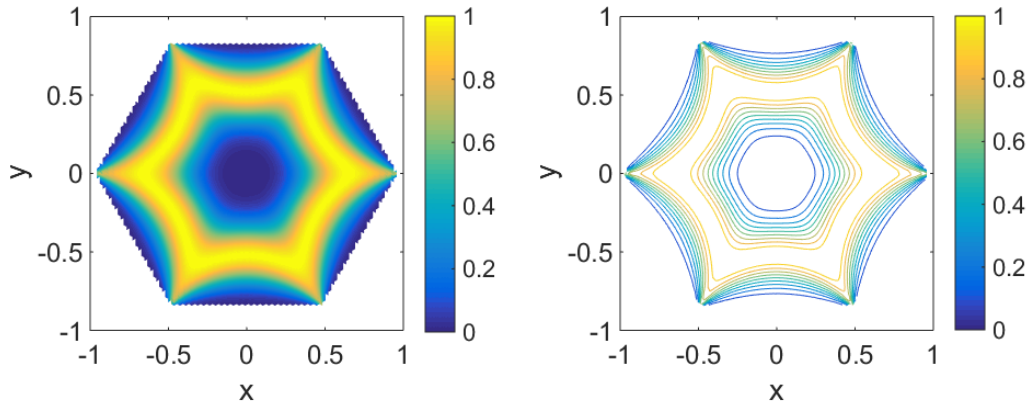
Figure 6-10: Plot and contour plot of biaxiality parameter $\beta^2(\mathbf{Q}(\mathbf{x}, t))$ for $\bar{\lambda}^2 = 3 \times 10^{-3}$ and at $t = 2$.
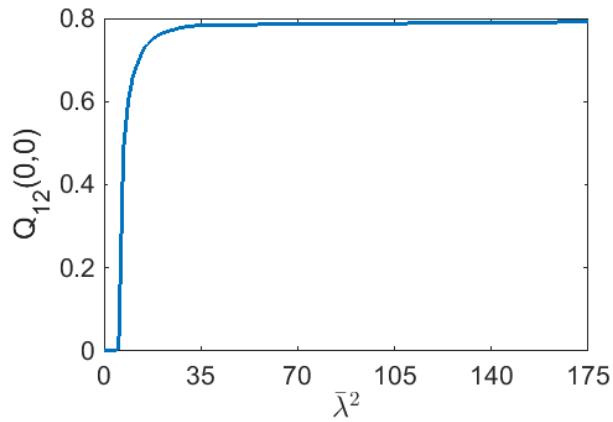
Figure 6-11: Q_{12} at the origin as $\bar{\lambda}^2$ varies. The critical value is $\bar{\lambda}^2 = 5.85$.
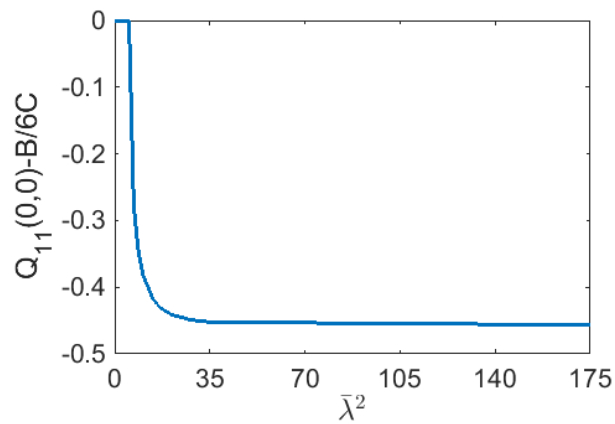
Figure 6-12: $Q_{11} - \frac{1}{6}$ at the origin as $\bar{\lambda}^2$ varies. The critical value is $\bar{\lambda}^2 = 5.85$.
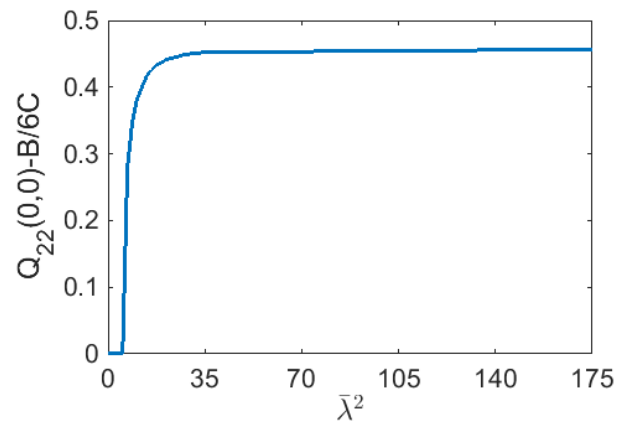
Figure 6-13: $Q_{22} - \frac{1}{6}$ at the origin as $\bar{\lambda}^2$ varies. The critical value is $\bar{\lambda}^2 = 5.99$.

Triple phase front propagation

The previous chapters employ a fourth-order Landau-de Gennes bulk potential with only isotropic or uniaxial critical points. In this chapter, we extend our analysis to a sixth-order bulk potential which admits isotropic, uniaxial and biaxial minimizers at a special temperature called the triple point temperature in Allender and Longa 2008 [3]. We work on a unit disc and consider the (u, v)-type critical points introduced in Chapter 5, which can include isotropic, uniaxial and biaxial states. We use the asymptotic methods in Rubinstein, Sternberg and Keller 1989 [96] to study the evolution of the two scalar order parameters, u and v, in the (u, v)-type dynamic solutions of the Landau-de Gennes gradient flow model. We impose suitable boundary and initial conditions compatible with isotropic-uniaxial, uniaxial-biaxial and isotropic-biaxial fronts and show that such fronts propagate according to mean curvature in the $L \to 0$ limit. Further, we follow the methods in Bronsard and Reitich 1993 [14] to show that for such (u, v)-type dynamic solutions, the triple phase fronts meet at angles of $\frac{2\pi}{3}$, if the fronts intersect. We complement our asymptotic study with a numerical study of the full Landau-de Gennes gradient flow system with sixth-order bulk potential to reveal interesting pattern formation with three stable phases.

7.1   Problem formulation

Recall from Chapter 2 that the biaxial nematic phase is described by a **Q**-tensor with three distinct eigenvalues within the Landau-de Gennes framework [31]. In order to describe first-order phase

transitions between biaxial and uniaxial or isotropic phases we use a sixth-order bulk potential given by

$$
\begin{aligned}
f_B(\mathbf{Q}) = {} & \frac{A}{2}\mathrm{tr}\mathbf{Q}^2 - \frac{B}{3}\mathrm{tr}\mathbf{Q}^3 + \frac{C}{4}\mathrm{tr}(\mathbf{Q}^2)^2 \\
& + \frac{D}{5}\mathrm{tr}\mathbf{Q}^2\mathrm{tr}\mathbf{Q}^3 + \frac{E}{6}(\mathrm{tr}\mathbf{Q}^2)^3 + \frac{(F-E)}{6}(\mathrm{tr}\mathbf{Q}^3)^2,
\end{aligned}
\tag{7.1}
$$

as introduced in [3]. This higher order bulk potential allows for phase transitions between biaxial and uniaxial or isotropic phases unlike the fourth-order bulk potential used previously which only allows for isotropic to uniaxial transitions. The parameters A, B, C, D, E and F are material dependent constants. As before, A depends on temperature with $A = A_0(T - T^*)$ where T^* is the supercooling temperature and $A_0 > 0$. We require $E > 0$ and $F > 0$ to guarantee the stability of the expansion [3]. This ensures that the coefficient of the highest order term in the bulk potential is positive, hence $f_B(\mathbf{Q}) \to \infty$ as $|\mathbf{Q}| \to \infty$ and all energy minima are achieved for finite $|\mathbf{Q}|$. There are no set values of the parameters in the literature. Further $\mathrm{tr}(\mathbf{Q}^2)$ and $\mathrm{tr}(\mathbf{Q}^3)$ satisfy the inequality $\frac{1}{6}\mathrm{tr}(\mathbf{Q}^2)^3 - \mathrm{tr}(\mathbf{Q}^3)^2 \geq 0$. This is an equality in the uniaxial phase. Therefore it is natural to define a biaxiality parameter $\beta^2(\mathbf{Q})$ by

$$
\beta^2(\mathbf{Q}) = 1 - 6\frac{(\mathrm{tr}\mathbf{Q}^3)^2}{(\mathrm{tr}\mathbf{Q}^2)^3}.
$$

This is a measure of the strength of biaxiality as discussed in [76] and Chapter 6. For uniaxial $\mathbf{Q}$-tensors $\beta^2(\mathbf{Q}) = 0$ and maximum biaxiality is achieved when $\beta^2(\mathbf{Q}) = 1$.

In this chapter we are interested in critical points of the Landau-de Gennes energy functional of the form

$$
\mathbf{Q} = \frac{u(r,\theta)}{2}\left(\hat{\mathbf{r}} \otimes \hat{\mathbf{r}} - \mathbf{m} \otimes \mathbf{m}\right) + v(r,\theta)\left(\mathbf{p} \otimes \mathbf{p} - \frac{\mathbf{I}}{3}\right),
\tag{7.2}
$$

where $\hat{\mathbf{r}} = (\cos\theta, \sin\theta, 0)$ is the two-dimensional unit radial vector, $\mathbf{m} = (-\sin\theta, \cos\theta, 0)$ and $\mathbf{p} = (0, 0, 1)$. Again, this is motivated by the (u, v)-type critical points of the Landau-de Gennes energy discussed in [33]. The non-dimensionalized Landau-de Gennes gradient flow system with sixth-order bulk potential is given by

$$
\begin{aligned}
\mathbf{Q}_t = {} & \nabla^2\mathbf{Q} - \frac{1}{L}\left[A\mathbf{Q} - B\left(\mathbf{Q}\mathbf{Q} - \frac{\mathbf{I}}{3}|\mathbf{Q}|^2\right) + C|\mathbf{Q}|^2\mathbf{Q}\right. \\
& \left. + E|\mathbf{Q}|^4\mathbf{Q} + (F-E)\mathrm{tr}\mathbf{Q}^3\left(\mathbf{Q}\mathbf{Q} - \frac{\mathbf{I}}{3}|\mathbf{Q}|^2\right)\right].
\end{aligned}
\tag{7.3}
$$

Throughout this chapter L is taken to be small. The substitution of the ansatz for $\mathbf{Q}$ in (7.2) into the system (7.3) yields the following system of coupled second-order partial differential equations

$$u_t = \nabla^2 u - \frac{4u}{r^2} - \frac{f(u, v)}{L},$$ (7.4)

$$v_t = \nabla^2 v - \frac{g(u, v)}{L},$$ (7.5)

where

$$
\begin{aligned}
f(u, v) =& u\left[A + \frac{2B}{3}v + C\left(\frac{u^2}{2} + \frac{2v^2}{3}\right) - \frac{2D}{5}\left(\left(\frac{u^2}{2} + \frac{2v^2}{3}\right) - \left(\frac{2v^3}{9} - \frac{u^2 v}{2}\right)\right)\right. \\
&\left. + E\left(\frac{u^2}{2} + \frac{2v^2}{3}\right)^2 - \frac{2(F - E)}{3}v\left(\frac{2v^3}{9} - \frac{u^2 v}{2}\right)\right],
\end{aligned}
$$

$$
\begin{aligned}
g(u, v) =& u\left[\frac{B}{4}u - \frac{3D}{20}u\left(\frac{u^2}{2} + \frac{2v^2}{3}\right) - \frac{(F - E)}{4}u\left(\frac{2v^3}{9} - \frac{u^2 v}{2}\right)\right] \\
&+ v\left[A - \frac{B}{3}v + C\left(\frac{u^2}{2} + \frac{2v^2}{3}\right) + \frac{3D}{10}\left(\frac{2}{3}v\left(\frac{u^2}{2} + \frac{2v^2}{3}\right) + \frac{4}{3}\left(\frac{2v^3}{9} - \frac{u^2 v}{2}\right)\right)\right. \\
&\left. + E\left(\frac{u^2}{2} + \frac{2v^2}{3}\right)^2 + \frac{(F - E)}{3}v\left(\frac{2v^3}{9} - \frac{u^2 v}{2}\right)\right].
\end{aligned}
$$

In this derivation we have used that

$$\text{tr}(\mathbf{Q}^2) = \frac{u^2}{2} + \frac{2v^2}{3}, \qquad \text{tr}(\mathbf{Q}^3) = \frac{2v^3}{9} - \frac{u^2 v}{2},$$

and

$$|\nabla \mathbf{Q}|^2 = \frac{1}{2}u_r^2 + \frac{2}{3}v_r^2 + \frac{1}{2r^2}u_\theta^2 + \frac{2}{3r^2}v_\theta^2 + \frac{2}{r^2}u^2.$$

Defining $W(u, v) = f_B(\mathbf{Q})$, $f(u, v)$ and $g(u, v)$ are given by

$$f(u, v) = 2W_u(u, v) \quad \text{and} \quad g(u, v) = \frac{3}{2}W_v(u, v).$$ (7.6)

7.2 Existence of a triple point temperature

Here we discuss the results in [3] which show the existence of a triple point temperature for which exists isotropic, uniaxial and biaxial minimizers of the sixth-order bulk potential with equal energies. In this paper, the authors reparametrize $\text{tr}(\mathbf{Q}^2)$ and $\text{tr}(\mathbf{Q}^3)$ using two scalar order parameters q and ω via:

$$\text{tr}(\mathbf{Q}^2) = q^2 \quad \text{and} \quad \text{tr}(\mathbf{Q}^3) = q^3(1 - \omega).$$ (7.7)

This allows the bulk potential to be written as the sum of a uniaxial energy and two biaxial energies,

$$f_B(\mathbf{Q}) = F_u(q) + F_b(q)\,\omega + \frac{1}{6}(F - E)q^6\omega^2, \tag{7.8}$$

where

$$F_u = \frac{A}{2}q^2 - \frac{B}{3}q^3 + \frac{C}{4}q^4 + \frac{D}{5}q^5 + \frac{F}{6}q^6,$$

$$F_b = \frac{B}{3}q^3 - \frac{D}{5}q^5 - \frac{F - E}{3}q^6.$$

This parametrization makes it simple to compute phase plane diagrams for this system. In what follows we summarise the methods in [3] and describe a resulting phase plane which includes a triple point. Phase diagrams are studied in the (A, B)-plane for fixed values of C, D, E and F and regions and lines of the (A, B)-plane are described parametrically in terms of q.

- For the uniaxial phase to be locally stable we require

$$\frac{\partial F_u}{\partial q} = q(A - Bq + Cq^2 + Dq^3 + Fq^4) = 0,$$

$$\frac{\partial^2 F_u}{\partial q^2} = A - 2Bq + 3Cq^2 + 4Dq^3 + 5Fg^4 > 0.$$

- Transitions between competing phases occur along lines in the (A, B)-plane where $f_B(\mathbf{Q})$ is a double welled potential. Therefore the transition between uniaxial and isotropic regions is a line in the (A, B)-plane along which $F_u(q)$ is a double welled potential. Hence, at the transition there must be non-trivial solutions of $F_u(q) = 0$ and $\frac{\partial F_u}{\partial q} = 0$. This gives

$$A = \frac{C}{2}q^2 + \frac{4D}{5}q^3 + Fq^4, \quad B = \frac{3C}{2}q + \frac{9D}{5}q^2 + 2Fq^3.$$

- For the biaxial phase to be locally stable at some $\omega = \omega_b$ we require

$$\left.\frac{\partial f_B}{\partial \omega}\right|_{\omega_b} = F_b(q) + \frac{F - E}{3}q^6\omega_b = 0, \tag{7.9}$$

$$\frac{\partial^2 f_B}{\partial q^2}\frac{\partial^2 f_B}{\partial \omega^2} - \left(\frac{\partial^2 f_B}{\partial q\partial\omega}\right)^2 \geq 0. \tag{7.10}$$

The condition in (7.10) is the requirement that the determinant of the second derivative of the bulk potential $f_B(\mathbf{Q})$ is positive for a local minimum. Equation (7.9) implies that in a

stable biaxial phase we must have

$$f_B(\mathbf{Q})|_{w_b} = F_u(q) - \frac{1}{6}(F - E)q^6\omega_b^2.$$

Therefore a stable biaxial state can only be achieved if $F - E > 0$.

- Referring back to the original expression for $f_B(\mathbf{Q})$ in (7.8), we note that the biaxial phase becomes energetically favourable over a uniaxial phase in regions of the (A, B)-plane where $F_b(q) \leq 0$. This is because if $F_b(q) \leq 0$, we can find ω such that

$$f_B(\mathbf{Q})|_\omega = F_u(q) + F_b(q)\omega + \frac{1}{6}(F - E)q^6\omega^2 < f_B(\mathbf{Q})|_{\omega=0}.$$

Hence the biaxial minimizer is of lower energy than the uniaxial minimizer in these regions. The transition between uniaxial and biaxial regions occurs when $F_b(q) = 0$ together with $\frac{\partial F_u}{\partial q} = 0$. This gives

$$A = -Cq^2 - \frac{2D}{5}q^3 - q^4, \quad B = \frac{3D}{5}q^2 + (F - E)q^3.$$

If this condition is satisfied then $f_B(\mathbf{Q})$ may be a single welled potential which transitions from admitting a uniaxial minimum to admitting a biaxial minimum across the (A, B)-line described above. This is a second-order phase transition. If the conditions for a stable biaxial state are also satisfied along part of this (A, B)-line then $f_B(\mathbf{Q})$ is a double welled potential and we have a first-order phase transition.

- The transition between biaxial and isotropic regions occurs when $f_B(\mathbf{Q})|_{w_b} = 0$ and $\frac{\partial f_B(\mathbf{Q})}{\partial q}\big|_{\omega_b} = 0$ for non-zero q which yields

$$A = -\frac{2BD}{5(F - E)} - \left(C - \frac{6D^2}{25(F - E)}\right)q^2 - q^4,$$

$$B^2 = -\frac{1}{2}q^4\left[4q^2 + 3\left(C - \frac{6D^2}{25(F - E)}\right)\right](F - E).$$

Taking $D = 0$, the above calculations give that the isotropic-uniaxial, uniaxial-biaxial and isotropic-

biaxial lines simplify to

$$B^2 = \frac{\sqrt{(C^2 + 16AF)^3} - C(C^2 - 48AF)}{16F},$$

$$B^2 = \frac{1}{2}\left(3AC - C^3 + (C^2 - A)\sqrt{C^2 - 4A}\right)(F - E)^2, \tag{7.11}$$

$$B^2 = \frac{F - E}{4}\left(C(C^2 - 6A) - (C^2 - 4A)^{\frac{3}{2}}\right),$$

respectively. Phase plane sketches in [3] are produced using the equations for A and B in (7.11). A triple point temperature is found when all three of these equalities hold at a point in the (A, B)-plane. The phase plane from [3] of interest is reproduced in Figure 7-1, showing the position of a triple point temperature denoted T. (The thicker dark lines are of interest and represent $C = -1$, $D = 0$, $E = 1$ and $F = 13.6$.) Figure 7-1 also displays a contour plot of $W(u, v)$ at a triple point temperature (for $A = 0.2387$, $B = 1.5920$, $C = -1$, $D = 0$, $E = 1$ and $F = 25$). This shows the existence of five equal energy minimizers; two for $v > 0$, two for $v < 0$ and one at $(u, v) = (0, 0)$. The $W(u, v)$ minimizers with $v \leq 0$ are physically relevant for this problem as illustrated in Chapter 5. The $W(u, v)$ minimizers with $v > 0$ are not relevant for the full Landau-de Gennes energy, including the Dirichlet energy. The state $(u, v) = (0, 0)$ is the isotropic state. Of the two minimizers with $v < 0$, the $W(u, v)$ minimizer with $u = -2v$ is uniaxial. The second minimizer with $v < 0$ is biaxial at the triple point temperature. In what follows we label these three minimizing states **a**, **b** and **c**.
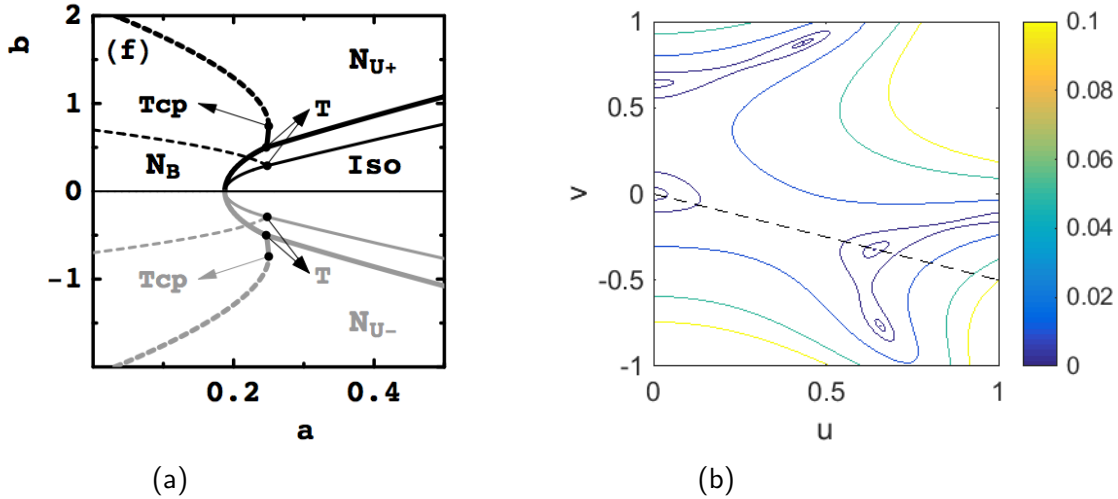

(a)   (b)

Figure 7-1: a) The relevant phase plane from [3] showing a triple point temperature denoted T, with solid lines representing first-order phase transitions and b) a contour plot of $W(u, v)$ at a triple point temperature showing five minimizing (u, v)-pairs and the line $u = -2v$ (dashed).

7.3 Triple phase front propagation

In this section we consider solutions of the system (7.4)-(7.5) with an initial condition consisting of the three stable biaxial, uniaxial and isotropic states, denoted **a**, **b** and **c**. These phases are separated by three fronts Γ_1, Γ_2 and Γ_3 which meet at a triple junction, following the set up in [14] and as shown in Figure 7-2. We take asymptotic expansions in three regions; an outer expansion far away from the interfaces, an inner expansion close to the interfaces and an expansion close to the triple junction where the three fronts meet.

Throughout this chapter we focus on the case where all fronts are well away from the origin which is contained in the isotropic region. This means that the $-\frac{4u}{r^2}$ term in equation (7.4) is of order one and can be neglected in higher order equations.
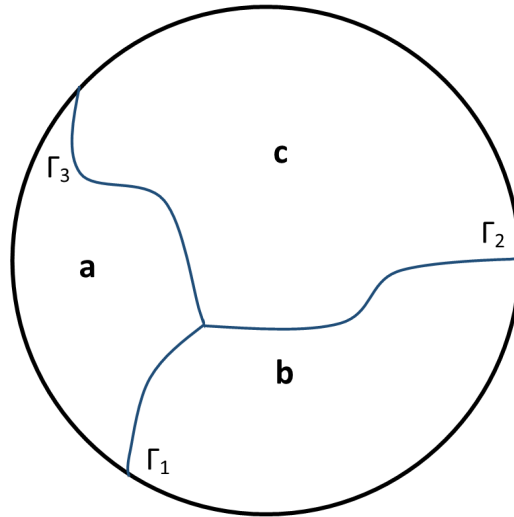

Figure 7-2: The three stable states are separated by three fronts Γ_i which meet at a triple junction.

7.3.1 Outer expansion on fast time scale

First we work on a fast time scale with $\tau = \frac{t}{L}$. Here equations (7.4)-(7.5) become

$$u_\tau = L\left(\nabla^2 u - \frac{4u}{r^2}\right) - f(u, v), \qquad (7.12)$$

$$v_\tau = L\nabla^2 v - g(u, v). \qquad (7.13)$$

We take an outer expansion on this time scale, writing u and v as

$$u = u_O^0(\mathbf{x}, \tau) + L u_O^1(\mathbf{x}, \tau) + L^2 u_O^2(\mathbf{x}, \tau) + ...,$$
$$v = v_O^0(\mathbf{x}, \tau) + L v_O^1(\mathbf{x}, \tau) + L^2 v_O^2(\mathbf{x}, \tau) + ...$$

Substituting these expressions for u and v into (7.12)-(7.13), we have to leading order

$$\frac{d u_O^0}{d\tau} = -f(u_O^0, v_O^0) = -2 W_u(u_O^0, v_O^0),$$
$$\frac{d v_O^0}{d\tau} = -g(u_O^0, v_O^0) = -\frac{3}{2} W_v(u_O^0, v_O^0).$$

Hence (u_O^0, v_O^0) tends to a minimizer of $W(u, v)$ which will be one of $\mathbf{a}$, $\mathbf{b}$ or $\mathbf{c}$ at the triple point temperature [14].

7.3.2 Inner expansion on slow time scale

For the inner expansion close to an interface Γ_i, we introduce a time scale that is slower than τ, but faster than t, given by $T = \frac{t}{\sqrt{L}}$. We let the front position be described by a function $\phi(\mathbf{x}, T, t)$ and take expansions of u and v close to the front given by

$$u = u_I^0(z, \mathbf{x}, \tau, T, t) + \sqrt{L} u_I^1(z, \mathbf{x}, \tau, T, t) + L u_I^2(z, \mathbf{x}, \tau, T, t) + ...,$$
$$v = v_I^0(z, \mathbf{x}, \tau, T, t) + \sqrt{L} v_I^1(z, \mathbf{x}, \tau, T, t) + L v_I^2(z, \mathbf{x}, \tau, T, t) + ...,$$

where $z = \phi(\mathbf{x}, T, t)/\sqrt{L}$. Substituting these expressions for u and v into (7.4)-(7.5) gives to leading order

$$\frac{\partial u_I^0}{\partial \tau} + \frac{\partial \phi}{\partial T} \frac{\partial u_I^0}{\partial z} - (\nabla \phi)^2 \frac{\partial^2 u_I^0}{\partial z^2} + f(u_I^0, v_I^0) = 0, \tag{7.14}$$
$$\frac{\partial v_I^0}{\partial \tau} + \frac{\partial \phi}{\partial T} \frac{\partial v_I^0}{\partial z} - (\nabla \phi)^2 \frac{\partial^2 v_I^0}{\partial z^2} + g(u_I^0, v_I^0) = 0. \tag{7.15}$$

We follow the steps in [96], which discusses the scalar Allen-Cahn equation, to show that the fronts are stationary on the T time scale and evolve according to motion by mean curvature on the t time scale. Note that (7.14) and (7.15) are equations for u_I^0 and v_I^0 in z and τ, with $\mathbf{x}$, T and t being thought of as parameters. In order to find ϕ we assume that u_I^0 and v_I^0 tend to travelling waves for $\tau \to \infty$. Hence we suppose that $u_I^0(z, \mathbf{x}, \tau, T, t) \sim Q(z - c\tau, \mathbf{x}, T, t)$ and $v_I^0(z, \mathbf{x}, \tau, T, t) \sim P(z - c\tau, \mathbf{x}, T, t)$ as $\tau \to \infty$ for some constant c which corresponds to the

wave speed. On substitution into equations (7.14) and (7.15), we find $Q(z)$ and $P(z)$ must satisfy

$$- (\nabla \phi)^2 Q'' + \left(\frac{\partial \phi}{\partial T} - c \right) Q' + f(Q, P) = 0, \tag{7.16}$$

$$- (\nabla \phi)^2 P'' + \left(\frac{\partial \phi}{\partial T} - c \right) P' + g(Q, P) = 0. \tag{7.17}$$

To match the solution away from the front we assume that $(Q(z), P(z))$ tends to $\mathbf{a}$, $\mathbf{b}$ or $\mathbf{c}$ as $z \to \pm \infty$, for example, $(Q, P) \to \mathbf{a}$ as $z \to -\infty$ and $(Q, P) \to \mathbf{b}$ as $z \to \infty$.

Multiplying equations (7.16) and (7.17) through by $\frac{Q'}{2}$ and $\frac{2P'}{3}$ respectively (scalings are motivated by (7.6)), adding the equations and integrating with respect to z yields

$$\left(\frac{\partial \phi}{\partial T} - c \right) \int_{-\infty}^{\infty} \frac{1}{2} (Q')^2 + \frac{2}{3} (P')^2 \, \mathrm{d}z = -[W], \tag{7.18}$$

where $[W] = W(Q(\infty), P(\infty)) - W(Q(-\infty), P(-\infty))$ and denotes the change in W over the front. Here $[W] = 0$ across each front because at the triple point temperature $W(u, v)$ is an equal triple welled potential. We introduce new functions R^u and R^v:

$$R^u \left(\frac{z - c\tau}{|\nabla \phi|} \right) = Q(z - c\tau, \mathbf{x}, T, t) \quad \text{and} \quad R^v \left(\frac{z - c\tau}{|\nabla \phi|} \right) = P(z - c\tau, \mathbf{x}, T, t).$$

Equations (7.16)-(7.17) and (7.18) give that $R^u(z)$ and $R^v(z)$ satisfy

$$R^{u\prime\prime} - f(R^u, R^v) = 0, \tag{7.19}$$

$$R^{v\prime\prime} - g(R^u, R^v) = 0. \tag{7.20}$$

Recall the assumption that u_I^0 and v_I^0 tend to travelling waves as $\tau \to \infty$. Then, in this limit, by the definitions of Q, P, R^u and R^v we can write

$$u_I^0(\mathbf{x}, T, L) \sim R^u \left(\frac{\phi - cT}{\sqrt{L}|\nabla \phi|} \right) \quad \text{and} \quad v_I^0(\mathbf{x}, T, L) \sim R^v \left(\frac{\phi - cT}{\sqrt{L}|\nabla \phi|} \right).$$

Hence, equations (7.19) and (7.20) give evolution equations for the fronts in the T time scale. The front position is given by solutions of $\phi - cT = 0$. As $[W] = 0$, then (7.18) gives that $\frac{\partial \phi}{\partial T} - c = 0$ and hence the front is stationary on the T time scale.

The second-order equations for the inner expansions of u and v in (7.4)-(7.5) are given by

$$\frac{\partial u_I^1}{\partial \tau} + \frac{\partial \phi}{\partial T}\frac{\partial u_I^1}{\partial z} - (\nabla \phi)^2 \frac{\partial^2 u_I^1}{\partial z^2} + \frac{\partial f(u_I^0, v_I^0)}{\partial u} u_I^1 + \frac{\partial f(u_I^0, v_I^0)}{\partial v} v_I^1$$
$$= -\frac{\partial u_I^0}{\partial T} + \nabla^2 \phi \frac{\partial u_I^0}{\partial z} + 2\nabla \phi \cdot \nabla \left(\frac{\partial u_I^0}{\partial z}\right) - \frac{\partial \phi}{\partial t}\frac{\partial u_I^0}{\partial z},$$

$$\frac{\partial v_I^1}{\partial \tau} + \frac{\partial \phi}{\partial T}\frac{\partial v_I^1}{\partial z} - (\nabla \phi)^2 \frac{\partial^2 v_I^1}{\partial z^2} + \frac{\partial g(u_I^0, v_I^0)}{\partial v} v_I^1 + \frac{\partial g(u_I^0, v_I^0)}{\partial u} u_I^1$$
$$= -\frac{\partial v_I^0}{\partial T} + \nabla^2 \phi \frac{\partial v_I^0}{\partial z} + 2\nabla \phi \cdot \nabla \left(\frac{\partial v_I^0}{\partial z}\right) - \frac{\partial \phi}{\partial t}\frac{\partial v_I^0}{\partial z}.$$

Again these are equations in z and τ only, with $\mathbf{x}$, T and t thought of as parameters. In a similar manner as before, again following the steps in [96], we assume $u_I^1(z, \mathbf{x}, \tau, T, t) \sim Q_1(z - c\tau, \mathbf{x}, T, t)$ and $v_I^1(z, \mathbf{x}, \tau, T, t) \sim P_1(z - c\tau, \mathbf{x}, T, t)$ as $\tau \to \infty$. We have seen previously that the front is stationary on the T time scale and $\frac{\partial \phi}{\partial T} - c = 0$. Hence $\nabla \phi$ is independent of T. Further Q and P are independent of T by equations (7.16) and (7.17). Therefore, we find

$$-(\nabla \phi)^2 Q_1'' + 2W_{QQ}(Q, P)Q_1 + 2W_{QP}P_1 = (\nabla^2 \phi + 2\nabla \phi \cdot \nabla)Q' - \frac{\partial \phi}{\partial t}Q', \qquad (7.21)$$

$$-(\nabla \phi)^2 P_1'' + \frac{3}{2}W_{PP}(Q, P)P_1 + \frac{3}{2}W_{QP}Q_1 = (\nabla^2 \phi + 2\nabla \phi \cdot \nabla)P' - \frac{\partial \phi}{\partial t}P'. \qquad (7.22)$$

Taking derivatives with respect to z in (7.16) and (7.17) gives that if $[W]=0$ then

$$-(\nabla \phi)^2 Q''' + 2W_{QQ}(Q, P)Q' + 2W_{QP}P' = 0, \qquad (7.23)$$

$$-(\nabla \phi)^2 P''' + \frac{3}{2}W_{PP}(Q, P)P' + \frac{3}{2}W_{QP}Q' = 0. \qquad (7.24)$$

Equations (7.21)-(7.22) are multiplied through by $\frac{Q'}{2}$ and $\frac{2P'}{3}$ respectively, added together and integrated over z. Two application of integration by parts leads to

$$\int_{-\infty}^{\infty} Q_1 \left[-\frac{1}{2}(\nabla \phi)^2 Q''' + W_{QQ}(Q, P)Q' + W_{QP}P'\right] dz$$
$$+ \int_{-\infty}^{\infty} P_1 \left[-\frac{2}{3}(\nabla \phi)^2 P''' + W_{PP}(Q, P)P' + W_{QP}Q'\right] dz \qquad (7.25)$$
$$= \int_{-\infty}^{\infty} \left(\nabla^2 \phi - \frac{\partial \phi}{\partial t}\right)\left[\frac{1}{2}(Q')^2 + \frac{2}{3}(P')^2\right] + 2\nabla \phi \cdot \left[\frac{1}{2}Q'\nabla Q' + \frac{2}{3}P'\nabla P'\right] dz.$$

By (7.23)-(7.24), the left-hand side of (7.25) is zero and we find

$$\frac{\partial \phi}{\partial t} = \nabla^2 \phi + \frac{\nabla \phi \cdot \nabla \int_{-\infty}^{\infty} \frac{1}{2}(Q')^2 + \frac{2}{3}(P')^2 \, dz}{\int_{-\infty}^{\infty} \frac{1}{2}(Q')^2 + \frac{2}{3}(P')^2 \, dz}.$$

By definition $Q' = R^{u'}/|\nabla \phi|$ and $P' = R^{v'}/|\nabla \phi|$ so we can rewrite this equation in terms of ϕ:

$$\frac{\partial \phi}{\partial t} = \nabla^2 \phi - \frac{\nabla \phi \cdot \nabla |\nabla \phi|}{|\nabla \phi|}. \tag{7.26}$$

The right-hand side of this equation can be expressed as $|\nabla \phi| \kappa_\phi$ where $\kappa_\phi = \nabla \cdot (\nabla \phi / |\nabla \phi|)$ is the mean curvature of the level set $\phi = $ constant. Hence we have

$$\frac{\phi_t}{|\nabla \phi|} = \kappa_\phi. \tag{7.27}$$

The left-hand side of (7.27) gives the normal velocity of a level set of ϕ [96]. Recalling the assumption that u_I^0 and v_I^0 tend to travelling waves as $\tau \to \infty$, we can write

$$u_I^0(\mathbf{x}, T, L) \sim R^u \left(\frac{\phi - cT}{\sqrt{L} |\nabla(\phi - cT)|} \right) \quad \text{and} \quad v_I^0(\mathbf{x}, T, L) \sim R^v \left(\frac{\phi - cT}{\sqrt{L} |\nabla(\phi - cT)|} \right).$$

One can see that if ϕ satisfies equation (7.27) then so does $\phi - cT$, hence the level sets of $\phi - cT$ evolve according to mean curvature on the t time scale. As the front position is defined by solutions of $\phi - cT = 0$, the front propagates according to mean curvature on the t time scale.

7.3.3 Front propagation near the origin

The $-\frac{4u^2}{r^2}$ term in (7.4) first appears in the second-order equation for the inner expansion of u when $r = O(L^{\frac{1}{4}})$ at a point on the front. In this case we find that

$$\frac{d}{dt}(\phi - cT) = |\nabla \phi| \kappa_\phi - \frac{\sqrt{L}}{r^2} \frac{4[Q]_{-\infty}^{\infty}}{\int_{-\infty}^{\infty} \frac{1}{2}(Q')^2 + \frac{2}{3}(P')^2 \, dz}.$$

This extra term is negative when we take the origin to be on the $z < 0$ side of the front (positive if we take the origin to be on the $z > 0$ side) and as the position is given by solutions of $\phi - cT = 0$, this term opposes front motion towards the origin, as would be expected.

7.3.4 Front behaviour at the triple junction

If the three fronts are distinct and do not meet, front evolution will be as discussed previously, with each interface evolving according to its mean curvature on the t time scale at the triple point temperature. Here we study the scenario that the three fronts meet at a triple junction. In this section we follow the steps in [14] to find an angle condition at this triple junction. Working on the t time scale on which the interfaces evolve at the triple point temperature, we define $\mathbf{m}(t)$ as the position of the triple junction. We introduce new coordinates:

$$\mathbf{X}_i = \frac{\mathbf{x} - \mathbf{m}(t)}{\sqrt{L}},$$

for $\mathbf{X}_i = (\xi_i, \eta_i)$ where ξ_i are coordinates tangent to front Γ_i and η_i are coordinates perpendicular to front Γ_i, as shown in Figure 7-3.
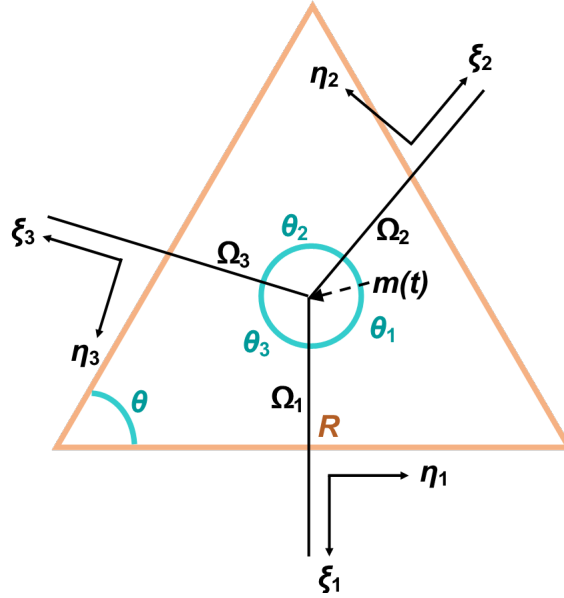
Figure 7-3: Diagram showing variables close to the triple junction over a triangular region Ω with base size R around $\mathbf{m}(t)$ with Ω_i being the tangent plane of Γ_i at $\mathbf{m}(t)$ [14].

We take asymptotic expansions of u and v near the triple junction and $\mathbf{X}_1 = 0$:

$$u = u_m^0(\mathbf{X}_1, t) + \sqrt{L}u_m^1(\mathbf{X}_1, t) + Lu_m^2(\mathbf{X}_1, t) + ..., \tag{7.28}$$

$$u = v_m^0(\mathbf{X}_1, t) + \sqrt{L}v_m^1(\mathbf{X}_1, t) + Lv_m^2(\mathbf{X}_1, t) + ... \tag{7.29}$$

On substitution of these expansions into (7.4)-(7.5) we find leading order behaviour

$$\nabla^2_{X_1} u^0_m - f(u^0_m, v^0_m) = 0, \tag{7.30}$$

$$\nabla^2_{X_1} v^0_m - g(u^0_m, v^0_m) = 0, \tag{7.31}$$

where $\nabla^2_{X_1}$ is the Laplacian with respect to the new variable $\mathbf{X}_1$. We need to match the solutions of equations (7.30) and (7.31) with u^0_{l1} and v^0_{l1}-the leading order solutions near the front Γ_1 and away from $\mathbf{m}(t)$, which are discussed in the previous subsection. In general this requires that

$$\lim_{\xi_i \to \infty} u^0_m(\xi_i, \eta_i) = u^0_{li}(\eta_i) \quad \text{and} \quad \lim_{\xi_i \to \infty} v^0_m(\xi_i, \eta_i) = v^0_{li}(\eta_i), \tag{7.32}$$

where η_i is fixed [108, 14] for $i = 1, 2, 3$ and the functions u^0_{li} and v^0_{li} are the leading order solutions of u and v near the front Γ_i and away from $\mathbf{m}(t)$.

The next step is to multiply equations (7.30) and (7.31) by $\frac{\partial u^0_m}{\partial \eta_1}$ and $\frac{\partial v^0_m}{\partial \eta_1}$ respectively and then integrate over Ω, the region depicted in Figure 7-3 [84, 14]:

$$\int\int_\Omega \frac{\partial u^0_m}{\partial \eta_1} f(u^0_m, v^0_m) \, d\mathbf{X}_1 = \int\int_\Omega \frac{\partial u^0_m}{\partial \eta_1} \frac{\partial^2 u^0_m}{\partial \eta_1^2} + \frac{\partial u^0_m}{\partial \eta_1} \frac{\partial^2 u^0_m}{\partial \xi_1^2} \, d\mathbf{X}_1,$$

$$\int\int_\Omega \frac{\partial v^0_m}{\partial \eta_1} g(u^0_m, v^0_m) \, d\mathbf{X}_1 = \int\int_\Omega \frac{\partial v^0_m}{\partial \eta_1} \frac{\partial^2 v^0_m}{\partial \eta_1^2} + \frac{\partial v^0_m}{\partial \eta_1} \frac{\partial^2 v^0_m}{\partial \xi_1^2} \, d\mathbf{X}_1.$$

These equations can be multiplied through by $\frac{1}{2}$ and $\frac{2}{3}$ respectively (see equation (7.6)), added together and rearranged to give

$$\int\int_\Omega \frac{\partial}{\partial \eta_1} \left[W(u^0_m, v^0_m) + \frac{1}{4}\left(\frac{\partial u^0_m}{\partial \xi_1}\right)^2 - \frac{1}{4}\left(\frac{\partial u^0_m}{\partial \eta_1}\right)^2 + \frac{1}{3}\left(\frac{\partial v^0_m}{\partial \xi_1}\right)^2 - \frac{1}{3}\left(\frac{\partial v^0_m}{\partial \eta_1}\right)^2 \right] d\mathbf{X}_1$$

$$= \int\int_\Omega \frac{\partial}{\partial \xi_1} \left(\frac{2}{3}\frac{\partial v^0_m}{\partial \eta_1}\frac{\partial v^0_m}{\partial \xi_1} + \frac{1}{2}\frac{\partial u^0_m}{\partial \eta_1}\frac{\partial u^0_m}{\partial \xi_1} \right) d\mathbf{X}_1.$$

An application of the Divergence theorem yields

$$\int_{\partial\Omega} \left[W(u^0_m, v^0_m) + \frac{1}{4}\left(\frac{\partial u^0_m}{\partial \xi_1}\right)^2 - \frac{1}{4}\left(\frac{\partial u^0_m}{\partial \eta_1}\right)^2 + \frac{1}{3}\left(\frac{\partial v^0_m}{\partial \xi_1}\right)^2 - \frac{1}{3}\left(\frac{\partial v^0_m}{\partial \eta_1}\right)^2 \right] v_1 \, ds \tag{7.33}$$

$$= -\int_{\partial\Omega} \left(\frac{2}{3}\frac{\partial v^0_m}{\partial \eta_1}\frac{\partial v^0_m}{\partial \xi_1} + \frac{1}{2}\frac{\partial u^0_m}{\partial \eta_1}\frac{\partial u^0_m}{\partial \xi_1} \right) v_2 \, ds,$$

where $\mathbf{v} = (v_1, v_2)$ is the outward unit normal vector to $\partial\Omega$.

Recalling the definitions of ξ_i and η_i, we have that

$$\eta_i = -\sin(\gamma_i)\eta_1 - \cos(\gamma_i)\xi_1 \quad \text{and} \quad \xi_i = \cos(\gamma_i)\eta_1 - \sin(\gamma_i)\xi_1, \tag{7.34}$$

where γ_i gives the angle between the η_1 axis and Ω_i, the tangent plane to Γ_i at $\mathbf{m}(t)$ (considering an anticlockwise rotation). The expressions for ξ_1 and η_1 in (7.34) give

$$\left(\frac{\partial u_m^0}{\partial \xi_1}\right)^2 - \left(\frac{\partial u_m^0}{\partial \eta_1}\right)^2 = -\cos(2\gamma_i)\left(\frac{\partial u_m^0}{\partial \xi_i}\right)^2 + 4\left(\frac{\partial u_m^0}{\partial \eta_i}\frac{\partial u_m^0}{\partial \xi_i}\sin(\gamma_i)\cos(\gamma_i)\right) + \cos(2\gamma_i)\left(\frac{\partial u_m^0}{\partial \eta_i}\right)^2,$$

$$\left(\frac{\partial v_m^0}{\partial \xi_1}\right)^2 - \left(\frac{\partial v_m^0}{\partial \eta_1}\right)^2 = -\cos(2\gamma_i)\left(\frac{\partial v_m^0}{\partial \xi_i}\right)^2 + 4\left(\frac{\partial v_m^0}{\partial \eta_i}\frac{\partial v_m^0}{\partial \xi_i}\sin(\gamma_i)\cos(\gamma_i)\right) + \cos(2\gamma_i)\left(\frac{\partial v_m^0}{\partial \eta_i}\right)^2,$$

for $i = 1, 2, 3$. In a similar vein we have that

$$-\frac{\partial u_m^0}{\partial \eta_1}\frac{\partial u_m^0}{\partial \xi_1} = \left(\frac{\partial u_m^0}{\partial \xi_i}\right)^2\cos(\gamma_i)\sin(\gamma_i) + \frac{\partial u_m^0}{\partial \xi_i}\frac{\partial u_m^0}{\partial \eta_i}\cos(2\gamma_i) + \left(\frac{\partial u_m^0}{\partial \eta_i}\right)^2\cos(\gamma_i)\sin(\gamma_i),$$

$$-\frac{\partial v_m^0}{\partial \eta_1}\frac{\partial v_m^0}{\partial \xi_1} = \left(\frac{\partial v_m^0}{\partial \xi_i}\right)^2\cos(\gamma_i)\sin(\gamma_i) + \frac{\partial v_m^0}{\partial \xi_i}\frac{\partial v_m^0}{\partial \eta_i}\cos(2\gamma_i) + \left(\frac{\partial v_m^0}{\partial \eta_i}\right)^2\cos(\gamma_i)\sin(\gamma_i),$$

also for $i = 1, 2, 3$. The next step in [14] is to write $d\eta_1 = ds$, $d\eta_2 = \sin(\gamma_2 + \theta)\,ds$ and $d\eta_3 = \sin(\gamma_3 - \theta)\,ds$ where θ is the angle shown in Figure 7-3 and apply this change of variables to the above expressions. These expressions are then substituted into (7.33). As in [14], we split $\partial\Omega$ into two domains and take the length of the base of the triangular region Ω, $R \to \infty$. The first domain is everywhere within a distance of α of front Γ_i and the second domain is everywhere outside a distance of α of front Γ_i. Working in the limits $R \to \infty$ and $\alpha \to \infty$, the integrals over the second domain in (7.33) vanish due the matching condition as $u_m^0 \to u_O^0$ in the integrand. Therefore, with the change of variables and the expressions above, the left-hand side of (7.33) reduces to

$$\lim_{\alpha \to \infty}\lim_{\substack{R \to \infty \\ |\eta_i| < \alpha}}\int_{\partial\Omega}\left[W(u_m^0, v_m^0) + \frac{1}{4}\left(\frac{\partial u_m^0}{\partial \xi_1}\right)^2 - \frac{1}{4}\left(\frac{\partial u_m^0}{\partial \eta_1}\right)^2 + \frac{1}{3}\left(\frac{\partial v_m^0}{\partial \xi_1}\right)^2 - \frac{1}{3}\left(\frac{\partial v_m^0}{\partial \eta_1}\right)^2\right]v_1\,ds$$

$$= \int_{-\infty}^{\infty}\left[\left(\frac{1}{4}\left(\frac{\partial u_{I2}^0}{\partial \eta_2}\right)^2 + \frac{1}{3}\left(\frac{\partial v_{I2}^0}{\partial \eta_2}\right)^2\right)\cos(2\gamma_2) + W(u_{I2}^0, v_{I2}^0)\right]\frac{\sin(\theta)}{\sin(\gamma_2 + \theta)}\,d\eta_2$$

$$- \int_{-\infty}^{\infty}\left[\left(\frac{1}{4}\left(\frac{\partial u_{I3}^0}{\partial \eta_3}\right)^2 + \frac{1}{3}\left(\frac{\partial v_{I3}^0}{\partial \eta_3}\right)^2\right)\cos(2\gamma_3) + W(u_{I3}^0, v_{I3}^0)\right]\frac{\sin(\theta)}{\sin(\gamma_3 - \theta)}\,d\eta_3.$$

The integral along $d\eta_1$ is zero because $v_1 d\eta_1 = 0$ as $v_1 = 0$ along the bottom edge of the triangle.

Using the same change of variable $(d\eta_1 = ds,\ d\eta_2 = \sin(\gamma_2 + \theta)ds,\ d\eta_3 = \sin(\gamma_3 - \theta)ds)$ the right-hand side of (7.33) becomes

$$\lim_{\alpha \to \infty} \lim_{\substack{R \to \infty \\ |\eta_i| < \alpha}} \int_{\partial\Omega} - \left(\frac{2}{3}\frac{\partial v_m^0}{\partial \eta_1}\frac{\partial v_m^0}{\partial \xi_1} + \frac{1}{2}\frac{\partial u_m^0}{\partial \eta_1}\frac{\partial u_m^0}{\partial \xi_1} \right) v_2 \, ds$$

$$= - \int_{-\infty}^{\infty} \left[\frac{1}{2}\left(\frac{\partial u_{I2}^0}{\partial \eta_2}\right)^2 + \frac{2}{3}\left(\frac{\partial v_{I2}^0}{\partial \eta_2}\right)^2 \right] \cos(\gamma_2)\sin(\gamma_2)\frac{\cos(\theta)}{\sin(\gamma_2 + \theta)} \, d\eta_2$$

$$- \int_{-\infty}^{\infty} \left[\frac{1}{2}\left(\frac{\partial u_{I3}^0}{\partial \eta_3}\right)^2 + \frac{2}{3}\left(\frac{\partial v_{I3}^0}{\partial \eta_3}\right)^2 \right] \cos(\gamma_3)\sin(\gamma_3)\frac{\cos(\theta)}{\sin(\gamma_3 - \theta)} \, d\eta_3,$$

and again the integral along $d\eta_1$ is zero, this is because $\cos(\gamma_1) = \cos(3\pi/2) = 0$. Equating the left- and right-hand sides of (7.33) we obtain

$$\int_{-\infty}^{\infty} \left[\left(\frac{1}{4}\left(\frac{\partial u_{I2}^0}{\partial \eta_2}\right)^2 + \frac{1}{3}\left(\frac{\partial v_{I2}^0}{\partial \eta_2}\right)^2 \right)\cos(2\gamma_2) + W(u_{I2}^0, v_{I2}^0) \right] \frac{\sin(\theta)}{\sin(\gamma_2 + \theta)} \, d\eta_2$$

$$- \int_{-\infty}^{\infty} \left[\left(\frac{1}{4}\left(\frac{\partial u_{I3}^0}{\partial \eta_3}\right)^2 + \frac{1}{3}\left(\frac{\partial v_{I3}^0}{\partial \eta_3}\right)^2 \right)\cos(2\gamma_3) + W(u_{I3}^0, v_{I3}^0) \right] \frac{\sin(\theta)}{\sin(\gamma_3 - \theta)} \, d\eta_3$$

$$= - \int_{-\infty}^{\infty} \left[\frac{1}{2}\left(\frac{\partial u_{I2}^0}{\partial \eta_2}\right)^2 + \frac{2}{3}\left(\frac{\partial v_{I2}^0}{\partial \eta_2}\right)^2 \right] \cos(\gamma_2)\sin(\gamma_2)\frac{\cos(\theta)}{\sin(\gamma_2 + \theta)} \, d\eta_2$$

$$- \int_{-\infty}^{\infty} \left[\frac{1}{2}\left(\frac{\partial u_{I3}^0}{\partial \eta_3}\right)^2 + \frac{2}{3}\left(\frac{\partial v_{I3}^0}{\partial \eta_3}\right)^2 \right] \cos(\gamma_3)\sin(\gamma_3)\frac{\cos(\theta)}{\sin(\gamma_3 - \theta)} \, d\eta_3.$$

(7.35)

The final step is to use the following lemma proved in [105, 14]. A slight change is required because we have $f(u, v) = 2W_u(u, v)$ and $g(u, v) = \frac{3}{2}W_v(u, v)$ (see (7.6)) as opposed to $f(u, v) = W_u(u, v)$ and $g(u, v) = W_v(u, v)$. The first relation in (7.36) has been scaled appropriately. This lemma gives properties of the geodesics connecting minima of W found by minimizing a weighted distance function.

Lemma 7.1. *Define*

$$\Phi^{ab}(b) = \inf_{\substack{p \in C^1 \\ p(-1) = a,\, p(1) = b}} \int_{-1}^{1} \sqrt{W(p_1(t), p_2(t))} \left(\frac{1}{4}\left(\frac{dp_1(t)}{dt}\right)^2 + \frac{1}{3}\left(\frac{dp_2(t)}{dt}\right)^2 \right)^{\frac{1}{2}} dt.$$

Let $\mathbf{p}_{ab}(t)$ be a geodesic connecting $\mathbf{a}$ to $\mathbf{b}$. Then there exists a smooth increasing function $\beta : (-\infty, \infty) \to (-1, 1)$ so that the curve $\gamma_{ab}(z) = \mathbf{p}_{ab}(\beta(z))$ is a solution of (7.19)-(7.20).

The function $\gamma_{ab} = (\gamma_{ab1}, \gamma_{ab2})$ satisfies

$$\frac{1}{4}\left(\frac{\partial \gamma_{ab1}}{\partial z}\right)^2 + \frac{1}{3}\left(\frac{\partial \gamma_{ab2}}{\partial z}\right)^2 = W(\gamma_{ab1}, \gamma_{ab2}) \quad \text{and} \quad \Phi^{ab}(b) = \int_{-\infty}^{\infty} W(\gamma_{ab1}(z), \gamma_{ab2}(z))\, dz.$$

$$(7.36)$$

Lemma 7.1 and relation (7.36) give that (7.35) can be written as

$$\cos^2(\gamma_2)\frac{\sin(\theta)}{\sin(\gamma_2 + \theta)}\Phi^{bc}(c) - \cos^2(\gamma_3)\frac{\sin(\theta)}{\sin(\gamma_3 - \theta)}\Phi^{ca}(a) =$$
$$- \cos(\gamma_2)\sin(\gamma_2)\frac{\cos(\theta)}{\sin(\gamma_2 + \theta)}\Phi^{bc}(c) - \cos(\gamma_3)\sin(\gamma_3)\frac{\cos(\theta)}{\sin(\gamma_3 - \theta)}\Phi^{ca}(a).$$

In the above we have used the relation $\cos(2\gamma_i) = 2\cos^2(\gamma_i) - 1$. On expanding $\sin(\gamma_2 + \theta)$ and $\sin(\gamma_3 - \theta)$ this becomes $\cos(\gamma_2)\Phi^{bc}(c) = -\cos(\gamma_3)\Phi^{ca}(a)$. Now, for θ_1 and θ_3 as in Figure 7-3, $\gamma_2 + \frac{\pi}{2} = \theta_1$ and $\frac{3\pi}{2} - \gamma_3 = \theta_3$ so

$$\sin(\theta_1)\Phi^{bc}(c) = \sin(\theta_3)\Phi^{ca}(a). \tag{7.37}$$

Rotating Ω so that Γ_2 is perpendicular to the base of the triangle in Figure 7-3, we can repeat the analysis to find the translated relation

$$\sin(\theta_2)\Phi^{ca}(a) = \sin(\theta_3)\Phi^{ab}(b). \tag{7.38}$$

Equations (7.37) and (7.38) give an angle condition at the triple junction $\mathbf{m}(t)$. If W is an equal triple welled potential with $[W] = 0$ across each front, such as at a triple point temperature, then (7.36) gives that $\Phi^{ca}(a) = \Phi^{ab}(b) = \Phi^{bc}(c)$. In this case $\sin(\theta_1) = \sin(\theta_2) = \sin(\theta_3)$, so all the angles are the same and hence equal $2\pi/3$.

7.4 Triple phase numerical simulations

We finish this chapter with numerical simulations of the full Landau-de Gennes gradient flow system on the unit disc. We work with the parameters used to generate the $W(u, v)$ contour plot in Figure 7-1 ($A = 0.2387$, $B = 1.5920$, $C = -1$, $D = 0$, $E = 1$, $F = 25$) and solve the full Landau-de Gennes gradient flow system with sixth-order bulk potential, non-dimensionalized and as given in (7.3).

We impose boundary and initial conditions compatible with fronts between the stable biaxial, uniaxial and isotropic states, denoted **a**, **b** and **c** respectively. In the first sets of simulations we impose the biaxial boundary condition

$$\mathbf{Q} = \frac{a_1}{2}\left(\hat{\mathbf{r}} \otimes \hat{\mathbf{r}} - \mathbf{m} \otimes \mathbf{m}\right) + a_2\left(\mathbf{p} \otimes \mathbf{p} - \frac{\mathbf{I}}{3}\right) \quad \text{on} \quad r = 1,$$

where a_1 and a_2 are the u and v components of $\mathbf{a} = (a_1, a_2)$ which corresponds to the biaxial stable state. In the next sets of simulations we impose discontinuous boundary conditions, where two or three states are imposed in different sections of the boundary. We compare the evolution of the fronts imposed in our initial conditions with the evolution predicted by our analysis. That is, motion by mean curvature of individual fronts and equal angles between each pair of fronts at a triple junction.

Our first initial condition has a front structure such that

$$\mathbf{Q}(\mathbf{x}, 0) = \begin{cases} 0 & \text{for} \quad 0 \leq r < r_1, \\ \frac{b_1}{2}\left(\hat{\mathbf{r}} \otimes \hat{\mathbf{r}} - \mathbf{m} \otimes \mathbf{m}\right) + b_2\left(\mathbf{p} \otimes \mathbf{p} - \frac{\mathbf{I}}{3}\right) & \text{for} \quad r_1 < r < r_2, \\ \frac{a_1}{2}\left(\hat{\mathbf{r}} \otimes \hat{\mathbf{r}} - \mathbf{m} \otimes \mathbf{m}\right) + a_2\left(\mathbf{p} \otimes \mathbf{p} - \frac{\mathbf{I}}{3}\right) & \text{for} \quad r_2 < r \leq 1, \end{cases} \tag{7.39}$$

where $0 < r_1 < r_2 < 1$ and b_1 and b_2 are the u and v components of $\mathbf{b} = (b_1, b_2)$ which corresponds to the uniaxial stable state. The initial condition is given explicitly by

$$\begin{aligned} \mathbf{Q}(\mathbf{x}, 0) =& \frac{1}{2}\left[1 + \tanh\left(\frac{r - r_2}{\sqrt{L}}\right)\right]\left(\frac{b_1}{2}\left(\hat{\mathbf{r}} \otimes \hat{\mathbf{r}} - \mathbf{m} \otimes \mathbf{m}\right) + b_2\left(\mathbf{p} \otimes \mathbf{p} - \frac{\mathbf{I}}{3}\right)\right) \\ &+ \frac{1}{2}\left[1 + \tanh\left(\frac{r - r_1}{\sqrt{L}}\right)\right]\left(\frac{a_1 - b_1}{2}\left(\hat{\mathbf{r}} \otimes \hat{\mathbf{r}} - \mathbf{m} \otimes \mathbf{m}\right) + (a_1 - b_2)\left(\mathbf{p} \otimes \mathbf{p} - \frac{\mathbf{I}}{3}\right)\right). \end{aligned}$$

We take $r_1 = 0.4$, $r_2 = 0.6$ and $L = 0.01$. Figure 7-4 illustrates the evolution of $|\mathbf{Q}(\mathbf{r}, t)|^2$ on the disc. The initial front remains radially symmetric as it collapses to the origin. Simulated front evolution is compared to motion by mean curvature in Figure 7-5 which corroborates the asymptotic analysis. The plots of the eigenvalues of $\mathbf{Q}(\mathbf{r}, t)$ in Figure 7-6 demonstrate the division of the disc into the three stable states. As for previous planar initial conditions, both fronts are arrested near the origin. We also consider an initial condition with a radially asymmetric front structure which is based on initial condition (7.39) and shown in the first time panel of Figure 7-7. The front becomes radially symmetric and travels inwards, suggesting motion by mean curvature as predicted.
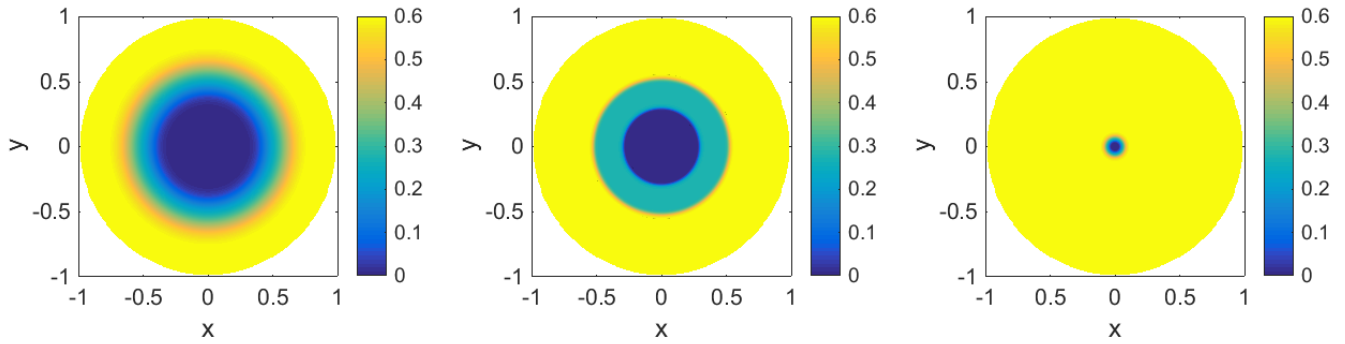
Figure 7-4: $|\mathbf{Q}(\mathbf{r}, t)|^2$ for initial condition (7.39) at $t = 0$, $t = 0.05$, and $t = 0.2$. The spatial resolution is $h = \frac{1}{256}$.
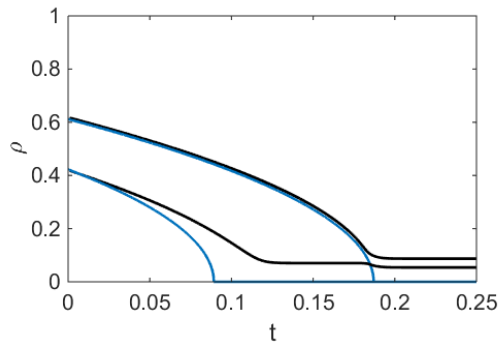
Figure 7-5: Front position ρ (black) for initial condition (7.39) and predicted position according to motion by mean curvature (blue) for the isotropic-uniaxial front (initial position $r = 0.4$) and the uniaxial-biaxial front (initial position $r = 0.6$). As in Chapters 3 and 5, we would expect the radius of the isotropic core of the steady solution to scale with $\sqrt{L}$ and for the fronts to be arrested at an $O(\sqrt{L})$ distance from the origin ($\sqrt{L} = 0.1$ in this figure). This contributes to the deviations from the predicted evolution by mean curvature seen in this figure.

Figure 7-6: Radial profiles of the eigenvalues of $\mathbf{Q}(\mathbf{r}, t)$ for initial condition (7.39) at $t = 0.002$, $t = 0.05$, and $t = 0.2$.

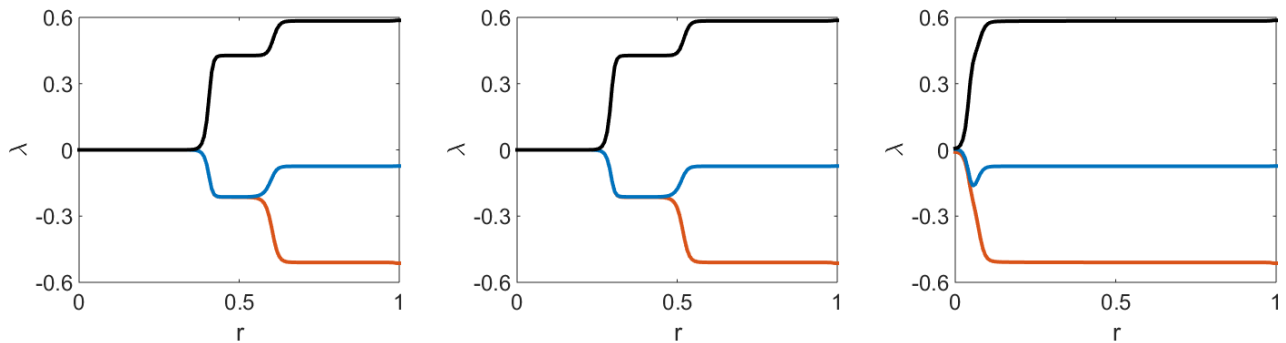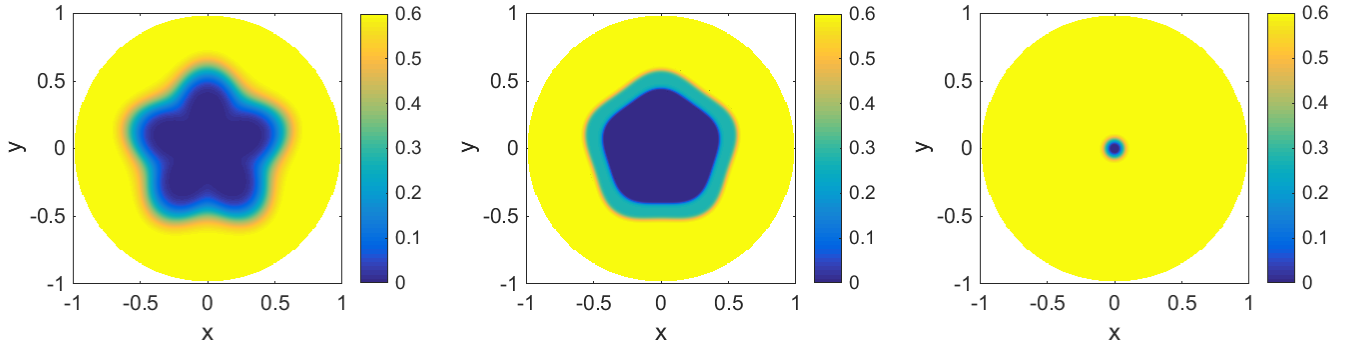Figure 7-7: $|\mathbf{Q}(\mathbf{r}, t)|^2$ for a radially asymmetric initial condition at $t = 0$, $t = 0.01$, and $t = 0.25$.

Next we consider an initial condition with a triple junction. This initial condition is shown in the first time panel of Figure 7-8. The three states, isotropic (dark blue), biaxial (yellow) and uniaxial (light blue), are separated by three fronts which meet at a triple junction. Our asymptotic analysis, which is restricted to (u, v)-type solutions of the Landau-de Gennes gradient flow system, predicts that for sufficiently small L, the fronts will evolve according to their mean curvature and each pair of interfaces will meet at angles of $\frac{2\pi}{3}$. However the numerical solutions of the full Landau-de Gennes gradient flow system do not exhibit this behaviour. Although the triple junction persists for a short time, the initial isotropic-biaxial front is not maintained and divides into isotropic-uniaxial and uniaxial-biaxial fronts. We conjecture that there is a point on the initial isotropic-biaxial interface where $(u, v) = (b_1 + \epsilon_1, b_2 + \epsilon_2)$ where ϵ_1, ϵ_2 are small (and $\mathbf{b} = (b_1, b_2)$ corresponds to the uniaxial state). This point on the isotropic-biaxial interface gets drawn towards the uniaxial minimizer and hence the front divides into isotropic-uniaxial and uniaxial-biaxial fronts. Once established, the new isotropic-uniaxial and uniaxial-biaxial fronts appear to evolve according to mean curvature, eventually forming straight fronts across the disc. This behaviour is illustrated with plots of $|\mathbf{Q}(\mathbf{r}, t)|^2$ in Figures 7-8 and 7-9.

Figure 7-8: $|\mathbf{Q}(\mathbf{r}, t)|^2$ for an initial condition with a triple junction at $t = 0$, $t = 0.001$, $t = 0.005$, $t = 0.01$, $t = 0.1$ and $t = 0.5$. The spatial resolution is $h = \frac{1}{256}$.
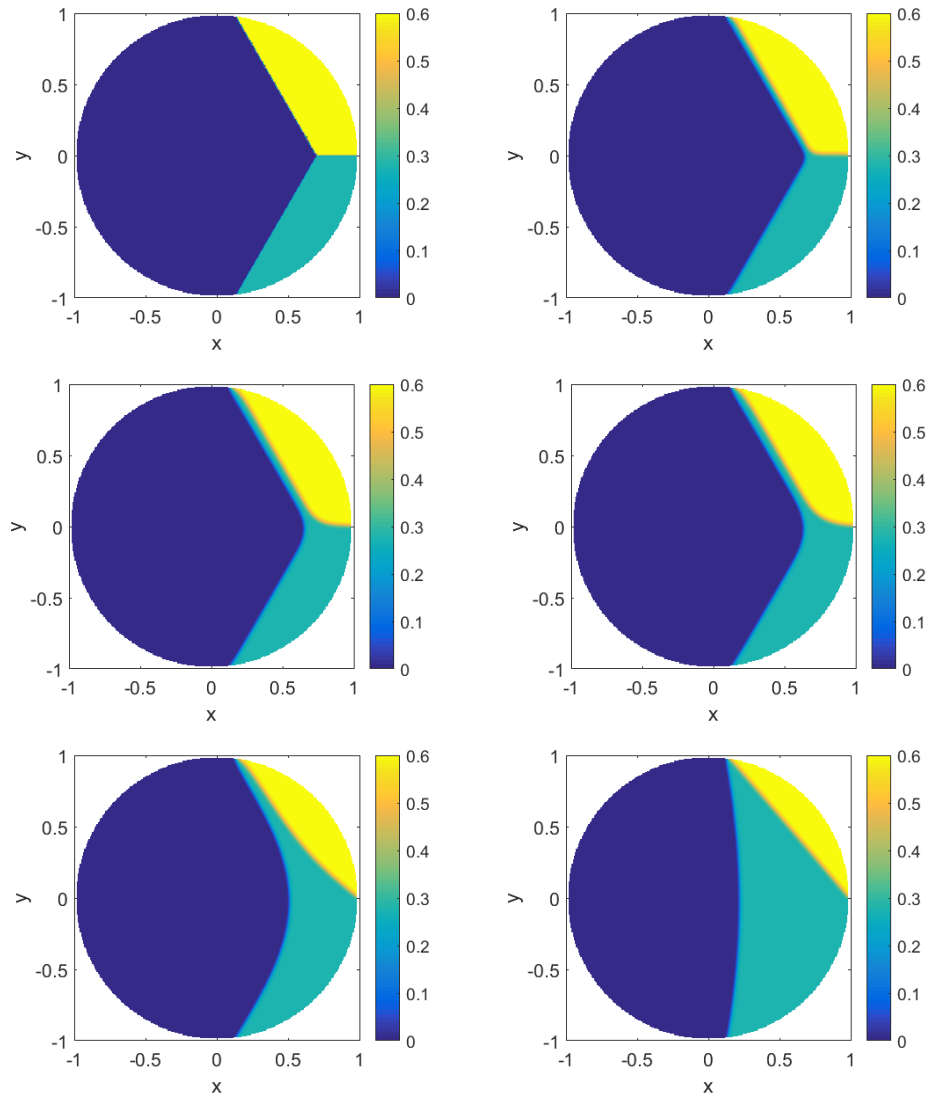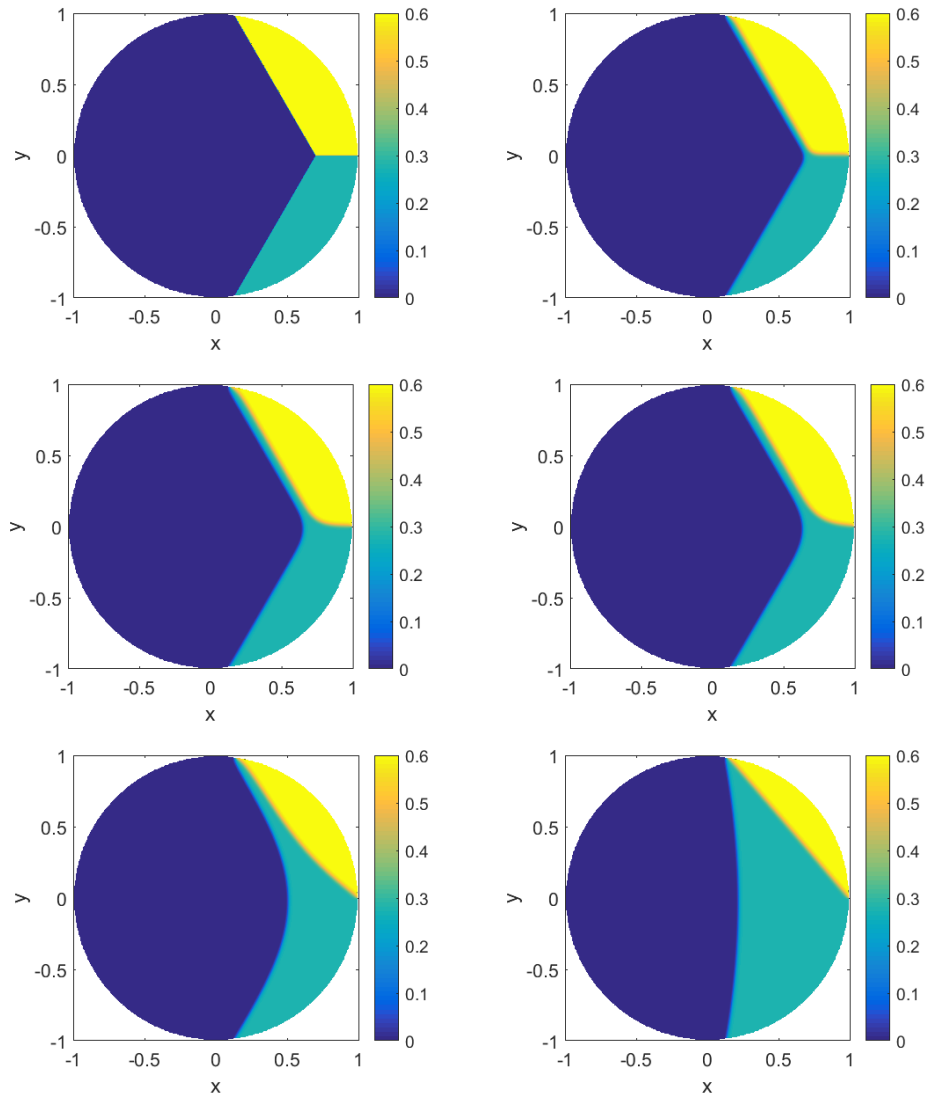
Figure 7-9: $|\mathbf{Q}(\mathbf{r}, t)|^2$ for an initial condition with a triple junction at $t = 0$, $t = 0.001$, $t = 0.005$, $t = 0.01$, $t = 0.1$ and $t = 0.5$. The spatial resolution is $h = \frac{1}{256}$.

Lastly, we consider an initial condition which allows us to study how the origin affects front motion, see the first time panel of Figure 7-10. Based on our analysis, we would expect the front to be arrested at the origin. However, we observe the front travelling across the origin, which is contained in the biaxial phase region of the converged solution in the last time panel of Figure 7-10. This suggests that the eigenvectors of $\mathbf{Q}(\mathbf{r}, t)$ do not have a singularity at the origin and have evolved from the eigenvectors of $\mathbf{Q}(\mathbf{r}, 0)$. Therefore, $\mathbf{Q}(\mathbf{r}, t))$ is no longer of the assumed (u, v)-form considered in the asymptotic analysis.
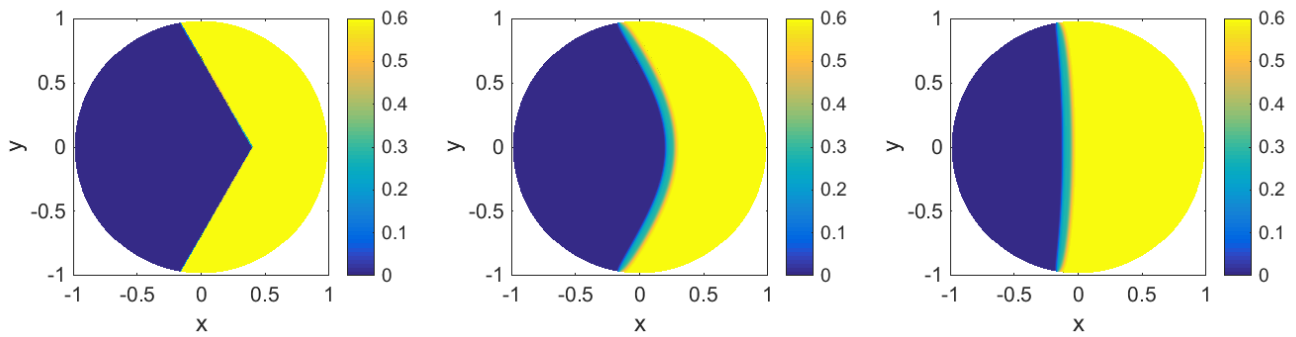
Figure 7-10: $|\mathbf{Q}(\mathbf{r}, t)|^2$ at $t = 0$, $t = 0.01$ and $t = 0.5$.

To conclude, our numerical simulations of the full Landau-de Gennes gradient flow system corroborate our asymptotic analysis of (u, v)-type solutions for individual interfaces, demonstrating that the fronts evolve according to their mean curvature for small L. However, our numerical simulations demonstrate a different behaviour at the triple junction than predicted by our asymptotic analysis. The three fronts are unable to meet at equal angles due to the division of the isotropic-biaxial front into isotropic-uniaxial and uniaxial-biaxial fronts. The numerical experiments also suggest that the $\mathbf{Q}$-tensor evolves from the ansatz assumed in the asymptotic analysis. In particular, the results imply that there is a minimizing biaxial $\mathbf{Q}$-tensor of the Landau-de Gennes energy in the limit $L \to 0$ which has no singularity at the origin.

Conclusions and future work

This thesis focuses on the gradient flow model of the Landau-de Gennes energy on prototype geometries, such as the sphere, the disc and the square, with Dirichlet boundary conditions and different representative initial conditions at the isotropic-nematic transition temperature. Here we summarize each chapter and discuss future perspectives.

8.1 Front propagation in spherical droplets

In Chapter 3 we consider the three-dimensional droplet with radial boundary conditions. In the case of uniaxial radially symmetric initial conditions with isotropic-nematic front structures, we adapt Ginzburg-Landau methods from [13, 15] to rigorously prove that the isotropic-nematic front propagates according to mean curvature in the $L \to 0$ limit. Further, numerical simulations show that the qualitative dynamics are universal for a large class of uniaxial and biaxial initial conditions, including radially asymmetric cases. The long-time dynamics are determined by the classical Radial Hedgehog solution which has been numerically demonstrated to be a global Landau-de Gennes energy minimizer in this regime [80].

In the future one could consider fluid flow across the interface between the isotropic and nematic states. This flow is not accounted for in the model discussed in Chapter 3 and therefore it would be interesting to study isotropic-nematic front propagation within, for example, the Beris-Edwards equations for nematodynamics as described in Sengupta 2013 [102]. These equations are

considered in Fei et al 2015 [43] to study isotropic-nematic front propagation using the method of matched asymptotics. The authors derive evolution laws for the velocity field, the director field of nematic alignment and the isotropic-nematic interface but do not consider the effects of boundary or initial conditions. We would focus on the effects of boundary and initial data on the persistence and evolution of isotropic-nematic fronts in the presence of fluid flow.

Another natural extension would be to rigorously prove motion by mean curvature of the isotropic-nematic front with radially asymmetric initial conditions. This could be achieved by a level set approach such as in Evans et al 1992 [41] for the Ginzburg-Landau framework.

8.2 Front propagation in heterogeneous materials

In Chapter 4 we study the propagation of isotropic-nematic fronts in a three-dimensional droplet in the presence of obstacles modelled by periodic forcing terms. We adapt arguments from [35] to the three-dimensional case with small elastic constant in model situations where forcing contributions are dominant over mean curvature contributions to front propagation and prove the existence of pulsating wave solutions for forcings greater in magnitude than a critical forcing. We provide estimates for the average front velocity in this regime. The critical forcing is verified via numerical simulations of the full Landau-de Gennes gradient flow system on the annulus.

In Chapter 4 we also investigate isotropic-nematic front propagation on the unit square with periodic forcing terms which induce forwards front motion and a moon-shaped obstacle opposing front motion. We demonstrate that for some forcing strengths, the interface is pinned by the long rounded side of the moon. However, if the moon-shaped obstacle is flipped and the front meets the two points of the moon, the front is able to pass through the obstacle.

For the future, it would be ideal to generalise these results to random obstacles with no radial symmetry. In particular, we are interested in randomly positioned obstacles of random strength as studied in Dirr, Dondl and Scheutzow 2011 [36] for the Quenched Edwards-Wilkinson equation. In this paper, a supersolution is found using a percolation result from Dirr et al 2010 [34] to show that the obstacles pin the front in certain situations. These arguments can be adapted to the two-dimensional disc as the supersolution construction is still applicable and we are currently generalising the methods to the three-dimensional sphere.

8.3 Equilibrium configurations on the disc

In Chapter 5 we focus on dynamic solutions of the Landau-de Gennes gradient flow system on the disc. Our results are largely numerical and complemented by heuristics and analytical reasoning.

We demonstrate how a choice of planar or non-planar initial condition can influence the long-time dynamic behaviour. Planar initial conditions generate planar dynamic solutions with an isotropic core at the centre for all times whereas non-planar solutions follow the planar dynamics for some time before relaxing into a completely uniaxial state for long times. We also look at non-minimal boundary conditions which do not minimize the bulk potential. Non-minimal boundary conditions allow for dynamic scenarios outside the scope of minimal boundary conditions and since minimal boundary conditions are an idealization, non-minimal Dirichlet conditions can be more physically relevant. The long-time dynamics can be understood in terms of local and global minimizers of the Landau-de Gennes energy. Our numerical results show that a large class of physically relevant liquid crystal model problems can exhibit a well-defined isotropic-nematic front for a length of time that can be observed experimentally. These results also give insight into how boundary and initial conditions can be used to yield either largely disordered or ordered profiles.

One could rigorously prove interfacial motion by mean curvature for radially symmetric initial conditions for this model problem, in the limit of vanishing elastic constant. In particular, for the (u, v)-system studied on the disc in Chapter 5, we could adapt results from Bronsard and Stoth 1998 [16] which proves front evolution by mean curvature for a similar two-dimensional vector system. Again, our dynamic equations differ from the Ginzburg-Landau model by an additional term. However, for L sufficiently small, this term should be controllable.

It would be interesting to analyse the minimizers of the Landau-de Gennes energy functional with non-minimal boundary conditions, motivated by the numerical study in Chapter 5. Recall that for minimal boundary conditions, in the limit of vanishing elastic constant, Landau-de Gennes minimizers converge uniformly to a limiting minimizing harmonic map away from singularities as discussed in [76]. The work in [76] is inspired by the analogous work in Bethuel et al 1994 [9] and Bethuel et al 1993 [8] for minimizers of the Ginzburg-Landau energy functional. In Andre and Shafrir 1998 [5] the authors adapt the arguments from [9] and [8] to prove convergence of Ginzburg-Landau minimizers to harmonic maps in the interior of a domain subject to non-minimal boundary conditions. A convenient form of the Landau-de Gennes energy functional is introduced in Majumdar, Pisante and Henao 2013 [75] (also see [80]) which allows us to write the Landau-de Gennes bulk potential as the sum of two separate contributions. The first contribution is the Ginzburg-Landau potential and the second contains information about the uniaxiality or biaxiality of the **Q**-tensor. This formulation would hopefully allow us to follow the steps in [5] to prove that global Landau-de Gennes minimizers converge to minimizing harmonic maps in the interior of a domain when non-minimal boundary conditions are imposed.

8.4 Equilibrium configurations on the square

We analytically and numerically study an Order Reconstruction-type Landau-de Gennes critical point on a square domain at a fixed temperature, motivated by the Well Order Reconstruction solution critical point reported in [60]. The WORS is distinguished by a constant eigenframe and a uniaxial cross with negative order parameter along the square diagonals. The WORS critical point is defined in terms of a scalar variational problem and is globally stable for edge lengths comparable to the biaxial correlation length of the order $\frac{\sqrt{L}}{\sqrt{C}}$. Stability is lost via a supercritical pitchfork bifurcation in the scalar variational setting as the edge length increases.

Recent numerical experiments in Robinson et al 2016 [95] show that there is a continuous branch of critical points emerging from the Well Order Reconstruction critical point for which the uniaxial cross continuously deforms from the diagonal towards the edges. In some cases, there can be up to 81 critical points for a given λ. Further, our numerical investigations on a square and a hexagon suggest that Order Reconstruction-type critical points exist and are globally stable for regular two-dimensional polygons with an even number of sides of sufficiently small length. It would be interesting to study the generic character of Order Reconstruction-type critical points further in future work.

8.5 Triple phase front propagation

In Chapter 7 we study the propagation of isotropic-uniaxial, uniaxial-biaxial and isotropic-biaxial fronts which meet at a triple junction. We work with a sixth-order Landau-de Gennes bulk potential which allows for isotropic, uniaxial and biaxial minima unlike the fourth-order potential employed in previous chapters. We discuss the existence of a triple point temperature at which there exists equal energy minimizing isotropic, uniaxial and biaxial states of the sixth-order bulk potential. We use asymptotic methods to show that all fronts evolve according to their mean curvature and the angle between each pair of interfaces is equal at a triple junction. We conclude with numerical experiments for the full Landau-de Gennes gradient flow system with sixth-order bulk potential. When circular fronts connect the three states our numerical simulations agree with the asymptotic analysis and the fronts evolve according mean curvature. However an initial condition with a triple junction does not yield the expected behaviour and the isotropic-biaxial fronts divides into isotropic-uniaxial and uniaxial-biaxial fronts. This may be because a pair of isotropic-uniaxial and uniaxial-biaxial fronts are energetically preferable to a single isotropic-biaxial front due to the positions of the wells of our potential in the plane.

Throughout the asymptotic analysis, we mostly assume that all fronts are well away from the

origin. It would be interesting to extend the asymptotic analysis of (u, v)-front evolution close to $r = 0$, where the fronts should be arrested. However, our numerical results suggest that the minimizing biaxial **Q**-tensor evolves from the ansatz assumed in the asymptotic analysis to a biaxial **Q**-tensor with no singularity at the origin. One may be able to extend the analysis in [76] to study the existence of minimizing biaxial **Q**-tensors of the Landau-de Gennes energy functional with sixth-order bulk potential in the $L \to 0$ limit.

8.6 Final conclusion

In this thesis, we study the Landau-de Gennes energy functional for nematic liquid crystals. We consider either a fourth-order Landau-de Gennes bulk potential which admits isotropic and uniaxial minima or, as in Chapter 7, a sixth-order bulk potential which admits biaxial minima in addition. We are interested in distinguished temperatures at which the bulk potential becomes an equal welled potential. Working at these special temperatures and on several geometries including the three-dimensional droplet, the disc and the square, we look for solutions to the Landau-de Gennes gradient flow system with front structures connecting the relevant minimizing states. In particular, we are interested in how Dirichlet boundary conditions and different types of initial conditions affect interface motion and persistence. We use the existence of different critical points of the Landau-de Gennes energy to study these transient dynamics. Namely, we study Radial Hedgehog-type solutions on the sphere, two parameter (u, v)-solutions on the disc and the Order Reconstruction solution on the square. Using various analytical techniques such as matched asymptotics and weighted energy methods as well as numerical investigations of the full Landau-de Gennes gradient flow system, we discover interesting interface dynamics which may be of practical relevance. That is, in each case we find that the front structures imposed by the initial conditions persist for an observable length of time. Further, these interfaces evolve according to the mean curvature of the geometry in the limit of $L \to 0$. This behaviour is a pronounced feature of the transient dynamics on each domain and for a wide range of initial conditions, suggesting interesting similarities and a generic character for front propagation in nematic liquid crystals for different geometries, critical points and transition temperatures.

Direct methods in the calculus of variations

In Chapter 6 we consider energy functionals of the form $I : \mathcal{A} \to \mathbb{R}$ where

$$I[u] = \int_\Omega f(\nabla u(x), u(x), x) \, dx,$$

for $f(p, z, x) : \mathbb{R}^2 \times \mathbb{R} \times \Omega \to \mathbb{R}$ and

$$\mathcal{A} := \left\{ u \in W^{1,2}(\Omega) : \ u = u_b \quad \text{on} \quad \partial\Omega \right\}.$$

The Sobolev space $W^{1,2}(\Omega)$ is the space of functions such that $u \in L^2(\Omega)$ and weak derivatives $u_{x_i} \in L^2(\Omega)$ for $i = 1, 2$, where $L^2(\Omega)$ is the set of square integrable functions on Ω. In general, $W^{k,p}(\Omega)$ is the space of functions such that $u \in L^p(\Omega)$ and all weak derivatives $u_{x_i}^\alpha \in L^p(\Omega)$ for $i = 1, 2$ and $\alpha = 1, ..., k$ [29, 40]. The weak derivative $u_{x_i}^\alpha$ is defined to satisfy

$$\int_\Omega u \phi_{x_i}^\alpha \, dx = (-1)^i \int_\Omega u_{x_i}^\alpha \phi \, dx, \tag{A.1}$$

for $i = 1, 2$ for all $\phi \in C_0^\infty(\Omega)$ (the set of all functions in $C^\infty(\Omega, \mathbb{R}^2)$ with closed and bounded support) [40].

The value $u(x)$ for $x \in \partial\Omega$ is the trace of u at the point x. The trace is a function which overcomes any problems which may arise from the fact that $u \in W^{1,2}(\Omega)$ may not be continuous [40]. From

[40], we have that if $\partial\Omega$ is C^1 then there exists a bounded linear function $T : W^{1,2}(\Omega) \to L^2(\partial\Omega)$ such that

(1) $T(u) = u|_{\partial\Omega}$ for all $u \in W^{1,2}(\Omega) \cap C(\bar{\Omega})$.

(2) $||T(u)||_{L^2(\partial\Omega)} \leq C||u||_{W^{1,2}(\Omega)} = C \left(\int_\Omega |\nabla u|^2 + u^2 \, dx\right)^{\frac{1}{2}}$ for all $u \in W^{1,2}(\Omega)$ for some constant C.

This result can be extended to Lipschitz domains [53] and hence this trace function T allows us to impose $u = u_b$ on $\partial\Omega$ in Chapter 6 as the boundaries of the domains in consideration are Lipschitz.

We are interested in the existence of a global minimizer of I over $\mathcal{A}$. From [29], a global minimizer of I exists provided that I satisfies the following properties:

(1) I is coercive over $\mathcal{A}$. That is,

$$I[u] \geq \alpha||u||_{W^{1,2}(\Omega)} + \beta \quad \text{for all} \quad u \in \mathcal{A}, \quad \text{for some} \quad \alpha > 0, \quad \beta \in \mathbb{R}.$$

(2) I is weakly lower semi-continuous. That is,

$$\liminf_{n\to\infty} I[u_n] \geq I(u) \quad \text{if} \quad u_n \rightharpoonup u \quad \text{in} \quad W^{1,2}(\Omega).$$

The sequence u_n converges weakly to u in $W^{1,2}(\Omega)$ which means that $\langle u_n, \phi \rangle_{W^{1,2}(\Omega)} \to \langle u, \phi \rangle_{W^{1,2}(\Omega)}$ for all $\phi \in W^{1,2}(\Omega)$. That is $\int_\Omega \nabla u_n \cdot \nabla \phi + u_n \phi \, dx \to \int_\Omega \nabla u \cdot \nabla \phi + u\phi \, dx$ for every $\phi \in W^{1,2}(\Omega)$.

The second condition is generally hard to verify. However, it is well known that convex functionals are weakly lower semi-continuous. A function $g : X \to \mathbb{R}$ is convex if $\lambda g(x) + (1 - \lambda)g(y) \geq g(\lambda x + (1 - \lambda)y)$ for every $x, y \in X$ and $\lambda \in [0, 1]$ [29]. We can use, for example, the following theorem from [40]:

Theorem A.1. *Assume that f is smooth, bounded from below and that the mapping $p \mapsto f(p, z, x)$ is convex for each $z \in \mathbb{R}$ and $x \in \Omega$. Then I is weakly lower semi-continuous in $W^{1,2}(\Omega)$.*

Once we know that I satisfies the properties (1) and (2), we have the existence of a minimizer of I over $\mathcal{A}$, provided that $\mathcal{A}$ is non-empty [40]. Throughout Chapter 6 we use that the minimizer

of our energy functional satisfies the Euler-Lagrange equations associated with the Landau-de Gennes energy functional. Consider the following theorem from [29]:

Theorem A.2. *Let $f(p, z, x) : \mathbb{R}^2 \times \mathbb{R} \times \Omega \to \mathbb{R}$ be a C^2 function. If $\bar{u} \in C^2(\Omega)$ and a solution of*

$$\inf \left\{ I[u] = \int_\Omega f(\nabla u, u, x) \, dx : \; u \in \mathcal{A} \right\}, \tag{A.2}$$

then $\bar{u}$ satisfies the Euler-Lagrange equations associated with I:

$$-\sum_{i=1}^{2} (f_{p_i}(\nabla u, u, x))_{x_i} + f_z(\nabla u, u, x) = 0. \tag{A.3}$$

However, in general it is not known that $\bar{u} \in C^2(\Omega)$ only that $\bar{u} \in W^{1,2}(\Omega)$. If we require that f_p and f_z satisfy further properties, we can show that $\bar{u} \in W^{1,2}(\Omega)$ is a solution of the weak form of the Euler-Lagrange equations (A.3), given by

$$\int_\Omega \sum_{i=1}^{2} f_{p_i}(\nabla u, u, x)\phi_{x_i} + f_z(\nabla u, u, x)\phi \, dx = 0 \quad \text{for all} \quad \phi \in W_0^{1,2}(\Omega), \tag{A.4}$$

using a theorem in [40]. The space $W_0^{1,2}(\Omega)$ is the space of functions in $W^{1,2}(\Omega)$ that vanish on the boundary $\partial\Omega$ [64] in the trace sense.

Theorem A.3. *Suppose f satisfies the following growth conditions:*

$$\begin{aligned} |f(p, z, x)| &\leq C(|p|^2 + |q|^2 + 1), \\ |f_p(p, z, x)| &\leq C(|p| + |z| + 1), \\ |f_z(p, z, x)| &\leq C(|p| + |z| + 1), \end{aligned} \tag{A.5}$$

for some constant C and all $p \in \mathbb{R}^2$, $z \in \mathbb{R}$ and $x \in \Omega$, and $\bar{u}$ satisfies (A.2). Then $\bar{u}$ is a weak solution of the Euler-Lagrange equations and satisfies (A.4).

From the weak form of the Euler-Lagrange equations we can use elliptic regularity and Sobolev embeddings to show that $\bar{u}$ is a classical solution of the Euler-Lagrange equations. For example in Proposition 6.2 we consider the energy functional

$$H[q] = \int_\Omega |\nabla q|^2 + \frac{\lambda^2}{L} \left(Cq^4 - \frac{B^2}{2C} q^2 \right) \, dA,$$

for $q \in W^{1,2}(\Omega)$ and satisfying suitable boundary conditions (see (6.5)) on $\partial\Omega$. As H satisfies the

necessary properties (1), (2) and (A.5) and Ω is Lipschitz, we have the existence of a minimizer $\bar{q}$ of H which is a weak solution of the Euler-Lagrange equations associated with H. That is,

$$\int_\Omega 2\nabla q \cdot \nabla \phi \, \mathrm{d}x = \int_\Omega \frac{\lambda^2}{L}\left(4Cq^3 - \frac{B^2}{C^2}q\right)\phi \, \mathrm{d}x,$$

for all $\phi \in W_0^{1,2}(\Omega)$. We employ the Elliptic Regularity Theorem and the Sobolev Embedding Theorem to show that $q \in C^2(\Omega)$ and is a classical solution of the Euler-Lagrange equation associated with H.

Theorem A.4 (Elliptic Regularity Theorem). *Suppose $u \in W^{1,2}(\Omega)$ such that*

$$\int_\Omega \nabla u \cdot \nabla \phi \, \mathrm{d}x = \int_\Omega f\phi \, \mathrm{d}x,$$

for all ϕ in $W_0^{1,2}(\Omega)$ and $f \in W^{k,2}(\Omega)$. Then $u \in W^{k+2,2}(\Omega)$ [2].

Theorem A.5 (Sobolev Embedding Theorem). *Let Ω be a bounded open domain with Lipschitz boundary, then $W^{k,p}(\Omega) \subseteq W^{l,q}(\Omega)$ provided $k - \frac{2}{p} > l - \frac{2}{q}$. Further $W^{k,p}(\Omega) \subset C^r(\Omega)$ provided $k - \frac{2}{p} > r$ [2].*

We first show that $f = \frac{\lambda^2}{L}\left(4Cq^3 - \frac{B^2}{C^2}q\right) \in W^{0,2}(\Omega) = L^2(\Omega)$ using that $q \in W^{1,2}(\Omega)$. This is achieved by showing that $q^3 \in W^{0,2}(\Omega)$ as $q \in W^{0,2}(\Omega)$ is clear. The Sobolev Embedding Theorem gives that $W^{1,2}(\Omega) \subseteq W^{0,q}(\Omega) = L^q(\Omega)$ for $2 \le q < \infty$. Hence $q \in L^6(\Omega)$ and so $q^3 \in L^2(\Omega)$ as needed. Therefore $f \in W^{0,2}(\Omega)$ and the Elliptic Regularity Theorem then gives that $q \in W^{2,2}(\Omega)$.

We then show that $f = \frac{\lambda^2}{L}\left(4Cq^3 - \frac{B^2}{C^2}q\right) \in W^{1,2}(\Omega)$ using that $q \in W^{2,2}(\Omega)$. This is achieved by proving that $q^3 \in W^{1,2}(\Omega)$. First we note that $q^3 \in L^2(\Omega)$ as $W^{2,2}(\Omega) \subseteq L^6(\Omega)$ by the Sobolev Embedding Theorem. Secondly, we need to show that $3q^2q_{x_i} \in L^2(\Omega)$. This follows from the Cauchy-Schwarz inequality and the Sobolev Embedding Theorem. The Elliptic Regularity Theorem then gives that $q \in W^{3,2}(\Omega)$.

We repeat the steps again to yield that $q \in W^{4,2}(\Omega)$. Then, by the second part of the Sobolev Embedding Theorem, $W^{4,2}(\Omega) \subset C^2(\Omega)$ and we have that $q \in C^2(\Omega)$. Therefore q is a classical solution of the Euler-Lagrange equations and hence satisfies

$$\nabla^2 q = \frac{\lambda^2}{L}\left(2Cq^3 - \frac{B^2}{2C}q\right).$$

A.0.1   The vector case

It is possible to apply the same approach to the vector case as for the scalar case discussed previously. This is required in Chapter 6 for the existence of a minimizer of the full Landau-de Gennes energy functional and for the system in Proposition (6.1). The energy functional is now of the form

$$I[\mathbf{u}] = \int_\Omega f(\nabla\mathbf{u}(x), \mathbf{u}(x), x)\,dx,$$

and the admissible space is

$$\mathcal{A} := \left\{\mathbf{u} \in W^{1,2}(\Omega, \mathbb{R}^m) : \mathbf{u} = \mathbf{u}_b \quad \text{on} \quad \partial\Omega\right\},$$

where $\mathbf{u} : \Omega \to \mathbb{R}^m$ and $f : \mathbb{R}^{2\times m} \times \mathbb{R}^m \times \Omega \to \mathbb{R}^m$ [40]. We can apply the previous theory to this case in a straightforward manner with the two following theorems from [40].

Theorem A.6. *If I is coercive, $f(p, z, x)$ is convex in the variable p and $\mathcal{A}$ is non-empty, then there exists $\bar{\mathbf{u}} \in \mathcal{A}$ solving*

$$\inf\left\{I[\mathbf{u}] = \int_\Omega f(\nabla\mathbf{u}, \mathbf{u}, x)\,dx : \mathbf{u} \in \mathcal{A}\right\}. \tag{A.6}$$

This theorem gives the existence of a minimizer of I over $\mathcal{A}$. The next theorem gives that minimizers of I are weak solutions of the Euler-Lagrange equations associated with I.

Theorem A.7. *If f satisfies the conditions* (A.5) *and $\bar{\mathbf{u}}$ satisfies* (A.6). *Then $\bar{u}$ is a weak solution of the Euler-Lagrange equations*

$$-\sum_{i=1}^n (f_{p_i^k}(\nabla\mathbf{u}, \mathbf{u}, x))_{x_i} + f_{z^k}(\nabla\mathbf{u}, \mathbf{u}, x) = 0 \quad \text{in} \quad \Omega,$$

for $k = 1, 2, ...m$ and $u^k = u_b{}^k$ on $\partial\Omega$. That is, $\bar{u}$ satisfies

$$\sum_{k=1}^m \int_\Omega \sum_{i=1}^2 f_{p_i^k}(\nabla\mathbf{u}, \mathbf{u}, x)\phi_{x_i}^k + f_{z^k}f(\nabla\mathbf{u}, \mathbf{u}, x)\phi^k\,dx = 0,$$

for all $\phi \in W_0^{1,2}(\Omega, \mathbb{R}^m)$.

Again, we can apply the Elliptic Regularity Theorem and the Sobolev Embedding Theorem to show that the energy minimizers in Chapter 6 are classical solutions of the relevant Euler-Lagrange equations.

Bibliography

[1] R. A. ADAMS, *The Rellich-Kondrachov theorem for unbounded domains*, Archive for Rational Mechanics and Analysis, 29 (1968), pp. 390–394.

[2] R. A. ADAMS AND J. J. FOURNIER, *Sobolev spaces*, vol. 140, Academic Press, 2003.

[3] D. ALLENDER AND L. LONGA, *Landau–de Gennes theory of biaxial nematics reexamined*, Physical Review E, 78 (2008), p. 011704.

[4] L. AMBROSIO AND E. G. VIRGA, *A boundary-value problem for nematic liquid crystals with a variable degree of orientation*, Archive for Rational Mechanics and Analysis, 114 (1991), pp. 335–347.

[5] N. ANDRÉ AND I. SHAFRIR, *Minimization of a Ginzburg-Landau type functional with nonvanishing Dirichlet boundary condition*, Calculus of Variations and Partial Differential Equations, 7 (1998), pp. 191–217.

[6] V. BADALASSI, H. CENICEROS, AND S. BANERJEE, *Computation of multiphase systems with phase field models*, Journal of Computational Physics, 190 (2003), pp. 371–397.

[7] J. BALL, *Mathematics of liquid crystals*, Cambridge Centre for Analysis short course, (2012), pp. 13–17.

[8] F. BETHUEL, H. BREZIS, AND F. HÉLEIN, *Asymptotics for the minimization of a Ginzburg-Landau functional*, Calculus of Variations and Partial Differential Equations, 1 (1993), pp. 123–148.

[9] ——, *Ginzburg-Landau Vortices*, vol. 13, Springer Science & Business Media, 2012.

[10] F. BISI, E. C. GARTLAND JR, R. ROSSO, AND E. G. VIRGA, *Order reconstruction in frustrated nematic twist cells*, Physical Review E, 68 (2003), p. 021707.

156

[11] A. BRAIDES, *A handbook of Γ-convergence*, Handbook of Differential Equations: Stationary Partial Differential Equations, 3 (2006), pp. 101–213.

[12] H. BREZIS, *The interplay between analysis and topology in some nonlinear PDE problems*, Bulletin of the American Mathematical Society, 40 (2003), pp. 179–201.

[13] L. BRONSARD AND R. V. KOHN, *Motion by mean curvature as the singular limit of Ginzburg-Landau dynamics*, Journal of Differential Equations, 90 (1991), pp. 211–237

[14] L. BRONSARD AND F. REITICH, *On three-phase boundary motion and the singular limit of a vector-valued Ginzburg-Landau equation*, Archive for Rational Mechanics and Analysis, 124 (1993), pp. 355–379.

[15] L. BRONSARD AND B. STOTH, *On the existence of high multiplicity interfaces*, Mathematical Research Letters, 3 (1996), pp. 41–50 1073–2780.

[16] ——, *The singular limit of a vector-valued reaction-diffusion process*, Transactions of the American Mathematical Society, 350 (1998), pp. 4931–4953.

[17] J. BUCHER, *Numerical analysis of ordinary differential equations*, Chichester:Wiley, 1987.

[18] G. CAGINALP, *An analysis of a phase field model of a free boundary*, Archive for Rational Mechanics and Analysis, 92 (1986), pp. 205–245.

[19] D. CALHOUN AND R. J. LEVEQUE, *A Cartesian grid finite-volume method for the advection-diffusion equation in irregular geometries*, Journal of Computational Physics, 157 (2000), pp. 143–180.

[20] G. CANEVARI, A. MAJUMDAR, AND A. SPICER, *Order reconstruction for nematics on squares and regular polygons: a Landau-de Gennes study*, arXiv preprint arXiv:1606.06575, (2016).

[21] A. CARPIO AND L. L. BONILLA, *Depinning transitions in discrete reaction-diffusion equations*, SIAM Journal on Applied Mathematics, 63 (2003), pp. 1056–1082.

[22] S. CHANDRASEKHAR, *Liquid Crystals*, Cambridge University Press, 1992.

[23] S. C. CHAPRA AND R. P. CANALE, *Numerical methods for engineers*, vol. 2, McGraw-Hill, 1998.

[24] P. COLELLA, D. T. GRAVES, B. J. KEEN, AND D. MODIANO, *A cartesian grid embedded boundary method for hyperbolic conservation laws*, Journal of Computational Physics, 211 (2006), pp. 347–366.

[25] H. J. COLES AND M. N. PIVNENKO, *Liquid crystal blue phases with a wide temperature range*, Nature, 436 (2005), pp. 997–1000.

[26] P. J. COLLINGS, *Liquid crystals: nature's delicate phase of matter*, Princeton University Press, 2002.

[27] P. J. COLLINGS AND M. HIRD, *Introduction to liquid crystals: chemistry and physics*, CRC Press, 1997.

[28] M. G. CRANDALL AND P. H. RABINOWITZ, *Bifurcation from simple eigenvalues*, Journal of Functional Analysis, 8 (1971), pp. 321–340.

[29] B. DACOROGNA, *Direct methods in the calculus of variations*, vol. 78, Springer Science & Business Media, 2007.

[30] H. DANG, P. C. FIFE, AND L. PELETIER, *Saddle solutions of the bistable diffusion equation*, Zeitschrift für angewandte Mathematik und Physik ZAMP, 43 (1992), pp. 984–998.

[31] P. G. DE GENNES AND J. PROST, *The physics of liquid crystals*, vol. 23, Clarendon Press Oxford, 1993.

[32] W. DEN BOER, *Active matrix liquid crystal displays: fundamentals and applications*, Elsevier, 2011.

[33] G. DI FRATTA, J. ROBBINS, V. SLASTIKOV, AND A. ZARNESCU, *Half-integer point defects in the Q-tensor theory of nematic liquid crystals*, Journal of Nonlinear Science, 26 (2016), pp. 121–140.

[34] N. DIRR, P. W. DONDL, G. R. GRIMMETT, A. E. HOLROYD, AND M. SCHEUTZOW, *Lipschitz percolation*, Electron. Comm. Probab, 15 (2010), pp. 14–21.

[35] N. DIRR AND N. K. YIP, *Pinning and de-pinning phenomena in front propagation in heterogeneous media*, Interfaces and Free Boundaries, 8 (2006), pp. 79–109.

[36] N. P. DIRR, P. DONDL, AND M. SCHEUTZOW, *Pinning of interfaces in random media*, Interfaces and Free Boundaries, 13 (2011), pp. 411–421.

[37] D. DUNMUR AND T. SLUCKIN, *Soap, science and flat-screen TVs: a history of liquid crystals*, Oxford University Press, 2010.

[38] S. ELSTON AND R. SAMBLES, *The optics of thermotropic liquid crystals*, Taylor & Francis, 1998.

[39] J. L. ERICKSEN, *Liquid crystals with variable degree of orientation*, Archive for Rational Mechanics and Analysis, 113 (1991), pp. 97–120.

[40] L. C. EVANS, *Partial differential equations*, American Mathematical Society, 1998.

[41] L. C. Evans, H. M. Soner, and P. E. Souganidis, *Phase transitions and generalized motion by mean curvature*, Communications on Pure and Applied Mathematics, 45 (1992), pp. 1097–1123.

[42] J. Fabero, A. Bautista, and L. Casasús, *An explicit finite differences scheme over hexagonal tessellation*, Applied Mathematics Letters, 14 (2001), pp. 593–598.

[43] M. Fei, W. Wang, P. Zhang, and Z. Zhang, *Dynamics of the nematic-isotropic sharp interface for the liquid crystal*, SIAM Journal on Applied Mathematics, 75 (2015), pp. 1700–1724.

[44] P. C. Fife and J. B. McLeod, *The approach of solutions of nonlinear diffusion equations to travelling front solutions*, Archive for Rational Mechanics and Analysis, 65 (1977), pp. 335–361

[45] D. S. Fisher, *Collective transport in random media: from superconductors to earthquakes*, Physics Reports, 301 (1998), pp. 113–150.

[46] M. Freiser, *Ordered states of a nematic liquid*, Physical Review Letters, 24 (1970), p. 1041.

[47] H. Garcke, B. Nestler, and B. Stoth, *On anisotropic order parameter models for multi-phase systems and their sharp interface limits*, Physica D: Nonlinear Phenomena, 115 (1998), pp. 87–108.

[48] E. C. Gartland, Jr and S. Mkaddem, *Instability of radial hedgehog configurations in nematic liquid crystals under Landau–de Gennes free-energy models*, Physical Review E, 59 (1999), pp. 563–567.

[49] D. Golovaty and J. A. Montero, *On minimizers of a Landau–de Gennes energy functional on planar domains*, Archive for Rational Mechanics and Analysis, 213 (2014), pp. 447–490.

[50] L. P. Gorkov, *Microscopic derivation of the Ginzburg-Landau equations in the theory of superconductivity*, Sov. Phys. JETP, 9 (1959), pp. 1364–1367.

[51] E. F. Gramsbergen, L. Longa, and W. H. de Jeu, *Landau theory of the nematic-isotropic phase transition*, Physics Reports, 135 (1986), pp. 195–257.

[52] G. W. Gray and S. M. Kelly, *Liquid crystals for twisted nematic display devices*, Journal of Materials Chemistry, 9 (1999), pp. 2037–2050.

[53] P. Grisvard, *Elliptic problems in nonsmooth domains*, vol. 69, SIAM, 2011.

[54] D. Henao and A. Majumdar, *Symmetry of uniaxial global Landau–de Gennes minimizers in the theory of nematic liquid crystals*, SIAM Journal on Mathematical Analysis, 44 (2012), pp. 3217–3241

[55] R. IGNAT, L. NGUYEN, V. SLASTIKOV, AND A. ZARNESCU, *Instability of point defects in a two-dimensional nematic liquid crystal model*, in Annales de l'Institut Henri Poincare (C) Non Linear Analysis, Elsevier, 2015.

[56] ——, *Stability of the melting hedgehog in the Landau-de Gennes theory of nematic liquid crystals*, Archive for Rational Mechanics and Analysis, 215 (2015), pp. 633–673.

[57] C. JONES, *Bistable liquid crystal displays*, in Handbook of Visual Display Technology, Springer, 2012, pp. 1507–1543.

[58] M. KARDAR, *Nonequilibrium dynamics of interfaces and lines*, Physics reports, 301 (1998), pp. 85–112.

[59] H. KITZEROW AND C. BAHR, *Chirality in liquid crystals*, Springer Science & Business Media, 2001.

[60] S. KRALJ AND A. MAJUMDAR, *Order reconstruction patterns in nematic liquid crystal wells*, Proceedings of the Royal Society of London Series A, 470 (2014), p. 40276.

[61] X. LAMY, *Some properties of the nematic radial hedgehog in the Landau–de Gennes theory*, Journal of Mathematical Analysis and Applications, 397 (2013), pp. 586–594

[62] ——, *Bifurcation analysis in a frustrated nematic cell*, Journal of Nonlinear Science, 24 (2014), pp. 1197–1230.

[63] ——, *Uniaxial symmetry in nematic liquid crystals*, in Annales de l'Institut Henri Poincare (C) Non Linear Analysis, vol. 32, Elsevier, 2015, pp. 1125–1144.

[64] G. LEONI, *A first course in Sobolev spaces*, vol. 105, American Mathematical Society Providence, RI, 2009.

[65] R. J. LEVEQUE, *Finite volume methods for hyperbolic problems*, vol. 31, Cambridge University Press, 2002.

[66] ——, *Finite difference methods for ordinary and partial differential equations: steady-state and time-dependent problems*, vol. 98, SIAM, 2007.

[67] F. H. LIN, *On nematic liquid crystals with variable degree of orientation*, Communications on Pure and Applied Mathematics, 44 (1991), pp. 453–468.

[68] F. H. LIN AND C. LIU, *Static and dynamic theories of liquid crystals*, J. Partial Differential Equations, 14 (2001), pp. 289–330.

[69] C. LUO, A. MAJUMDAR, AND R. ERBAN, *The dynamics of bistable liquid crystal wells*, Journal of Computational Physics, (2011).

[70] ——, *Multistability in planar liquid crystal wells*, Physical Review E, 85 (2012), p. 061702.

[71] A. MAJUMDAR, *Equilibrium order parameters of nematic liquid crystals in the Landau-de Gennes theory*, European Journal of Applied Mathematics, 21 (2010), pp. 181–203

[72] ——, *Order parameters in the Landau–de Gennes theory–the static and dynamic scenarios*, Liquid Crystals, 38 (2011), pp. 169–181

[73] ——, *The radial-hedgehog solution in Landau–de Gennes' theory for nematic liquid crystals*, European Journal of Applied Mathematics, 23 (2012), pp. 61–97

[74] A. MAJUMDAR, P. A. MILEWSKI, AND A. SPICER, *Front propagation at the nematic-isotropic transition temperature*, SIAM Journal on Applied Mathematics, 76 (2016), pp. 1296–1320.

[75] A. MAJUMDAR, A. PISANTE, AND D. HENAO, *Uniaxial versus biaxial character of nematic equilibria in three dimensions*, arXiv preprint arXiv:1312.3358, (2013).

[76] A. MAJUMDAR AND A. ZARNESCU, *Landau–de Gennes theory of nematic liquid crystals: the Oseen–Frank limit and beyond*, Archive for Rational Mechanics and Analysis, 196 (2010), pp. 227–280

[77] S. MEIBOOM, J. P. SETHNA, P. ANDERSON, AND W. BRINKMAN, *Theory of the blue phase of cholesteric liquid crystals*, Physical Review Letters, 46 (1981), p. 1216.

[78] G. MEIER, E. SACKMANN, AND J. G. GRABMAIER, *Applications of liquid crystals*, Springer Science & Business Media, 2012.

[79] K. MERKEL, A. KOCOT, J. VIJ, R. KORLACKI, G. MEHL, AND T. MEYER, *Thermotropic biaxial nematic phase in liquid crystalline organo-siloxane tetrapodes*, Physical Review Letters, 93 (2004), p. 237801.

[80] S. MKADDEM AND E. GARTLAND JR, *Fine structure of defects in radial nematic droplets*, Physical Review E, 62 (2000), p. 6694.

[81] J. MORGAN, *Global existence for semilinear parabolic systems*, SIAM Journal on Mathematical Analysis, 20 (1989), pp. 1128–1144

[82] N. J. MOTTRAM AND C. J. NEWTON, *Introduction to Q-tensor theory*, arXiv preprint arXiv:1409.3542, (2014).

[83] OLEG D. LAVRENTOVICH, LIQUID CRYSTAL INSTITUTE, KENT STATE UNIVERSITY, National Science Federation www.nsf.gov.

[84] N. OWEN, J. RUBINSTEIN, AND P. STERNBERG, *Minimizers and gradient flows for singularly perturbed bi-stable potentials with a Dirichlet condition*, Proceedings of the Royal Society of London Series A, 429 (1990), pp. 505–532.

[85] R. S. PALAIS, *The principle of symmetry criticality*, Communications in Mathematical Physics, 69 (1979), pp. 19–30.

[86] P. Palffy-Muhoray, E. Gartland, and J. Kelly, *A new configurational transition in inhomogeneous nematics*, Liquid Crystals, 16 (1994), pp. 713–718.

[87] M. A. Peletier, *Energies, gradient flows, and large deviations: a modelling*, (2011).

[88] P. S. Pershan, *Structure of liquid crystal phases*, vol. 23, World Scientific, 1988.

[89] L. M. Pismen, *Patterns and interfaces in dissipative dynamics*, Springer, 2006.

[90] V. Popa-Nita and T. Sluckin, *Kinetics of the nematic-isotropic interface*, Journal de Physique II, 6 (1996), pp. 873–884

[91] V. Popa-Nita, T. Sluckin, and A. Wheeler, *Statics and kinetics at the nematic-isotropic interface: effects of biaxiality*, Journal de Physique II, 7 (1997), pp. 1225–1243

[92] A. Prostakov, E. Larin, and M. Stryukov, *Phenomenological theory of phase transition from isotropic to uniaxial, biaxial, and reentrant nematic phases in achiral liquid crystals*, Crystallography Reports, 47 (2002), pp. 1041–1048.

[93] S. C. Reddy and L. N. Trefethen, *Stability of the method of lines*, Numerische Mathematik, 62 (1992), pp. 235–267.

[94] M. Renardy and R. C. Rogers, *An introduction to partial differential equations*, vol. 13, Springer Science & Business Media, 2006.

[95] M. Robinson, C. Luo, A. Majumdar, R. Erban, and P. Farrell, *Lattice and off-lattice based models for bistable liquid crystal devices*, In preparation, 2016.

[96] J. Rubinstein, P. Sternberg, and J. B. Keller, *Fast reaction, slow diffusion, and curve shortening*, SIAM Journal on Applied Mathematics, 49 (1989), pp. 116–133.

[97] D. H. Sattinger, *On the stability of waves of nonlinear parabolic systems*, Advances in Mathematics, 22 (1976), pp. 312–355.

[98] T. Scharf, *Polarized light in liquid crystals and polymers*, John Wiley & Sons, 2007.

[99] M. Schatzman, *On the stability of the saddle solution of Allen-Cahn's equation*, Proceedings of the Royal Society of Edinburgh: Section A Mathematics, 125 (1995), pp. 1241–1275.

[100] N. Schopohl and T. Sluckin, *Defect core structure in nematic liquid crystals*, Physical Review Letters, 59 (1987), p. 2582.

[101] A. Sengupta, *Topological microfluidics: nematic liquid crystals and nematic colloids in microfluidic environment*, Springer Science & Business Media, 2013.

[102] A. Sengupta, U. Tkalec, M. Ravnik, J. M. Yeomans, C. Bahr, and S. Herminghaus, *Liquid crystal microfluidics for tunable flow shaping*, Physical Review Letters, 110 (2013), p. 048303.

[103] I. SHAFRIR, *On a class of singular perturbation problems*, Stationary Partial Differential Equations, 1 (2004), pp. 297–383.

[104] P. STERNBERG, *The effect of a singular perturbation on nonconvex variational problems*, Archive for Rational Mechanics and Analysis, 101 (1988), pp. 209–260

[105] ——, *Vector-valued local minimizers of nonconvex variational problems*, J. Math, 21 (1991), pp. 799–807.

[106] I. W. STEWART, *The static and dynamic continuum theory of liquid crystals: a mathematical introduction*, CRC Press, 2004.

[107] C. TSAKONAS, A. DAVIDSON, C. BROWN, AND N. MOTTRAM, *Multistable alignment states in nematic liquid crystal filled wells*, Applied Physics Letters, 90 (2007), p. 1913.

[108] M. VAN DYKE, *Perturbation methods in fluid mechanics*, Parabolic Press, Incorporated, 1975.

[109] E. G. VIRGA, *Variational theories for liquid crystals*, vol. 8, CRC Press, 1995.

[110] E. W. WEISSTEIN, *Spherical Bessel Differential Equation*, From Mathworld–A Wolfram Web Resource: http://mathworld.wolfram.com/SphericalBesselDifferentialEquation.html.

[111] V. WILLIAMS, *Nematic liquid crystal*, https://www.youtube.com/watch?v=8jS2nvwqzpA, (2015).

[112] S. XIA, L. PONSON, G. RAVICHANDRAN, AND K. BHATTACHARYA, *Adhesion of heterogeneous thin films I: Elastic heterogeneity*, Journal of the Mechanics and Physics of Solids, 61 (2013), pp. 838–851.

[113] ——, *Adhesion of heterogeneous thin films II: Adhesive heterogeneity*, Journal of the Mechanics and Physics of Solids, 83 (2015), pp. 88–103.

[114] L. YU AND A. SAUPE, *Observation of a biaxial nematic phase in potassium laurate-1-decanol-water mixtures*, Physical Review Letters, 45 (1980), p. 1000.